On the Atmospheric Saliency of Space Debris Reentries: Estimating Distribution, Lifetime and Radiative Forcing of Reentry-Ablated Alumina

by

Asha Kailin Jain

B.S., University of Texas at Austin, 2021

Submitted to the Department of Aeronautics and Astronautics
in partial fulfillment of the requirements for the degree of

MASTER OF SCIENCE IN AERONAUTICS AND ASTRONAUTICS

at the

MASSACHUSETTS INSTITUTE OF TECHNOLOGY

June 2023

Authored by: Asha Kailin Jain
Department of Aeronautics and Astronautics
May 2023

Certified by: Daniel E. Hastings
Professor of Aeronautics and Astronautics, Thesis Supervisor

Accepted by: Jonathan P. How
R. C. Maclaurin Professor of Aeronautics and Astronautics
Chair, Graduate Program Committee

On the Atmospheric Saliency of Space Debris Reentries: Estimating Distribution, Lifetime and Radiative Forcing of Reentry-Ablated Alumina

by

Asha Kailin Jain

Submitted to the Department of Aeronautics and Astronautics
on May 2023, in partial fulfillment of the
requirements for the degree of
MASTER OF SCIENCE IN AEROSPACE ENGINEERING

Abstract

As the space economy grows, numerous satellite operators are looking to build megaconstellations in Low Earth Orbit (LEO). These megaconstellations are expected to have hundreds to thousands of satellites operating in altitudes from 350km to 650km. Once built, many of these constellations will require satellite replenishment to replace spent satellites, leading to a continuous flow of new satellites and rocket bodies into LEO.

To make room for future satellites, decommissioned space objects are often removed from LEO via atmospheric reentry. During reentry, unshielded satellites and rocket bodies experience extreme heating loads and material ablation, depositing small metallic particles in atmosphere. These particles can remain suspended in the atmosphere and interact with important atmospheric processes. However, the salience of these particles and their atmospheric effects are unknown.

To address this gap, this thesis estimates the atmospheric consequences of reentry-ablated alumina, characterizing its distribution, lifetime and radiative effect using a state-of-the-art atmospheric model. We consider a future scenario where all of the megaconstellations with public Federal Communications Commission filings are deployed and maintained, leading to steady flux of 13,900 satellite reentries and 500 rocket body reentries per year by 2040. As a first order, conservative approximation, this work finds that reentries in this scenario produce alumina particles that persist in the atmosphere for one to two years, leading to a modest radiative forcing of approximately $-0.2 mW/m^2$. We present various metrics to normalize this radiative forcing and compare these metrics across other industries. Reentries produce a stronger radiative forcing per reentry event than the radiative forcing that aviation produces per flight. We conclude that future work is necessary to increase the fidelity of our results and better understand the full scope of atmospheric consequences of reentry-ablated alumina.

Acknowledgments

This work would not have been possible without the generous support of numerous people.

First, I would like to express my deepest gratitude to my advisor, Dr. Daniel Hastings. Your early and steadfast support of my curiosity in space, sustainability and policy gave me the opportunity to chase my interests. Your confidence in me helped me find my footing during times of uncertainty. As my mentor, I truly appreciate the advice and experience you've shared, especially as I begin navigating the space policy arena.

To Dr. Sebastian Eastham, I would like to express my sincere appreciation for your guidance, time and mentorship. I am extremely grateful for the time you dedicated to this endeavor and to teaching me the art and science of atmospheric modeling and interpretation. Without your guidance, support and investment, this research would not have been possible.

Many thanks to Dr. Arlene Fiore and Dr. Jeffery Scott in the Department of Earth and Planetary Sciences at MIT. Your kindness and support of my work gave me the opportunity to explore additional experiments and identify interesting sensitivities. Thank you, Arlene, for granting me access to your research group's cluster and for helping me navigate the Community Earth System Model (CESM). Thank you, Jeff, for the numerous hours you spent to get the Whole Atmosphere Community Climate Model (WACCM) running and validated and for teaching me the basics on how to use your supercomputing system.

I would also like to thank a number of researchers at the University Corporation for Atmospheric Research: Dr. Douglas Kinnison, Dr. Mike Mills, Dr. Francis Vitt, Dr. Simone Tilmes, Dr. Charles Bardeen, and Dr. Louisa Emmons. Your expertise in modeling aerosols within WACCM lead to crucial advise for selecting the appropriate component model set up to address my research question. I thank you for your willingness to help solve bugs and answer my questions as I learned to use WACCM. A special thank you to Simone and Mike who went above and beyond to help me identify the appropriate modeling methodology and solve modeling errors. Thank you to Simone and Dr. Rebecca Buchholz for providing access to UCAR's supercomputing system which was necessary to finish this work.

Many thanks to Dr. Natalie Mahowald and Sarah Deutsch for teaching me how to modify emission inputs to CESM and interact with the terrestrial dust model. I truly appreciate

your willingness to answer my questions on the Modal Aerosol Model (MAM4). Thank you for your help to identify a method to remove prognostic dust emissions.

I had the pleasure of working with Dr. Christopher Maloney at the National Oceanic and Atmospheric Administration. Chris, thank you for sharing your advice on modeling alumina aerosols, and its radiative forcing. I appreciate the reference to previous work to characterize alumina's refractive indices.

I'd also like to acknowledge the large team at Aerospace Corporation that helped produce and release space debris reentry forecasts. Thank you Dr. Grant Cates for your eager willingness to collaborate and share essential reentry forecasting predictions. Thank you to Patrick Bauer, Catrina Melograna, Karen Jones and Dr. Josef Koller for supporting the initiative to publish these reentry forecasts.

Thank you to Dr. Wuhu Feng and Dr. John Plane at the University of Leeds in the United Kingdom. I greatly appreciate the time you spent answering my questions regarding the atmospheric chemistry of meteoric aluminum and your approach to modeling these interactions. Thank you, Wuhu, for your kindness in laying out detailed steps on how to modify CESM chemical processors and configuration files to allow for user-specified changes.

Thanks should also go to Dr. Grant Stokes and his team at MIT Lincoln Laboratory. Your feedback and insightful responses to my research presentation helped identify new questions to address, including how present-day reentries compare to the historical reentry population.

Lastly, I would be remiss if I did not mention my friends and family who supported me throughout my journey in graduate school. Thank you to my loving partner, Jerome. I deeply appreciate your unwavering support of my education and my choice to attend MIT that took us across the country, away from family and your place of work, to start life anew in Cambridge. Thank you to my family who has supported me every step of the way. And thank you to my peers and friends in the Aero/Astro community. I am grateful for the support and kindness this community has shown me.

Contents

List of Figures

List of Tables

Chapter 1

Executive Summary

As policymakers look to regulate megaconstellations and discuss atmospheric reentry as a means of space debris disposal, it is important to understand the environmental impacts of reentry by-products. During reentry, aluminum in space debris objects rapidly melts, forming small alumina (Al_2O_3) particles that settle in the global atmosphere. A study was conducted to quantify the lifetime of reentry-ablated alumina and its direct radiative forcing, a measure of how these particles trap light in Earth's atmosphere and contribute to global warming. Positive radiative forcing warms while negative radiative forcing cools Earth's surface.

We consider a 2040 economic scenario where all megaconstellations filed at the Federal Communications Commission (FCC) are fully developed, leading to 13,900 satellite and 500 rocket body reentries per year. This flux corresponds to a reentry event occurring once every 40 mins globally. We assume that reentering satellites are 21% aluminum of which 58% ablates, and rocket bodies are 70% aluminum of which 31% ablates, resulting in 1.33 Gg of alumina released in the atmosphere per year in the 2040 economic scenario.

We find that reentry-ablated alumina persists in the atmosphere for 1 to 2 years, accumulating at altitudes between 20 and 50 km with a nearly uniform distribution across the Northern and Southern Hemispheres.

In the 2040 economic scenario, space debris reentries produce -0.2 mW/m^2 cooling radiative forcing. To compare, the aviation industry produces a net warming radiative forcing of 100 mW/m^2, contributing approximately 4% to the global human-induced radiative forcing

[69, 76]. Space debris reentries in the 2040 economic scenario therefore produce 0.2% of aviation's present-day radiative forcing. A 2025 influx of 150 Mg of alumina produces -0.0224 mW/m^2 cooling radiative forcing, amounting to 0.02% of aviation's present day radiative forcing.

These results are sensitive to different assumptions for alumina's initial particle size and coagulation properties, both of which remain uncertain. This study found that larger alumina particles have a 50% shorter lifetime than small alumina particles, producing a 10% smaller radiative forcing. These uncertainties should be refined with laboratory and in-situ verification.

Current reentry practices produce a modest radiative forcing. Policies that promote space debris reentry and satellite design for demise are likely to increase the amount of reentry-ablated alumina, thereby increasing its direct radiative forcing. At present-day reentry fluxes, these policies are tolerable, although active monitoring of the space debris aluminum influx will help decision makers and scientists track and reevaluate the consequences of reentry-ablated aluminum over time, especially as megaconstellations grow. This monitoring could include collecting data on satellite aluminum composition and reentry date.

Reentry by-products could affect other important atmospheric processes that were not assessed in this study, including the potential for stratospheric heating, interactions with existing stratospheric particles, modification of natural clouds, and ozone depletion. Further study is warranted to capture and monitor the impact of these effects.

Chapter 2

Introduction

The recent increase in space activity has marked the start of the New Space economy. Diversifying away from large government programs, several new commercial companies and young national agencies have begun operating space systems in Low Earth Orbit (LEO). Many of these new space actors are building megaconstellations, groups of hundreds to tens of thousands of satellites that work together to provide a service and require numerous launches per year to develop and maintain [129, 118].

These remarkable constellations are expected to operate in unprecedented orbital conditions. In-orbit, there are more than 40,000 tracked objects, a large fraction of which is debris, with millions more undetectable, and untrackable pieces. As governments, space agencies, and commercial operators address the growing space debris problem, atmospheric reentry is often recommended for Low Earth to geostationary transfer orbits to remove unwanted objects [102]. Several policies also impose mandatory deadlines to dispose of a space object once its mission has completed. As a result of the growing space activity and requirements to deorbit, the number of atmospheric reentries will grow over the next decade. Recent data from the Aerospace Corporation gives evidence of this trend with reentries in 2021 demonstrating a 1.6 fold increase over 2020 [45].

Despite plans to reenter thousands of satellites per year, the environmental consequences of these debris reentries are poorly understood. This unprecedented level of space activity in LEO places importance on understanding what is a sustainable and safe rate of reentry.

Historically, the scientific community has been assumed that space debris reentries do

not significantly alter the composition nor behavior of the atmosphere. The atmosphere has assumed to be an "infinite" sink. Others have argued that since the meteor entry mass far exceeds the anthropogenic reentry mass, the effects of space debris are negligible [141]. The rapid growth in the space object population and notable differences in space debris material composition compared to meteors call these assumptions into question [129, 135, 74]. As the public's attention to environmental consequences grows, there is an increasing interest among government regulators, corporations and aerospace consumers to understand the atmospheric salience of space debris reentries [65].

Unlike any other human activity, the space industry directly emits into all layers of the atmosphere. Given the relative isolation of the upper atmosphere from other human and terrestrial emissions, space debris reentries have the potential to become a significant source of high-altitude emissions that could possibly alter the composition and behavior of the upper atmosphere [20].

Space debris reentries are comprised of satellites, rocket bodies and other jettisoned components, such as explosive bolts and covers. These objects are usually decommissioned such that batteries are depleted and stored propellants are released, although some objects will die prior to decommissioning. Some objects, like rocket bodies on geostationary transfer orbits, are also intentionally maneuvered onto a reentry trajectory. During these maneuvers, the object's perigee is lowered to increase the influence of atmospheric drag. At the time of reentry, the majority of space debris reentries are uncontrolled which implies that the object's orientation and trajectory are not being controlled by an operator but rather are influenced by atmospheric drag, gravity and solar radiation pressure. As a result, most reentry objects are tumbling at the time of reentry [154].

Uncontrolled space debris reentries enter Earth's atmosphere at shallow flight path angles, leading to long flight path trajectories, a high total heat input and a modest maximum heating rate compared to reentries with steep flight path angles [103]. As a result, debris reentries can achieve surface temperatures between 1200K and 3000K [108]. The vast majority of reentry objects do not have heat shields to withstand this heating load. Exceptions include sample and human return missions, albeit these missions are an extremely small percentage of all reentries. Without a heat shield, reentry objects begin to demise.

Reentry aerodynamic forces often break up reentering space debris. Solar panels, antennas and other protruding bodies separate early in the reentry trajectory as high as 120km. As these debris pieces continue to descend, the atmosphere density increases, transitioning from a rarefied gas to a continuum flow, and inducing stronger drag forces on the object. At approximately 85km, a hypersonic bow shock forms around the object. Across this bow shock, nitrogen and oxygen gas disassociate and a tremendous amount of heat is generated. Behind the shock, nitrogen and oxygen atoms can recombine to form nitrogen oxides (NO and NO_2 collectively known as NO_x) or interact with the object's surface to form metal oxides. Both of these gases eventually dissipate into the plume behind the reentry [108, 143].

The heat generated from the hypersonic shock propagates to the reentry object's surface. This heat induces several mass loss phenomena collectively called ablation. These phenomena included melting, sublimation, evaporation, non-equilibrium heterogeneous chemistry, and material spraying [108, 104, 71, 40, 66]. These processes are visually summarized in Figure 2-1.

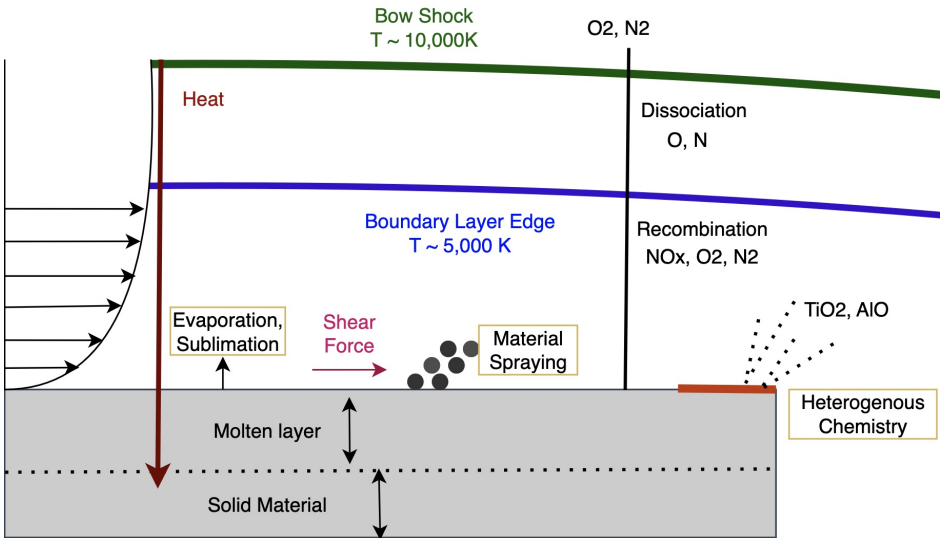

Figure 2-1: Main Material Ablation Phenomena on Unshielded Space Debris Reentries

,

Materials with high melting points, like titanium, and carbon-carbon composites, such as carbon composite wrapped tanks, do not melt or contribute to particle spraying. For reactive materials with high melting points, heterogeneous chemical reactions with atomic nitrogen and oxygen can become an important mass loss mechanism. In general, materials

with high melting points will largely survive reentry. In fact, several titanium and composite components have been recovered nearly intact after an unshielded reentry [78].

On the other hand, materials with low melting points will ablate rapidly. For these more fusible materials, heat generated in the hypersonic bow shock can induce melting, evaporation, and sublimation depending on the phase change temperatures of the surface material. Aerodynamic shear forces over this molten surface causes material spraying, forming small metallic particles. A common space debris material, aluminum, and its alloys rapidly succumb to this mass loss process due to their low melting temperatures (between 736K and 944K) compared to the average reentry surface temperatures of 1200K to 3000K [108, 147]. As a result, space debris reentries release metallic particles between 30km and 60km, far above aviation emissions at 12km to 18km. While the full extent of these particle's atmospheric effects is unknown, reentry-ablated aluminum particles can accumulate in the atmosphere and interact with heterogeneous ozone chemistry, cloud formation and Earth's radiative transfer, known as radiative forcing [62]. Radiative forcing describes how particles, clouds and gases scatter and absorb light, changing how much solar light reaches Earth's surface and similarly, how much radiation can re-radiate from Earth's surface out to space. This interference changes Earth's energy balance, leading to global temperature changes, and consequently, climate change.

This thesis explores the atmospheric salience of reentry-ablated aluminum particles. The lifetime, distribution and radiative forcing consequences of these particles are investigated using a state-of-the-art 3D atmospheric transport model, the Whole Atmosphere Community Climate Model (WACCM). Chapter 3 presents the current understanding of space debris reentry emissions and atmospheric consequences. Chapter 4 presents a justification for studying space debris aluminum over other space debris materials. Chapter 5 details the scope of known atmospheric consequences for aluminum particles. Chapter 6 discusses the use of WACCM, including the set up, assumptions and test cases while Chapter 7 presents results which are further discussed in Chapter 8.

Chapter 3

Literature Review

To date, very little research has been conducted on the atmospheric consequences of space debris reentry resulting from material particulates and NO_x emissions. Overall, several atmospheric effects and chemical mechanisms have yet to be characterized.

A handful of studies have attempted to quantify the effect of reentry NO_x on ozone depletion. Most of these studies combine rocket launch and reentry emissions. Larson et al. studied the atmospheric effects of a hypothetical reusable vehicle, the Skylon spaceplane. The study considered reentry NO_x, and two combustion by-products, H_2O and NO_x, to represent the vehicle's atmospheric emissions [73]. This study found that NO_x emissions resulted in 0.5% loss of the globally averaged ozone column with 2% losses at the North and South Pole at steady state. The effect of reentry NO_x on ozone ranged from -0.1 to -0.7 Dobson units (DU) depending on the atmospheric model used in the study. A Dobson unit describes the amount of ozone in a single column of air which is on average 300 DU for Earth's atmosphere [22]. For reference, the ozone hole recovery resulting from the Montreal Protocol is estimated to be between 2% and 4% per decade, and therefore, the expected ozone depletion from Skylon spaceplane would significantly inhibit the ozone hole recovery [70, 53, 24]. While the atmospheric impacts found in this study are substantial, the study assumed an extremely high flight rate of 10^4 to 10^6 flights per year. These flight rates are several orders of magnitude larger than current launch rates. Launches in 2021 set a new record at 144 attempted rocket launches [13]. As a result, the study concludes that a flight rate of 10^5 per year of a reusable hydrogen launch vehicle are necessary to significantly impact

the global climate. Based on these results, others have concluded that NO_x emissions from launch vehicles and reentries is negligible at the current level of space activity [86].

Exploring modern rocket fleets, Ryan et al. modeled reentry NO_x emissions and launch combustion emissions from space activity in 2019. This study found that reentry NO_x and chlorine emissions from solid rocket motors contribute equally to stratospheric ozone depletion which amounted to 0.1% loss in the global stratosphere[128]. This study assumed a constant ratio of 17.5% to convert a reentry object's mass to NO_x emissions. This ratio was derived from Space Shuttle reentry modeling which has limited comparability to typical space debris objects. Due to their smaller form factor and shallow reentry angle, space debris reentries likely produce less reentry NO_x than the Shuttle orbiter.

In the mid-1990s, Smith et al. briefly explored the consequences of alumina emissions from meteoric and space debris particles [142]. This study was done by TRW Space & Electronics Group for the Environmental Branch of the U.S. Air Force Space and Missile Systems Center in 1999. While the introduction and conclusion state that the authors present analysis on the atmospheric consequences of space debris reentries, the publicly available document of their study does not contain any such analysis. The study concludes that deorbiting debris and meteors do not have significant impact on the global stratospheric ozone because of the low particle density of the emissions and slow reaction rates with ozone depleting chemistry. However, the lack of methodology presented in the publicly available report leaves this conclusion unsubstantiated.

The European Space Agency (ESA) sponsored two studies to explore space debris reentry impacts on stratospheric ozone concentrations and certain radiative forcing mechanisms [37, 11, 14]. Limited information on the methodology, assumptions and modeling uncertainty in these studies is published. No written publications to support their findings were referenced in their presentations nor found online. From their publicly available documents, Bekki et al. presented results that indicate reentry NO_x causes minimal ozone depletion with the most potent effects at high altitudes over Antarctica [66]. This study also found that the radiative forcing from 20 years of consistent levels of reentries were insignificant. Similarly, Bianchi et al. investigated the effects of a single reentry and yearly reentries on ozone depletion and radiative forcing and found negligible changes [107]. However, important radiative forcing

mechanisms, such as from the direct radiative effect of alumina particles, were neglected in both studies [37].

Building on previous work, this thesis addresses a major gap in the current literature by estimating the direct radiative effect of space debris alumina. This thesis also presents results on the distribution and lifetime of particles emitted in the upper atmosphere to quantify what has only been speculated that these particles will persist for 3-5 years and accumulate in the polar regions [156].

3.1 Adjacent Literature Review that Supports Thesis Methodology

Adjacent to the atmospheric consequences of reentries, some studies have characterized the reentry population, aerothermochemical ablation during reentry, material demisability and estimations for the ablated particle sizes.

Schulz and Glassmeier in 2021 made one of the earliest, publicly available estimations of metals introduced into the atmosphere from reentries [135]. This study created a reentry population based on 2019 launch rates and an altitude-dependent satellite mass distribution generated by Liou et al. [135, 77]. This study assumed that 890 metric tons of anthropogenic objects reentered each year with 87% of the mass being rocket bodies, including suborbital components. Of this mass, Schulz and Glassmeier estimated that 210 metric tons were aluminum. Reentry of satellites, orbital rocket bodies, and suborbital rocket components were assumed to experience 80%, 65% and 30% mass fraction loss, respectively, due to ablation. Importantly, satellites in large constellations were assumed to completely burn up in the atmosphere. Schulz and Glassmeier found that anthropogenic aluminum emissions from reentries are approximately 161% of the meteoric aluminum flux [135]. This study did not evaluate any other reentry historical reentry data nor provide longitude, latitude and altitude estimates for where metal emissions from reentries occur in the atmosphere.

Reentry modeling tools like NASA's Object Reentry Survival Analysis Tool (ORSAT), and ESA's Spacecraft Atmospheric Re-entry and Aerothermal Break-up (SACRAB) have

been used to study satellite demisability and model thermal protection system performance [66, 78, 107, 160]. These modeling tools provide estimations for temperature and heat loading profiles over altitude for the reentry object which are combined with material properties to determine an ablation mass fraction profile.

Other studies have estimated by-products formed during hypothetical reentries with assumed material compositions and reentry trajectory characteristics [107, 21]. These reentry emission products include atomic and ionic nitrogen and oxygen, NO_x and metal oxides like alumina. One study showed that ablation of an aluminum sphere predominately forms alumina, representing more than 98% of the by-product mass.

More broadly, a larger body of literature exists to characterize meteors and natural cosmic dust, including estimating their reentry characteristics, material composition, and influence on atmospheric behaviors [135, 113]. Meteoric ablation is responsible for several metal layers in the mesosphere-lower thermosphere between 80km and 105km [133, 109]. Above these altitudes, meteor ablation products exist as ions and below 85km, these particles polymerize, forming meteor smoke particles [133, 109]. In general, meteor ablation products are thought to interact with sporadic region formation, nucleation of high-altitude, clouds, stratospheric ozone depletion, and sulfate aerosol condensation [133, 109]. Similar particulates from reentries could have similar atmospheric consequences. Although exact meteor composition varies, meteors typically contain trace metals. Major metallic elements in meteorites by abundance are thought to be: Mg 14.4%, Si 13.6%, Fe 12.1%, Al 1.7%, Ca 0.82%, Na 0.80%, Ni 0.67%, K 0.05%, and Ti 0.03% [109]. As a result, consistent reentry of predominately metallic space debris has the potential to introduce large amounts of trace metals into the atmosphere.

Finally, studies have estimated the atmospheric consequences of rocket exhaust, including NO_x, and black carbon and alumina emissions which have effects on ozone depletion and radiative forcing. This larger body of research can highlight potential consequences for space debris reentries [145, 84, 123, 125].

This work combines these different bodies of literature to justify the importance of studying reentry-ablated aluminum emissions. In Chapter 4, we leverage models of material ablation and meteoric ablation to estimate the anthropogenic and meteoric aluminum influx.

Furthermore, Chapter 5 analyzes the similarities and differences of space debris reentry by-products with meteoric and rocket emissions to determine the possible scope of atmospheric effects from reentry-ablated aluminum. These two chapters make the case that space debris aluminum is a significant emission in the upper atmosphere that warrants more detailed investigation with a 3D transport atmospheric model.

Chapter 4

Justification of Studying Alumina: Comparing Space Debris Reentries to Meteor Influx

The saliency of space debris reentries depends on whether these reentries are able to compete with meteoric emissions, a natural source of metals in the upper atmosphere (see Figure 4-1), and whether these metals have chemical and physical properties that exhibit important atmospheric consequences. These two criteria will drive which space debris materials are important for evaluating their atmospheric impact. This section presents results that show that the influx of space debris aluminum outpaces the meteoric influx, satisfying the first criteria for saliency. Chapter 5 will explore in depth the scope of atmospheric impacts of space debris aluminum, drawing on the known effects of meteoric smoke particles and rocket emissions.

4.1 Comparing Space Debris Reentries to Meteors: Population and Ablation Characteristics

Space debris reentries are notably different than meteor entries into Earth's atmosphere and as a result, the ablation product characteristics differ. At a high level, both kinds

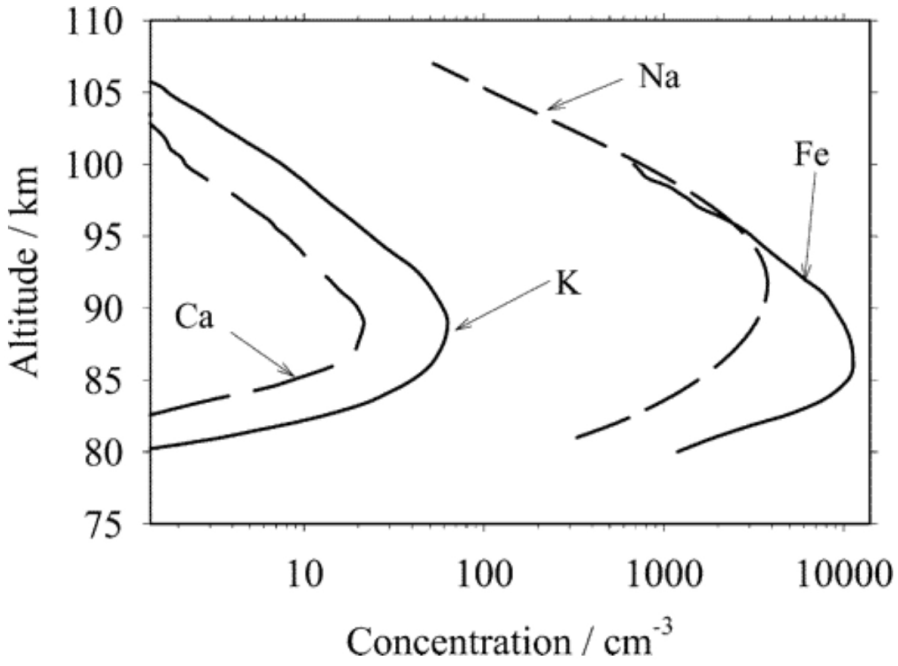

Figure 4-1: Vertical Profile of Annual Mean Concentration at Mid-Latitudes of Meteoric Metals [56, 38, 47]

,

of atmospheric entries share a similarity of forming NO_x in their plumes, and achieving temperatures sufficient for material ablation.

The absolute mass of the meteor population that enters Earth's atmosphere is much larger than the space debris reentry population. While still widely debated and uncertain, typical estimates of the meteoric entry mass range from 10,220 to 43,800 metric tons per year [9, 153]. Compared to meteors, the space debris mass influx is small. Schulz and Glassmeier assumed 890 metric tons of space debris objects reenter each year [135]. This estimate is two orders of magnitude smaller than the lowest estimates for yearly meteoric influx.

At least 20% of the meteor influx is made of dust and micrometeroids with masses between 10^{-6} gram and 1 gram [19]. The entry velocity of these objects ranges from 11.5 km/s to 72 km/s with a velocity distribution skewed towards the lower bound, although some measurements have recorded an average entry velocity of 40-50 km/s [61, 113, 88, 110]. Comparatively, the majority of space debris reenters at approximately 7.8 km/s from natural orbit decay. Furthermore, space debris typically reenter at shallow angles, between 0° and -1°[135, 115]. Meteroic entries can achieve much higher entries angles between 0°and 90°. As

a result of their entry angle and velocity, meteors can achieve surface temperatures above 3,000K during entry, while space debris reentries typically achieve surface temperatures between 850K to 1950K [135]. This lower surface temperature limits space debris emissions to materials with relatively lower melting points. Materials like aluminum with a melting point at 850K will ablate, while titanium with a melting point at 1,941K will likely not ablate.

Most meteors originate within the solar system from the breakup of asteroids and comets, but a small fraction is interstellar cosmic dust [58]. The major metal constituents of these meteors by weight are often assumed to be 12.5% Mg, 11.5% Fe, 11% Si, 1.7% Al, 1.5% Ni 1% Ca and 0.6% Na, based on ordinary chondrites composition [88, 114]. Space debris, on the other hand, contains a significant amount of aluminum with other trace metals, including iron, nickel and copper and germanium, and relatively low amounts of magnesium [61, 135]. The relative scarcity of aluminum in meteors and comparative abundance in space debris makes aluminum an interesting candidate for further study and gives anthropogenic aluminum a chance to compete with meteoric influx.

Given the difference in entry velocity, geometry and composition, meteor ablation occurs at high altitudes, above 100km in most cases and at higher altitudes for higher velocity entries [89]. NASA's Long Duration Exposure Facility experiment collected data that suggested peak meteor ablation occurs at 90km with 62% of the entry mass vaporizing [110, 87]. Meteors are thought to undergo differential ablation where more reactive materials, like sodium and potassium, ablate earlier compared to refractory metals such as calcium [110, 89]. A highly refractory metal, aluminum mass in meteors has an estimated 14% ablation fraction. This relatively low fraction further underscores the scarcity of meteoric aluminum in the atmosphere, increasing the opportunity for anthropogenic aluminum to outpace the natural aluminum flux.

4.2 Comparing Meteoric and Anthropogenic Aluminum Influx: A Historical Model and Forecast of Space Debris Reentries

To determine if space debris reentries could outpace meteoric influx of aluminum, a model of the historic reentry population and its emissions was created. This model combines reentry object datasets, material composition estimates, and reentry ablation model results to estimate reentry emissions. For many of these steps, rocket bodies and satellites were addressed separately, due to varying material composition, mass, and reentry ablation characteristics

Unlike launches, there is no requirement in the "Convention on Registration of Objects Launched into Outer Space", adopted by the United Nations General Assembly in 1974, to register space object reentries [101]. As a result, independent entities, including space agencies, the US military, companies and amateurs, record and maintain datasets for reentries. Across these datasets, NORAD identification numbers for reentry objects are used to link information between datasets. This model combines three sources of reentry data: i) the Space Track dataset provided by the US military , ii) the DISCOS database maintained by the European Space Agency (ESA), and iii) an amateur, crowdsourced catalog, Johnathan's Space Catalog. These three datasets contain different lists of reentry objects and differ on mass estimation and time of reentry for the same object. Table 1 shows how the three datasets and the model's merged database compare.

The Space Track and DISCOS datasets were merged such that only objects with a NORAD identification number that existed in both datasets were kept in the consolidated database. Consequently, 1,559 unique objects were excluded from consideration. This approach provides a conservative estimate of the number of reentries in the model.

To consolidate mass estimations across the datasets, the model selects mass information from ESA's DISCOS dataset. Any missing mass estimates are pulled from the amateur dataset. Space Track does not provide mass estimations for reentry objecst, directly, although estimating masses from TLE data an active area of research[52]. If neither dataset contained a mass estimation for an object, then the object is excluded from consideration.

Table 4.1: Characteristics of Datasets Used to Generate Histotical Reentry Population

	NORAD Space Track	ESA DISCOS	Amateur Dataset	Model Merged Database
Number of Reentries	26,950	26263	24,318	25,826
Number of Reentries with Mass Estimates	None	11,124	8,998	11,356
Number of Ablative Reentries with mass Estimates excluding Shuttle/Buran	None	10,989	8,998	11,221
Reentry Mass of Ablative Objects (metric tons)	None	22,121	10,684	21,601
Number of Ablative Payloads and Payload Debris	22,877	5,480	2,694	5,849
Contains Reentry Prediction Times	Yes	Depends. Yes - on website. No - downloaded data.	Yes	Yes

Out of the 25,826 data points available in the merged database, 14,470 reentry objects were removed, reducing the modeled population by approximately 56%. Another limation of these datasets is that only objects that are assigned NORAD identification numbers were recorded. As a result, suborbital rocket components, like certain first stages, and non-trackable micro-debris are not included in the model. Shuttle orbiters and the Buran were removed from the model since these vehicles were controlled, heat-shielded reentries with ablation characteristics unlike uncontrolled, non-shielded objects. The Columbia accident (STS-107) reentry mass was kept in the model.

Data on satellite material composition was collected from the Federal Communications Commission (FCC) public license records. Satellite operators must apply for a license to use electromagnetic spectrum in the United States, and as a part of the licensing process, operators must show limited risk of reentry causality in an Orbital Debris Assessment Report

(ODAR). These FCC filings often contain simulation results from NASA Debris Assessment Software (DAS) which provides low-fidelity demise and survivability analysis for a reentry object.

Many operators voluntarily provide and publicly disclose their DAS simulations and log files which contain an approximate understanding of the satellite materials and layout. Alternatively, other operators provide a summary table of their DAS inputs, including the component name, quantity, mass and main materials. Over 100 ODARs were reviewed for material composition information. Several ODARs did not contain either DAS input tables or log files. As a result, only 89 satellite ODARs contained information on material composition. Out of the 89 ODARs, only 58 reports recorded more than 70% of the satellite's dry mass in their DAS simulation inputs. Figure 4-2 shows the aluminum mass fraction over satellite dry mass from these 58 ODARs.

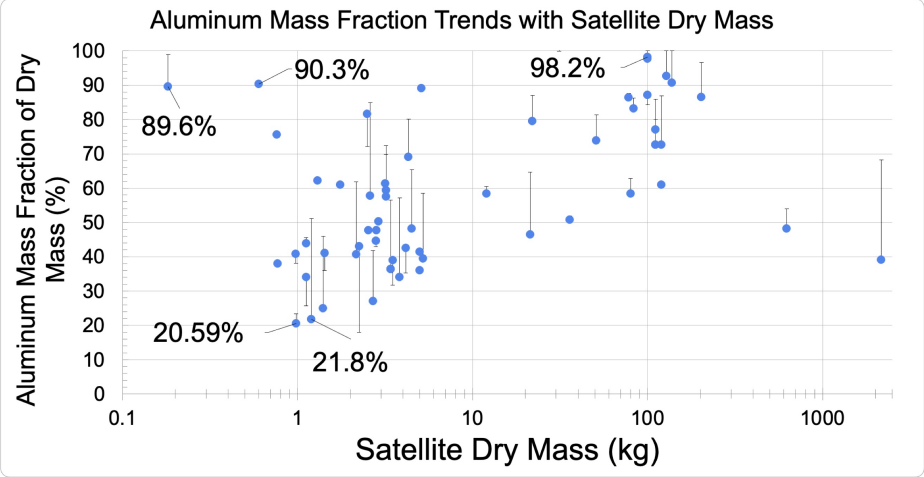

Figure 4-2: Satellite aluminum composition as a function of satellite dry mass. Data shown is derived from ODAR reports filed publicly at the FCC and from private commercial companies. All data shown had at least 70% of the satellite dry mass reported in ODAR filing. Error bars show percent error from underreported mass in ODARS (between 0-30%). Error bars show increases if the ODAR reported mass is lower than the satellite reported dry mass. Error bars show decreases if the ODAR reported mass is higher than satellite reported dry mass. [61]

,

The material mass fractions shown in Figure 4-2 are percentages of the total dry mass of the satellite, not of the reported mass of the DAS simulations. The error bars indicate the percent of underreported mass. For example, satellites with ODARs that only reported 70%

of the dry mass in their DAS inputs have upwards of 30% additional aluminum composition. Overall, aluminum and steel were the two most reported metals, although printed circuit boards (PCBs) and FR-4 (a glass- reinforced epoxy laminate material) were common non-metal materials.

Some data points in Figure 4-2 are clear outliers. The nano satellites missions reported approximately 90% of the satellite dry mass is aluminum. This finding could have resulted from a skewed and oversimplified representation of the satellite in the ODAR information. For example, with such a small satellite mass, it is possible that only large, metallic components were thought to be relevant to DAS modeling, leading to an oversimplification of the satellite material composition, and an overestimation of the aluminum content. In general, uncertainty from oversimplified satellite representation applies to the entire dataset. For example, one 100kg satellite reported 98.2% aluminum, hinting at an oversimplified representation of the satellite.

As Figure 4-2 shows, more than 50% of satellites contain more than 50% aluminum, while more than 90% of satellites contain more than 21% aluminum. To remain conservative, this model assumes that a satellite's dry mass contains 21% aluminum. Future work aims to expand the ODAR dataset and extrapolate a trendline that can be applied to the reentry population. At present, the reentry emission model allows the user to specify a material mass fraction or provide a distribution of material mass fractions over dry mass.

Rocket body material composition was also estimated. The majority of rocket bodies are predominantly made of aluminum alloy [135]. However, some exceptions include Centaur, Antares and Delta II upper stages which are mainly stainless steel, an alloy of iron, chromium, and other elements [9, 10, 50]. In this model, we assume approximately 70% of a rocket body dry mass is made of aluminum with an exception for Centaur, Antares, and Delta II bodies which are assumed to be 5% aluminum. The 70% aluminum mass fraction for rocket bodies aligns with previous work. Schulz and Glassmeier assumed rocket body propulsion tanks are made of 80% AA2219 Al-alloy and 5% AA2198 Al-Li-alloy while liquid fuel engines contained 5% aluminum [135]. Their study also assumed that 8% of a rocket body dry mass is engine mass, leading to an overall finding that 78.6% of a rocket body's dry mass is aluminum.

Up to this point, the model can estimate a reentry object's mass and material compo-

sition. To understand what material is emitted into the atmosphere, the model also must include an ablation profile for each material.

Ablation modeling tools like Object Reentry Survival Analysis Tool (ORSAT) from NASA and Spacecraft Atmospheric Reentry and Aerothermal Break-up (SACRAB) and Spacecraft Aerothermal Model (SAM) from ESA can predict the amount of material ablated over the reentry trajectory [110, 115, 58]. However, these models are not publicly accessible and have restricted use. While requested, no modeling tool was released to the authors to be used in this research. Instead, the model employs publicly available results from ESA's SAM ablation model to estimate the material ablation over altitude profiles. Bekki et al. produced ablation mass fraction over altitude curves for certain materials on a "typical spacecraft and rocket body" shown in Figure 4-3 [114]. Unfortunately, the exact characteristics of the reentry objects used by Bekki et al. to produce their results is unknown. As shown in Figure 4-3, these ablation profiles for aluminum resemble the shape of a typical heat flux curve for a reentry trajectory.

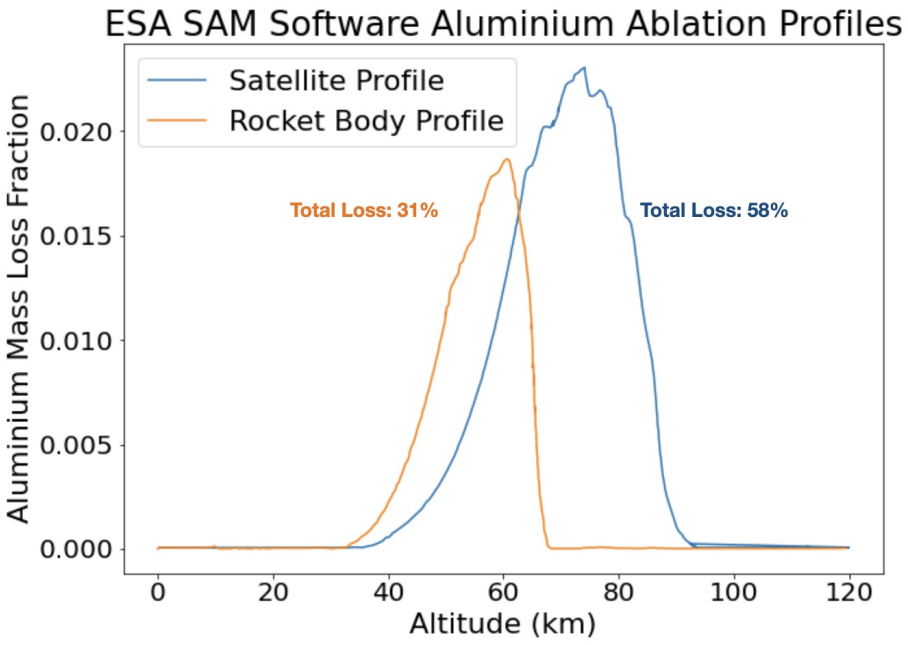

Figure 4-3: Aluminum Ablation Profile using the European Space Agency's SAM Ablation Model to predict aluminum mass fraction loss over altitude for a typical rocket body and satellite [11, 12]

,

The SAM results indicate that spacecrafts begin ablating around 90km with peak ablation around 75km [114]. Rocket bodies begin ablation at 70km with peak ablation around 58km [114]. Bekki et al. note that these results differ significantly with assumed material properties [11, 12]. This ablation profile is applied to all objects in the reentry dataset. More specifically, every spacecraft is estimated to ablate 58% of its aluminum mass and every rocket body is estimated to ablate 31% of its aluminum mass. No exceptions were made for extremely large spacecraft, like space stations. It is likely that extremely large spacecraft will have lower-altitude ablation profiles, similar to rocket bodies, but refining this uncertainty warrants future work.

As shown in Figure 4-4, the model results can vary widely with assumptions on the reentry population, including material composition and ablation. The model is linear with these parameters, and thus very sensitive to minute changes. Since there is considerable uncertainty in characterizing the reentry population, the model is most useful for testing hypothetical scenarios with assumed parameters.

Schulz and Glassmeier estimated the anthropogenic sources of materials in the atmosphere from space debris using a similar linear method, where material composition and ablation fractions are applied uniformly to the reentry population [135]. Their anthropogenic aluminum injected estimates were more than three times this model's average aluminum influx estimate. This difference is likely due to Schulz and Glassmeier's inclusion of sub-orbital rocket component reentry mass and their consideration of 450km reentry threshold to determine spacecraft reentry mass from an altitude-dependent mass distribution by Liou et al. [135, 77]. In contrast, this model uses historical data to determine the reentry population. Due to missing mass estimates, this paper's model excluded 46% of known 2019 reentries, leading to an underestimation of the reentry mass. Figure 4-5 shows the temporal distribution of this missing data.

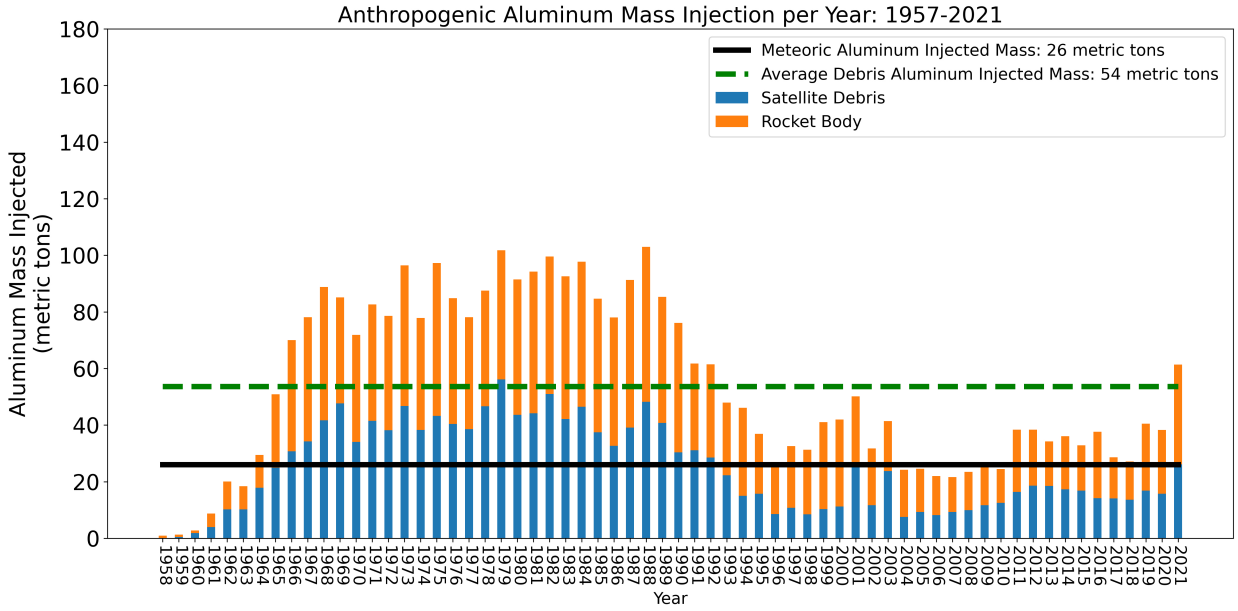

(a) Base Case: 21% Satellite Mass is Al, 58% ablates, 70% Rocket Body Mass is Al, 31% ablates. Meteoric aluminum injection is an approximate average from Plane et al [87]. Meteor influx typically varies across seasons and years.

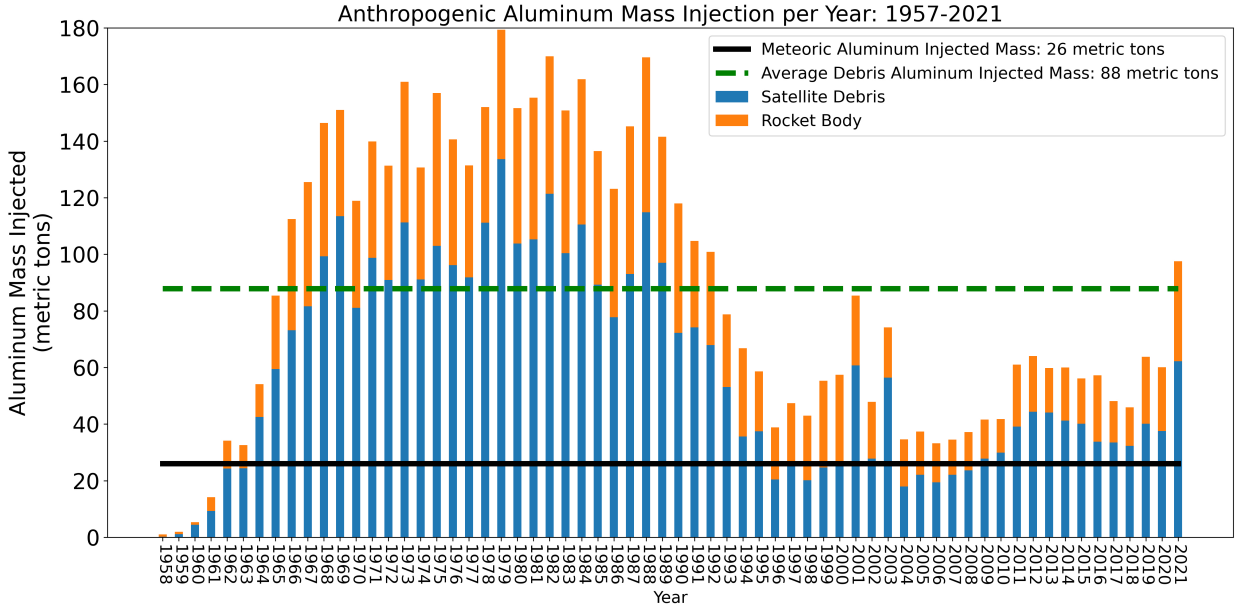

(b) Case 1: 50% Satellite Dry Mass is Al of which 58% ablates, 70% of Rocket Body Mass is Al of which 31% ablates. Meteoric aluminum injection is an approximate average from Plane et al [87]. Meteor influx typically varies across seasons and years.

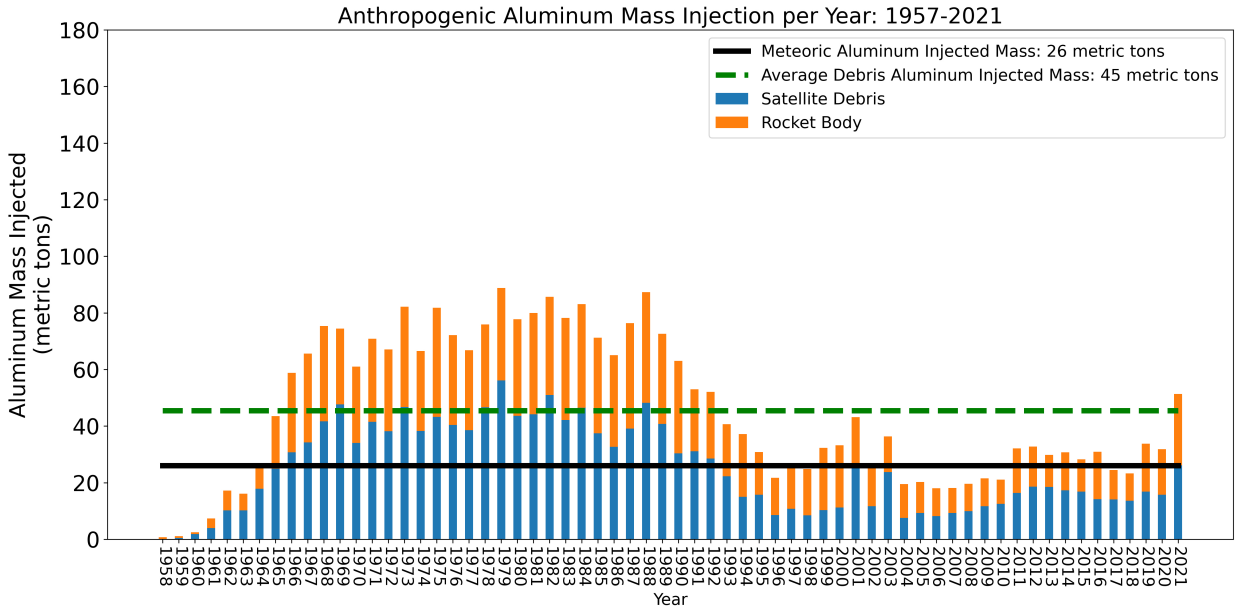

(c) Case 2: 21% Satellite Mass is Al, of which 58% ablates, 50% Rocket Body Mass is Al of which 31% ablates. Meteoric aluminum injection is an approximate average from Plane et al [112]. Meteor influx typically varies across seasons and years.

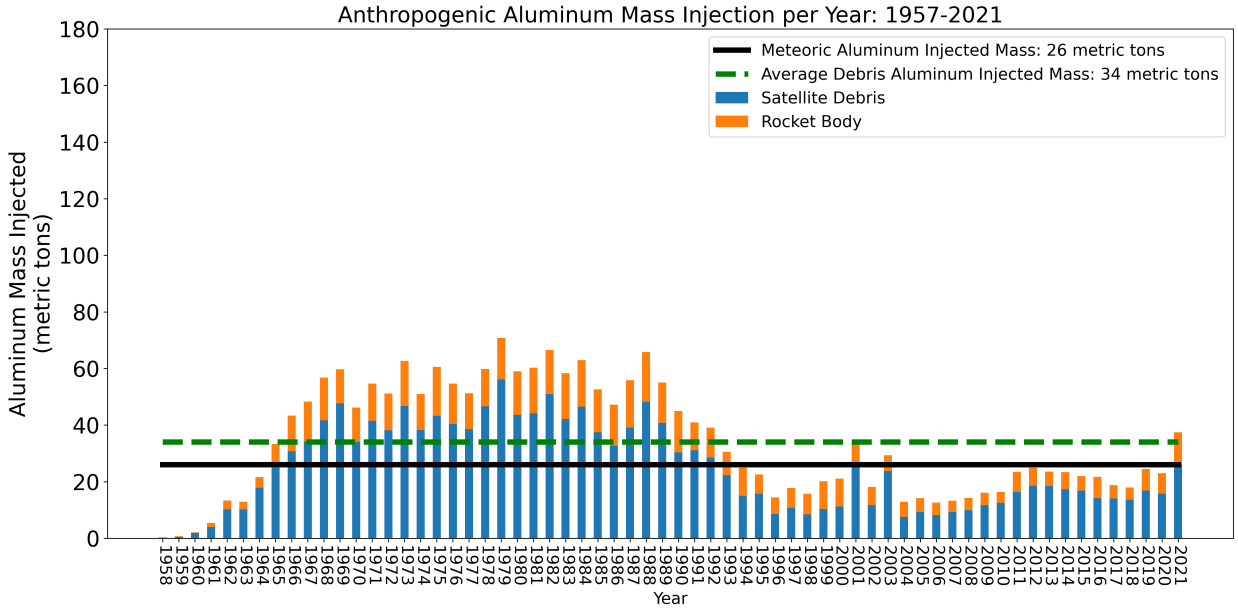

(d) Case 3: 21% Satellite Mass is Al, of which 58% ablates 70% Rocket Body Mass is Al, of which 10% ablates. Meteoric aluminum injection is an approximate average from Plane et al [112]. Meteor influx typically varies across seasons and years.

Figure 4-4: Sensitivity of Anthropogenic Aluminum Influx to Varying Assumptions on the Reentry Population and Ablation Characteristics

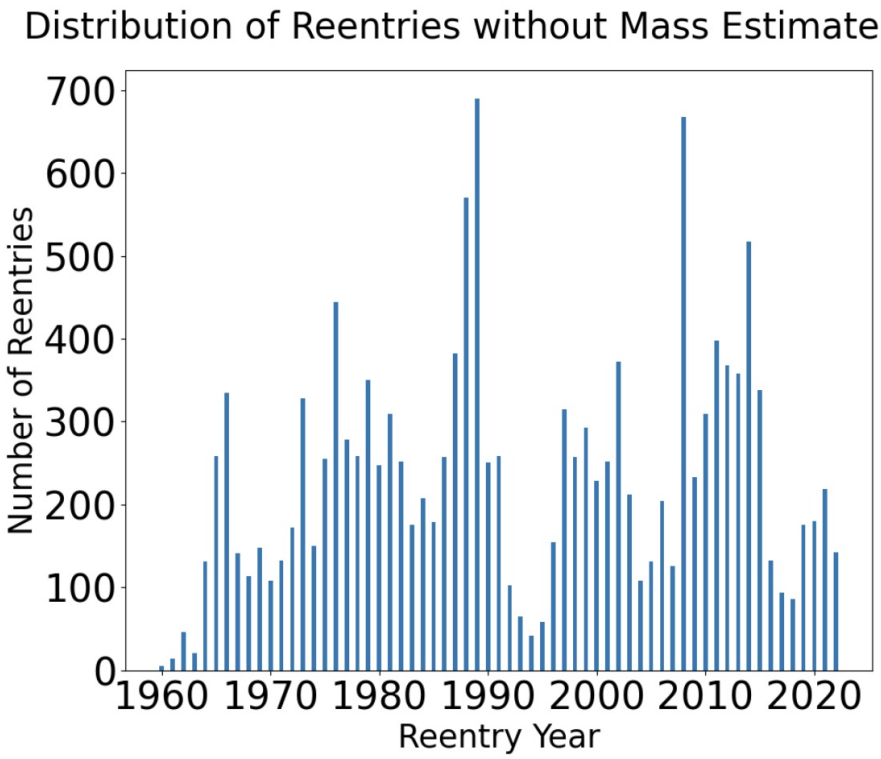

Figure 4-5: Histogram of Historical Reentry Objects with No Mass Estimates

,

It is important to note that the data used in the model may not fully capture the effect of megaconstellations. Starlink has deployed about 3,500 satellites out of their proposed plan for 12,000 satellites [117]. Similarly, OneWeb's constellation is 66% complete [46]. Several hundred satellites are planned to be launched in 2023 [138]. Reentry of these objects will occur over the next 25 years. As a result, best current data from 2021 cannot fully capture the change in reentry mass from spacecrafts due to megaconstellations and the global growth of the space industry.

4.2.1 Forecasting the Future Reentry Population

The Aerospace Corporation published results forecasting the satellite and rocket body reentries based on FCC filings, public announcements of proposed satellite constellations and Department of Defense launch schedules [65]. This forecast includes SpaceX, OneWeb, and Kuiper constellations. Only 100,000 of the possible 300,000 small satellites from E-space

are considered. The author of this forecast took a lower bound estimate of the E-Space constellation since deploying and operating this size constellation is unprecedented, and consequently, has a more uncertain future. E-space has also indicated that it will only build to market demand despite the plans outlined in the company's FCC filings [18]. In this forecast, cube satellites and non-US missions are not well captured. The International Space Station reentry is also not included.

The reentry year for each satellite is estimated from the publicly filed information with suggested spacecraft design lifetimes. For objects with unknown lifetimes, the design orbital altitude is used to estimate the reentry year. For objects in LEO, the reentry year is 10 years after the launch year. Satellites are replenished to maintain the constellation size.

A market optimistic and modest forecast were published, representing two scenarios with all or some of these proposed satellite systems coming to fruition. More specifically, the market modest forecast uses present day launch rates and launch capacity to estimate the growth of the future satellite population [65]. The market optimistic case assumes all the of megaconstellations filed with the FCC are developed and maintained. Both future scenarios assume that SpaceX's Starship becomes operational, significantly reducing the number of rocket bodies disposed in space after 2030.

In the market optimistic case, the average satellite mass is estimated to be 600kg while the average rocket body mass is 2,800kg [65]. However, in the market modest case, the averaged satellite mass is 300kg and the average rocket body mass is 3,000kg [65].

In every case, the forecasts show that the satellite reentries will eventually dominate the total reentry mass, driven by megaconstellation satellite reentries. Compared to the historic reentry population, these forecasts represent at least an order of magnitude growth in the reentry mass. Larger LEO satellites and the rise of numerous constellations drive this trend.

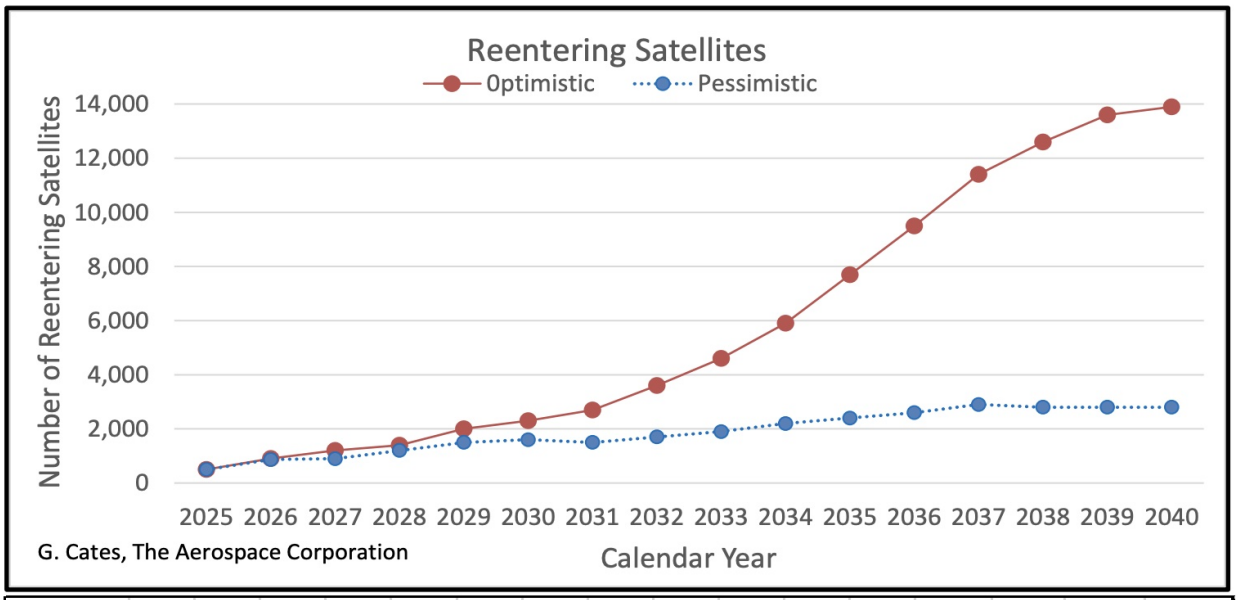

Year	2025	2026	2027	2028	2029	2030	2031	2032	2033	2034	2035	2036	2037	2038	2039	2040
Optimistic	500	910	1,200	1,400	2,000	2,300	2,700	3,600	4,600	5,900	7,700	9,500	11,400	12,600	13,600	13,900
Pessimistic	500	870	900	1,200	1,500	1,600	1,500	1,700	1,900	2,200	2,400	2,600	2,900	2,800	2,800	2,800

(a) Forecast for Satellite Reentries

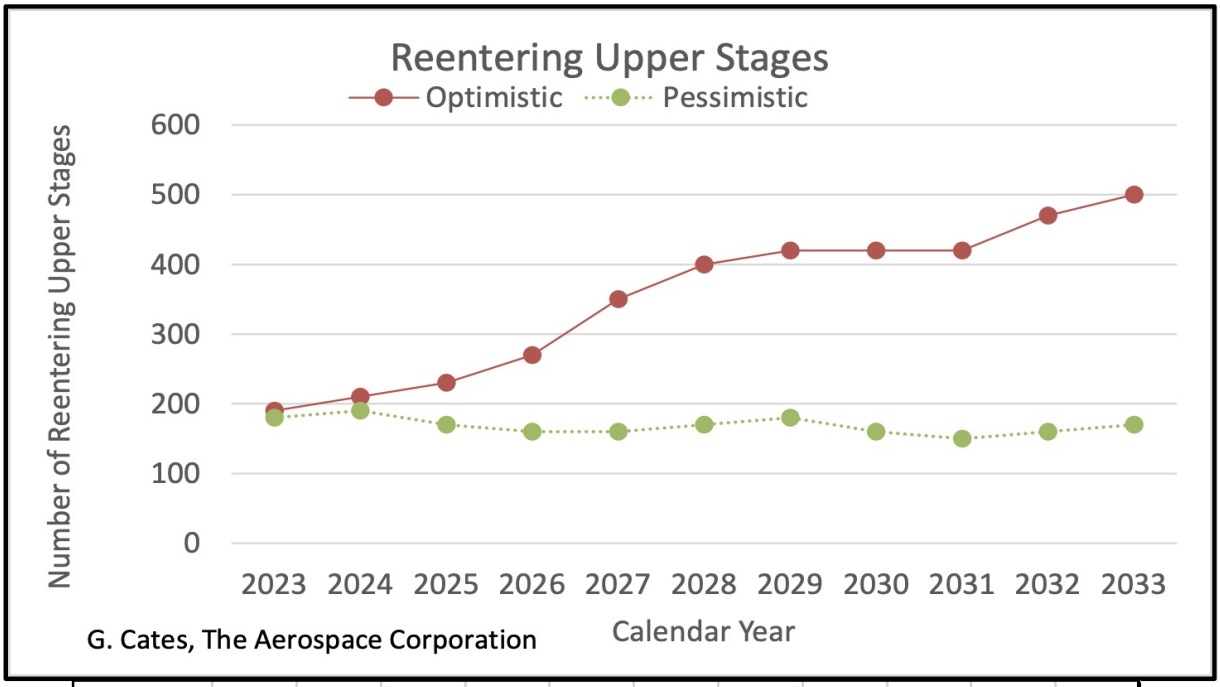

Year	2023	2024	2025	2026	2027	2028	2029	2030	2031	2032	2033
Optimistic	190	210	230	270	350	400	420	420	420	470	500
Pessimistic	180	190	170	160	160	170	180	160	150	160	170

(b) Forecast for Rocket Bodies

Figure 4-6: Reentry Population Forecasting from [65]

4.2.2 Anthropogenic Aluminum Influx Outpaces Meteoric Aluminum Influx

Given the range of meteoric entry mass estimates, the natural aluminum influx could range from 10.5 to 105.4 metric tons per day, assuming aluminum is 1.72% of the meteoric composition of which 14% ablates. Most estimates for the meteoric entry mass lie around 28 meteoric tons a day, leading to 24.6 metric tons of aluminum injected into the atmosphere per year.

Figure 4-4a shows that several years have an anthropogenic aluminum influx greater than 24.6 metric tons. Furthermore, several years between 1973 and 1988 achieved an aluminum influx near 100 metric tons, close to the meteoric aluminum influx upper bound. It is important to note that the historic model presents conservative estimates for the aluminum influx due to limitations in available data (see Figure 4-5 for the missing reentry object data per year). If we assume that the missing reentry objects had an average mass of rocket bodies and satellites of their respective years, the average aluminum flux grows to 131 metric tons. This average aluminum reentry flux outpaces the meteoric aluminum influx.

The anthropogenic aluminum influx grows when considering the forecasted reentry population. Assuming a future similar to the market modest forecast, the anthropogenic aluminum influx is approximately 183.7 metric tonnes, assuming the same material composition and ablation profiles as in Figure 4-4a. This aluminum influx far surpasses the upper bound of meteoric aluminum influx by nearly 130%. The upper bound of meteoric aluminum is derived from the upper bound estimate of the meteoric entry mass per day, taken to be 105.4 metric tons per day, of which 1.7% is aluminum and from that aluminum mass, only 14% ablates. These assumptions result in an upper bound meteoric aluminum influx mass of 91 metric tons per year. In the optimistic case, the expected aluminum influx mass is 1,337 metric tons per year which is more than 14 times larger than the upper bound meteoric aluminum influx.

While these results are sensitive to several uncertain parameters, the bounding cases indicate that human activities in space are matching, if not outpacing, the natural influx of aluminum. Unlike other space debris materials, aluminum is both abundant in space debris

and scarce in meteors, leading to an excess of aluminum emissions due to space activities. Other common space debris materials that are rare in meteors include titanium, tungsten, beryllium, and germanium. However, these materials have a low absolute mass which may not be sufficient to influence the atmosphere in any measurable, or observable way.

As the number of on-orbit satellites in LEO continue to grow, the disparity between natural and anthropogenic aluminum emissions will widen, warranting further study of reentry aluminum byproduct emissions. Aluminum ablation byproducts from natural decay reentries are dominated by alumina (Al_2O_3) with more than 90% of the mass loss resulting in alumina aerosol particles [107]. Therefore, the saliency of space debris aluminum emissions depends on whether alumina particles interact with important atmospheric processes. The next section explores the known effects of meteoric smoke particles and rocket alumina emissions to sketch the possible scope of atmospheric impacts of space debris alumina and complete the justification for studying the atmospheric consequences of space debris alumina.

Chapter 5

Scope of Theoretical Atmospheric Consequences of Alumina Particles

Injected high in the atmosphere, alumina particles have the opportunity to interact with a variety of atmospheric processes, ranging from upper atmosphere chemistry to cloud formation to changes in Earth's radiative balance. To better understand the scope of possible consequences of these emissions, we can compare similarities across meteor byproducts, solid rocket motor particles, and their respective atmospheric interactions to identify likely consequences of space debris alumina.

5.1 Comparing Space Debris Alumina to Meteor Ablation Products

Meteoric ablation creates unique ablation profiles for each metal in its composition. These metals accumulate in the mesosphere-lower thermosphere (MLT), existing as atoms between 80km and 105km, and as atomic ions at higher altitudes. Metal layers peek at 86km, 90km, 91km and 93km for iron, calcium, potassium and sodium respectively [110]. Iron and sodium vertical profiles are much wider and contain higher concentrations compared to other meteoric metal vertical profiles [110]. Below 85km, meteoric metals form oxides, hydroxides and carbonates and eventually polymerize into meteor smoke particles (MSPs) [110, 113].

Residual meridional circulation of the mesosphere tends to blow these MLT metals towards the poles, particularly during the polar winter [111]. MSPs are thought to participate in several atmospheric phenomena, including high altitude cloud formation, stratospheric ozone depletion and sulfate aerosol condensation [110, 113]. However, research to prove these chemical mechanisms in laboratory environments and in-situ are ongoing [110, 113]. Eventually, meteor smoke particles will settle on Earth's surface after approximately 4-5 years [110, 113].

A model of a generic satellite reentry reached peak ablation at 75km with 58% of the dry mass ablating while a generic rocket body experienced peak ablation at 58km with 31% ablating [12]. As a result, space debris reentries are injecting metallic particles at atypical altitudes compared to meteors. This difference suggests that the behavior of anthropogenic particles may more similar to meteor smoke particle behavior, rather than meteoric metal atoms and ion behavior.

5.1.1 Suspected Meteoric Particle Behavior and Applicability to Space Debris Particulates

Meteor ablation products have been studied in some detail. As a result, we can compare similarities across meteor entry and space debris reentry characteristics to inform which atmospheric consequences may be perturbed by space debris ablation products.

Mesosphere - Lower Thermosphere Interactions: Ionic Density, Radio Interference and Lidar Measurements

Meteor ablation products contribute to the formation of ionic regions in the thermosphere, including the D and E ionic regions at 70-95km and 95-170km respectively [113]. In the D region, negatively charged meteor smoke particles, proton hydrates and negative ions are commonly found [113]. In contrast, O_2^+, NO^+ are the most common ions in the E region, alongside free electrons. The E region can have sporadic regions form with unexpected intense ion densities that last for several hours [113].

Meteor ablation can directly result in ionic species and neutral metal atoms can pho-

Table 5.1: Aluminum Photo-ionization Pathways [35]

Reaction	Photoionoziation Threshold (Angstrom)
$Al + h\nu \rightarrow Al^{+}(^{1}S^{e}) + e^{-}$	2068
$Al + h\nu \rightarrow Al^{+}(^{3}P^{o}) + e^{-}$	1192
$Al + h\nu \rightarrow Al^{+}(^{1}P^{o}) + e^{-}$	927
$Al + h\nu \rightarrow Al^{+}(^{1}P^{o}) + e^{-}$	927

Table 5.2: Aluminum Ionization Pathways with Ion Collisions [111]

Reaction	Reaction Rate
$AlOH + NO^{+} \rightarrow AlOH^{+} + NO$	$1.7 \times 10^{-9}(T/300)^{-0.22}$
$AlOH + O_2^{+} \rightarrow AlOH^{+} + O_2$	$2.3 \times 10^{-9}(T/300)^{-0.165}$

toionize or ionize due to interactions with NO^{+} or O_2^{+}. Faster meteor entries lead to larger fractions of meteoric material ablating into ions [113]. The same principle applies to space debris reentries, although the significantly lower reentry speed of debris and shallow reentry angle drastically lowers the expected ionization fraction. Schultz and Glassimier estimated that 75% of a reentries' ablated mass vaporizes into an aerosol while the remaining mass likely ends up in a neutral atomic form, rather than ionized particles [135]. Park et al. modelled the reentry of spheres of varying materials, and found that the reentry of an aluminum sphere with a mass of 17.318kg predominately ablates into Al_2O_3 [107]. Aluminum ion production was not shown in the results, but investigated [107]. The present understanding of space debris by-products indicates that any ionized particles formed from space debris reentries are created through secondary ionization processes, such as photo-ionization and interaction with common ions. Given that aluminum is the most common space debris material, expected neutral aluminum species ionization pathways are shown below.

Solar radiation that can penetrate Earth's atmosphere below ∼85km and into the D region include X rays ($\lambda \leq 10$Å), Lyman α ($1,216$Å) and wavelengths greater than $1,800$Å [105].

Thus, the first photoionization pathway for aluminum is possible and likely to occur, while the second and third are less likely to occur.

Satellite reentries are thought to start ablating around 90km, and thus could release metals directly into the D region. From Figure 4-3, satellite reentries contribute 21% of their total aluminum ablation distribution above 70km. In 2021, this amounted to 13 tons

of aluminum material injected into the D region. Comparatively, Plane et al. found that the distributions of the global annual mean injection of meteoric aluminum occurs entirely above 70 km [111]. Taking the meteoric aluminum composition to be 1.7%, with an ablation fraction of 14% and the daily meteoric influx as 24 metric tons a day, meteoric aluminum in the D region accounts for approximately 20 metric tons [111]. Accordingly, current space debris aluminum emissions into the D region are on par with meteoric aluminium influx into the same region. Whether space debris particles remain in the D region after injection is unknown.

While not yet modeled, it is possible that some space debris ablation products are transported to higher altitudes, reaching the E region and other meteoric metallic layers. In that case, satellite aluminum particles could interact with E region composition and behavior, possibly altering the region's conductivity and the formation of sporadic E regions [113]. At present, sporadic E regions are thought to be related to meteor showers and auroral activity which create large amounts of ions. While space debris reentries likely do not create large amounts of metallic ions upon reentry, the presence of additional metallic material at those altitudes could aid MLT ionization during intense auroral activity, possibly increasing the occurrence or intensity of measurable sporadic E regions. However, these potential consequences depend heavily on whether space debris aluminum species can remain suspended, climb to altitudes above 90km, and contribute a sufficiently large enough mass to meaningfully alter the ionic composition and density of the region.

It is also possible that anthropogenic aluminum in the D region helps remove other metals, like *Fe* and *Mg*. Plane et al. suggest that AlO, $AlOH$ and possibly $Al(OH)_2$ may polymerize with other meteoric, metal-containing molecules, like $FeOH$ and $Mg(OH)_2$ [111]. The permanent removal of these meteoric metals could alter the behavior of the metallic layers in the mesosphere-lower thermosphere (MLT). This alteration, if significant enough, could skew our interpretation of measurements in this region. Lidar measurements of MLT metals have lead to inferences on temperature and wind profiles [113]. As a result of space debris reentries, these measurements may need to consider the effect of space debris aluminum when making inferences on observations of the MLT through lidar scans of the MLT metal layers.

Missing *AlO* Layer

Interestingly, a recent study by Plane et al. attempted to model meteoric aluminum in the MLT using a global atmosphere model, Whole Atmosphere Community Climate Model (WACCM), and a model for meteor atmospheric entries [111]. The model results showed that aluminum species were most concentrated at high latitudes and a large fraction of meteoric aluminum results in *AlO* which happens to have a large absorption cross section at 484.23nm [111, 51]. Accordingly, Plane et al. attempted to observe the expected *AlO* layer at 90km using a lidar based in Germany but were unable to detect a statistically meaningful signal.

Estimates of space debris aluminum injection into the D region are similar to meteoric aluminum estimates. Since Plane et al. only considered meteoric sources, this finding indicates that the aluminum mass considered in their study underestimates the potential atmospheric aluminum concentration. The atmospheric aluminum concentration at 90km could be as large as twice the concentration considered in their study. Accordingly, the inability to detect an *AlO* layer is puzzling and suggests additional important chemistry is missing or other supporting assumptions may be incorrect, including whether space debris aluminum can remain suspended at 90km. In addition, detecting aluminum using polar lidars may be more successful.

5.1.2 High Altitude Cloud Formation and Ice Nucleation

Between 82km and 85km, polar mesospheric (PMC) can form given extremely low temperatures, less than 145K [113]. Recently, the occurrence of these high altitude clouds have increased, corresponding to increasing water vapor concentrations and colder temperatures in the mesosphere caused by human emission activities [113]. As a result, PMCs have now been detected as low as 37.2°N [126]. PMCs are often thought of as an indicator for climate change given the correlation between their appearance and the temperature of the mesosphere [110].

Polar mesospheric summer echoes (PMSEs) occur when ice particles of 10nm or less aggregate, hold a negative charge and collectively cause an intense radar backscatter [113]. When PMCs are observed, PMSEs are often recorded [110]. Accordingly, the occurrence of

PMSEs has also increased since 1994, interfering with certain radio signals [139, 17].

Meteor smoke particles (MSPs) are thought to act as condensation nuclei for PMCs at 87 km [110]. This hypothesis is supported by a recent finding that metal atoms are removed in the vicinity of PMCs [113]. Recent observations have shown up to an order of magnitude difference in *Fe* concentrations in the vicinity of a PMC [110]. The growing cloud eventually undergoes gravitational settling down to 82km. Particles within these clouds usually achieve a median radius of 30nm, but the largest particles can surpass 50 nm. Thus, MSPs are transported and dispersed at lower altitudes upon evaporation of the cloud.

In the vicinity of PMCs, atomic oxygen and ozone are significantly depleted due to the ice particle surface catalyzing the recombination of O and the gas-phase catalytic cycles driven by hydrogen species [110]. Furthermore, PMCs may be contributing to the concentration of the ozone depleting hydrogen species via photolysis of PMC ice particles [110].

Space debris metals could be contributing to the formation of PMCs, and consequently PMSEs and mesospheric ozone depletion. The injection of additional metallic material that can polymerize with other metals, oxides, hydroxides and carbonates likely increases the concentration of particles capable of acting as ice nucleation sites. In other applications, aircraft aluminium is treated to prevent ice accretion, demonstrating aluminum's ability to serve as a condensation site for ice [131]. Albeit, this property of aluminum must be tested at mesospheric temperatures and pressures to validate that the same behavior occurs at 85km.

5.1.3 Ozone Interactions

Meteor ablation can lead to NO_x emissions and MSPs in the mesosphere and stratosphere which can interact with ozone chemistry. MSPs in the mesosphere interact with the balance of odd oxygen, ozone and hydrogen species, including OH and HO_2 which participate in ozone depleting cycles [113]. Sinking lower into the atmosphere, MSPs are thought to create polar stratospheric clouds and possibly directly participate in stratospheric ozone depletion. This next section will explore the ozone depleting pathways.

NO_xmissions from High Velocity Atmospheric Entry

Certain meteor entries, like space debris reentry, create NO_x as a result of aerothermal interactions in the plume. Nitrogen oxides participate in several ozone depleting cycles, and can regulate HO_x and halogen ozone depleting cycles [39, 158]. Thus, depending on background concentrations of NO_x, ozone depletion can improve or worsen with additional emissions of NO_x [158]. Some studies have investigated the consequences of meteoric, space debris and launch emissions of NO_x on the ozone layer and found relatively small changes to ozone levels compared to other industries, such as aviation [141, 73, 37, 127]. In cases of extremely large meteors, the NO_x production can be substantial. For example, the Tunguska meteor fall in 1908 is estimated to have generated 30 million tons of NO in the stratosphere and mesosphere, leading to a 45% decrease in ozone in the Northern Hemisphere [149]. A study of a hypothetical spaceplane launching and reentering at extremely high rates (10^5 events per year) found that reentry NO_x caused 0.5% loss in globally averaged ozone columns [73]. This reentry NO_x mass was estimated to be an order of magnitude larger than meteoric NO_x. Thus, from these results, we can conclude that reentry NO_x formation from space debris reentries is not likely to be a major source of concern for global ozone levels even as the space debris reentry population grows and reentry of reusable or human spacecraft vehicles increases.

However, the compounding secondary effects of additional NO_x levels in the upper atmosphere, such as increases in nitric acid (leading to possible decreases in ozone depletion) and effects on polar stratospheric cloud formation, could still be of concern.

Polar Stratospheric Clouds

Polar stratospheric clouds (PSCs) are a significant sink of odd nitrogen in the polar regions, leading to greater potential for chlorine-catalyzed ozone depletion [155]. Furthermore, less reactive chlorine species are activated on these cloud particles, releasing additional molecules of reactive chlorine [130]. Consequently, the formation of these clouds leads to significant ozone depletion in their vicinity and enhances the long-term damage caused by chlorine emissions.

PSCs form at altitudes between 15km and 25km when strong winter vortexes create temperatures below 196K [155, 130]. The Antarctic region experiences these polar vortexes to a greater extent than the Arctic, yet PSCs have been observed in both regions [130].

Three primary species—water, nitric acid (HNO_3) and sulfuric acid (H_2SO_4)—make up these clouds [130]. Nitric acid trihydrate (NAT) particles condense onto sulfuric acid particles, creating condensation sites for water [148]. Water condenses onto these sites despite temperatures being above the pure water condensation point [130], growing the cloud.

Meteor ablation products, including MSPs and solid non-ablated fragments, are capable of nucleating NAT particles, and thus, seeding PSCs [63]. Of interest, meteoric aluminum compounds were found to remain as solid particles in the stratosphere, whereas other metallic compounds dissolved with stratospheric sulfate aerosol, potentially increasing NAT production [33, 98]. Furthermore, MSPs that dissolve into liquid $H_SSO_4 \cdot H_2O$ droplets can act as nuclei for PSCs, helping uptake water and nitric acid [132]. These meteoric species are thought to produce NAT particles early in winter polar vortex seasons, leading to early sightings of PSCs [63]. The extension of PSC formation window in the polar winters directly corresponds to prolonged ozone depletion [130].

Space debris aluminum and other metallic emissions, if small enough to remain suspended in the stratosphere, may be contributing to the condensation of NAT particles, and thus increasing the occurrence of PSCs in polar winters. This significant pathway to ozone depletion has not yet been explored by previous studies of space debris reentry particles and their effect on ozone chemistry, but should be explored [37, 127].

Proposed Direct Metal Ozone Interactions

Meteoric, metallic compounds may directly interact with chlorine catalyzed ozone depletion. It has been proposed that these metals can react with HCl, resulting in a metal chloride that can easily photodissociate, releasing a reactive Cl atom and a metal atom that will rapidly form a new and separate compound, repeating the cycle [97]. Atomic chlorine breaks down ozone, and thus, the creation of atomic chlorine from HCl is harmful. Some debate whether metal chlorides will accelerate or impede the production of atomic chlorine. Instead of photodissociating, the metal chloride could polymerize due to its long-range, dipole-dipole

forces, causing the molecule to grow in size and diffuse out of the stratosphere [72, 110]. This alternative pathway could remove harmful chlorine from the atmosphere, helping end the long-term damage caused by chloroflurocarbon emissions.

Aluminum is among the metals proposed to interact with HCl, forming a metal chloride. Furthermore, alumina (Al_2O_3) is known to catalyze the conversion of HCl and $ClONO_2$ into chlorine gas and HNO_3 [94]. In models of rocket emission products, this alumina-chlorine reaction was found to increase stratospheric ozone depletion of the modeled rocket fleet by 22% [29]. As a result, space debris aluminum is a likely source of ozone depleting species.

Some studies have examined the potential ozone depleting consequences of space debris particles, and found insignificant ozone depletion for present day reentry mass and future scenarios with higher reentry masses [37]. However, it is not clear if these studies included this direct metal chemistry, or included the effects of other meteoric metallic particles. In addition, it does not appear that high altitude cloud formation and its related ozone depletion was studied. Instead, these studies appear to focus on NO_x-driven ozone depletion and alumina-chlorine chemistry.

5.1.4 Stratospheric Sulfur Interactions

MSPs have also been hypothesized to remove sulphuric acid from the gas-phase in the upper stratosphere, above 40km [132]. One study measured the dissolution rate of iron-based silicate powders in sulphuric acid and found much faster dissolution rates than crystalline iron, leading to estimates of complete dissolution under stratospheric conditions in less than a week [33]. In situ, meteoric iron and magnesium have been detected in samples of lower stratosphere droplets with iron in half of the analyzed particles [99]. Given that space debris metals contain a very small fraction of iron, the effect of space debris reentries on sulphuric acid concentrations is likely insignificant compared to meteors which are iron rich. It is unclear if aluminum has a similar dissolution rate as iron, and consequently, if space debris aluminum is of any importance to the chemistry of stratospheric sulphuric acid.

5.2 Other Known Atmospheric Phenomena and Applicability to Space Debris Particulates

Beyond meteoric effects, certain atmospheric phenomena may be applicable to space debris reentry particulates. These potential consequences were derived from rocket emission studies and other known atmospheric trends.

5.2.1 Thermosphere Contraction

Greenhouse gas emissions cause radiative cooling above the stratosphere, and are thought to be responsible for a decline in thermospheric temperature and consequently density [75, 36]. Plane et al. proposed that meteoric metals, including aluminum, could react with CO_2, producing reservoir forms of CO_2 that eventually polymerize and sink out of the atmosphere. Depending on relative reaction rates and concentrations of reactants, space debris metals could help remove these unwanted greenhouse gas species from the mesosphere to lower thermosphere. To explore this possibility, Figure 5-1 presents meteoric reaction rates for the uptake of CO_2 for temperatures between 120 K and 220 K.

Figure 5-1 shows that AlO and Al^+ have slow reaction rates with CO_2 while potassium species have some of the fastest reaction rates [111, 113]. While the disassociation and polymerization rates also need to be compared in a 0-D chemical model, space debris aluminum is not likely to significantly increase CO_2 reservoir species such that CO_2 levels decrease.

5.2.2 Radiative Forcing of Alumina

Rocket emissions produce alumina particulates which have been shown to accumulate in the stratosphere and cause stratospheric heating through radiative forcing (RF) [125]. Radiative forcing is the principle that particles and gases in the atmosphere can trap long-wave infrared radiation emitted from Earth's surface while blocking sunlight from above [124]. The net difference results in a positive or negative RF where a positive RF indicates a warming effect, and a negative RF indicates a cooling effect.

Rocket-emitted alumina accounts for 28% of rocket RF which is approximately 16 $\pm$

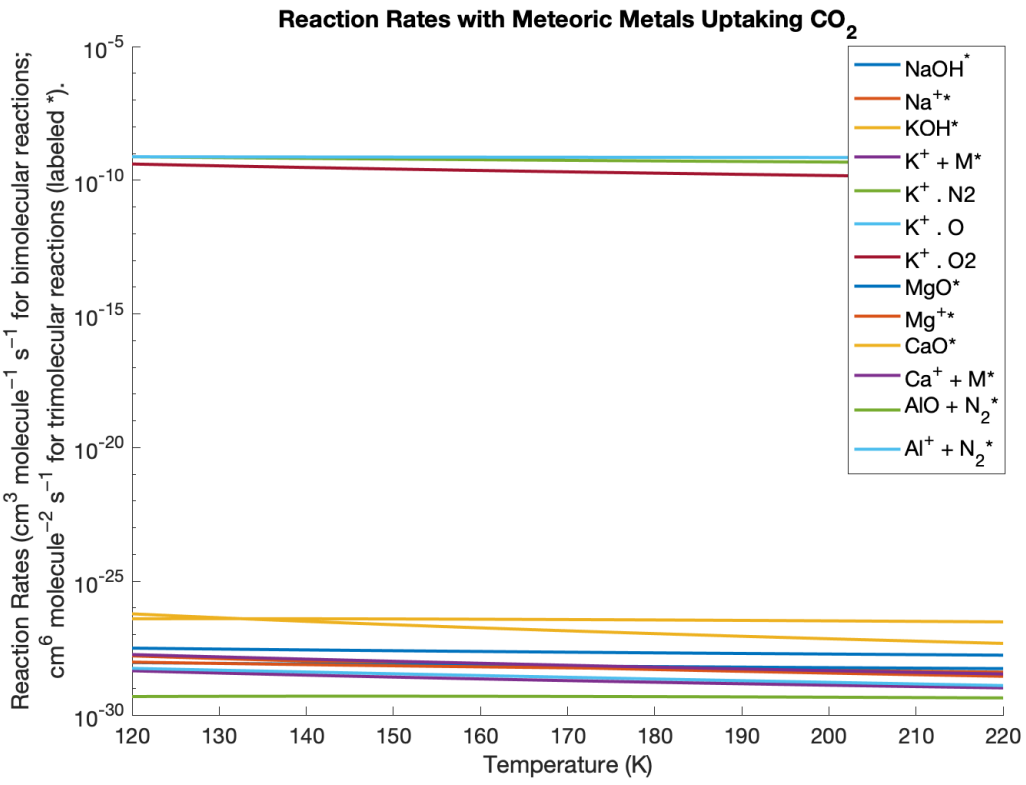

Figure 5-1: Reaction rates for meteoric metals reacting with CO_2. Reaction rates collected from [113, 111]

,

$8mW/m^{-2}$ [125]. While this RF is small at present, rocket launch rates are expected to increase. At approximately 1,000 launches of a generic rocket fleet, rocket RF reaches similar levels as aviation RF.

Warmer temperatures in the stratosphere can have secondary effects on climate change and reaction rates which accelerate at higher temperatures. This consequence could accelerate ozone depleting reactions [28]. To date, the literature on space debris reentry particles have not explored the RF of space debris alumina, nor its possible secondary effects.

One key difference between space debris alumina and rocket alumina is the emission altitude. Rockets emit the majority of their combustion products below 20km [125]. In contrast, almost no space debris reentries will emit particles below 20km. Instead, space debris reentry particles may eventually sink and settle in the stratosphere after being emitted at higher altitudes. The distribution and settling time of space debris reentry particles is

poorly understood.

However, if there are alumina particles small enough to remain suspended in the stratosphere, space debris aluminum may be contributing to and accelerating the accumulation of anthropogenic alumina, leading to temperature variation sooner than expected compared to rocket modeling predictions.

In general, the scientific understanding of the upper atmosphere and characteristics of space debris ablation particles is poor. Laboratory studies on space debris ablation particle characteristics and in-situ observation are necessary to improve modeling of this region and the consequences of reentry-ablated alumina particles.

Chapter 6

Atmospheric Modeling of Space Debris Emissions using WACCM

While there are numerous questions to be explored on the atmospheric effects of space debris alumina, this research focuses on two important questions: 1) the distribution, lifetime and accumulation of space debris alumina particles and 2) the radiative forcing of these particles. The first question influences the saliency of space debris alumina emissions. If these emissions have short lifetimes, and fail to accumulate, the ability for these particles to meaningfully alter atmospheric processes will be limited. The second question explores the climate change impact of these aerosol emissions and provides a way to compare these emissions to the environmental impact of other human activities.

This research uses a forecast of the satellite and rocket body orbital population to estimate the future number of reentries. This forecast is based on a market optimistic scenario where several megaconstellations are completely developed, as described in Subsection 4.2.1. This hypothetical scenario specifies a yearly reentry flux of 13,900 satellites and 500 rocket bodies, resulting in a reentry approximately every 40 mins.

Several factors could restrict the future satellite reentry mass, including: i) disturbances to the space economy such as supply chain issues, shrinking available financing, and failed business cases, ii) changes to satellite operations such as in-space recycling, in-space repair, and use alternative disposal methods for satellites, iii) shifts in mission architectures away from megaconstellations driven by government policies, economics, or technology changes.

Factors like lower launch costs with high capacity, reusable launch vehicles, greater access to satellite spectrum, and strong government and private investment into the commercial space economy could contribute to achieving a high reentry mass.

We neglect the market modest case where the present day launch rate remains constant because the alumina emission signal is too small compared to natural surface dust emissions in the model. As Subsection 6.1.6 will discuss in further detail, we had to scale the market optimistic emissions by a factor of 1000 to improve the signal to noise ratio.

In this work, we characterize the equilibrium behavior of the atmospheric model given reentry emission perturbations. Space debris alumina emissions are identically repeated year-over-year to achieve steady state. We explore the equilibrium case, over the transient case where emissions vary from year to year, to simplify identifying the debris alumina signal from model noise and provide insight on the long term consequences of a specific reentry alumina influx. Subsection 6.1.4 gives additional details on the selected experimental tests cases.

6.1 Model Setup

The Whole Atmosphere Community Climate Model (WACCM) is a state of the art numerical model of the atmosphere between 0 to 140 km described in [85]. WACCM works with a common numerical framework, the NCAR Community Earth System Model (CESM), which integrates individual component models for the atmosphere, land, land ice, river runoff, ocean, wave and sea ice interactions (see Figure 6-1). In CESM 2.2 WACCM (version 6, noted as WACCM6) works in conjunction with Community Atmosphere Model (CAM6) to model the atmospheric physics [44]. Note that at the time of this research CESM 2.2 was published under a developmental release, however several publications have shown scientifically reasonable results.

WACCM6 uses the Modal Aerosol Model with 4 particle size distribution bins (MAM4) to handle aerosols. MAM4 is described in [81]. Dust, sea salt, primary organic matter, black carbon, and sulfate are the aerosols implemented in MAM4. Some of these aerosols participate in heterogeneous chemistry, but all of them contribute to radiative forcing. These

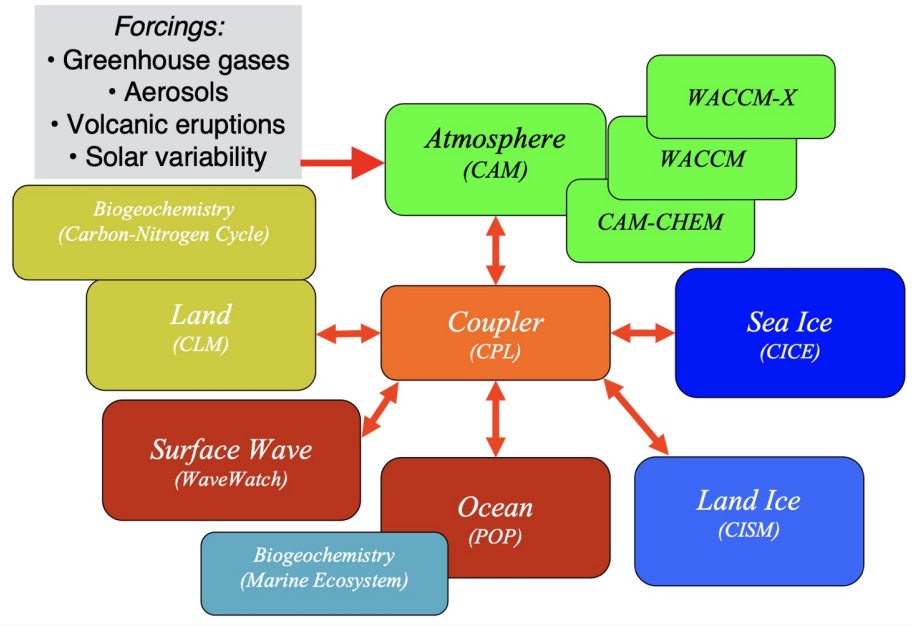

Figure 6-1: Schematic of Component Models used together in the Community Earth System Model (CESM) [79]

,

aerosols are grouped into the model's four bins: Aitken, accumulation, coarse, and primary carbon. The Aitken, accumulation and coarse bins correspond to different particle size distributions, ranging from 0.01 to 10 microns, while the primary carbon bin is reserved for black carbon emissions. The Figure 6-2 shows how these aerosols are categorized and phenomena that transition aerosols across bins. Table 6.4 details the terrestrial dust particle sizes modeled in the Aitken, accumulation and coarse bins.

MAM4 aerosols are internally mixed within a particle size bin, resulting in fractal particles that are proportionally comprised of the various aerosols in the mode. For example, if the Aitken mode was comprised of 50% dust and 50% sulfate, each fractal particle would be half dust and half sulfate. While MAM4 assumes internally mixed particles within a bin, each mode is independent and not externally mixed across modes. As a result, particles can coagulate across modes and within a mode.

As Figure 6-2 shows, particles in the Aitken mode can transition into the accumulation mode and likewise, the accumulation mode particles can transition into the coarse mode. Larger particles tend to effectively coagulate with smaller particles since the probability of a

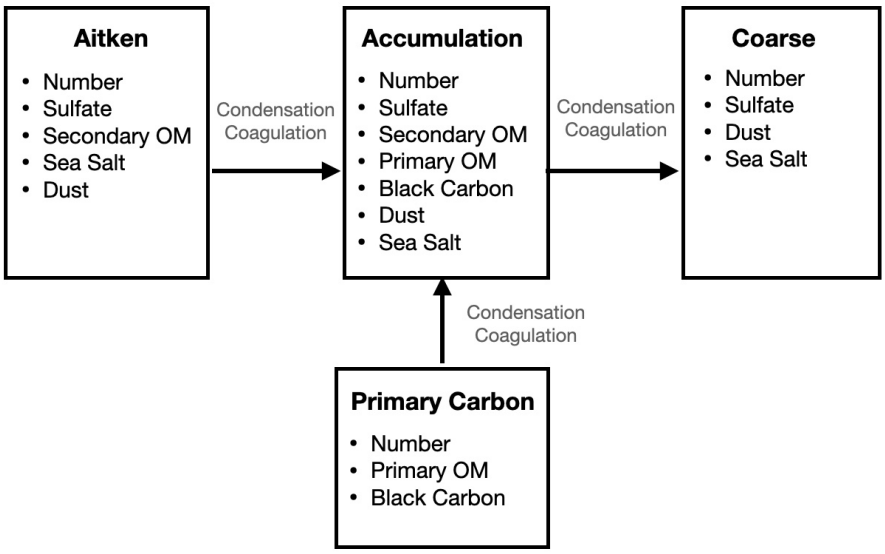

Figure 6-2: Modal Aerosol Model 4 Schematic showing the aerosol modes and associated tracers. Adopted from [81]

collision increases with larger radii [119]. This phenomena drives quick transitioning between modes.

The Rapid Radiative Transfer Model for General Circulation Models (GCM)s, termed RRTM-G, is used in WACCM6 to compute the radiative fluxes cross the tropopause and the top of the atmosphere, as described in [59, 93, 60, 26]. This model is scientifically validated and widely used in atmospheric models to compute radiative transfer [161].

CESM-WACCM requires significant computational capacity, far beyond the capabilities of a personal laptop. UCAR operates several supercomputers, some of which are accessible to US students at NSF-supported universities. Each student can receive a single, on-time allocation of up to 400,000 core hours on Cheyenne, a supercomputer with configurations to support WACCM6-CESM-MAM4 out-of-the-box [152]. Student allocations also include storage space on three directories (scratch, work, and home) with 10 Tb, 1 Tb and 50 Gb of available storage respectively.

CESM2.2 was installed and validated on the author's student account on Cheyenne. Validation tests cases provided by UCAR were run and passed with no modifications to Cheyenne's configuration (located in *env_machines.xml*).

Table 6.1: CESM Component Model Setup and Specifications

	Value	Description
Initialization Time	2000	2000 present day, an additional initialization times defined by components
Resolutions	f09_f09_mg17	grids are: atm:0.9x1.25 lnd:0.9x1.25 ocnice:0.9x1.25
Atmosphere	CAM60%WCSC	CAM cam6 physics: WACCM specified chemistry
Land	CLM50%SP	clm5.0:Satellite phenology
Sea-Ice	CICE%PRES	Sea Ice (cice) model version 5: prescribed cice
Ocean	DOCN%DOM	DOCN prescribed ocean mode
River runoff	MOSART	MOSART: Model for Scale Adaptive River Transport
Land Ice	CISM2%NOEVOLVE	cism2: cism ice evolution turned off
Wave	SWAV	Stub wave component

6.1.1 Component Model Set Up in CESM and Baseline Emissions

To run CESM, each component model must be selected in a *component set*. University Corporation for Atmospheric Research (UCAR) maintains a database of available, scientifically validated component sets for CESM 2.2 and available grid resolutions for each set [44]. Each component set has naming conventions to help identify the component model configurations. For this work, the component set *FWsc2000climo* was selected (see Table 6.1). This component set is supported in only one grid resolution, the *f09 f09 mg17* resolution, which has a 0.9x1.25 degrees grid cells in the atmosphere and 70 pressure levels.

This component set up uses a prescribed ocean model with fixed sea surface temperature from year 2000 data and specified chemistry, greatly reducing the computational cost of running this model. To illustrate, Table 6.2 lists the estimated computational cost for different

Table 6.2: CESM Computational Cost of Various Component Model Setups with WACCM [2]

Component Set Up	Computational Cost per Simulated Year	Description
FW2000	16,843	WACCM with chemistry and year 2000 forcings
FWmadHIST	11,666	WACCM middle atmosphere with D region chemistry, transient free running
FWmaSD	11,388	WACCM middle atmosphere driven by specified dynamics
FWscHIST	4,663	WACCM with specified chemistry
FWsc2000climo	5,000	WACCM with specified chemistry and year 2000 forcings

component sets with and without full chemistry.

The WACCM specified chemistry configuration runs 12 reactions with 29 solution species and 8 invariant species which is considerably smaller than other configurations of WACCM. Table 6.3 shows how this specified chemistry configuration with WACCM compares to other chemistry configuration options.

To achieve lower computational costs, specified chemistry models prescribe the concentration of various chemicals which would otherwise fluctuate and respond to changes in atmospheric dynamics and chemistry. In WACCM6-SC, radiatively active chemical species, like ozone, are prescribed using datasets from a chemically-interactive WACCM6 run [48]. Stratospheric aerosols are also prescribed. However, cloud formation and its subsequent radiative forcing are computed interactively. Despite these simplifying assumptions, WACCM-SC produces nearly identical climatology, and variability of the stratosphere, troposphere and surface climate when compared to full chemistry, free-running WACCM6 experiments [140].

One limitation of selecting WACCM6-SC is that this model will not capture the indirect effect of alumina aerosol emissions on ozone levels since the ozone concentration is prescribed.

Table 6.3: Chemical Mechanisms in CESM and WACCM [3]

Chemical Mechanism Name	Associated Model	Number of Species	Number of Reactions
TSMLT1	WACCM troposphere, stratosphere, mesosphere and lower thermosphere	231 solution, 2 invariant	433 kinetic, 150 photolysis
TS1	CAM-Chem troposphere and stratosphere	221 solution, 3 invariant	405 kinetic, 123 photolysis
MA	WACCM middle atmosphere (stratosphere, mesosphere, lower thermosphere)	98 solution, 2 invariant	207 kinetic , 91 photolysis
MAD	WACCM middle atmosphere with D region chemistry	135 solution, 2 invariant	489 kinetic, 104 photolysis
SC	WACCM Specified Chemistry	29 solution, 8 invariant	11 kinetic, 1 photolysis
CAM	CAM aerosol chemistry	25 solution, 7 invariant	6 kinetic, 1 photolysis

Furthermore, the prescribed shortwave heating above 65 km will obscure any shortwave radiative effects of user-specified emissions in this region. This drawback is negligible since the majority of the emitted reentry mass is expected to quickly descend below 65 km after emission and eventually accumulate in the stratosphere.

Each component model assumes a baseline set of chemical and aerosol emissions that occur on the surface and aloft for both natural and anthropogenic emitters. For example, these species include nitrogen oxides, sulfates, black carbon, primary organic matter, and dimethlysufide (DMS). Users of the model can also add, modify or remove these forcings. For this study, the Coupled Model Inter-comparison Project Phase 6 (CMIP6) emission datasets for year 2000 are used to specify emissions for volcanoes, aircraft, and various surface emissions from natural and anthropogenic sources (see Appendix A for more information) [5]. These year 2000 emissions are repeated cyclically in the model to generate the same year-over-year emissions. However, within year 2000, WACCM and CESM perform linear interpolation between data points in CMIP6 datasets. For example, CMIP6 data that is specified monthly is linearly interpolated between months over the entire year and reset back to January 2000 emissions at the start of the following year.

Repeating year 2000 emissions cyclically introduces an assumption that the atmosphere and ocean temperatures are time-invariant. Similarly, this assumes that anthropogenic and natural emissions remain constant. For certain species, studies have shown a remarkable increase in their atmospheric concentration since 2000. Carbon dioxide emissions have grown substantially, while chlorofluorocarbons have undergone a steady decline (see Figure 6-3 and Figure 6-4). The constant year 2000 forcings do not capture these changes to the atmosphere, and consequently underestimates carbon dioxide and overestimates chlorofluorocarbons and their respective atmospheric consequences.

6.1.2 Alumina Emission Characteristics

To simulate reentries emissions, a new user-defined emission file that represents these emissions must be added to the model. These files determine the timing, location and amount of an emitted species. This section discuss in detail how emission files for reentries were constructed in this work.

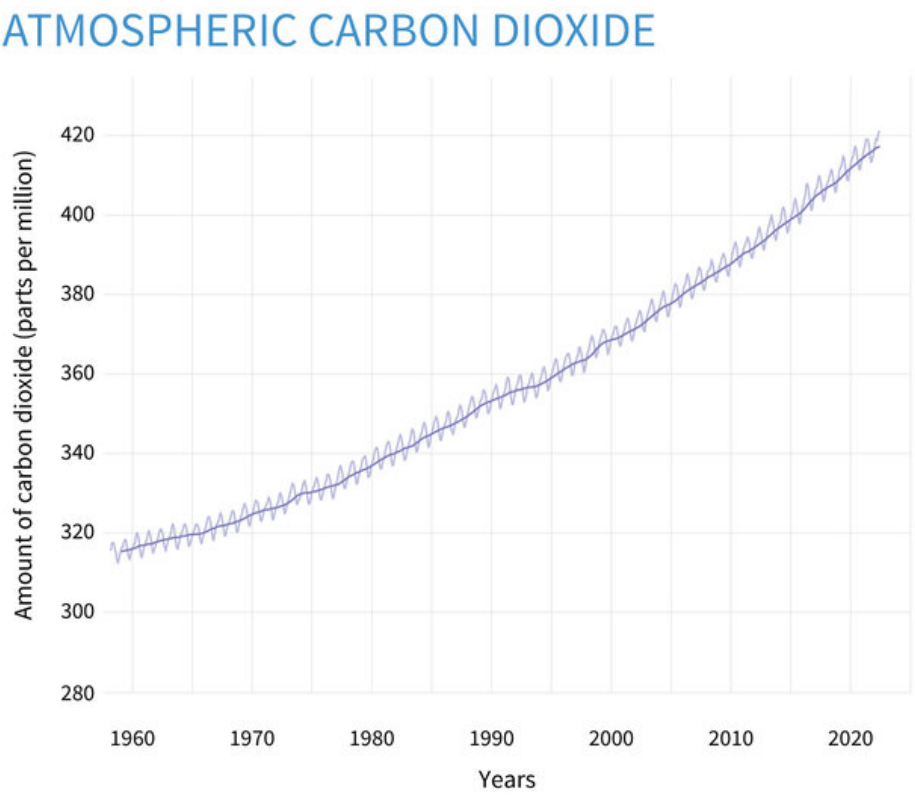

Figure 6-3: Monthly Averaged Carbon Dioxide Measurements taken from Mauna Loa Observatory over Time [4, 6]

,

The reentry forecasts described in Subsection 4.2.1 are used to determine the number of reentry events, total reentry mass and the average satellite and rocket body mass. For the market optimistic scenario, we assume 13,900 satellite reentries with an average satellite mass of 600 kg and 500 rocket bodies with an average rocket body mass of 2,800 kg.

Each of these reentry objects is treated as a discrete event such that there are several impulse emissions over the course of a year. The reentry emissions are not considered as a uniform, constant emission over a fix latitude, longitude or altitude region. Instead, each emission can have varying emitted mass over differing altitudes and locations.

Note that WACCM and CESM's default time step is 30 minutes. While this time step can be lowered, it significantly increases the computational cost. Reentry events typically occur over 2-3 minutes, but it is unreasonable to adjust the model timestep to this interval. Accordingly, all reentry emissions have a 30 minute duration. Over numerous simulated years, 30 minute emissions versus 3 minute emissions will result in insignificant changes to

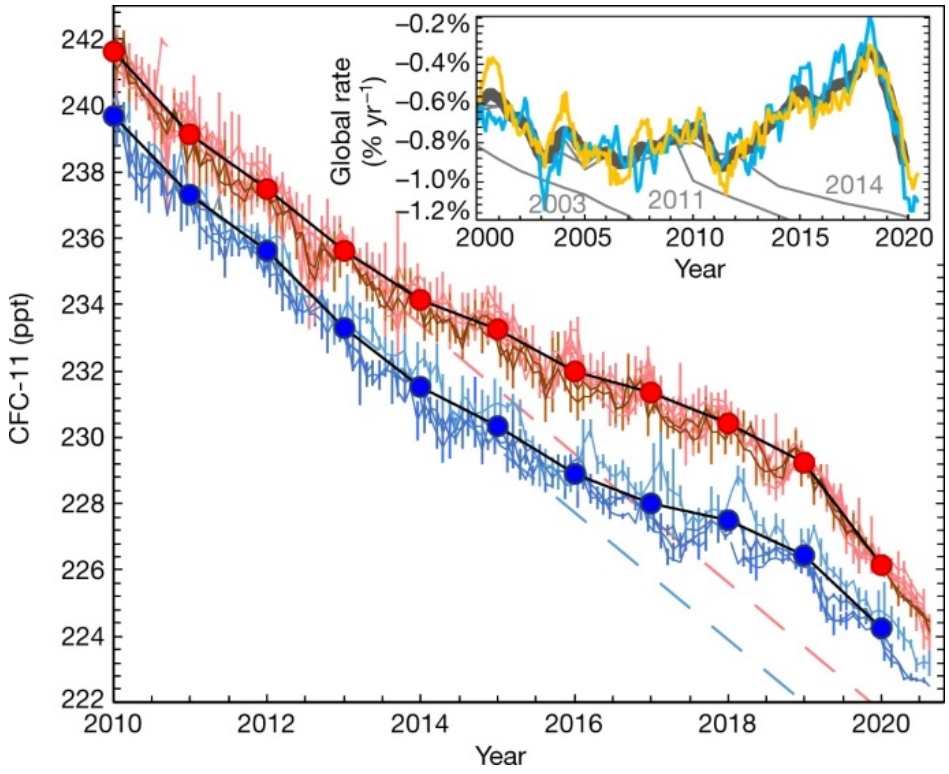

Figure 6-4: Measured Atmospheric Mole Fractions of CFC-11 and Global Mean Rate of Change [95]

,

the aerosol distribution.

Discrete emissions best replicate repetitive reentry events but consequently creates extremely large input emission files on the order of hundreds of gigabytes. CESM uses NETCDF files to store and read in data. These files uses multidimensional arrays to represent time-varying, global data at various pressure levels. In CESM, the outer most array represents the time dimension followed by the altitude or pressure level, latitude and longitude dimensions. In WACCM, there are 192 latitude, 288 longitude, and 70 pressure level increments to create the atmospheric grid. As a result, increasing the time array to capture discrete events rapidly increases in the size of the multidimensional data array. One additional time entry results in 3.8 million additional array entries. To reduce the emission file size, we use 30 altitudes over the altitude range of 30 to 94 km with 2 km intervals. The Riemann sum integration with these altitude steps introduces less than 1% error in the computed emitted mass and the expected reentry mass.

To create a discrete, step emissions, an additional three time entries are needed to pad the emission event with sufficient zeros to prevent linear interpolation between reentry events. The first zero pad starts one second prior to the model time step when the emission starts followed by a second time entry which contains the emission. The third time entry is one second before the time step when the emission ends followed by a forth time entry on the model time step filled with zeros.

To walk through an example, let an reentry event occur on January 1, 2000 at 10am and assume the model time step is 30 minutes. The first zero pad should occur at January 1 at 9:59am followed by a time entry with the emission data at 10am. The emission end time should generate a third time entry at 10:29am followed by a zero-pad time entry at 10:30am. This scheme causes the model to linearly interpolate between zeros, rather than the emission values, to create discrete emissions with stepwise changes.

The emission timing is randomly sampled over the emission year using a uniform distribution where each second in a year has equal probability of being selected. This sampled reentry time is subsequently rounded to the nearest model timestep, using increments of 30 mins.

Each reentry event also has a specified latitude, longitude and a range of altitudes to characterize the location of the emissions. The ablation profile for rocket bodies and satellites is shown in Figure 4-3 in Chapter 4. These emissions are assumed to occur directly above each latitude-longitude location, rather than along a reentry trajectory. This simplifying assumption is not expected to change the distribution of the aerosol over a multi-year study since the aerosols will be transported and redistributed across much further distances compared to the length of a reentry trajectory.

Since it is difficult to estimate where a reentry will occur, the latitude and longitude for each emission is sampled from a histogram of reentry object ground tracks. Figure 6-5 shows this groundtrack distribution.

To create this histogram, Two-line Element (TLE) data was downloaded from Space Track for each reentry object in the historic reentry population (described in Chapter 4). The Space Track data records all reentry predictions for an object, and as a result, there are several database entries for a single NORAD identification number. These multiple entries

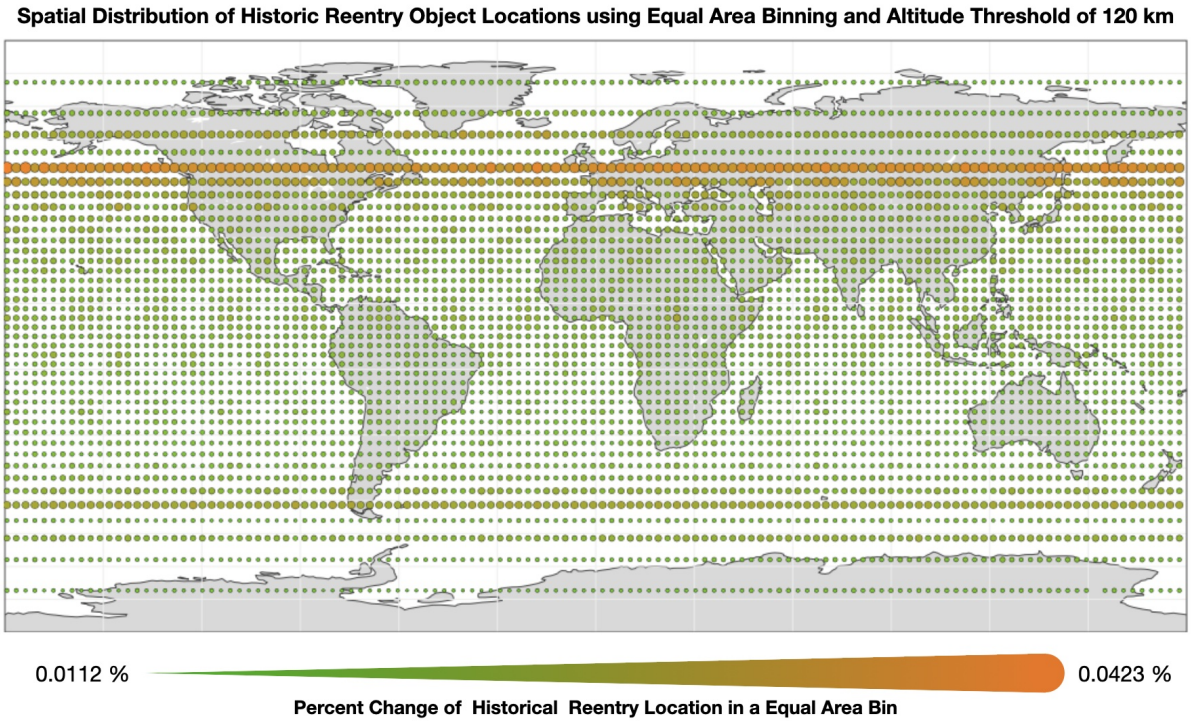

Figure 6-5: Histogram of Historic Reentry Ground Tracks using TLE data propagated over 24 hours using equal area bins of 100,000 km^2 with 120 km altitude threshold

,

must be consolidated. The model preferentially saves the reentry prediction with the latest issued Tracking and Impact Prediction (TIP) message. However, not all reentry objects in Space Track have TIP messages. Space Track records TIP, decay, SATCAT and 60-day reentry messages. If an entry in the Space Track dataset does not have a TIP message, the script records the SATCAT prediction followed by the 60-day prediction as a last resort.

Every reentry object in the historic reentry population was matched to its latest Two-Line Element orbital information from Space Track. If an object had a TLE that was older than 5 days from the reentry prediction, the object was removed from the dataset. TLE data poorly predicts an object's orbital location after approximately 5 days [32]. These exclusions reduced the population size to 9,911 reentry objects. This population was used to create the ground track histogram.

The ground track for each reentry object was computed using Simplified General Perturbations-4 (SPG4) orbital propagator at one minute intervals with the SkyField Python library [121]. SPG4 is a low-fidelity orbital propogator that neglects fluctuations in atmospheric density

from solar influences and has simplified gravitational effects [15]. However, SPG4 was specifically designed to work with TLE data which contains insufficient data to run other higher fidelity models.

Ground track propagation occurs over a reentry prediction window. Space Track TIP messages provide these reentry prediction windows. Objects that did not have predicted reentry windows were assigned a +/-24-hour reentry window. However, reentry prediction windows were shortened if the TLE epoch occurred after the lower bound of the window, and if the TLE validity (set to 5 days after epoch) expired prior to the upper bound of the window.

Latitude and longitude locations for each ground track were recorded if the orbital altitude was less than or equal to 120 km. This threshold ensured that the object was close to reentering and ignores ground track locations that correspond higher altitudes. This check is particularly important for highly elliptical reentries which spend considerable time at higher altitudes. Including these data points would have skewed the ground track histogram and included locations which did not correspond to an object approaching its reentry. Figure 6-6 shows a histogram of the eccentricity and inclination of the reentry object population.

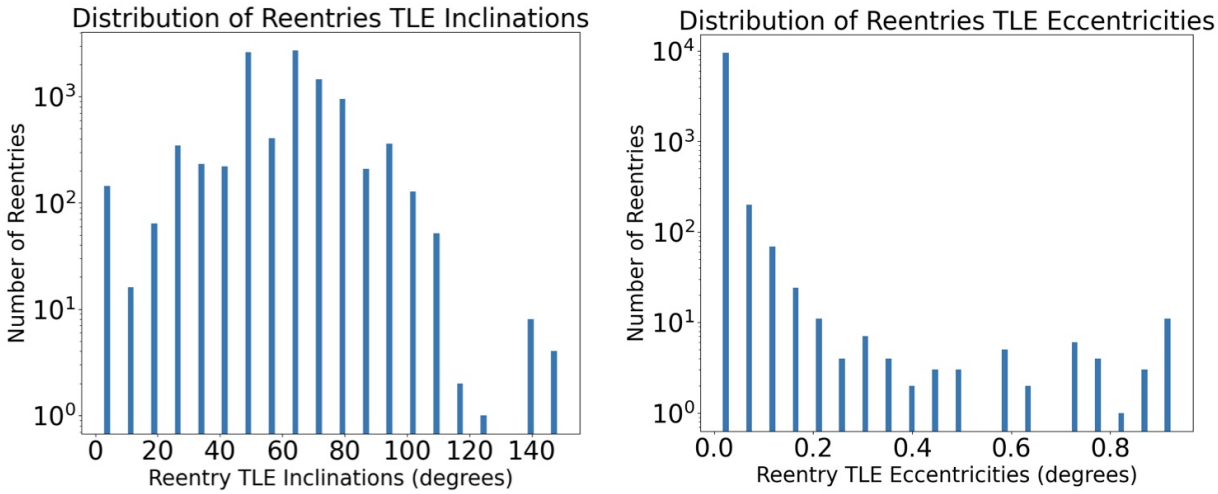

Figure 6-6: Histogram of Eccentricity and Inclination of Historical Reentry Object Population

,

Once all reentry objects ground tracks were propagated and recorded, the ground track locations were binned with equal area partitioning of the Earth's surface using Matlab's

hista function. This function requires an input parameter to specify the size of the equal area bins. An arbitrary value of 100,000 km^2 was selected. The markers in Figure 6-5 show the center points of these equal area bins. Each bin count was normalized by the total bin counts to create a discretized geospatial probability distribution of reentry locations. The size and color of the markers in Figure 6-5 indicate these probabilities.

Uniform sampling of the discrete cumulative distribution derived from the ground track histogram leads to a random sampling of a reentry location according to the probability distribution of historic reentry locations. Each latitude and longitude pair represent a single entry on the independent axis in the cumulative distribution. Uniform random sampling between 0 and 1 selects a point on the dependent axis which is rounded to the nearest discrete point. Mapping this point to the independent axis is the sampled reentry location. Each emission has a sampled reentry location that is computed using this method.

In WACCM6-MAM4, user-defined emissions are specified in a file called, *user_nl_cam* where each emission is either a surface emission (*srf_frc_sp*) or a 3D , vertical emission (*ext_frc_specifer*). Each emission file corresponds to a species, denoted by a species variable name. Appendix A shows how emission files are connected to species name in the *user_nl_cam*.

It is important that each emission that is specified in *user_nl_cam* is also listed in the *Ext Forcing* section of the chemical mechanism file. For *FWsc2000climo*, the chemical mechanism file is *pp_waccm_sc_mam4* (see Appendix A). If these emissions are not also listed in *Ext Forcing* of the chemical mechanism file, then the model will throw a run time error.

To specify aerosol emissions, WACCM users must define both a mass emission file (in units of $molecules/cm^3/s$) and number emission files (in units of $(particles/cm^3/s)$ $(molecules/mole)(g/kg)$). MAM4 uses these two emission files and an assumed particle size distributions to create aerosols emissions with varying particle sizes. The unit for number emission files is particular to CESM and stems from default scaling that occurs when CESM reads in user specified emissions. To cancel the effects of CESM's default scaling, number emission files are prescaled, resulting in the unit of $(particles/cm^3/s)(molecules/mole)(g/kg)$ (see Appendix B for more details). Equation 6.1 shows the equation relating mass emissions

Table 6.4: Dust Size Distributions in CAM6 - MAM4 [67, 80, 82]

Dust Bin	Minimum Radius (μm)	Maximum Radius (μm))	Geometric Standard Deviation	Dust Volume/-Mass Weighted Diameter (m)
Aikten	0.01	0.1	1.6	8.874e-8
Accumulation	0.1	1	1.6	7.806e-7
Coarse	1	10	1.2	3.898e-6

to number emissions. In Equation 6.1, MW is the molecular weight of the species, ρ is the species density and d is the volume/mass weighted mean diameter for the species in a given particle size mode.

$$E_{num} = E_{mass} \frac{MW}{\frac{\pi}{6}\rho d^3} \tag{6.1}$$

6.1.3 Using Dust as a Proxy for Alumina

Ideally, the space debris alumina emission files would point to an alumina ($Al2O3$) species tracer in WACCM6. Unfortunately, alumina is not a supported aerosol in WACCM6-MAM4 and MAM4 does not easily support adding a new aerosol into the model without significant source code changes [8]. To work around this issue, we use dust as a proxy for alumina in this model. Terrestrial dust is an existing aerosol, modeled as $AlSiO_5$, in MAM4. WACCM6 receives dust emissions from the land model which uses surface wind profiles to compute soil loss to the atmosphere [136]. This dust can exist in three size distributions, the Aitken, accumulation and coarse modes, corresponding to species names, *dst_a2*, *dst_a1*, and *dst_a3* respectively. The particle size distributions for each mode are shown in Table 6.4

The particle size distribution of space debris alumina particles is unknown. While there have been some arc-jet studies on the demisability of aluminum, these studies were interested in the demise time and did not characterize the aluminum ablation particles.

Furthermore, computational fluid dynamics modeling tools of reentry flows do not yet predict particle size distributions of ablated particles [137]. One molecular dynamics study attempted to generate size distribution for ablated alumina, but given the computational limitations of molecular dynamics algorithms, this study was only able to study particle

sizes up to 40 nanometers [43]. Arc-jet studies of Phenolic Impregnated Carbon Ablator (PICA), a carbon-carbon ablative heat shield material, have tracked and captured spallation particles, finding that these particles range from 10 to 100 microns for semi-spherical test samples [116, 30]. However, the spallation phenomena of PICA is poorly understood and its unclear if the same phenomena applies to aluminum ablation during reentries [30].

Given the uncertainty surrounding the particle size distribution of ablated alumina, this work assumes that the dust particle size distributions are a reasonable estimation. Furthermore, we conduct a sensitivity analysis across the dust size modes to determine the effect of different particles size assumptions. No modifications to the dust size distributions were made to test additional particle size distributions beyond Table 6.4. Any modifications to these dust properties would alter the surface dust emissions, leading to potentially significant error in the terrestrial dust behavior and lifetime in the troposphere. This error may cause unreasonable atmospheric behavior and poor model results. For this reason, no physical nor optical properties of dust are modified to better mimic alumina.

To remove terrestrial dust, these particles experience wet and dry deposition and gravitational settling on the surface. Rocket-borne alumina also interacts with sulfates and experiences the same deposition phenomena as dust [157]. As a result, it is reasonable to assume that reentry-ablated alumina particles will experience sulfate coating, dry and wet deposition and gravitational settling, albeit the rate at which this occurs is not understood, and thus cannot be compared to terrestrial dust.

While dust and alumina both participate in heterogeneous chemistry, MAM4 does not yet model heterogeneous chemistry for dust. Therefore, dust does not act as a surface for any chemical reactions, including ozone depleting reactions.

Like alumina, dust is radiatively active in WACCM6. RRTMG uses the refractive indices of an aerosol over several bands of wavelengths to compute the single scattering albedo, or the ratio of the scattering efficiency to the total extinction efficiency [146, 64]. This parameter is then used to compute changes to radiative transfer due to aerosols [146]. The refractive indices for alumina and dust are shown in Figure 6-7a and Figure 6-7b, assuming a sign convention of $\bar{n} = n + i\kappa$ where $\bar{n}$ is complex refractive index, n is the real part, and κ is the imaginary part, also known as the absorption coefficient. Note that WACCM-RRTMG uses

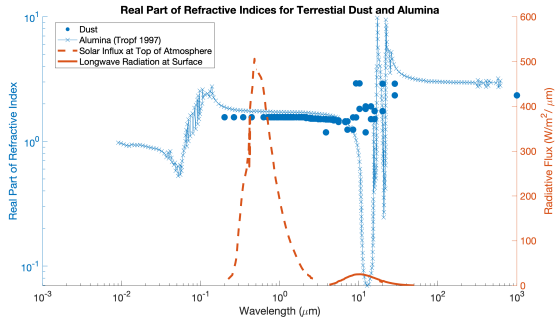

(a) Real Refractive Indices

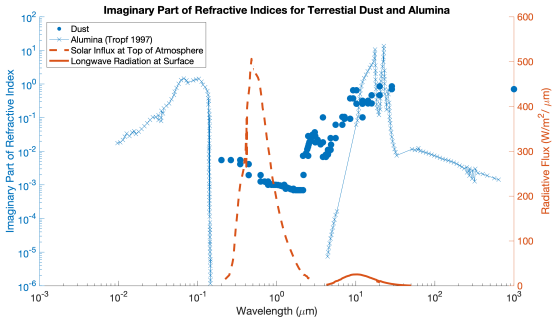

(b) Imaginary Refractive Indices

Figure 6-7: Refractive Indices of Terrestrial Dust ($AlSiO_5$) taken from WACCM-RRTMG and Alumina (Al_2O_3) taken from [106] compared to the Solar Influx and Earth's Outgoing Longwave Radiation (taken from [68])

the opposite sign convention ($\bar{n} = n - i\kappa$) which has been corrected for in Figure 6-7b. The right-hand axis shows the incoming solar irradiance and Earth's outgoing radiation.

The real part of a refractive index characterizes how well an aerosol scatters light while the imaginary part indicates how well an aerosol absorbs light [83]. As Figure 6-7a shows, the real part of dust and alumina are very similar over a number of wavelengths, including over the solar irradiance band. In this region, dust has real refractive indices within 10% error of alumina. At the largest wavelengths, dust underestimates alumina's real refractive index by approximately 20%. Over band of wavelengths of Earth's outgoing radiation, we see that alumina's real refractive index differs significantly from dust. Alumina is more transparent than dust to Earth's outgoing radiation over a small band, limiting this source of error. Overall, terrestrial dust represents a first order approximation of alumina in terms of scattering efficiency.

Comparing the absorption coefficients, dust significantly overestimates alumina's absorptivity in short wavelengths, but is a good proxy for long wavelengths, above 100 microns. This mismatch will lead to dust absorbing more light than alumina, leading to warmer radiative forcing results than alumina would otherwise produce. As a result, we can conclude that dust as a proxy for alumina results in conservative estimates of the direct radiative effect of alumina.

6.1.4 Test cases

Several test cases were run to analyze the sensitivity of a number of assumptions. Two test cases explore the effect of selecting different size distributions for the initial emitted mass. One test case explores the effect of modeling reentries as discrete events with distinct plumes compared to using a time-averaged representation of reentries. Another test case explores the importance of reentry location, testing specifically the influence of concentrated reentry events in the South Pacific. Due to its isolation, this region has been the site of at least 263 intentional space debris reentries since 1971 to minimize harm to human life and property [31]. With this test case, we aim to understand whether concentrating reentries in this location is a sustainable and recommendable practice. Table 6.5 summarizes each of these test cases explored in this work.

Importantly, test cases 1 and 2 share the same emission mass files which preserves the reentry location, timing and emitted amount across the two cases. The number emission file of case 1 was scaled by the cubed ratio of the accumulation dust diameter over the Aikten dust diameter (shown in Table 6.4) to generate the appropriate number emission file for case 2. This approach ensures that the only difference between these two cases is the emitted particle size.

The emission file for case 4 was generated by limiting the scope of possible reentry locations to the South Pacific, defined by latitudes 70°S to 10°S and longitudes 140°W to 70°W. Each latitude and longitude are independently picked from a uniform distribution. The total number of satellite and rocket body reentries per year and the average satellite and rocket body mass are kept the same as case 1 and case 2 (refer to Figure 4-6 for these values).

Derived from the emission files of case 1, the time-averaged emission file was generated by computing the year-averaged emitted mass per grid cell. The yearly emitted mass is kept constant across case 1 and 3, as a result. Figure 6-8 shows the spatial distribution of these time-averaged emissions at 50 km in altitude.

Based on the Market Optimistic scenario, the yearly emitted alumina mass totals 1.337 Gg. This emitted alumina mass is calculated assuming 21% of a satellite's dry mass is

Table 6.5: Test Cases

Test Case Name	Emitted Dust Mode	Description	Sensitivity Explored
Base Case	None	Control Case	N/A
Case 1	Accumulation Mode (medium size)	Reentry emissions are generated from the Market Optimistic scenario. Emissions are discrete events that occur over globe.	Emitted Particle Size
Case 2	Aikten Mode (smallest size)	Reentry emissions are generated from the Market Optimistic scenario. Emissions are discrete events that occur over globe.	Emitted Particle Size
Case 3	Accumulation Mode (medium size)	Time-averaged emissions with constant forcing over time. Emissions are generated from the Market Optimistic scenario.	Saliency of Modeling Discrete Reentry Plumes
Case 4	Accumulation Mode (medium size)	Reentry emissions are generated from the Market Optimistic scenario. Emissions are discrete events that occur only in the South Pacific.	Emission Location

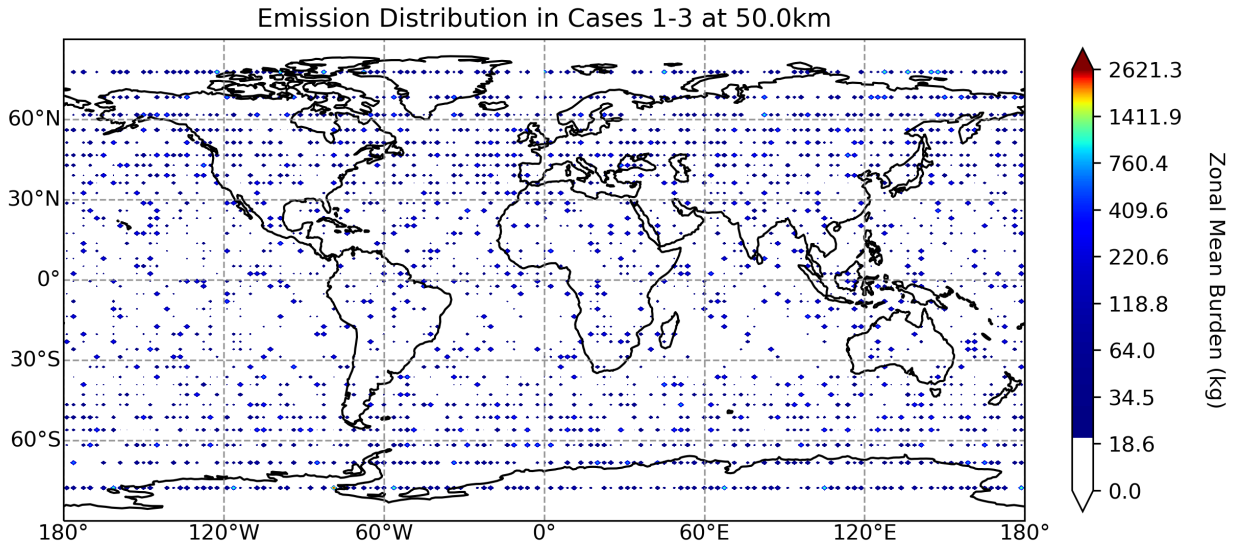

Figure 6-8: Yearly Averaged Emissions Distribution at 50 km

,

aluminum of which 58% ablates and 70% of a rocket body's dry mass is aluminum of which 31% ablated. These assumptions are taken from material composition analysis and ablation modeling, presented in Chapter 4.

6.1.5 Double Runs and Output Variables

In all of the test cases, we use double radiation calls to isolate the radiative effect of dust. Double radiation calls are a built-in feature within WACCM and RRTMG that allows users to request additional radiation computation for different sets of radiatively active species. A major advantages of these calls is that the same atmospheric makeup is used across each radiation call, ensuring that the radiation calculations are comparable across different calls and over time. As a result, we can use a double radiation call to isolate the radiative effect of a dust mode by defining a radiation call with and without dust as a radiatively active species.

Since dust can transition between across modes, it is important to isolate the radiative effect of all of the possible modes of dust. For example, since accumulation dust can transition into the coarse mode, we must isolate the radiative effect of both accumulation and coarse dust in a double radiation call. Similarly, for Aitken dust, which can transition into the

Table 6.6: Radiation Calls in the Base Case

Radiation Call Ids	Excluded Species
0	No Exclusions, All Species are Included
1	All Aerosols
2	Accumulation Dust
3	Accumulation and Aikten Dust
4	Coarse Dust
5	Aitken Dust
6	Accumulation and Coarse Dust
7	Accumulation, Aikten and Coarse Dust

accumulation mode and later into the coarse mode, all three modes must be accounted for. To do so, we define a double radiation call with various dust modes excluded from the radiatively active species.

The base case has numerous double radiation calls which are listed in Table 6.6. These calls are used to determine the radiative effect of dust emitted from Earth's surface. For example, to determine the radiative effect of surface emitted dust in the accumulation mode, we subtract the radiation call "0" with radiation call "6". Similarly, each perturbed test case contains double radiation calls.

To isolate the radiative effect of reentry "dust", we subtract the zeroth radiation call in the perturbed case with its respective double radiation call. This subtraction results in the radiative effect of both reentry and surface dust emissions. To remove the surface dust contribution, we subtract the surface dust radiative effect computed from differencing the base case radiation calls. In this approach, we are implicitly assuming that the surface dust radiative contribution is nearly identical across the base case and the perturbed cases. We will explore this assumption further in Chapter 7 when we review and compare results from the perturbed and base cases.

6.1.6 Adjustments to Model Methodology to Control Surface Dust Variance

The model setup described up until this point does not control the surface dust emissions. Surface dust emissions in WACCM-SC are normally calculated dynamically, responding to

changing wind patterns and precipitation levels. Since the model's meteorology is not prescribed in WACCM-SC, it is possible that the wind patterns and precipitation levels between the base and perturbed cases differs significantly, and consequently obscure the reentry "dust" emissions in the stratosphere and troposphere.

Early results confirmed that the surface dust emission variance obscures the reentry "dust" emissions in the stratosphere and troposphere. Figure 6-9a shows the accumulation dust burden computed by differencing the Case 1 accumulation dust levels from the base case. It is clear from this result that reentry emissions on the order of 10^6 will be lost in the natural variance of surface dust emissions which can vary on the order of 10^{10}.

Referencing Figure 6-9b, we can see that the reentry "dust" emissions begin to become indistinguishable from the surface dust emissions around 6 hPa which approximately corresponds to 33 km in altitude. Unfortunately, this altitude is in the middle of the upper stratosphere, a region we are interested in characterising due to the potential for reentry "dust" to accumulate in stratospheric circulation. As a result, we cannot simply limit our our analysis to pressure levels above 33 km where the reentry "dust" signal is distinguishable.

Figure 6-9c, Figure 6-9d, and Figure 6-9e provides more insight the core differences that drive the large variance in the accumulation dust burden shown in Figure 6-9a. Had the wind patterns and precipitation between the perturbed and base cases been identical, the surface flux of accumulation dust between the two cases would have been equivalent. However, Figure 6-9c shows significant differences up to 200 kg/s in the surface dust flux. For reference, the reentry "dust" emissions in the Market Optimistic scenario are approximately 0.04 kg/s, four orders of magnitude smaller than the differences in surface dust flux.

Motivated by these results, we implement additional modifications to the model to control the surface dust flux. Unfortunately, the specified chemistry version of WACCM6 does not support prescribed meteorology in the troposphere which is necessary to control the wind and precipitation patterns that influence the variance in the wet and dry deposition rates. As a result, we have prescribed the surface dust flux without prescribing the meteorology which decouples the natural feedback between surface dust flux and meteorology. We assume that this error is negligible and limited to the troposphere over short time scales.

To prescribed surface dust emissions, we had to remove the prognostic calculation of

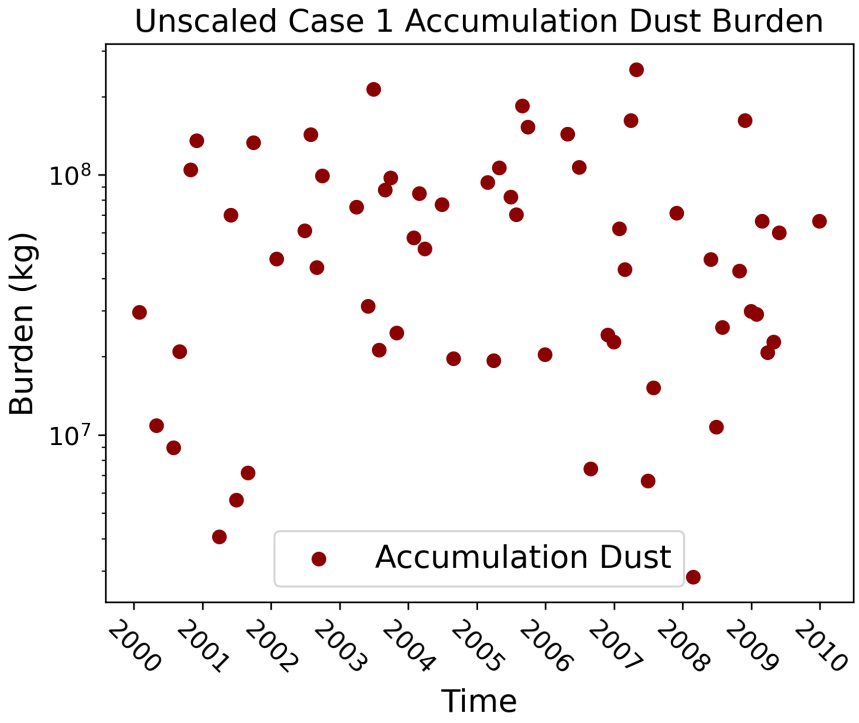

(a) Accumulation Dust Burden over Time

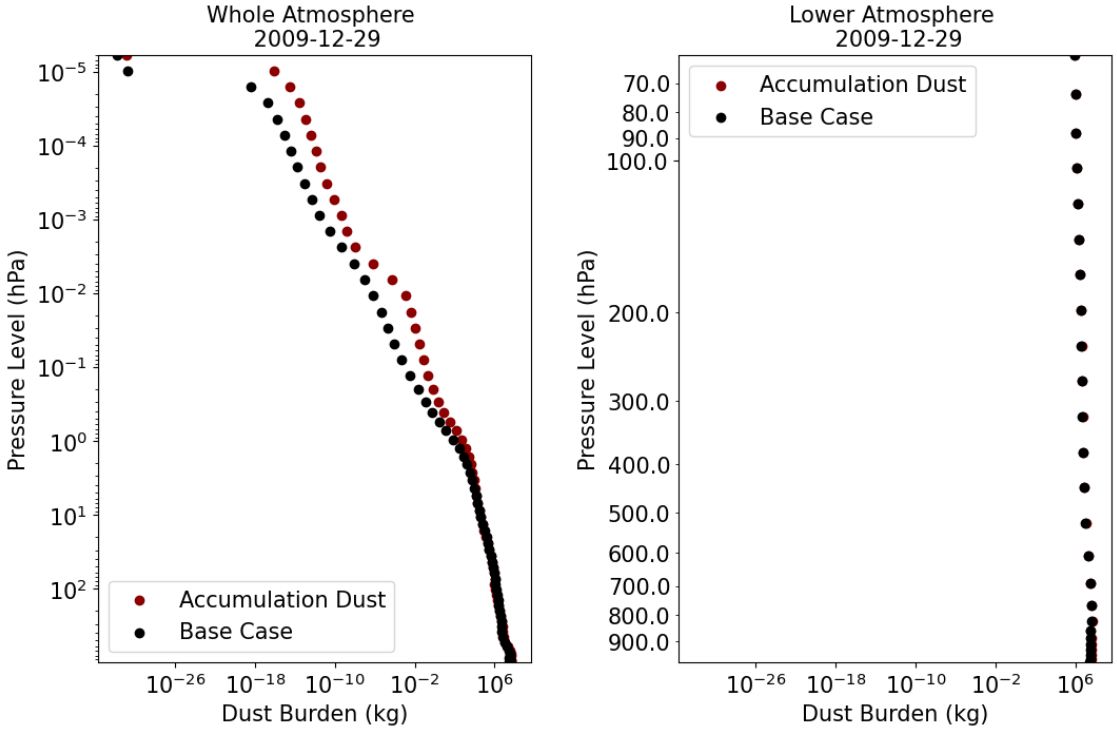

(b) Vertical Profile of Accumulation Dust Burden Summed over Year 2010 (Tenth Simulation Year)

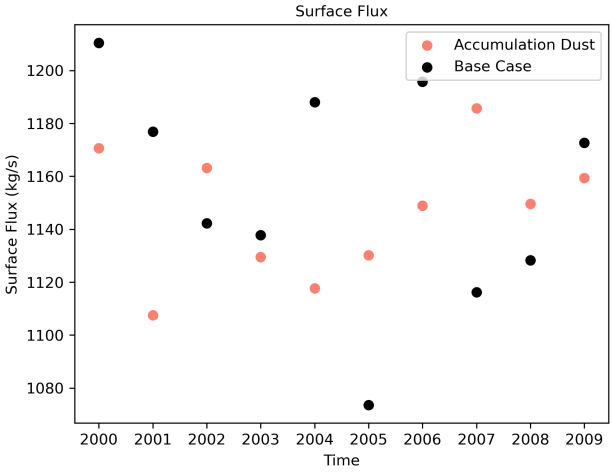

(c) Yearly Averaged Surface Flux

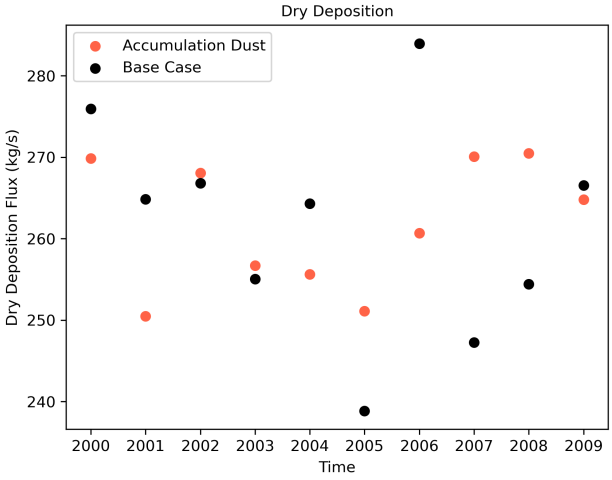

(d) Yearly Averaged Surface Flux

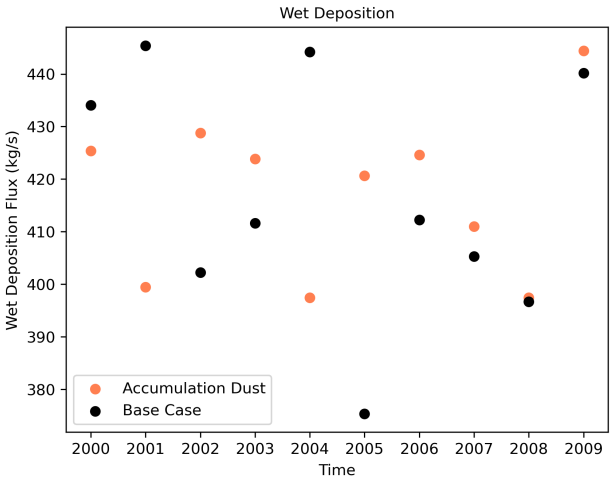

(e) Yearly Averaged Emissions Deposition and Surface Flux at 50 km

Figure 6-9: Chaos in Early Dust Results Motivating User-specified Surface Dust Emissions and Reentry "Dust" Scaling

surface dust flux and create user-specified emissions files to represent the yearly surface dust fluxes. The first task was accomplished by scaling the prognostic dust emissions by a dust emission factor, called *dust_emis_fact*, which was set to the largest value that could be saved in a Fortran double variable, 10^{300}. This scaling factor divides the surface dust flux, zeroing out the dynamically calculated dust emissions.

User-specified emission files for the surface dust fluxes in all three dust modes were generated using data from a base case run of SC-WACCM without any modifications to the default value of *dust_emis_fact*. Figure 6-10 shows these surface dust emissions for all three dust modes. Importantly, like other user-specified emissions, these terrestrial surface dust emissions are repeated identically year-over-year.

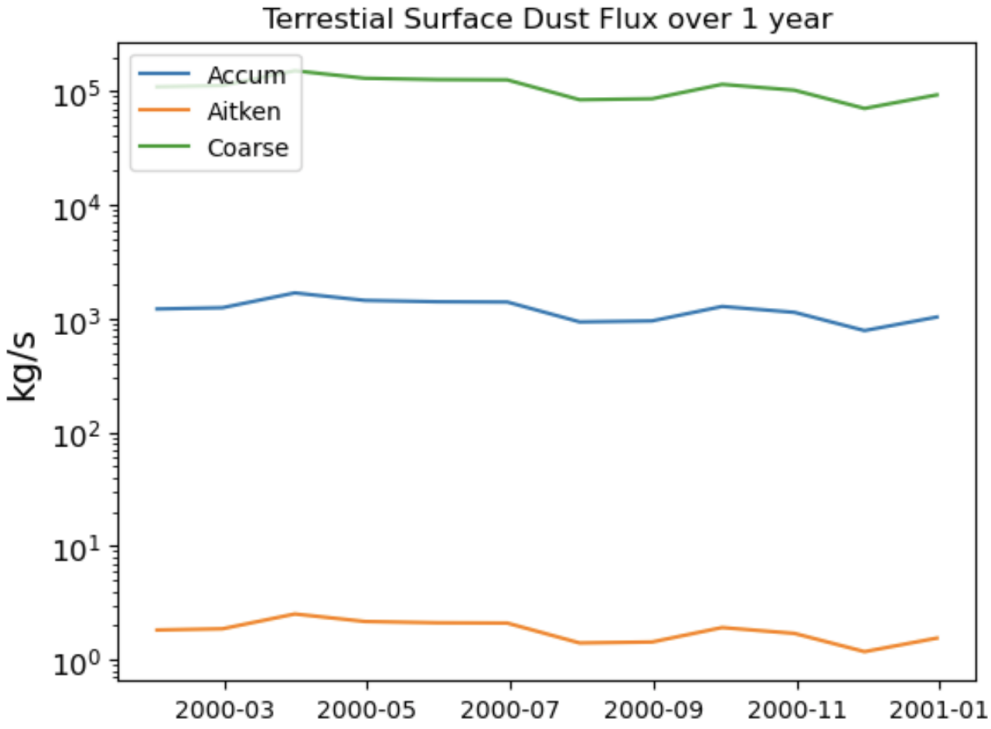

Figure 6-10: User-specified Surface Dust Emissions for the All Dust Modes

,

In addition to controlling the surface dust flux, we also scaled the reentry "dust" emissions by a factor of 1000 such that the reentry "dust" could be resolved through the stratosphere. As a result, each test case emits 1.337 Tg rather than 1.337 Gg. In order to re-scale back to the Market Optimistic scenario, we assume a linear relationship between the emitted

mass and the radiative effects of reentry "dust." Several studies on atmospheric aerosols have used this approach to improve signal-to-noise ratios in their respective atmospheric models [25, 91, 54, 54]. Following this literature, we assume a linear relationship between the reentry "dust" emitted mass and its direct radiative forcing and downscale the results shown in Figure 7-8, Figure 7-9, Figure 7-10 and Figure 7-11 by a factor of 1000 to estimate the direct radiative effect of reentry "dust" in the Market Optimistic scenario. Table 7.3 summarizes the scaled and downscaled total direct radiative effect of reentry "dust" in each test case.

Sensitivity studies have shown that the direct radiative forcing of black carbon, sulfate and dust aerosols can be estimated to a first-order approximation by assuming a linear relationship with the specie's emitted mass [122, 25, 91]. Each of these studies caveat their results with a note that this linear relationship was only determined over the small range of scaling parameters. None of these studies tested a scaling parameter as large as 1000 times. Due to limited computational resources, we could not perform a sensitivity analysis on these results, but instead, include this study in future work.

Appendix C provides a consolidated summary of the assumptions in this methodology for clarity and quick reference.

Chapter 7

WACCM Results

In this chapter, we present the burden, lifetime, distribution and direct radiative forcing effects of reentry "dust" across all test cases. All of the results presented in this chapter were generated using monthly averaged output data from WACCM.

Atmospheric burden is the measure of the amount of mass of a species in the atmosphere. In this work, we present the reentry "dust" burden in terms of mass. Atmospheric burden can be plotted over time to identify when the system has reached steady state. This equilibrium occurs when a species' burden becomes stable or oscillatory about a steady state burden.

Some test cases reached steady state much faster than others, and as a result, some test cases were simulated for fewer years to save computational resources. We present the steady state ranges in Table 7.2 and uses these windows to compute steady state averages for each case.

Once steady state has been reached, we can compute the lifetime of reentry "dust." The steady state lifetime is defined in Equation 7.1 where C is the global, annual mean burden and S is the global annual emission rate of a species at steady state. Note that S is equivalent to the loss rate of a species at steady state since production and loss rates are equivalent at equilibrium [27].

$$\tau_{ss} = \frac{C}{S} \tag{7.1}$$

The lifetime of a particle indicates the average time a particle remains in the atmosphere.

Therefore, particles with longer lifetimes tend to accumulate and interact with atmospheric processes over long time scales. For aerosols, the particle's lifetime is highly dependent on the particle size [42]. The smallest particle sizes in the Aitken mode are most efficiently removed by cloud nucleation and coagulation with larger particles [49]. The largest particles sizes in the coarse mode are efficiently influenced by gravitational settling. Therefore, the middle size particles in the accumulation mode are least effected by deposition mechanisms in the atmosphere and typically have the longest lifetimes [49].

Recall that dust in MAM4 can transition between different particle size modes due to coagulation (see Figure 6-2). The Aitken mode can transition into the Accumulation mode which can transition into the coarse mode. Clouds can uptake dust in each mode, as well. These transitional effects have been accounted for in post-processing.

In addition to lifetime calculations, we present the steady state distribution of the reentry "dust" burden using zonal averaging. Zonal averaging reduces three-dimensional data to two dimensions by taking the average burden over all the longitudes at a give latitude and altitude. This approach works well since the reentry "dust" is nearly uniform in distribution across longitudes and varies more significantly across latitude and altitude (see the column sum distributions in Appendix F).

When analyzing the reentry "dust" distributions, we refer to three atmospheric regions: the polar, mid-latitude and tropic regions. Figure 7-1 defines these regions. The 23.5 degree parallel corresponds to the Tropic of Cancer and Capricorn in the Northern and Southern hemispheres, accordingly. Similarly, the 66.5 degree parallel corresponds to the Arctic and Antarctic circle.

7.1 Burden, Distribution and Lifetime of Reentry Dust

For each test case, we present the steady state burden, spatial distribution and lifetime of each dust mode. To do so, we first compute the burden of each dust mode over time and determine when steady state is achieved.

In every test case, the reentry "dust" emissions are only discernible from terrestrial dust within a specific altitude band. Demonstrating this effect, Figure 7-2 shows the vertical

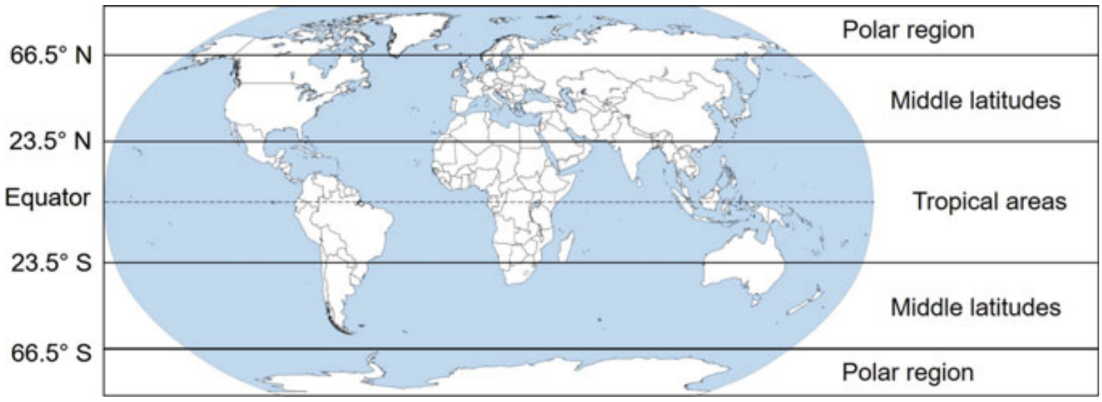

Figure 7-1: Definition of Mid-Latitude, Tropic and Polar Regions [34]

,

profile of the accumulation dust mass over time for Case 2, the market optimistic case with reentry emissions in the Aitken dust mode.

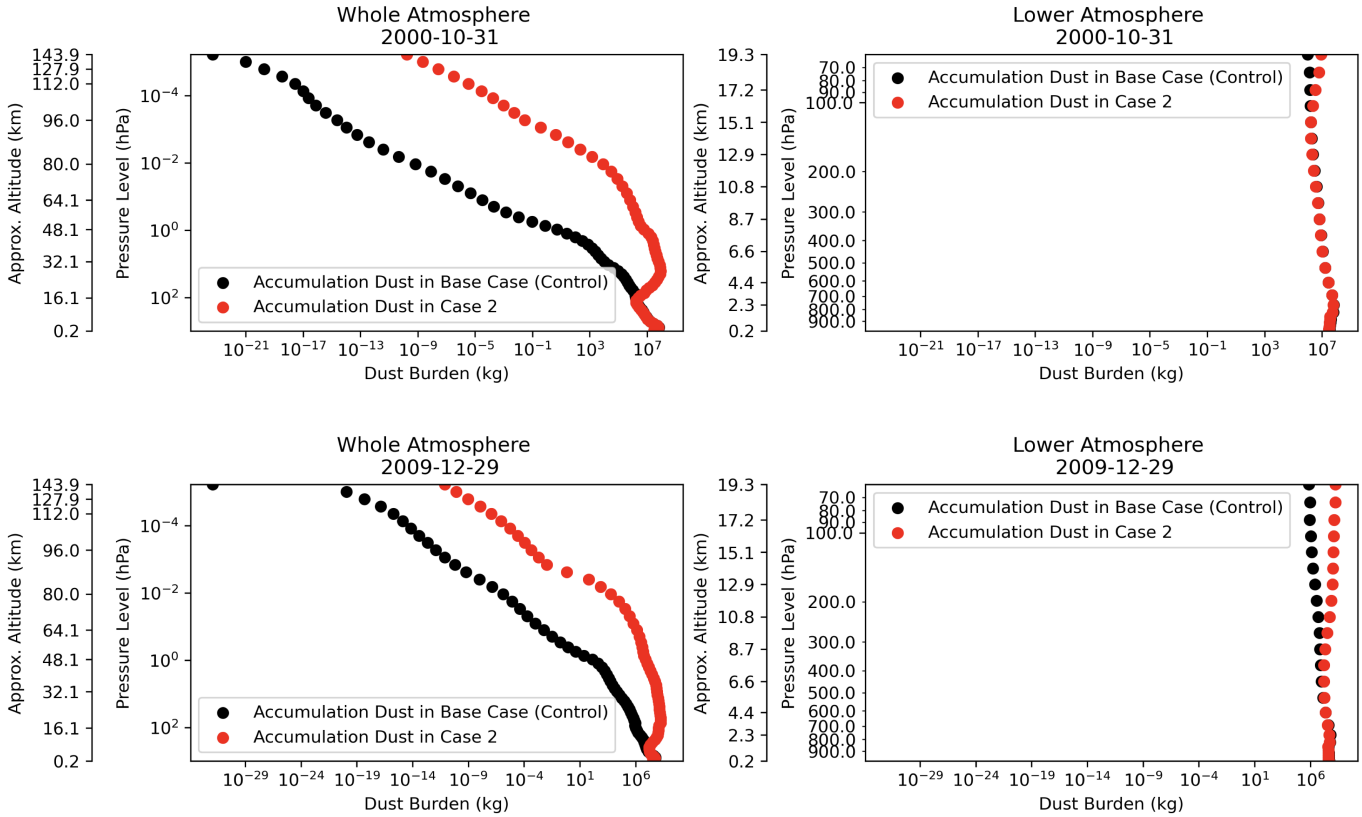

Figure 7-2: Vertical Profiles of Accumulation Dust in Case 2 at Different Times

From Figure 7-2, we can see that the reentry "dust" emission signal in 2001 is distinguishable over the base case until approximately 142 hPa (or 13 km in altitude) after which the

base case dust mass becomes equivalent or even larger than than the perturbed dust mass. In 2009, the signal is distinguishable until 445 hPa which corresponds to approximately 6 km in altitude. This altitude is well below the tropopause which lies between 8-10 km at high latitudes and 17-19 km at the equator [120]. We can conclude that reentry "dust" signal can be fully resolved in the stratosphere, an important region of the atmosphere where reentry "dust" can accumulate, but not in the troposphere. Instead, in the troposphere, there is a sufficient amount of terrestrially-emitted dust that remains suspended to create a background dust level that is on a similar order of magnitude as the reentry "dust" emissions at the same altitude. As a result, the difference between the dust mass in perturbed and base case for these altitudes results in noise driven by the natural variance in the meteorology between the two cases. This phenomena occurs in every test case, as indicated by the vertical profiles listed in Appendix D.

To address this issue, we ignore the reentry "dust" mass in the troposphere and its contribution to the burden and lifetime of reentry "dust." Since the lifetime of terrestrial dust in the troposphere is less than 5 days, reentry "dust" will have very short lifetime in the troposphere. Ignoring reentry "dust" in the troposphere will lead to a slight underestimation of the reentry "dust" burden and a maximum error of 5 days for the reentry dust lifetime. Both of these sources of error are insignificant, given the significantly longer lifetime of particles in the stratosphere.

We compute the subset of pressure levels at which the reentry dust signal is resolvable by comparing the magnitude of the dust burden at each time and pressure level in the perturbed case and base case. Any pressure level where the difference in these magnitudes is at least one is considered a part of the pressure level subset. This approach ensures that the perturbed dust mass is at least one order of magnitude larger than the background dust mass which is sufficient to resolve the reentry "dust" signal. We apply this approach to each dust mode and its respective cloud state. Using this approach, Figure 7-3 shows the burden of each dust mode summed with its respective dust mass in the cloud state for each test case.

Figure 7-3 show that each test case reached a steady state equilibrium as indicated by the horizontal portions of the dust burden curves. Some curves exhibit oscillatory behavior

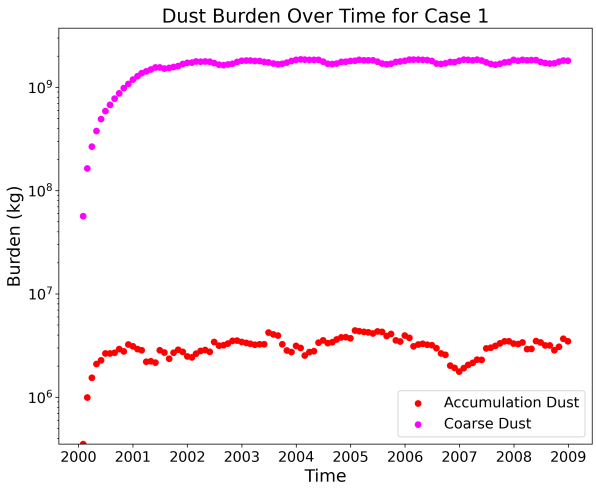

(a) Dust Burden in Case 1: Market Optimistic Scenario with Emissions in the Accumulation Mode that are scaled by 1000

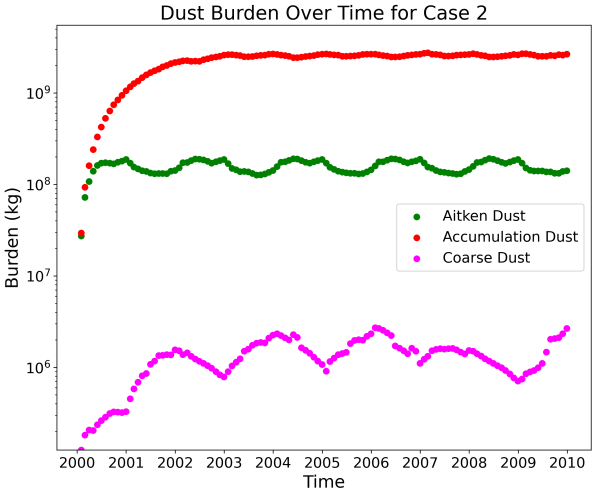

(b) Dust Burden in Case 2: Market Optimistic Scenario with Emissions in the Aitken Mode that are scaled by 1000

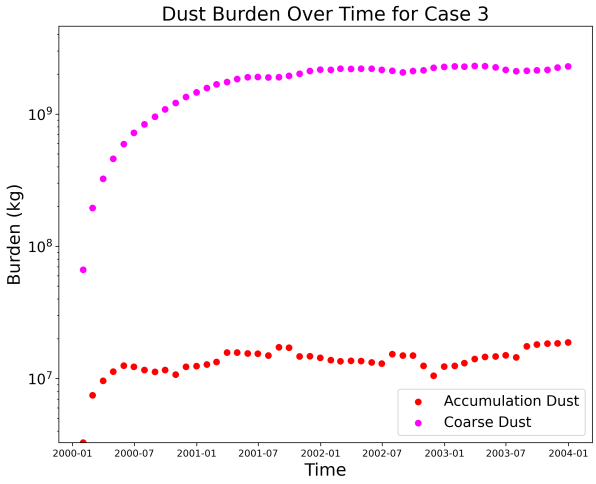

(c) Dust Burden in Case 3: Time-averaged Emissions derived from the Market Optimistic Scenario with Emissions in the Accumulation Mode that are scaled by 1000

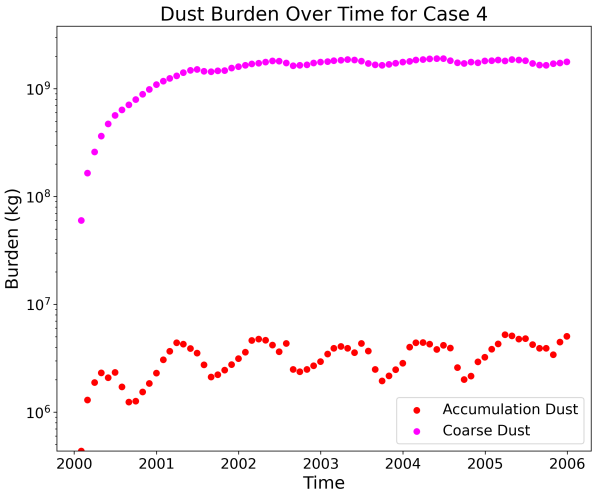

(d) Dust Burden in Case 4: Market Optimistic Scenario with Emissions in the Accumulation Mode that are scaled by 1000 and only in the South Pacific

Figure 7-3: Dust Burdens for Each Test Cases

Table 7.1: Transitions between Dust Modes

Emitted Dust Mode	i	m	Corresponding Case
Accumulation	2	3	Case 1, 3, 4
Aitken	1	3	Case 2, 5
Coarse	3	3	None

around their equilibrium burdens, highlighting WACCM's under-damped response to the reentry "dust" emissions. In Case 1 and 2, the dust burden reached its steady state behavior by the third simulation year, 2003, while in case 3 and 4, steady state was established by 2002 and 2004 respectively. The steady state burdens for each test case and each dust mode are shown in Table 7.2. These steady state burdens were computed by taking the average value over a number of years as specified in Table 7.2.

From these steady state burdens, we can compute the steady state lifetime for dust. Since dust can transition between particle size modes in MAM4, we expand Equation 7.1 to reflect that mass from dust emissions may transition into another species, leading to Equation 7.2. In Equation 7.2, i refers to the dust mode of the reentry emissions where the Aitken mode corresponds to $i = 1$, the accumulation mode corresponds to $i = 2$, and the coarse mode corresponds to $i = 3$. The symbol m represents the possible transition modes: Aitken dust can transition to accumulation dust and accumulation dust can transition to coarse dust (refer to Figure 6-2). These transitions results in different values for m depending on the particle size mode of the emitted dust, as shown in Table 7.1.

$$\tau_{ss} = \frac{\sum_{n=i}^{m} C_n}{\sum_{n=1}^{m} S_n} \tag{7.2}$$

Unfortunately, we cannot compute the lifetime of each dust mode due to a lack of sufficient information. To demonstrate why, let us consider Case 1 where reentry "dust" emissions are emitted in the accumulation mode. At steady state, the production and loss rates of accumulation dust are equivalent, leading to Equation 7.3. Similarly, we can express the equilibrium balance of the coarse dust mode, as shown in Equation 7.4. Lifetime calculations use these steady state expressions to determine the value of S in Equation 7.1. For accumulation dust, S is equivalent to P_{accum} which is a known constant from the reentry "dust" emission file. However, P_{coarse} is less obvious. Since Case 1 only emits reentry "dust" in the accumulation

Table 7.2: Steady State Burden and Lifetimes of Reentry Dust for Every Test Case

Test Case	Steady State Averaged Period	Accumulation Dust (kg)	Aikten Dust (kg)	Coarse Dust (kg)	Dust Lifetime (days)
Case 1	2004 - 2010	2.948e6	N/A	1.784e9	487
Case 2	2004 - 2010	2.595e9	1.543e8	1.369e6	749
Case 3	2002 - 2004	1.479e7	N/A	2.097e9	604.7
Case 4	2002 - 2006	3.725e6	N/A	1.772e9	485

mode, we can observe that the only production mechanism of coarse reentry "dust" is the transition of accumulation dust to the coarse mode, described by $L_{accum \rightarrow coarse}$. We can conclude that without knowing either $L_{accum \rightarrow coarse}$ directly or the loss of reentry accumulation "dust" to ground, it is not possible to estimate P_{coarse}. WACCM does not output the loss rate of particles across particle size modes directly. This shortcoming eliminates the ability to know $L_{accum \rightarrow coarse}$ directly. Furthermore, estimating $L_{accum \rightarrow ground}$ is also not possible. Since the meteorology across the base and perturbed cases is not constant, the deposition rate of terrestrial dust in the perturbed case cannot be estimated by using the deposition rates of the base case. These constraints preclude any estimation of the individual lifetimes of each dust mode in any perturbed case where reentry dust transitioned across modes.

$$P_{accum} - L_{accum \rightarrow coarse} - L_{accum \rightarrow ground} = 0 \tag{7.3}$$

$$P_{coarse} - L_{coarse \rightarrow ground} = 0 \tag{7.4}$$

From Figure 7-3 and Table 7.2, we can see several interesting differences in how reentry "dust" behaved across the test cases. First, reentry "dust" in Case 1 quickly coagulates from the accumulation mode to the coarse mode. However, in Case 2, the emitted Aitken dust rapidly coagulates into accumulation dust but accumulation dust does not quickly convert into the coarse mode as it did in Case 1. This difference suggests that Aitken dust in Case 2 is able to quickly find other particles for coagulation while in the reentry plume, but over time as the plume disperses, the resultant accumulation particles do not quickly interact with other particles to grow into the coarse mode. From Table 7.2, accumulation

dust in Case 3 maintains a higher steady state burden than in Case 1 which indicates that accumulation dust in Case 3 is transitioning into the coarse mode less efficiently than in Case 1. This difference is driven by the time-averaged emissions in Case 3 compared to the discrete reentry event emissions in Case 1. Reentry "dust" is coagulating efficiently in reentry plumes which is not well captured by a time-constant representation of the same emitted mass.

We can observe from Table 7.2 that Case 2 achieved the longest reentry "dust" lifetime at 749 days with majority of the reentry "dust" persisting in the accumulation mode. In general, accumulation particles tend to be less effective at coagulation compared to smaller particles and coarse particles tend to more efficiently nucleate into clouds or deposit on the surface. Therefore, it follows that the case with the most reentry "dust" persisting in the accumulation mode has the longest lifetime. Following similar reasoning, Case 3 has the second longest lifetime of 604.7 days. The time-averaged emissions in Case 3 cause slower coagulation and thus slower transitioning from the accumulation to the coarse mode than Case 1, resulting in a higher accumulation steady state burden. In fact, Case 3 has an order of magnitude more accumulation dust than Case 1. This result indicates that modeling reentry events as discrete emissions with reentry plumes plays an important role in characterizing the lifetime of reentry "dust". Case 1 has discrete reentry plume emissions in the accumulation mode which results in a lifetime that is 20 % shorter than the lifetime time-averaged, accumulation mode emissions in Case 3.

Despite the concentration of emissions in the South Pacific, Case 4 shows that the reentry "dust" lifetimes are similar to Case 1 which had global emissions in the same dust mode. This finding suggests that the reentry "dust" lifetime is less sensitive to reentry location than the emitted particle size. When comparing the steady state burdens, we can also see that Case 1 has slightly faster transitioning between the accumulation and coarse mode.

In addition to the steady state lifetime and burden of reentry "dust", it is important to understand where reentry "dust" is accumulating to inform what regions may be disproportionately affected by space debris reentries. The steady state distribution of reentry "dust" also better informs which atmospheric processes may be interacting with reentry dust, narrowing down the potential scope of interactions as listed in Chapter 5.

Figure 7-4, Figure 7-5, Figure 7-6, Figure 7-7 show zonal distribution of each dust mode in each case. Zonal distributions reflect the averaged dust mixing ratio along all longitudes for a given latitude and altitude. Each zonal distribution was averaged over several years, capturing the oscillatory dust mass at steady state. These years are listed in Table 7.2. Each plot uses the same color bar, improving the comparability across cases.

Note that Figure 7-4, Figure 7-5, Figure 7-6 and Figure 7-7 present a subset of the pressure levels modeled in WACCM. The lower limit is determined by the lowest altitude at which the reentry "dust" signal can be discerned over the background terrestrial dust following the process as aforementioned.

In Case 1, the zonal distribution shows that reentry "dust" in the coarse and accumulation mode is evenly distributed across the northern and southern latitudes. Reentry "dust" is the most abundant in the stratosphere, but persists in high mixing ratios above 40 km in the mesosphere. Case 2 and 3 show similar distributions in the dominate coarse mode, the accumulation dust and coarse dust, respectively.

Case 4 differs significantly from the other cases, as the reentry "dust" accumulates strongly in the Southern hemisphere and persists at higher altitudes. Some reentry "dust" does transition into the Northern hemisphere in the lower mesosphere and stratosphere. This result indicates that reentries localized in the South Pacific will lead to stronger particle accumulation in the Southern Hemisphere and will not diffuse across the entire atmosphere uniformly.

The Case 1 and 2 distributions also have less reentry "dust" mass in the tropical region at low altitudes. This absence of dust is likely due to precipitation, since the tropopause rests around 16 to 18 km in the equator, or from Hadley convection which blows air up and away from the equator [144, 41].

In Case 2, the zonal distribution of Aitken and coarse dust shows that the dust is occurring rapidly transitioning after 100 hPa, or 75 km, but this transitioning is dependent on latitude. his transition occurs most rapidly in the Southern mid-latitudes in the stratosphere, and less efficiently at the poles.

Figure 7-6 shows that the time-averaged representation of the Case 1 emissions lead to high mixing ratios of accumulation dust in the poles, unlike Case 1. Furthermore, accumu-

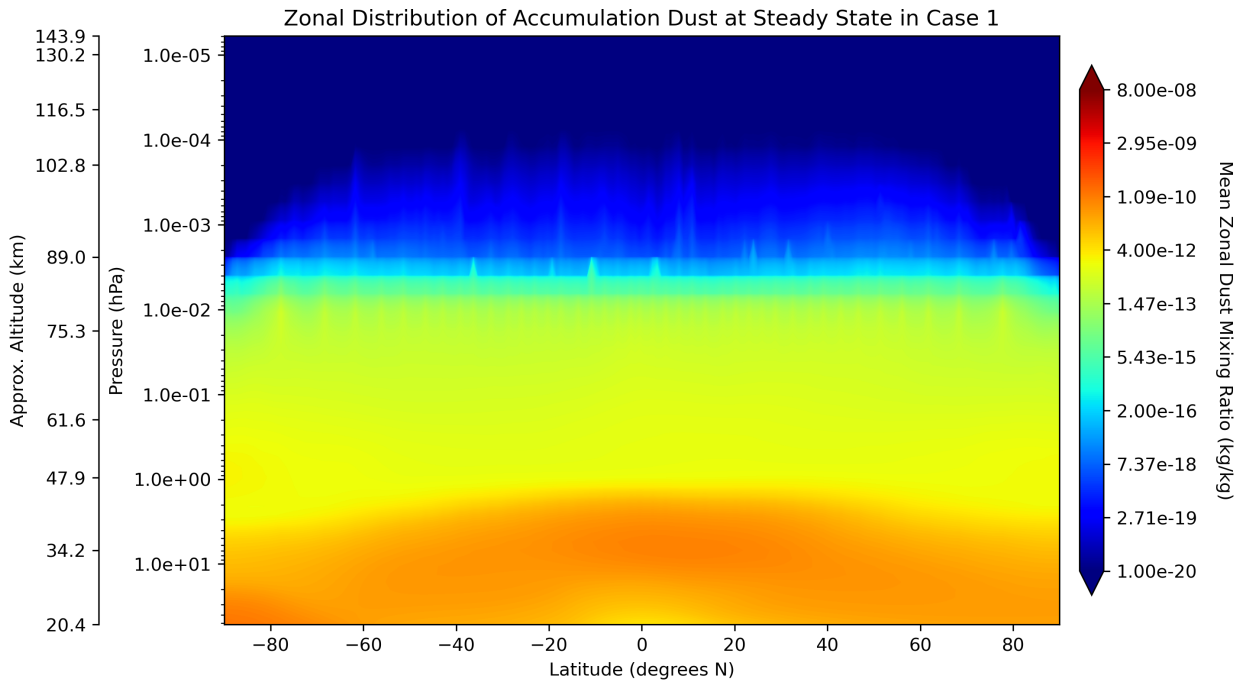

(a) Accumulation Dust Zonal Distribution

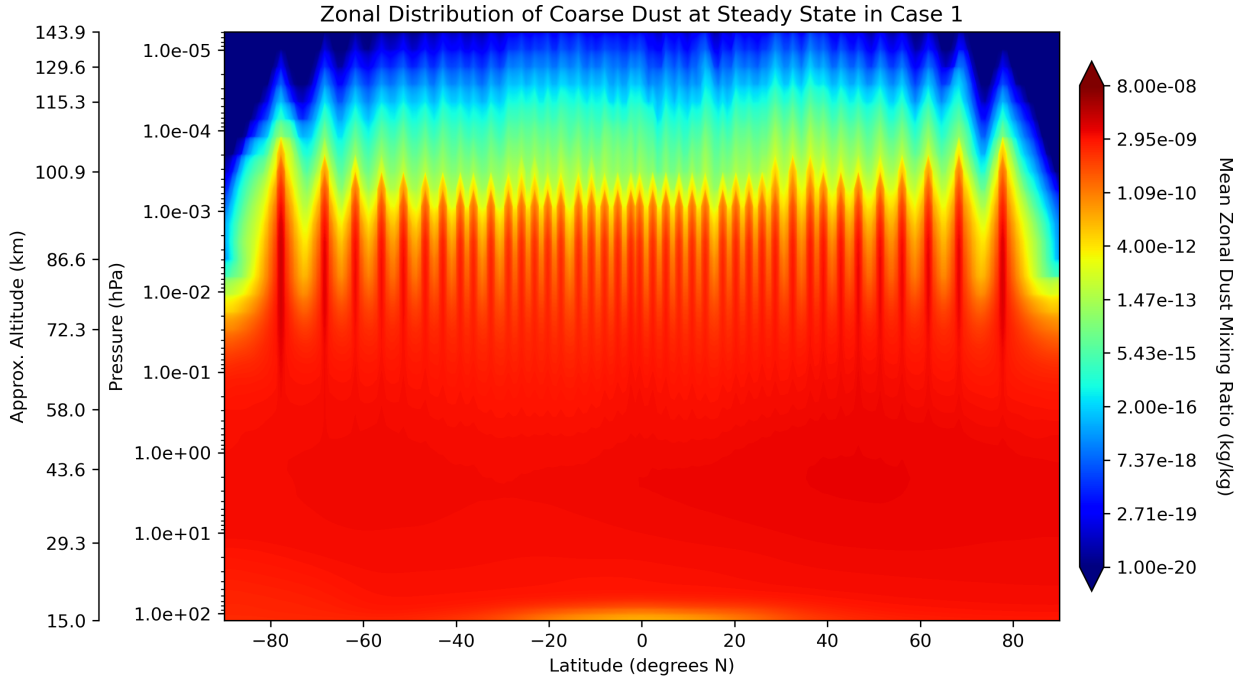

(b) Coarse Dust Zonal Distribution

Figure 7-4: Case 1: Dust Zonal Distribution at steady State Averaged over 2004-2010 in Case 1

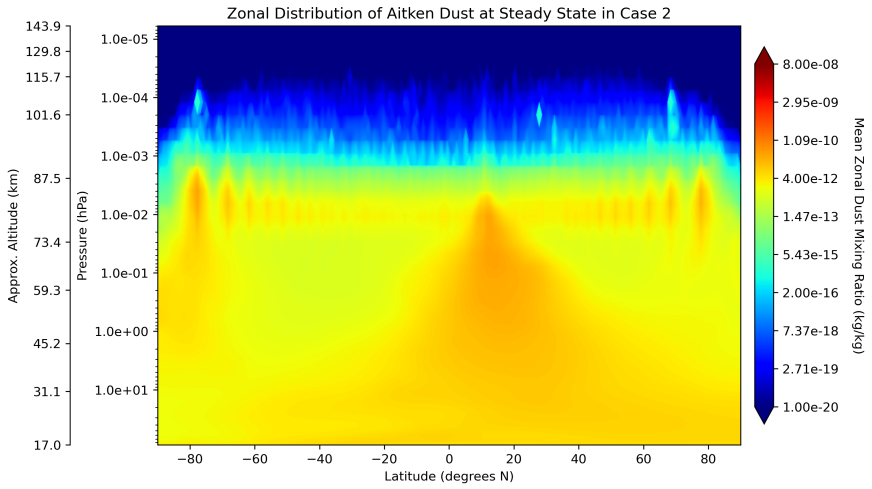

(a) Aitken Dust Zonal Distribution

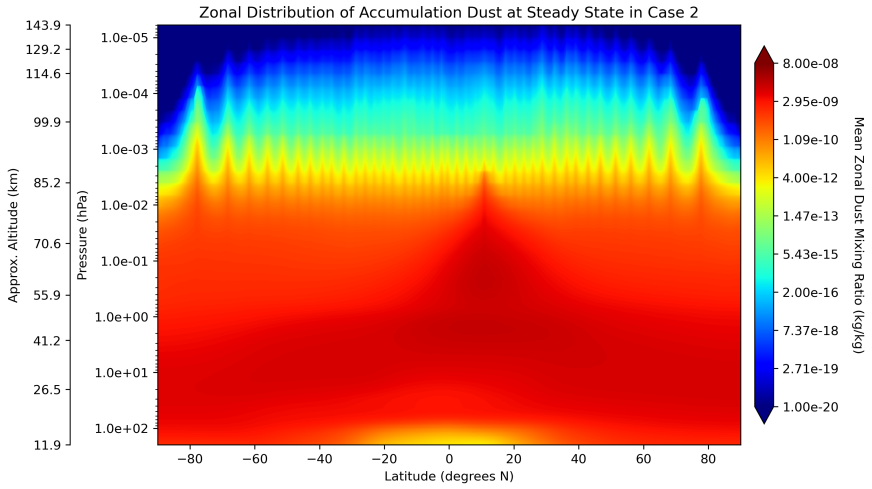

(b) Accumulation Dust Zonal Distribution

(c) Coarse Dust Zonal Distribution

Figure 7-5: Case 2: Dust Zonal Distribution at steady State Averaged over 2004-2010

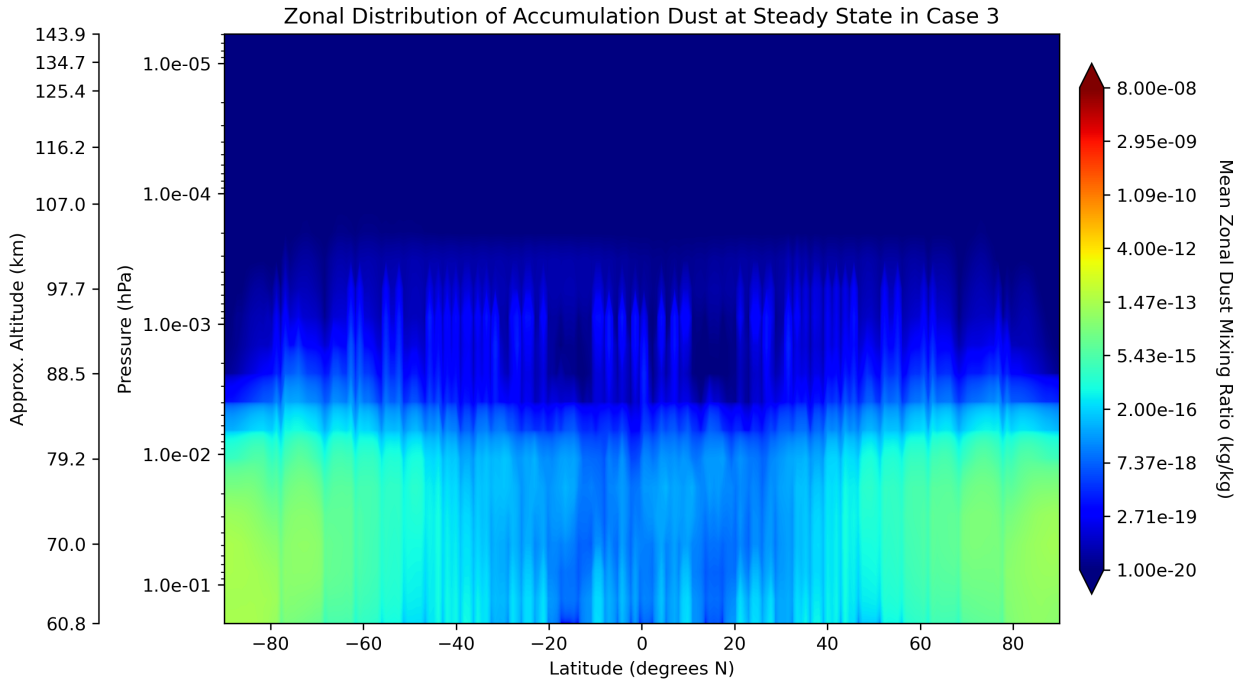

(a) Accumulation Dust Zonal Distribution

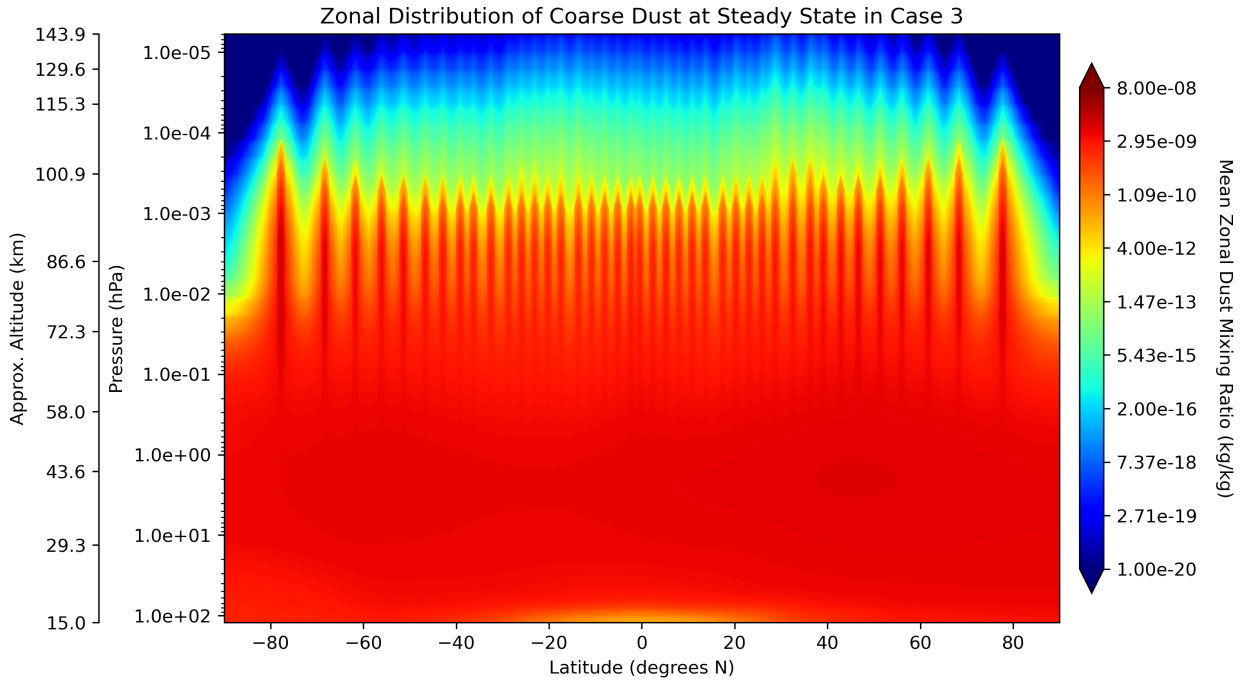

(b) Coarse Dust Zonal Distribution

Figure 7-6: Case 3: Dust Zonal Distribution at steady State Averaged over 2002-2004

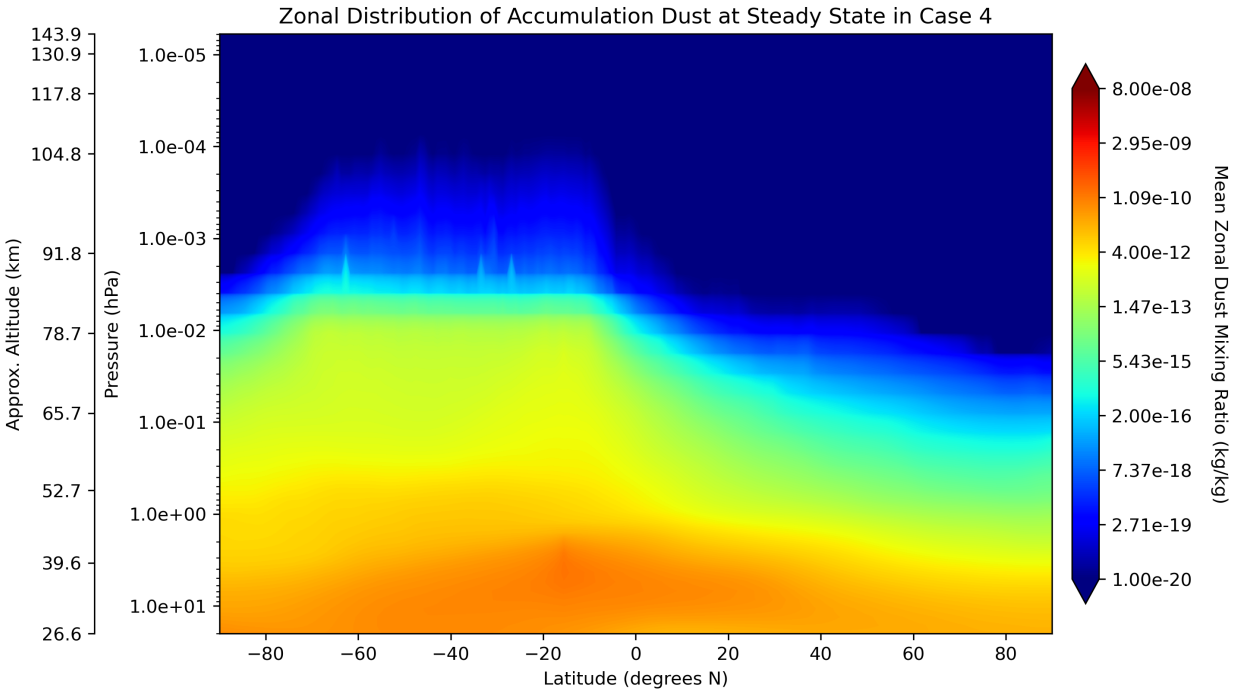

(a) Accumulation Dust Zonal Distribution

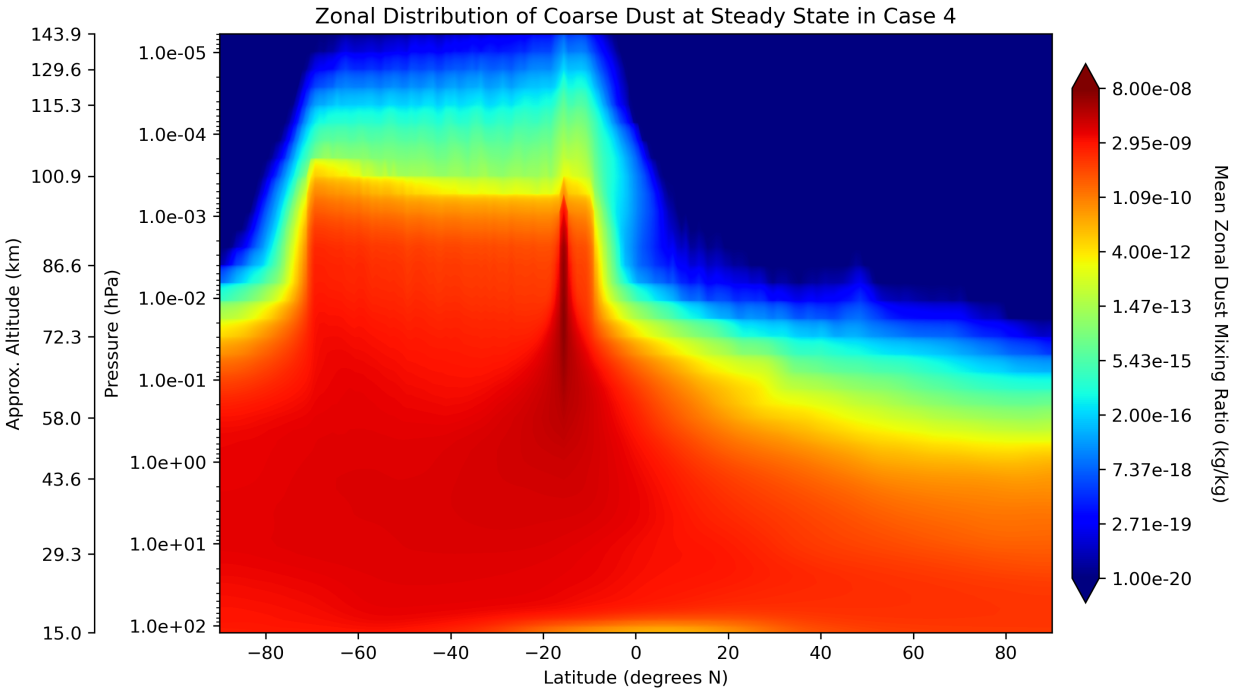

(b) Coarse Dust Zonal Distribution

Figure 7-7: Case 4: Dust Zonal Distribution at steady State Averaged over 2002-2006

lation dust accumulates lower in the atmosphere, below 70km, whereas accumulation dust in Case 1 continues to have high mixing ratios up to 89 km. This difference implies that modelling the discrete reentry events leads to significantly different distributions of reentry "dust," and consequently, opens the possibility for different conclusions regarding reentry "dust" behavior.

Figure 7-7 shows that concentrating reentry "dust" emissions in the South Pacific leads to persistent accumulation in that region. Over a number of altitudes, accumulation and coarse dust remain most abundant between 20 and 80 degrees South. A significant amount of dust persists in the Southern polar region, but not the Northern polar region.

Across all test cases, these results indicate that at reentry "dust" at this extremely high reentry flux can achieve significantly large mixing ratios in the upper atmosphere, increasing the potential for these particles to interact with upper atmospheric chemistry. Furthermore, reentry "dust" will strongly accumulate in the stratosphere, giving these particles the ability to interact with stratospheric ozone chemistry.

Importantly, these distributions may not correspond to where reentry "dust" is settling on Earth's surface. The distribution of where reentry "dust" settles cannot be resolved with this method, since terrestrial, surface-emitted dust obscures reentry "dust" close to the surface.

7.2 Radiative Forcing

For each test case, we compute the direct radiative forcing of reentry "dust". Direct radiative forcing is the change in the radiative balance between a perturbed and base case due to a specify species. Leveraging double radiation calls, Equation 7.5 describes how direct radiative forcing of reentry "dust" is computed where T is the default radiation call will all radiatively active species and D is the radiative output of a double radiation call with the appropriate species ignored from the radiative calculation. Note that T and D are multidimensional arrays representing latitude and longitude.

$$\delta R_{lat,lon} = (T_{perturbed} - D_{perturbed}) - (T_{base} - D_{base}) \tag{7.5}$$

We can sum $\delta R_{lat,lon}$ over latitude and longitude with grid area weighting to compute

the global direct radiative effect, as shown in Equation 7.6. This area weighting reflects the fact that each atmospheric grid cell does not have the same area. The area weighting (represented by $A_{lat,lon}$) converts the radiative flux in each grid cell to net energy input that can be summed over latitude and longitude to find the total net energy into Earth. This input energy is divided by A_t, the global surface area, to find the global net flux, or global direct radiative forcing.

$$\delta R_G = \sum_{lat=1}^{N_{lat}} \sum_{lon=1}^{N_{lon}} \delta R_{lat,lon} \frac{A_{lat,lon}}{A_t} \tag{7.6}$$

We difference the radiation output in the perturbed case with the base case to remove the contribution of surface-emitted dust. In the base case, we can isolate the effect of terrestrial dust using a double radiation call. In this approach, we assume that the terrestrial dust burden, and consequently, its contribution to radiative forcing, is constant across the perturbed and base case. In practice, the difference in meteorology between the two cases implies that terrestrial dust may be advected differently across cases, resulting in different distributions and burdens. Since we are able to resolve the direct radiative effect of reentry "dust" with this approach, it is clear that the variance in terrestrial dust between the base and perturbed case is not sufficient to obscure the effect of the reentry "dust."

Figure 7-8, Figure 7-9, Figure 7-10 and Figure 7-11 show the global direct radiative effect of reentry "dust" at the top of the atmosphere, tropopause and Earth's surface for the shortwave and longwave light bands.

It is important to note that WACCM's RRMTG uses different conventions for positive and negative for the shortwave and longwave radiative calculations. The net longwave radiative calculation treats outgoing flux as the positive direction while the net shortwave radiative calculation treats incoming flux as positive. The results we present in this chapter correct for this inconsistent sign convention. We assume downward flux as positive. Therefore, the total net radiative effect is computed using the sum of the shortwave net flux and the longwave net flux, shown in Equation 7.7.

$$\delta R_t = \delta R_s + \delta R_l \tag{7.7}$$

Table 7.3: Global Direct Radiative Forcing of Reentry "Dust" with Scaled and Downscaled Emissions

Test Case	Direct Radiative Forcing mW/m^2					
	Top of the Atmosphere		Tropopause		Surface	
	Scaled	Downscaled	Scaled	Downscaled	Scaled	Downscaled
Case 1	-210	-0.21	-280	-0.28	-220	-0.22
Case 2	-240	-0.24	-330	-0.33	-300	-0.3
Case 3	-260	-0.26	-340	-0.34	-270	-0.27
Case 4	-210	-0.21	-280	-0.28	-230	-0.23

We apply Equation 7.7 in Figure 7-8, Figure 7-9, Figure 7-10 and Figure 7-11 to present the total net radiative effect of reentry "dust" over time. We also show the average value at steady state. In Case 1 and 2, we define the steady state period as the last three years in the simulation while in case 3 and 4, we take the last two years.

Equation 7.7 in Figure 7-8, Figure 7-9, Figure 7-10 and Figure 7-11 show the direct radiative effects of reentry "dust" emissions that are derived from a reentry mass flux which is 1000 times larger than the Market Optimistic scenario reentry flux, shown in Figure 4-6a and Figure 4-6b. In other words, using the assumptions of Chapter 4, the Market Optimistic scenario corresponds to a yearly aluminum influx of 1.337 Gg, but the results in Figure 7-8, Figure 7-9, Figure 7-10, Figure 7-11 assumed an aluminum reentry mass of 1.337 Tg. Recall that this scaling was performed to raise the reentry "dust" emission signal above the natural variance of the terrestrial dust burden (see Subsection 6.1.6).

From Table 7.3, we can see that the cases with the longest reentry "dust" lifetimes (Case 2 and 3) have the strongest direct radiative effects. This result follows the logic that the longer reentry "dust" can persist in the atmosphere, the longer it can interact with Earth's radiative balance. Comparing Case 1 and 2, we can see that reentry "dust" emissions with smaller particle sizes leads to approximately 114% larger direct radiative effect over larger particle sizes.

Interestingly, we can see a clear difference in the direct radiative forcing between Case 1 and Case 3. The time-averaged emissions in Case 3 lead to a longer reentry "dust" lifetime and consequently, 124% increase in the direct radiative effect.

Case 4, where reentry emissions occur only in the South Pacific, has a similar lifetime

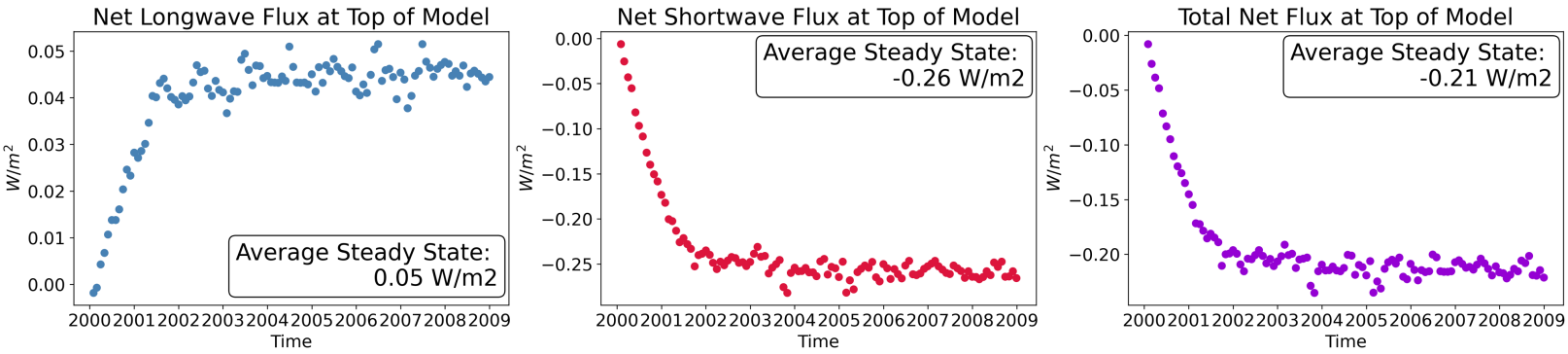

(a) Top of the Atmosphere

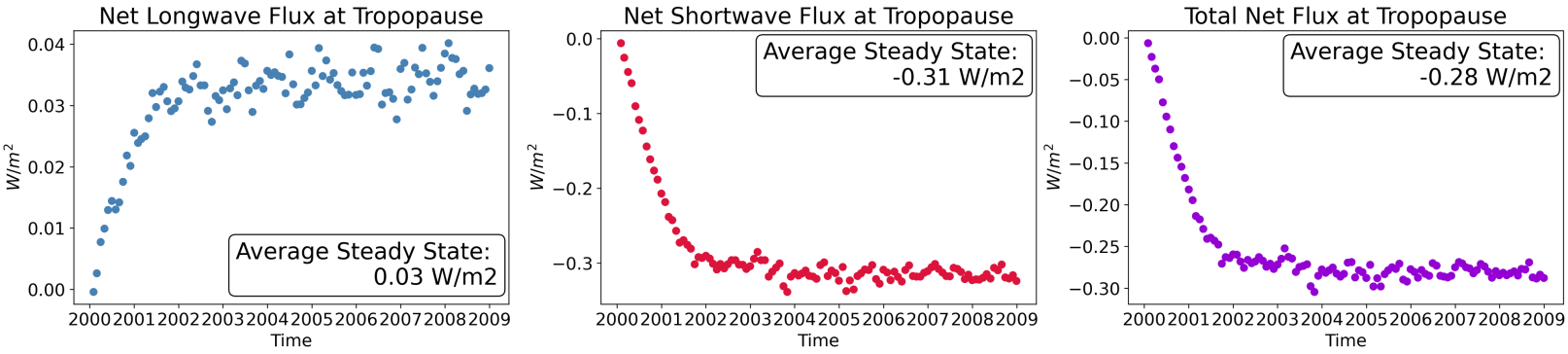

(b) Tropopause

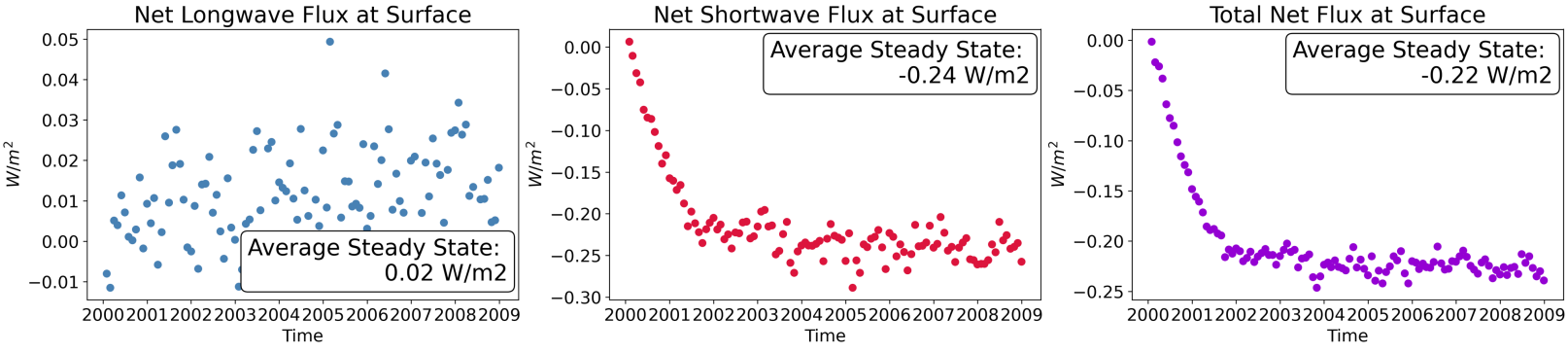

(c) Surface

Figure 7-8: Case 1: Direct Radiative Forcing of Reentry "Dust"

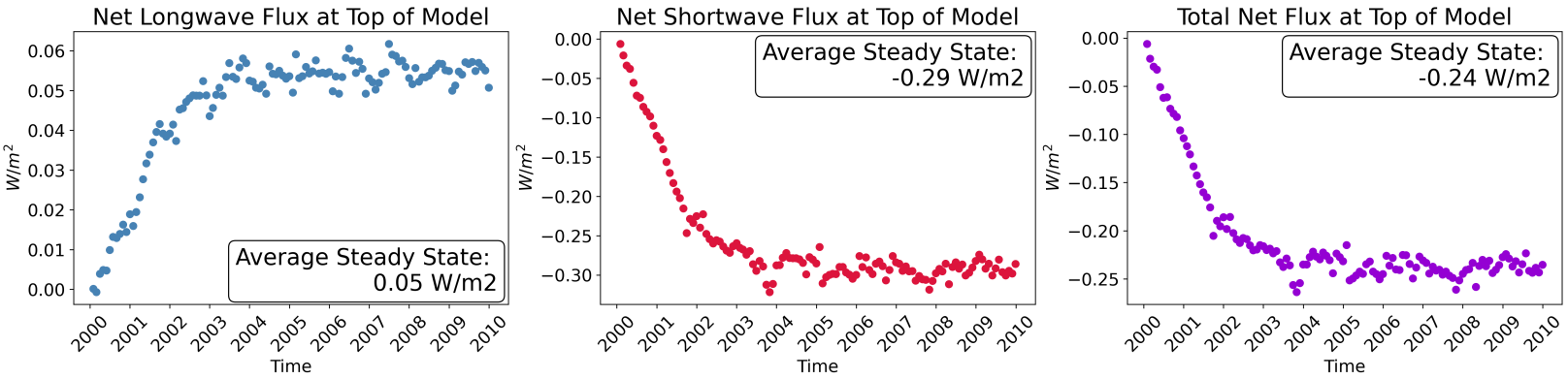

(a) Top of the Atmosphere

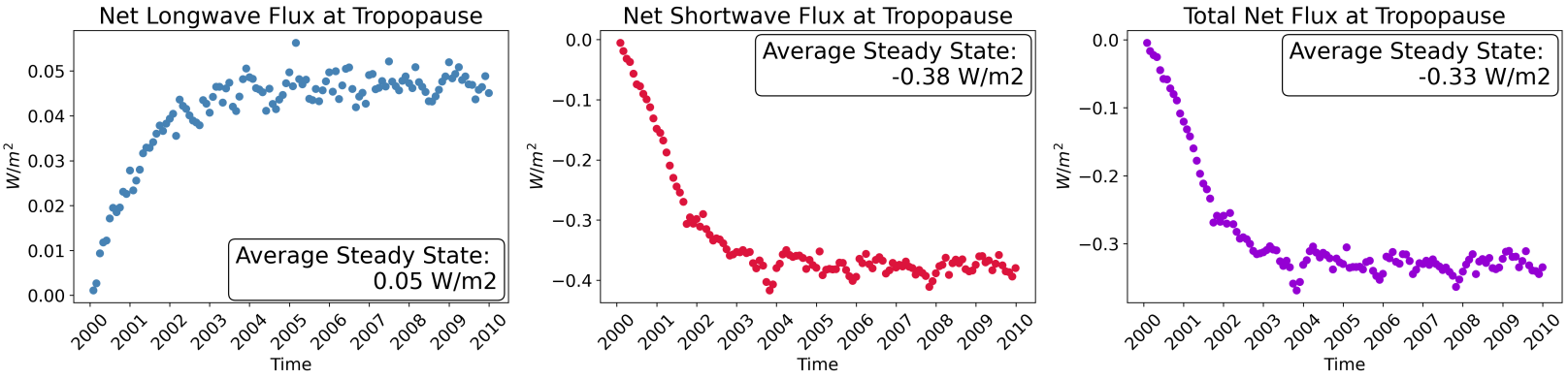

(b) Tropopause

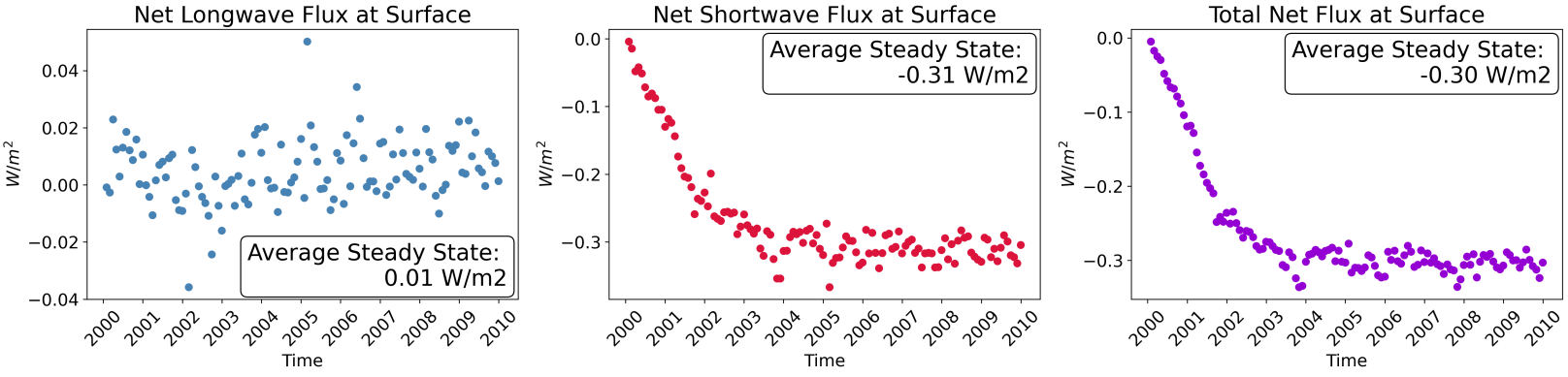

(c) Surface

Figure 7-9: Case 2: Direct Radiative Forcing of 1000x Scaled Reentry "Dust"

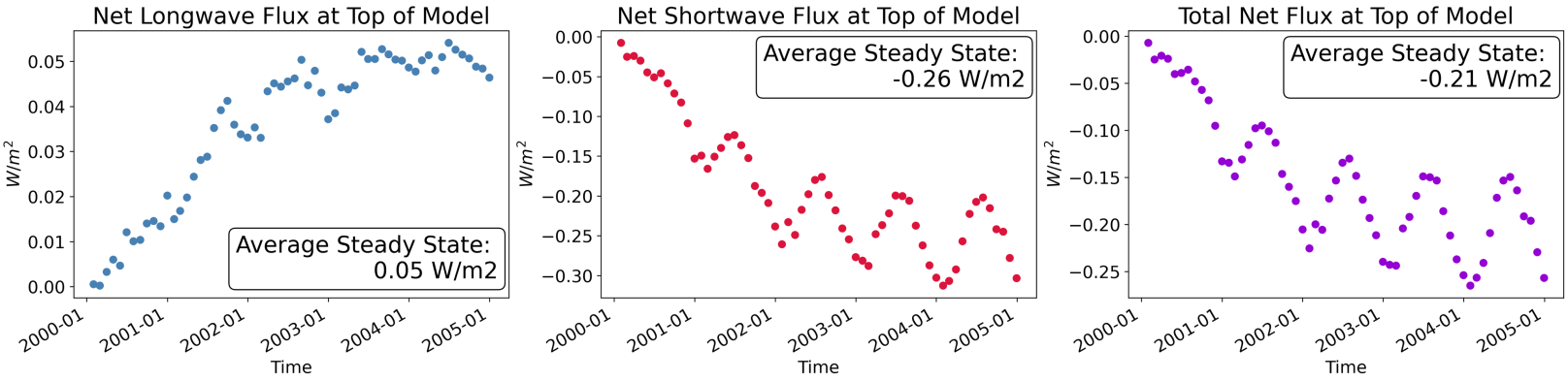

(a) Top of the Atmosphere

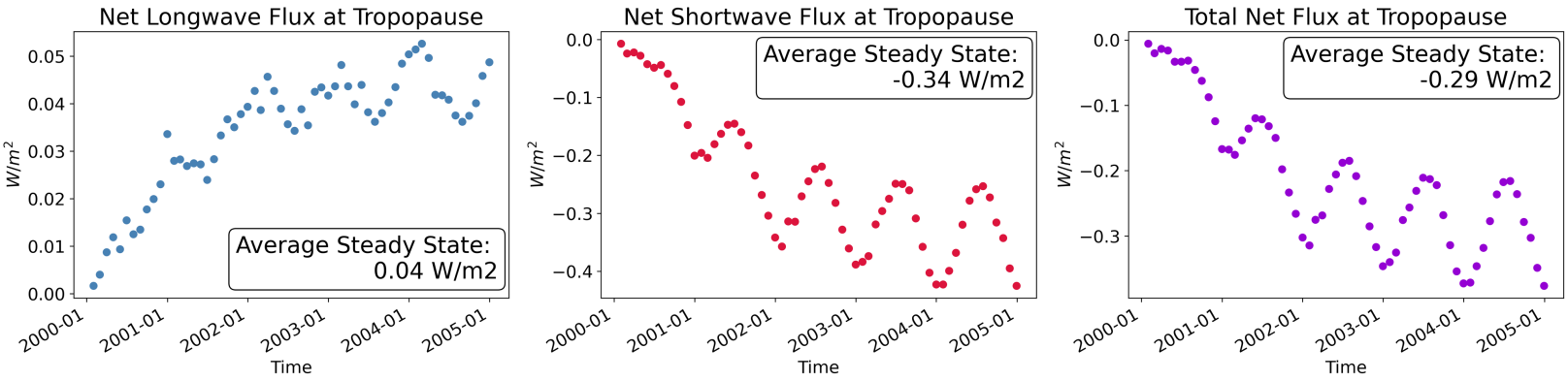

(b) Tropopause

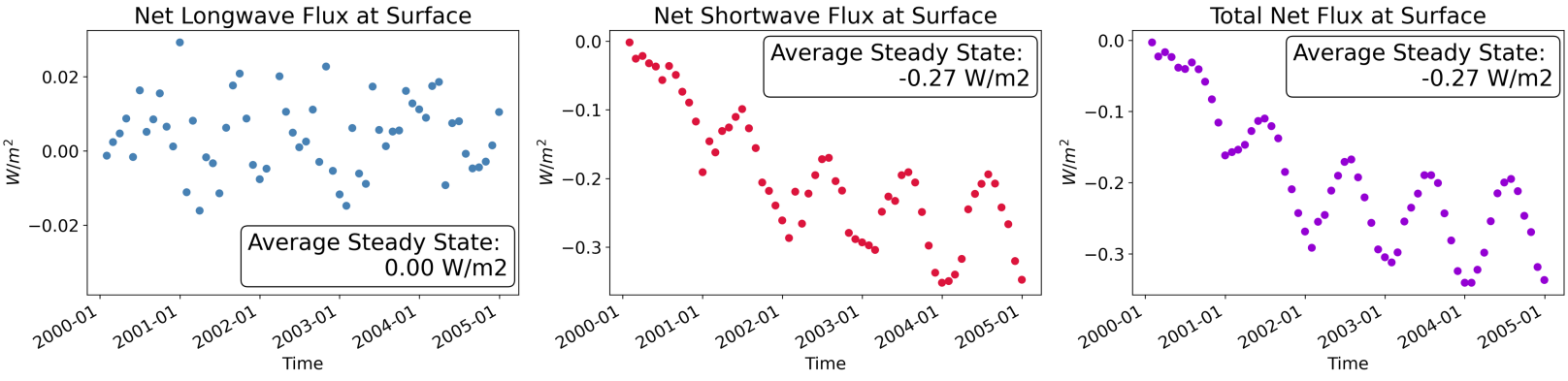

(c) Surface

Figure 7-10: Case 3: Direct Radiative Forcing of 1000x Scaled Reentry "Dust"

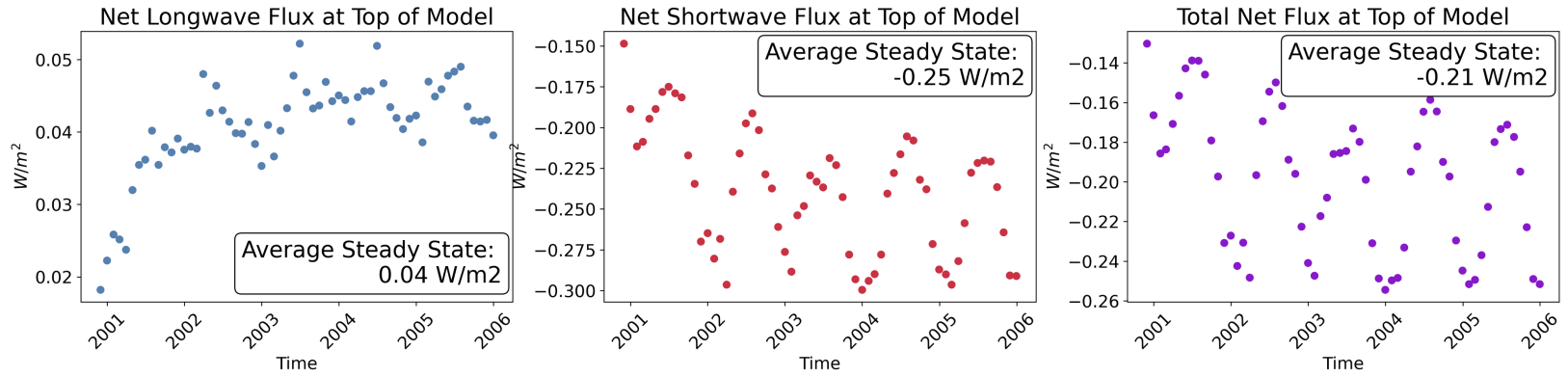

(a) Top of the Atmosphere

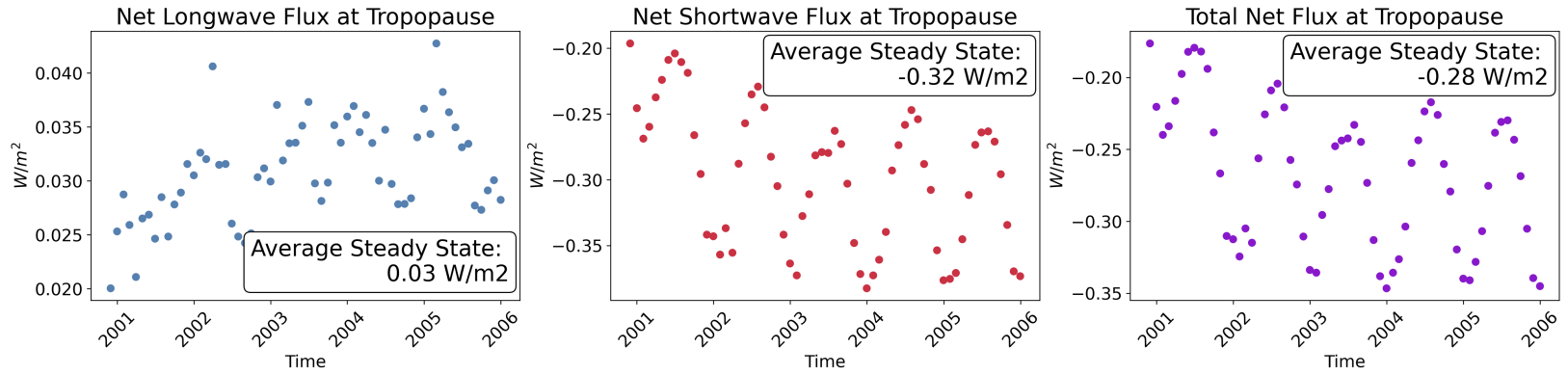

(b) Tropopause

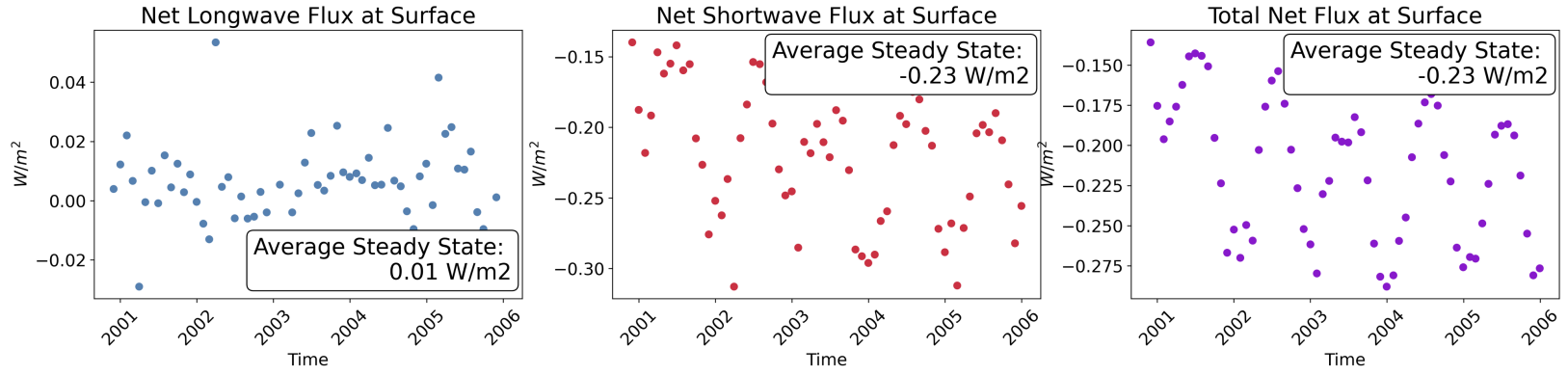

(c) Surface

Figure 7-11: Case 4: Direct Radiative Forcing of 1000x Scaled Reentry "Dust"

and global direct radiative forcing to Case 1, despite a clear difference in the reentry "dust" distribution. To examine these results in more detail, Figure 7-12 shows the distribution of the direct radiative effect of reentry "dust" at the top of the atmosphere for each test case. In Figure 7-12d, we can see that Case 4 has stronger direct radiative effects in the South Pacific than anywhere else in the world, unlike Case 1 which shows nearly uniform radiative effects across the northern and southern mid-latitudes. Therefore, while the global direct radiative forcing is similar between Case 1 and 4, reentry "dust" in Case 4 has direct radiative effects that disproportionately impact the South Pacific. This kind of imbalance over the long-term can lead to changes in global climate and circulation. Several studies of geoengineering with emissions on the order of several terragrams have shown that asymmetrical forcing can move the inter-tropical convergence zone (ITCZ), increase tropical cyclone activity and changes to precipitation in the Sahel region in Africa [55, 23]. Shifts in the ITCZ results in drastic changes to rainfall in many equatorial countries [134]. Since Case 4 shows a stronger negative radiative effect in the South Pacific, the reduced energy influx would lead to a colder Southern hemisphere. Studies have shown a colder Southern hemisphere implies a more northerly ITCZ, stronger tropical cyclone activity and more precipitation in the Sahel region at the cost of drought in the Amazon rain forest. The degree to which Case 4 induces these secondary consequences was not captured in this study and is reserved for future work.

Comparing Figure 7-12a and Figure 7-12c, we can see that the time-averaged emissions in Case 3 lead to a stronger radiative effects in the northern and southern mid-latitude regions than in Case 1. This result further emphasizes that the discrete representation of reentry events leads to differences in direct radiative forcing, despite the distribution of the reentry dust being very similar.

7.3 Caveats to Results

The results in this study come with the caveats and limitations related to using dust as a proxy for alumina. The coagulation characteristics from alumina particles generated from reentry ablation are not understood. It is possible that dust coagulates more rapidly than alumina with sulfates and other suspended particles. Faster coagulation would cause smaller

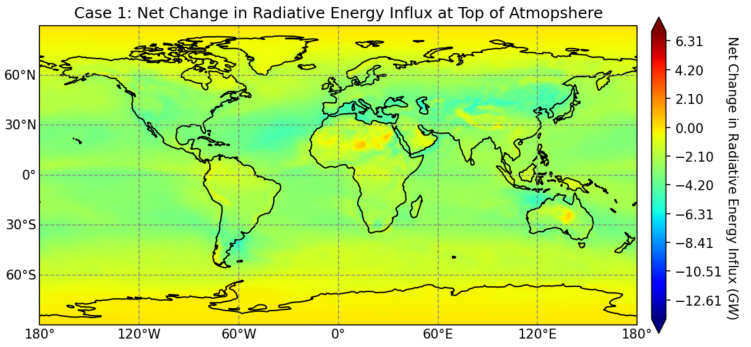

(a) Case 1

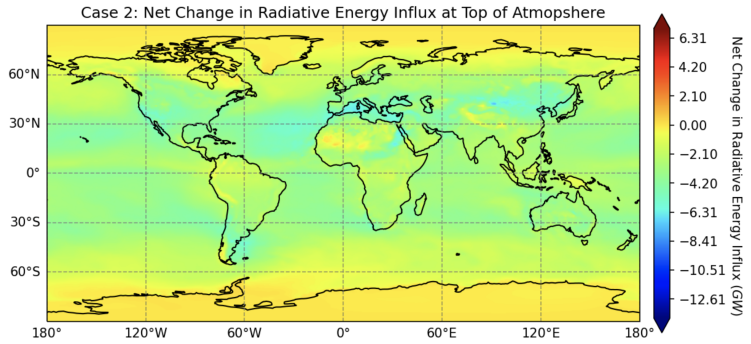

(b) Case 2

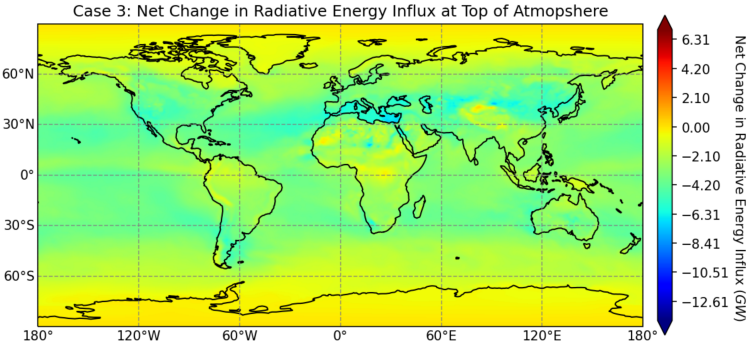

(c) Case 3

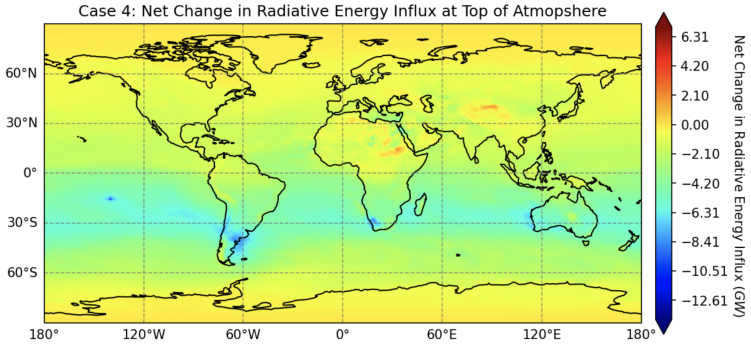

(d) Case 4

Figure 7-12: Spatial Distribution of the Net Change of Radiative Energy Influx due to Reentry "Dust" for Each Test Case

particles to transition into larger particles more quickly, which would adjust their lifetime in the atmosphere. The opposite is also true. For example, the rapid transition between the Aitken and accumulation modes may not occur as quickly if alumina is less reactive with sulfates as compared to dust. We can see in Case 1 and 2 that reentry "dust" rapidly transitions between particle size modes which greatly effects the particle lifetime. Particles in Case 2 transition rapidly into the accumulation mode and have a lifetime of 749 days, while particles in Case 1 rapidly transition into the coarse mode with a shorter lifetime of 487 days. However, if alumina transitions slowly between modes, the lifetimes of alumina particles in these two cases would be significantly longer.

As aforementioned, terrestrial dust is less effective at scattering light than alumina by approximately 10% to 20%. This difference leads to an error in the direct radiative forcing of at least 20%. Therefore, the direct radiative forcing results are a conservative estimation. We also had to assume a linear relationship between the emission amount and direct radiative effect, which may not be true for a large scaling factor.

Chapter 8

Analyzing WACCM Results

8.1 Burden, Lifetime and Distribution

Comparing our reentry "dust" results with studies of meteoric smoke particles lead to several interesting conclusions. Meteor ablation produces metallic material that coagulates to form oxides, hydrates, and carbonates known as meteor smoke particles [109]. These particles grow in size and descend into the mesosphere and stratosphere. Figure 8-1 shows the zonal distribution of meteoric material in the upper atmosphere.

From Figure 8-1, we can see that meteoric material forms layers at above 80 km across all latitudes and seasons. However, meteoric material is most concentrated at the poles between 20 and 40 km. In this region, meteor smoke particles continue to coagulate, interact with cloud formation and ozone chemistry and eventually settle on Earth's surface.

Appendix E presents zonal distributions of the average reentry dust concentration at steady state for all cases. By comparing these results with the zonal distribution of meteor smoke particles, we can observe that reentry "dust" achieves similar maximum concentration in a similar altitude band. Notably different, meteor smoke particles achieve their maximum concentration in the polar regions, while reentry "dust" achieves maximum concentrations nearly uniformly in latitude in the stratosphere. Furthermore, reentry "dust" does not form mesospheric layers like meteor smoke particles, although the concentration of reentry "dust" in this region is similar to meteor smoke particles. In general, we observe that in the upper atmosphere, reentry "dust" produce less uniform distributions than in the lower atmosphere,

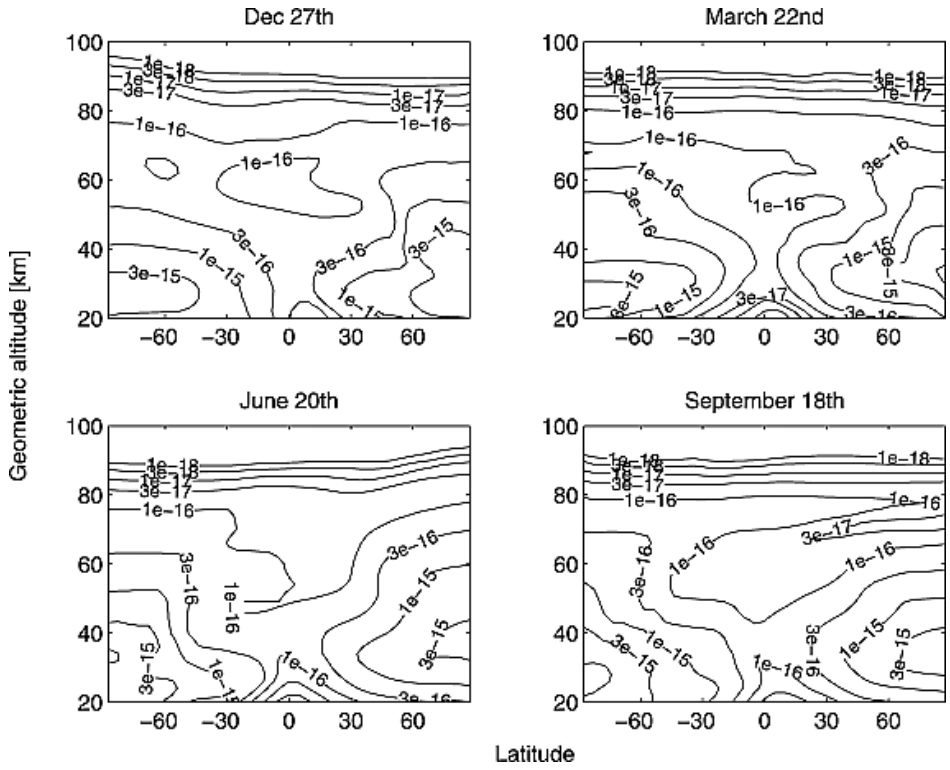

Figure 8-1: Meteoric Material Distribution (shown in g/cm^3) at Various Seasons [90]

,

unlike meteors.

The significant concentration of reentry "dust" in the upper atmosphere indicates that reentry "dust" could interact with upper atmospheric phenomena over long time scales, like meteors. These atmospheric phenomena include mesospheric cloud formation, sporadic E-region formation, interference with upper atmosphere observations and upper atmosphere metal chemistry, outlined in Chapter 5. Exploring to what extent reentry-ablated alumina participates in these atmospheric processes warrents future work.

In addition, reentry particles may significantly impact stratospheric processes, given their strong accumulation in this region. Important interactions in this region include heterogeneous chemistry and stratospheric cloud formation. While this method could not capture these effects, studies on using alumina as a material for geoengineering have shown that alumina can lead to ozone depletion due to chlorine activation, albeit this ozone depletion is less drastic when compared to sulfate geoengineering particles [157].

In addition to informing where reentry particles may be interacting with important at-

mospheric processes, the reentry particle distributions also highlight regions where these particles could be detected and sampled in situ. For example, we can conclude that using meteoric metal observation techniques are unlikely to detect reentry debris particles [112]. These lidars aim to measure metallic concentrations above 90 km [112]. This region lacks high concentrations of reentry particles. Instead, our results indicate that stratospheric sampling may be a better detection method to measure reentry ablation particles in situ.

Another interesting conclusion of these results is the lifetime of reentry particles. These results show reentry "dust" particles have a lifetime of between 1 to 2 years, depending on differing assumptions for the initial particle size distribution of reentry-ablated alumina. These results are in line with previous studies of alumina emissions from solid rocket motors. Figure 8-2 shows the lifetime of alumina emitted solid rocket motors under precipitation only (Case A), precipitation and sedimentation (Case B) and precipitation, sedimentation and coagulation (Case C).

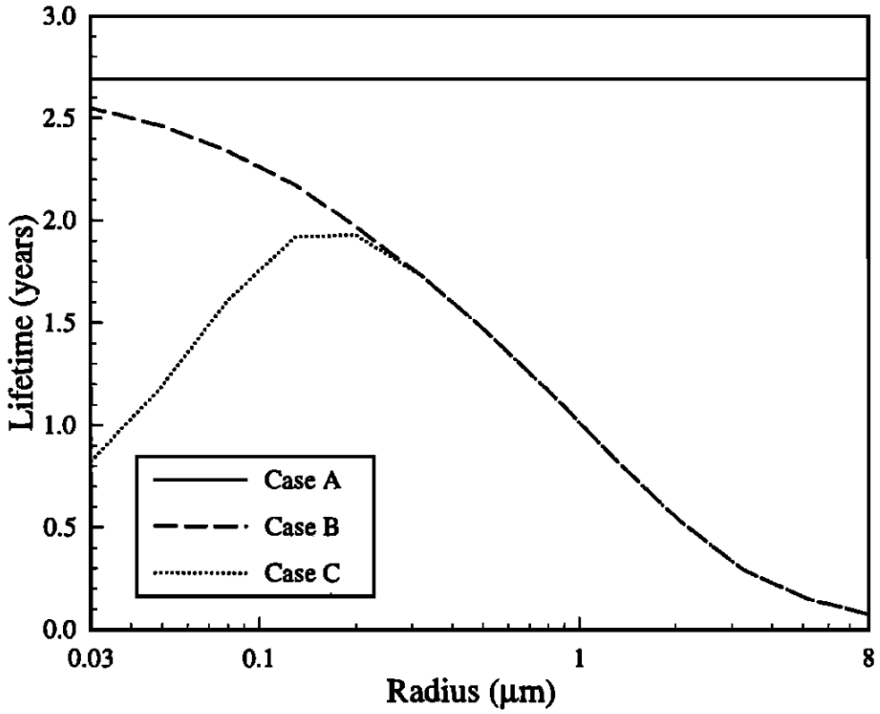

Figure 8-2: Alumina Lifetime in the Stratosphere Considering Various Aerosol Deposition Mechanisms [29]

,

We can see from Figure 8-2 that under precipitation, sedimentation and coagulation,

alumina particles can have a maximum lifetime of 2 years. This maximum lifetime corresponds to particles between 0.1 and 1 microns, represented in this work by the accumulation mode. In Case 2, reentry dust particles transition quickly into the accumulation mode and predominately persists in this mode, leading to a lifetime of 2 years (see Table 7.2). As Figure 8-2 shows, if reentry alumina particles can maintain a size distribution between 0.1 and 1 microns, these particles will persist the longest. Larger particles will sediment faster while smaller particles will rapidly coagulate into larger particles. We can conclude that the reentry "dust" lifetimes found in this study are well aligned with previous work on stratospheric alumina aerosols.

8.2 Radiative Forcing

In order to put the direct radiative forcing of reentry Alumina into context, we compare these radiative forcing to meteors, rockets and airplanes. We also propose and present a variety of metrics to normalize the climate impact per unit of societal value to better compare the performance of the space and aviation industry.

The direct radiative forcing of reentry alumina in the market-optimistic scenario is approximately -0.2 mW/m^2. Cases 2 and 3 show a stronger radiative cooling over Case 1 due to the longer lifetime of reentry particles in those cases. The smaller dust size in Case 2 and the time-averaged representation of reentry in Case 3 cause these longer lifetimes, and consequently stronger radiative forcing. We also see in Case 4 that while the direct radiative effect is similar to Case 1, the emissions in the South Pacific lead to an asymmetrical distribution of the radiative effect, causing significantly more cooling in the Southern hemisphere. As aforementioned, asymmetrical changes to radiative transfer can cause more serious secondary consequences, like major shifts in precipitation.

A negative radiative forcing implies a cooling effect on the atmosphere because there is less incoming radiative energy into the Earth system as a result of scattering. Dust scatters light back into space preventing that energy from warming Earth's surface. Unfortunately, we could not capture the surface temperature change as a result of alumina's direct radiative effect due to limited computational resources. Capturing surface temperature changes

requires a multitude of simulations with perturbed initial conditions to explore the variance in the temperature response to a given radiative forcing. The numbers of simulations required exceeded our computational resources. Consequently, capturing surface temperature variations is reserved for future work.

Based on the Market Optimistic scenario, we can determine an upper bound on the aluminum influx by assuming the entire reentry mass is aluminum that completely ablates in the atmosphere. Under these assumptions, the aluminum reentry flux increases by one order of magnitude to approximately 10 Gg or 0.01 Tg. If we apply the assumption of a linear relationship between radiative forcing and emission amount, this scenario would result in a radiative forcing of $-2mW/m^2$. This estimation serves as an upper bound for the direct radiative effect of the space debris reentries in the Market Optimistic scenario.

Figure 8-3 shows the global effective radiative effect of aviation emissions from 1940 to 2018.

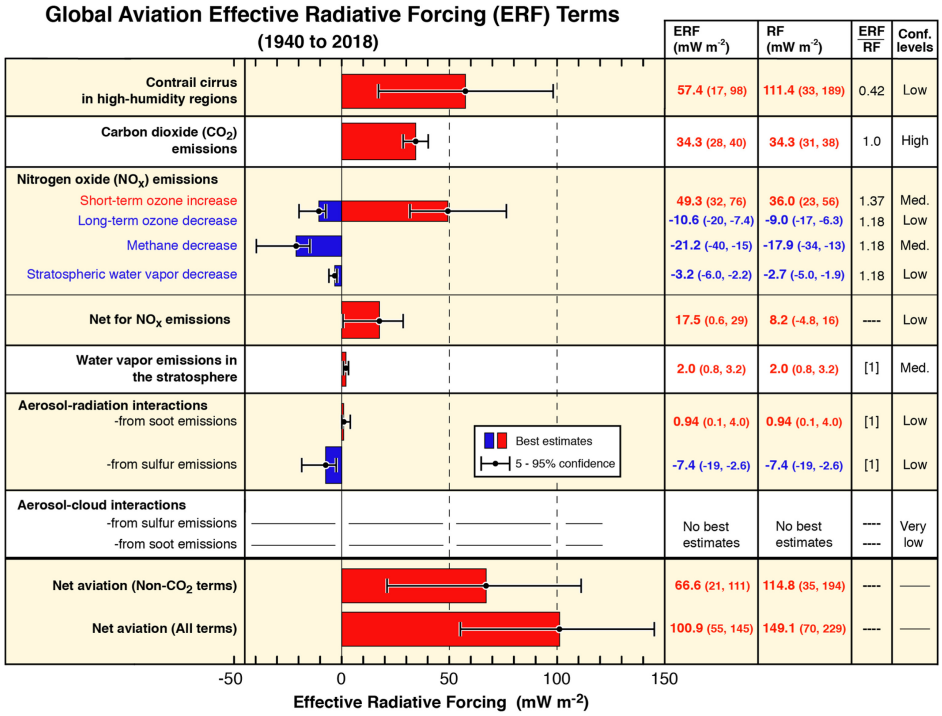

Figure 8-3: Global Radiative Effect of Aviation Emissions from 1940 to 2018 [76]

,

Note that Figure 8-3 introduces two metrics, the effective radiative forcing (ERF) and radiative forcing (RF). The radiative forcing measures the energy imbalance after allowing

the stratospheric temperature to adjust. Also a measure of energy imbalance, the effective radiative forcing is evaluated after allowing the atmospheric temperature, water vapor and clouds to adjust to the new forcing. In this work, we present the direct radiative effect, or also known as the instantaneous radiative forcing, which does not account for temperature, water vapor or cloud perturbations.

The net aviation effect radiative forcing is approximately 100 mW/m^2. Interestingly, aviation aerosol emissions contribute approximately 0.94 mW/m^2 while CO_2 emissions and contrails drive the majority of this total effect. In regards to all of human activity, aviation emissions have contributed 4% to anthropogenic global warming [69]. Figure 8-4 shows the breakdown of anthropogenic radiative forcing and the total net effect.

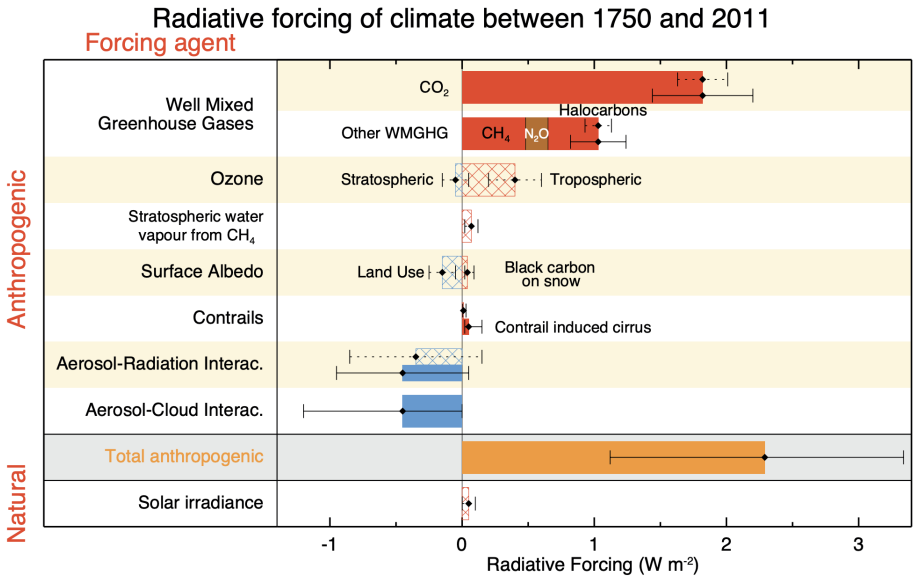

Figure 8-4: Global Radiative Forcing from Human Activities between 1750 to 2011 shown with 5 to 95 % confidence bars [100]

,

In comparison to the total aviation ERF, reentry-ablated alumina produces a very small radiative effect, approximately 0.02%. This percentage grows to 2% of the total aviation ERF when we assume the upper bound estimate of the direct radiative forcing for the Market Optimistic case. Reentry-ablated alumina begins to produce a larger radiative effect than present-day aviation if we assume a reentry aluminum flux 100 to 1000 times larger than the Market Optimistic scenario. This result indicates that even under the most optimistic

economic scenario with several megaconstellations in operation, the direct radiative effect of the subsequent space debris reentries is small.

Furthermore, this analysis shows that the present day space debris reentry flux leads to an insignificant radiative effect. We can estimate the present day reentry alumina mass from year 2025 in Figure 4-6a and Figure 4-6b with the assumptions of 21% of the satellite dry mass is aluminum of which 58% ablates, while 70% of the rocket body mass is aluminum of which 31% ablates. This leads to an alumina emission mass of 150 Mg, or four orders of magnitude smaller than the alumina emissions in this work. The corresponding direct radiative effect of 150 Mg alumina emissions would be approximately -0.0224 mW/m^2, assuming a linear relationship between the emitted mass and direct radiative effect. In other words, present day reentry-ablated alumina amount to 0.0224% of aviation's total radiative forcing effect.

Certain assumptions used in this work will impact these findings. For example, if reentry-ablated alumina does not coagulate quickly, these alumina particles may have longer lifetimes causing stronger radiative effects. We see this pattern between Case 1 and Case 2, where reentry particles in Case 2 had longer lifetimes than Case 1, leading to a stronger radiative effect. Furthermore, alumina is more effective at scattering light than terrestrial dust, at least over short wavelengths (see Subsection 6.1.3). The results presented in this work underestimate the radiative effect of alumina by at least 20%. The material composition and ablation profile assumptions could also be sources of error, underestimating the alumina mass that ablated into the atmosphere.

Even so, if we assume all the reentry mass is aluminum that ablates into the atmosphere, the alumina emitted mass increases by only one order of magnitude, not three orders of magnitude which is necessary for reentry-ablated alumina to induce radiative effects on the same scale as aviation. The remaining sources of error are unlikely to amount to a 100-fold increase to close this gap. For example, we can see from Figure 8-2 that under the influence of only precipitation and sedimentation, and not coagulation, alumina particles in the stratosphere have a maximum lifetime of 2.5 years, or 912.5 days. This lifetime is a modest increase over the lifetime estimated in Case 2 of 749 days. The difference in the direct radiative effect of a particle that persists for 912.5 days versus 749 days is not 100-fold.

It is important to note this comparison relies on aviation radiative forcing from 1940-2018

while the space debris reentry radiative effect corresponds to a 2050 reentry flux. By 2050, the net radiative effect of aviation may be smaller than 100 mW/m^2, despite the projected in the number of flights per year over, as the aviation industry looks to decarbonize [92]. We can see from Figure 8-5 that several organizations plan to reduce future carbon emissions by more than 50% compared to 2019 carbon emissions by 2050. As the aviation radiative forcing decreases, the ratio of reentry and aviation radiative forcing will grow.

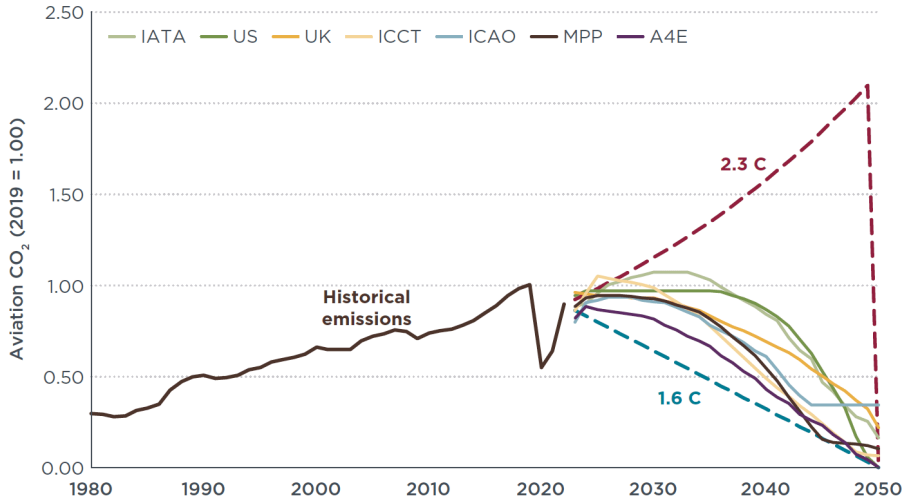

Figure 8-5: Global Aviation Carbon Emission Projections According to Various Decarbonization Plans of Different Organizations. Baseline carbon emissions are taken from year 2019. [92]

,

We can also compare how the radiative of reentry-ablated alumina compares to rockets. Acknowledging caveats on poorly constrained alumina and black carbon optical properties, one study estimated global rocket launches in 2030 would produce a direct radiative forcing of 36 mW/m^2 [125]. Another study used the 2019 rocket fleet and applied an launch growth rate of 5.6% per year [128]. After a decade of growing rocket emissions, the direct radiative effect of this rocket fleet was 3.9 mW/m^2 [128]. This same study also explored a space tourism scenario with 400 Virgin Galactic suborbital flights per year, daily Blue Origin suborbital flights and weekly Space X launches [128]. In this case, the direct radiative effect of rockets of approximately 7.7 mW/m^2 [128]. However, the composition of the future rocket fleet plays a significant role in determining the direct radiative effect. For example, a rocket burning liquid hydrogen and oxygen produces an effective radiative forcing of 60 W/m^2 at

Table 8.1: Comparing Rocket and Reentry-ablated Alumina Direct Radiative Forcings (DRF). Reentry-ablated alumina direct radiative forcing is evaluated at the top of the atmosphere

Rocket (mW/m^2)	Ratio of Reentry Alumina to Rocket DRF (%)			
	Case 1	Case 2	Case 3	Case 4
36 [125]	0.58	0.66	0.72	0.58
3.9 [128]	5.4	6.2	6.7	5.4
7.7 [128]	2.7	3.2	3.4	2.7

a launch rate of 10^5 flights per year [73]. This launch cadence is three orders of magnitude larger than present day launch rates, indicating that the radiative effect of these kind of rockets is insignificant, even in under future scenarios with several launches per day.

Table 8.1 shows how the direct radiative forcing of reentry-ablated alumina in the Market Optimistic case compares to various assumptions of the rocket radiative forcing. We can see that reentry-ablated alumina is a small fraction of the rocket radiative effect, between 0.5 and 5 %. If we take the upper bound case for reentry alumina at $-2mW/m^2$, then space debris reentries are between 5 to 51% of rocket-induced radiative forcing.

Comparing these absolute values, this analysis shows that the current practice of reentering space debris into Earth's atmosphere will not compromise the international goal of mitigating global warming. The present reentry mass is four orders of magnitude smaller than the necessary reentry mass to constitute a direct radiative effect similar to aviation, which itself is only 4% of the total human-induce radiative forcing [69].

However, it is also interesting to express these radiative effects in terms of per unit of societal value. Most human activities have an environment cost. Consequently, we should aim to maximize the effectiveness of a human activity to provide value with minimal environmental cost. We can normalize these direct radiative effects to interpret how well each of these industries generate value for their respective direct radiative forcings.

8.2.1 Normalizing Direct Radiative Forcing

The societal value of that industry must be measured, and due to complexities of socioeconomic systems, societal value can be estimated using a variety of metrics. A stakeholder

value network graphically summarizes what different stakeholders value and how value is transferred between stakeholders. Figure 8-6 shows a stakeholder value network for a mega-constellation system that provides satellite communication and internet services. In the Market Optimistic Scenario, the majority of the reentry mass is due to satellite communication constellations, although several satellite imagery and Earth observation constellations were included in the analysis.

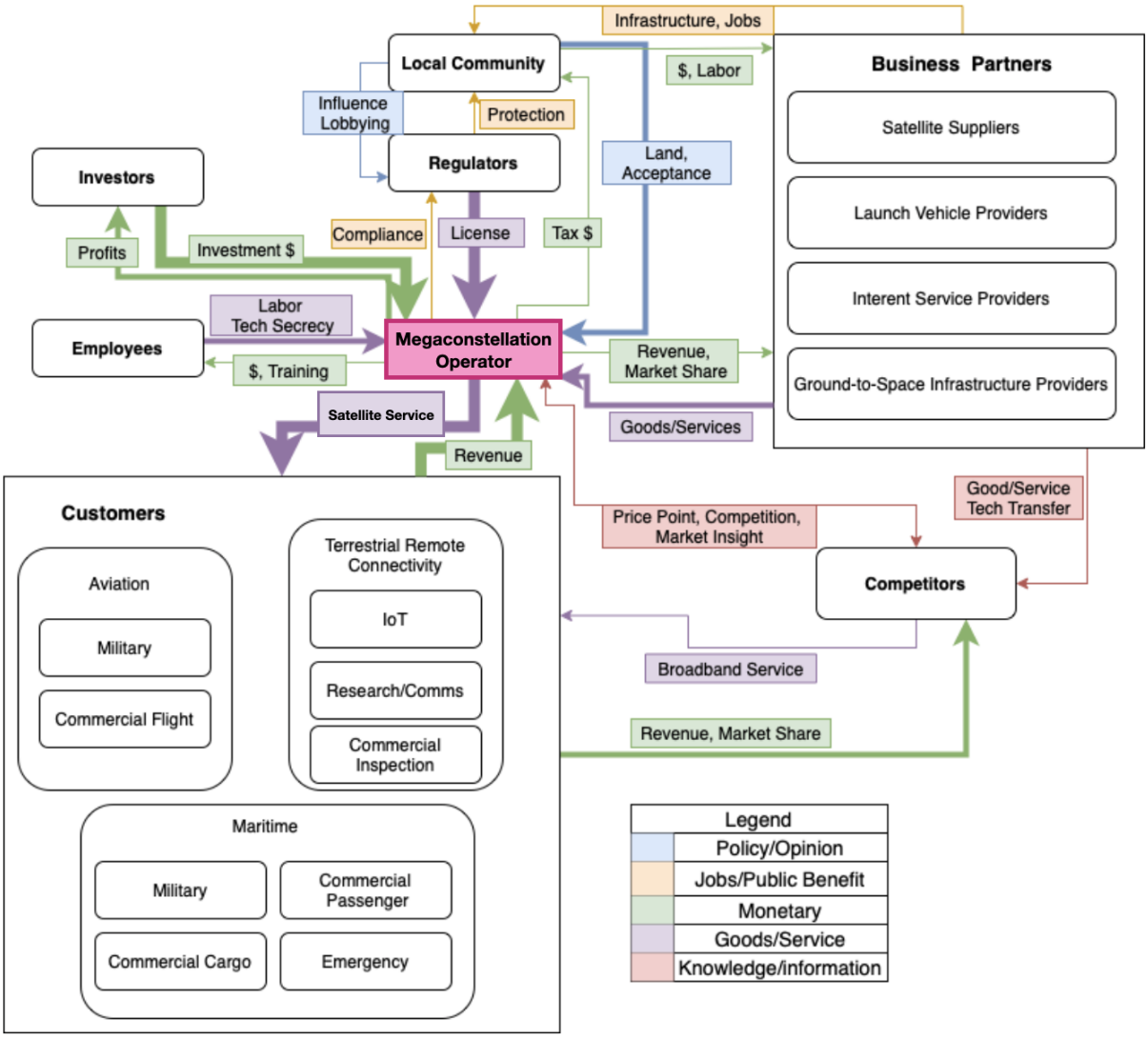

Figure 8-6: Stakeholder Value Network of a Megaconstellation System

,

From Figure 8-6, we can see that there are a variety of stakeholders that exchange revenues, goods, services, information and authorization. Customers pay for satellite services

provided by a megaconstellation operator. Space industry suppliers depend on contracts, goods and services from this operator. Further, this operator compensates employees for their labor and services. Analyzing these exchanges highlights a number of possible metrics for measuring societal value, including the number of customers served by a megaconstellation operator, operator revenues, dollar-value of supplier contracts, and number of employees.

In this work, we focus on three metrics: (i) normalizing the direct radiative effect of debris reentries by the number of individual customers, (ii) the revenue earned from selling these services, and (iii) the number reentry events. We focus these metrics on civil, commercial satellite services since this category of satellite systems are the predominate business model for the megaconstellations in development, including Starlink, OneWeb, Kuiper, E-space, and Planet Labs. To estimate the number of individual customers, we consider projections for satellite internet subscribers only.

To compare across industries, we identify analog metrics for the aviation industry. We can normalize aviation's effective radiative forcing by the number of passengers, the revenues from these customers and the number of commercial flights. Note that these aviation metrics disregard the commercial aviation cargo industry which is responsible for approximately 18% of the total aviation carbon dioxide emissions (see Appendix G)[16]. Military and recreational aviation is also neglected, although these sectors comprise less than 10% of the aviation industry's carbon dioxide emissions [16]. As Figure 8-3 shows, carbon dioxide emissions account for approximately half of aviation's radiative forcing.

Serving as an estimation for future LEO constellation revenues, Morgan Stanley estimates that by 2040, satellite internet systems may generate revenues over 88 billion USD per year [96]. This estimate is a lower bound estimate of the revenue generated by LEO constellations. Morgan Stanley estimated that broadband will become available to approximately 75% of the world's population by 2040, of which satellite internet will capture 33% of that market[96]. Using these estimates, we find that satellite connectivity constellations will have approximately 1.98 billion users.

We can estimate similar quantities for the aviation industry.

The global commercial aviation industry prior to the COVID-19 pandemic earned revenues of approximately 838 billion USD in 2019 from operating 38.9 million flights [7]. Post-

Table 8.2: Normalized Metrics to Compare the Radiative Effect per Unit of Societal Value for Space Debris Reentries and the Aviation Industry

Metric	Space Debris Reentries				Global Aviation
	Case 1	Case 2	Case 3	Case 4	
mW/m^2 per Billion Serviced Customers / Passengers	-0.106	-0.121	-0.131	-0.106	22.01
mW/m^2 per Annual Revenue (Billions Dollars)	−2.39e−3	−2.73e−3	−2.95e−3	−2.39e−3	0.119
mW/m^2 per Number of Events/Flights	−1.46e−5	−1.67e−5	−1.81e−5	−1.46e−5	2.57e−6

pandemic, the airline industry has shown signs of recovery, posting revenues of 782 billion USD from operating 33.8 million flights in 2022. The number of passengers booked on flights was 4.543 billion in 2019 and 3.781 billion in 2022.

Using these measures of societal value, Table 8.2 shows the normalized radiative effect for space debris reentries and the aviation industry. When considering the absolute value of these ratios, a larger ratio implies a stronger radiative consequences for the same amount of societal value. We sum data from 1940 to 2004 to estimate the industry's revenue, number of flights, and number of passengers. This time period corresponds to the industry's effective radiative forcing of 100 mW/m^2 integrated over the same time period. The space debris metrics are derived from the instantaneous radiative forcing from Cases 1-4 assuming projections for the space economy between 2040 to 2050 which is approximately when the Market Optimistic scenario suggests there will be 14,400 reentry events per year, as modeled in this work.

From Table 8.2, we can see that across the customer and revenue metrics, space debris reentries have a lower radiative impact for the same societal value when compared to aviation. However, per event, space debris reentries are more effective at perturbing Earth's radiative balance than aviation.

It is important to note that these findings do not change if we instead consider the revenue, passenger traffic and flight volumes summed over 1940 to 2018 which corresponds to the time period used to estimate present day effective radiation forcing from aviation. For example, the passenger traffic of aviation over that time period would have be at least a trillion people

in order to match the corresponding space debris reentry metric. As Appendix G shows, the aviation industry carried approximately 55 billion people from 2004 to 2022. If we assume that this passenger volume is constant with time, then the passenger volume since 1940 would be approximately 217 billion people. Of course, this assumption is an overestimate as access to commercial aviation in 1940 was limited and grew with time. Yet, even this overestimate is not sufficient to change the conclusion that space debris reentries produce weaker radiative effects per customer than aviation. The same logic and conclusion can be shown for aviation's revenue. On the other hand, if we consider the number of flights since 1940, the normalized radiative effect of aviation per flight will decrease significantly, widening the gap between space debris reentries and aviation.

Chapter 9

Conclusion

The number of space debris reentries is likely to increase for the next several decades, given the rising number of orbiting objects, growing number of space actors and the development of mega-constellations. In an economic scenario where several megaconstellations are fully developed, reentry events could occur as often as every 40 mins.

During their descent, space debris reentries disintegrate in Earth's atmosphere. Fusible materials, like aluminum, rapidly melt and form small metallic particles. In the case of aluminum, alumina (Al_2O_3) particles form. These particles dissipate into the reentry plume and eventually in the greater atmosphere where they can interact with important atmospheric phenomena. The extent to which these particles persist and interact with atmospheric processes is not well understood.

This work presents results that characterize the distribution, lifetime and direct radiative effect of reentry-ablated alumina using a state-of-the-art general circulation model, the Whole Atmosphere Community Climate Model (WACCM). Our methodology uses terrestrial dust as a proxy for alumina in WACCM since alumina is not currently a modeled aerosol. Dust can be represented in three different particle size distributions and can coagulate between these distributions. Like alumina, dust is effective at scattering light albeit less effective than alumina.

We explore a reentry flux of 14,400 reentry events per year with 13,900 satellites and 500 rocket bodies. This reentry flux corresponds to a market optimistic scenario where all of the megaconstellations filed in the Federal Communication Commission are built and

maintained. We assume an aluminum composition of 21% for satellites and 70% for rocket bodies with an ablation fraction of 58% and 31% respectively. These assumptions amount to an aluminum reentry flux of 1.337 Gg per year.

With these reentry emissions, we evaluate several test cases to identify the effect of various assumptions on particle size, emission location and the representation of reentry plumes as discrete events. In each case, we evaluate the steady state behavior with the reentry emissions repeating identically year-over-year.

Our results show that the lifetime and distribution of reentry-ablated alumina particles varies with different assumptions on the emitted particle size. Emissions modeled with discrete reentry plumes in the smallest particle size distribution result in the longest particle lifetime of 749 days. However, similar emissions in the middle particle size distribution results in a significantly shorter lifetime of 489 days. Subject to the assumptions in this methodology, these findings suggest that reentry particles will not persist as long in the atmosphere as suspected, and do not adhere to the average stratospheric aerosol lifetime of 4 years [125].

It is important to note that if reentry-ablated alumina does not coagulate efficiently, the lifetimes of these particles will be underestimated in this work.

Furthermore, we have shown that modeling reentry emissions with discrete reentry plumes results in significantly shorter particle lifetimes than a homogeneous emissions. Without modeling discrete plume emissions, the particle lifetimes will be overestimated by approximately 25%. Consequently, the extent to which these particles interact with atmospheric processes will also be overestimated using non-discrete representations of reentry plumes.

We also find that unlike meteor particles, globally-emitted space debris reentry particles are uniformly concentrated both hemispheres in the mesosphere and stratosphere. These results suggest that reentry particles could alter upper atmosphere and stratospheric processes, including ozone chemistry and high-altitude cloud formation.

Furthermore, this work has shown that reentry-ablated alumina produces a cooling instantaneous radiative forcing of approximately -200 mW/m^2 for a yearly reentry flux of 1.337 Tg which is 1000 times larger than the estimated alumina influx in the market optimistic scenario. To compare, the aviation industry produces a total net radiative forcing of

100 mW/m^2, contributing approximately 4% to the global human-induce radiative forcing [76, 69].

We assume a linear relationship between the reentry mass and the direct radiative effect to estimate the direct radiative forcing in the market optimistic scenario and for the present-day reentry flux. With 1.337 Gg of reentry-ablated alumina, the estimated direct radiative forcing is -0.2 mW/m^2 or 0.2% of aviation's radiative forcing. Taking the 2025 reentry-ablated alumina mass as 150 Mg, we find a direct radiative effect of -0.0224 mW/m^2, amounting to 0.0224% of aviation's radiative forcing. From these results, we can conclude that the present-day and future flux of space debris reentries produces very small changes to Earth's radiative balance. We can also observe that optimizing satellite design for demisability will increase the direct radiative effect of space debris reentries, but not sufficiently to cause a radiative forcing comparable to the aviation industry.

Normalizing the direct radiative effect of space debris reentries by a unit of societal value also demonstrates that space debris reentries generate less radiative forcing per unit of societal value compared to the aviation industry. We considered normalizing by industry revenues and number of customers served and both metrics showed that aviation produces more radiative forcing per dollar earned and per customer than reentries. On the other hand, reentries produce far more radiative forcing per occurrence, indicating that reentries are more effective at perturbing Earth's radiative balance than airplanes.

This work explored the distribution of the direct radiative effect of space debris reentries. When space debris reentries only occur in the South Pacific region, these particles remain in concentrated in the Southern Hemisphere, creating an asymmetrical radiative effect that disproportionately cools the Southern Hemisphere compared to the Northern Hemisphere. Asymmetrical heating or cooling can lead to severe climate consequences, including intense drought, and increased cyclone activity. Reentering space debris objects across the global leads to more uniform radiative effects which limits the potential for these negative consequences of asymmetrical radiative forcing. We can conclude that from a radiative forcing perspective, it is not advantageous to implement policies that recommend or require space debris objects to reenter over a singe region, such as the South Pacific.

Overall, this work finds that the status quo of reentering space debris across the globe

does not significantly alter Earth's radiative budget. Furthermore, we find that the same conclusion holds true in a future scenario with several megaconstellations in operation. We can conclude, then, that designing megaconstellation satellites for maximum demisability is advantageous to reduce risk to human life and property, despite the modest increase in reentry radiative forcing.

9.1 Future Work

As this work has shown, the characteristics of reentry-ablated alumina can significantly alter the particle's lifetime and direct radiative effect. To reduce uncertainties in this model, future work should measure the particle size distribution of reentry-ablated alumina and characterize the optical and coagulation properties of these particles. Arc-jet experiments with aluminum could provide a representative environment to produce ablated particles that can be captured using an in-stream aerogel, similar to previous PICA spallation particle studies [116, 30]. These particles could then be extracted from the aerogel and characterized.

With improved understanding of reentry-ablated alumina, future studies can improve upon the methodology presented in this work and implement an alumina aerosol in a general circulation model, like WACCM. This new approach will allow reentry alumina to be directly modeled without a proxy. Better estimations of the reentry radiative forcing can be estimated, and coupled interactions between alumina's heterogeneous chemistry and indirect radiative forcing can be captured. Furthermore, this improved approach can also capture the deposition distribution of alumina. Studies of alumina as a geoengineering agent have shown that larger deposits of alumina over land can lead to human and biota poisoning [57, 159]. The extent to which space debris reentries cause these serious consequences has not yet been quantified.

To validate results of this work and future modeling, in-situ sampling is vital. Atmospheric sampling through stratospheric planes, sounding rockets or weather balloons may be able to collect these particles and characterize their coagulation and size characteristics. It is also possible that satellite observations may be able to detect reentry particle accumulation. These observations will ground model results and likely improve our understanding of how

alumina particles interact in the upper atmosphere.

Bibliography

[1] Airline industry - passenger traffic worldwide 2004-2022. URL: https://www.statista.com/statistics/564717/airline-industry-passenger-traffic-globally/.

[2] Cesm2 timing, performance & load balancing data. URL: https://csegweb.cgd.ucar.edu/timing/cgi-bin/timings.cgi.

[3] Chemistry specific modifications — camdoc documentation. URL: https://ncar.github.io/CAM/doc/build/html/users_guide/CAM-chem-specifics.html.

[4] Climate change. URL: http://www.climate.gov/news-features/understanding-climate/climate-change-atmospheric-carbon-dioxide.

[5] Cmip6 homepage. URL: https://pcmdi.llnl.gov/CMIP6/.

[6] Global monitoring laboratory - carbon cycle greenhouse gases. URL: https://gml.noaa.gov/ccgg/trends/data.html.

[7] Revenue of airlines worldwide 2003-2022. URL: https://www.statista.com/statistics/278372/revenue-of-commercial-airlines-worldwide/.

[8] Waccm6-tsmlt-ssp245 and arise-sai-1.5 fields complete list. URL: https://www2.cgd.ucar.edu/ccr/strandwg/WACCM6-TSMLT-SSP245/.

[9] United Launch Alliance. Delta ii payload planners guide, Dec 2006. URL: https://ula.bsshost.me/docs/default-source/rockets/deltaiipayloadplannersguide2007.pdf.

[10] United Launch Alliance. Atlas v launch services users guide, Mar 2010. URL: https://www.ulalaunch.com/docs/default-source/rockets/atlasvusersguide2010.pdf.

[11] Slimane Bekki, James Beck, Tobias Lips, James Merrifield, Martin Spel, and Tobias Langener. Environmental impacts of atmospheric emissions from spacecraft re-entry demise, 2021. URL: https://indico.esa.int/event/321/contributions/6403/attachments/4335/6538/esa-csid-21-bekki.pdf.

[12] Slimane Bekki, Daniel Cariolle, Neil Murray, Ralf Toumi, James Beck, Tobias Lips, and Julian Austin. Impacts of space vehicles' launch & re-entry on the ozone layer and climate, 2017. URL: https://indico.esa.int/event/181/contributions/1487/attachments/1318/1543/01_2017_CSID_Bekki_CNRS.pdf.

[13] Eric Berger. The world just set a record for sending the most rockets into orbit, Jan 2022. URL: https://arstechnica.com/science/2022/01/thanks-to-china-and-spacex-the-world-set-an-orbital-launch-record-in-2021/.

[14] Simone Bianchi, Lilith Grassi, Hiroshi Yamashita, Katrin Dahlmann, Volker Grewe, Patrick Jöckel, Pénélope Leyland, Stefano Mischler, and Javier Navarro Laboulais. Ara – atmoshperic re-entry assessment, 2021. URL: https://indico.esa.int/event/321/contributions/6376/attachments/4334/6537/DESI_Bianchi_CleanSpaceIndustrialDays_ARA.pdf.

[15] H Bolandi, Mh Ashtari Larki, Sh Sedighy, Ms Zeighami, and M Esmailzadeh. Estimation of simplified general perturbations model 4 orbital elements from global positioning system data by invasive weed optimization algorithm. *Proceedings of the Institution of Mechanical Engineers, Part G: Journal of Aerospace Engineering*, 229(8):1384–1394, Jun 2015. URL: http://journals.sagepub.com/doi/10.1177/0954410014550323, doi:10.1177/0954410014550323.

[16] Ph.D. Brandon Graver, Kevin Zhang, and Ph.D. Dan Rutherford. Co2 emissions from commercial aviation, 2018, 2019. URL: https://theicct.org/wp-content/uploads/2021/06/ICCT_CO2-commercl-aviation-2018_20190918.pdf.

[17] J Bremer, P Hoffmann, R Latteck, W Singer, and M Zecha. Long-term changes of (polar) mesosphere summer echoes. *Journal of atmospheric and solar-terrestrial physics*, 71(14-15):1571–1576, 2009.

[18] Jon Brodkin. Firm planning 100,000 satellites claims it will "clean space" by capturing debris, Feb 2022. URL: https://arstechnica.com/information-technology/2022/02/firm-planning-100000-satellites-claims-it-will-clean-space-by-capturing-debris/.

[19] P. Brown, J. Jones, R. J. Weryk, and M. D. Campbell-Brown. The velocity distribution of meteoroids at the earth as measured by the canadian meteor orbit radar (cmor). *Earth, Moon, and Planets*, 95(1–4):617–626, Feb 2006. URL: http://link.springer.com/10.1007/s11038-005-5041-1, doi:10.1007/s11038-005-5041-1.

[20] Rodrigo Caballero. *Physics of the Atmosphere*. 2053-2563. IOP Publishing, 2014. URL: https://dx.doi.org/10.1088/978-0-7503-1052-9, doi:10.1088/978-0-7503-1052-9.

[21] Jean-Sébastien Cagnone, Song Gao, John Stokes, and Laith Zori. Numerical simulations of thermo-chemical non-equilibrium flows in the transitional flow regime using ansys fluent. In *ASCEND 2021*, Las Vegas, Nevada & Virtual, Nov 2021. American Institute of Aeronautics and Astronautics. URL: https://arc.aiaa.org/doi/10.2514/6.2021-4246, doi:10.2514/6.2021-4246.

[22] NASA Goddard Space Flight Center. What is a dobson unit, Feb 2023. URL: https://ozonewatch.gsfc.nasa.gov/facts/dobson_SH.html#:~:text=The%20Dobson%20Unit%20is%20a,of%202%20pennies%20stacked%20together.

[23] Wei Cheng, Douglas G. MacMartin, Ben Kravitz, Daniele Visioni, Ewa M. Bednarz, Yangyang Xu, Yong Luo, Lei Huang, Yongyun Hu, Paul W. Staten, Peter Hitchcock, John C. Moore, Anboyu Guo, and Xiangzheng Deng. Changes in hadley circulation and intertropical convergence zone under strategic stratospheric aerosol geoengineering. *npj Climate and Atmospheric Science*, 5(1):32, Apr 2022. URL: https://www.nature.com/articles/s41612-022-00254-6, doi:10.1038/s41612-022-00254-6.

[24] Martyn P. Chipperfield, Slimane Bekki, Sandip Dhomse, Neil R. P. Harris, Birgit Hassler, Ryan Hossaini, Wolfgang Steinbrecht, Rémi Thiéblemont, and Mark Weber. Detecting recovery of the stratospheric ozone layer. *Nature*, 549(7671):211–218, Sep 2017. URL: https://www.nature.com/articles/nature23681, doi:10.1038/nature23681.

[25] Serena H. Chung. Climate response of direct radiative forcing of anthropogenic black carbon. *Journal of Geophysical Research*, 110(D11):D11102, 2005. URL: http://doi.wiley.com/10.1029/2004JD005441, doi:10.1029/2004JD005441.

[26] S.A. Clough, M.W. Shephard, E.J. Mlawer, J.S. Delamere, M.J. Iacono, K. Cady-Pereira, S. Boukabara, and P.D. Brown. Atmospheric radiative transfer modeling: a summary of the aer codes. *Journal of Quantitative Spectroscopy and Radiative Transfer*, 91(2):233–244, Mar 2005. URL: https://linkinghub.elsevier.com/retrieve/pii/S0022407304002158, doi:10.1016/j.jqsrt.2004.05.058.

[27] B. Croft, J. R. Pierce, and R. V. Martin. *Interpreting aerosol lifetimes using the GEOS-Chem model and constraints from radionuclide measurements*. Dec 2013. URL: https://acp.copernicus.org/preprints/13/32391/2013/acpd-13-32391-2013.pdf, doi:10.5194/acpd-13-32391-2013.

[28] J.A. Dallas, S. Raval, J.P. Alvarez Gaitan, S. Saydam, and A.G. Dempster. The environmental impact of emissions from space launches: A comprehensive review. *Journal of Cleaner Production*, 255:120209, May 2020. URL: https://linkinghub.elsevier.com/retrieve/pii/S0959652620302560, doi:10.1016/j.jclepro.2020.120209.

[29] M. Y. Danilin, R.-L. Shia, M. K. W. Ko, D. K. Weisenstein, N. D. Sze, J. J. Lamb, T. W. Smith, P. D. Lohn, and M. J. Prather. Global stratospheric effects of the alumina emissions by solid-fueled rocket motors. *Journal of Geophysical Research: Atmospheres*, 106(D12):12727–12738, Jun 2001. URL: http://doi.wiley.com/10.1029/2001JD900022, doi:10.1029/2001jd900022.

[30] Raghava Davuluri, Kristen J. Price, Sean Bailey, Kaveh Tagavi, and Alexandre Martin. Numerical reconstruction of spalled particle trajectories in an arc-jet environment: Cylinder and hemicylinder samples. In *AIAA SCITECH 2023 Forum*, National Harbor, MD & Online, Jan 2023. American Institute of Aeronautics and Astronautics. URL: https://arc.aiaa.org/doi/10.2514/6.2023-1911, doi:10.2514/6.2023-1911.

[31] Vito De Lucia and Viviana Iavicoli. From outer space to ocean depths: The 'spacecraft cemetery' and the protection of the marine environment in areas beyond national

jurisdiction. *California Western International Law Journal*, 49(2), Jun 2019. URL: https://scholarlycommons.law.cwsl.edu/cwilj/vol49/iss2/4.

[32] Stéphanie Delavault, Paul Legendre, Romain Garmier, and Bruno Revelin. Improvement of the tle accuracy model based on a gaussian mixture depending on the propagation duration. In *AIAA/AAS Astrodynamics Specialist Conference and Exhibit*, Honolulu, Hawaii, Aug 2008. American Institute of Aeronautics and Astronautics. URL: https://arc.aiaa.org/doi/10.2514/6.2008-6772, doi:10.2514/6.2008-6772.

[33] S. S. Dhomse, R. W. Saunders, W. Tian, M. P. Chipperfield, and J. M. C. Plane. Plutonium-238 observations as a test of modeled transport and surface deposition of meteoric smoke particles: Pu-238 and meteoric smoke deposition. *Geophysical Research Letters*, 40(16):4454–4458, Aug 2013. URL: http://doi.wiley.com/10.1002/grl.50840, doi:10.1002/grl.50840.

[34] B. Di Mauro, R. Garzonio, G. Baccolo, S. Gilardoni, M. Rossini, and R. Colombo. *Light-Absorbing Particles in Snow and Ice: A Brief Journey Across Latitudes*, page 1–29. Springer International Publishing, Cham, 2021. URL: https://link.springer.com/10.1007/978-3-030-87683-8_1, doi:10.1007/978-3-030-87683-8_1.

[35] M Le Dourneuf, Vo Ky Lan, K T Taylor, and P G Burke. The photoionization of neutral aluminium. *Journal of Physics B: Atomic and Molecular Physics*, 8(16):2640–2653, nov 1975. doi:10.1088/0022-3700/8/16/021.

[36] J. T. Emmert, M. H. Stevens, P. F. Bernath, D. P. Drob, and C. D. Boone. Observations of increasing carbon dioxide concentration in earth's thermosphere. *Nature Geoscience*, 5(12):868–871, Dec 2012. URL: http://www.nature.com/articles/ngeo1626, doi:10.1038/ngeo1626.

[37] Esa. On the atmospheric impact of spacecraft demise upon reentry, 2022. URL: https://blogs.esa.int/cleanspace/2022/08/11/on-the-atmospheric-impact-of-spacecraft-demise-upon-reentry/.

[38] V. Eska, U. Von Zahn, and J. M. C. Plane. The terrestrial potassium layer (75-110 km) between 71°s and 54°n: Observations and modeling. *Journal of Geophysical Research: Space Physics*, 104(A8):17173–17186, Aug 1999. URL: http://doi.wiley.com/10.1029/1999JA900117, doi:10.1029/1999ja900117.

[39] M. J. Evans. Coupled evolution of bro x -clo x -ho x -no x chemistry during bromine-catalyzed ozone depletion events in the arctic boundary layer. *Journal of Geophysical Research*, 108(D4):8368, 2003. URL: http://doi.wiley.com/10.1029/2002JD002732, doi:10.1029/2002jd002732.

[40] Andrea Fagnani, Olivier Chazot, Annick Hubin, and Bernd Helber. Comprehensive characterization of the aerothermomechanical response of space debris to atmospheric entry plasmas: 10th vki phd symposium. Mar 2019.

[41] Rhodes W. Fairbridge and John E. Oliver. *Hadley cell, hadley regime*, page 466–466. Kluwer Academic Publishers, Dordrecht, 1987. URL: http://link.springer.com/10.1007/0-387-30749-4_81, doi:10.1007/0-387-30749-4_81.

[42] J. Feichter and T. Leisner. Climate engineering: A critical review of approaches to modify the global energy balance. *The European Physical Journal Special Topics*, 176(1):81–92, Sep 2009. URL: http://link.springer.com/10.1140/epjst/e2009-01149-8, doi:10.1140/epjst/e2009-01149-8.

[43] José P. Ferreira, Ziyu Huang, Ken-ichi Nomura, and Joseph Wang. *Impacts of Satellite Reentry on Atmospheric Composition in the Era of Mega-Constellations: Molecular Dynamics Simulations*. Dec 2022. URL: https://www.authorea.com/users/568618/articles/614399-impacts-of-satellite-reentry-on-atmospheric-composition-in-the-era-of-mega-commit=0998ed5ef789a027dcaa2b5c6c4187d4db12041b, doi:10.22541/essoar.167214515.55390432/v1.

[44] University Corporation for Atmospheric Research. Component set definitions. URL: https://www2.cesm.ucar.edu/models/cesm2/config/compsets.html.

[45] Center for Orbital and Reentry Debris Studies. Reentries. URL: https://aerospace.org/reentries.

[46] Jeff Foust. Oneweb slashes size of future satellite constellation, Jan 2021. URL: https://spacenews.com/oneweb-slashes-size-of-future-satellite-constellation/.

[47] M. Gerding, M. Alpers, U. Von Zahn, R. J. Rollason, and J. M. C. Plane. Atmospheric ca and ca + layers: Midlatitude observations and modeling. *Journal of Geophysical Research: Space Physics*, 105(A12):27131–27146, Dec 2000. URL: http://doi.wiley.com/10.1029/2000JA900088, doi:10.1029/2000ja900088.

[48] A. Gettelman, M. J. Mills, D. E. Kinnison, R. R. Garcia, A. K. Smith, D. R. Marsh, S. Tilmes, F. Vitt, C. G. Bardeen, J. McInerny, H.-L. Liu, S. C. Solomon, L. M. Polvani, L. K. Emmons, J.-F. Lamarque, J. H. Richter, A. S. Glanville, J. T. Bacmeister, A. S. Phillips, R. B. Neale, I. R. Simpson, A. K. DuVivier, A. Hodzic, and W. J. Randel. The whole atmosphere community climate model version 6 (waccm6). *Journal of Geophysical Research: Atmospheres*, 124(23):12380–12403, Dec 2019. URL: https://onlinelibrary.wiley.com/doi/10.1029/2019JD030943, doi:10.1029/2019JD030943.

[49] Robert J. Griffin. The sources and impacts of tropospheric particulate matter | learn science at scitable, 2013. URL: https://www.nature.com/scitable/knowledge/library/the-sources-and-impacts-of-tropospheric-particulate-102760478/.

[50] Northrop Grumman. Antares user's guide, Sep 2020. URL: https://www.northropgrumman.com/wp-content/uploads/Antares-User-Guide-1.pdf.

[51] J. C. Gómez Martín, C. Seaton, M. P. de Miranda, and J. M. C. Plane. The reaction between sodium hydroxide and atomic hydrogen in atmospheric and flame chemistry. *The Journal of Physical Chemistry A*, 121(40):7667–7674, Oct 2017. URL: https://pubs.acs.org/doi/10.1021/acs.jpca.7b07808, doi:10.1021/acs.jpca.7b07808.

[52] Doyle Hall, Tom Kelecy, Kris Hamada, and Maj. Dennis Stocker. Satellite maneuver detection using two-line element (tle) data. ResearchGate, Jan 2007. URL: https://www.researchgate.net/profile/Doyle-Hall/publication/242742404_Satellite_Maneuver_Detection_Using_Two-line_Elements_Data/links/02e7e53beaf5088f66000000/Satellite-Maneuver-Detection-Using-Two-line-Elements-Data.pdf.

[53] N. R. P. Harris, B. Hassler, F. Tummon, G. E. Bodeker, D. Hubert, I. Petropavlovskikh, W. Steinbrecht, J. Anderson, P. K. Bhartia, C. D. Boone, A. Bourassa, S. M. Davis, D. Degenstein, A. Delcloo, S. M. Frith, L. Froidevaux, S. Godin-Beekmann, N. Jones, M. J. Kurylo, E. Kyrölä, M. Laine, S. T. Leblanc, J.-C. Lambert, B. Liley, E. Mahieu, A. Maycock, M. de Mazière, A. Parrish, R. Querel, K. H. Rosenlof, C. Roth, C. Sioris, J. Staehelin, R. S. Stolarski, R. Stübi, J. Tamminen, C. Vigouroux, K. A. Walker, H. J. Wang, J. Wild, and J. M. Zawodny. Past changes in the vertical distribution of ozone – part 3: Analysis and interpretation of trends. *Atmospheric Chemistry and Physics*, 15(17):9965–9982, 2015. URL: https://acp.copernicus.org/articles/15/9965/2015/, doi:10.5194/acp-15-9965-2015.

[54] J. M. Haywood and K. P. Shine. The effect of anthropogenic sulfate and soot aerosol on the clear sky planetary radiation budget. *Geophysical Research Letters*, 22(5):603–606, Mar 1995. URL: http://doi.wiley.com/10.1029/95GL00075, doi:10.1029/95GL00075.

[55] Jim M. Haywood, Andy Jones, Nicolas Bellouin, and David Stephenson. Asymmetric forcing from stratospheric aerosols impacts sahelian rainfall. *Nature Climate Change*, 3(7):660–665, Jul 2013. URL: http://www.nature.com/articles/nclimate1857, doi:10.1038/nclimate1857.

[56] Magdalena Helmer, John M. C. Plane, Jun Qian, and Chester S. Gardner. A model of meteoric iron in the upper atmosphere. *Journal of Geophysical Research: Atmospheres*, 103(D9):10913–10925, 1998. URL: https://agupubs.onlinelibrary.wiley.com/doi/abs/10.1029/97JD03075, arXiv:https://agupubs.onlinelibrary.wiley.com/doi/pdf/10.1029/97JD03075, doi:https://doi.org/10.1029/97JD03075.

[57] J. Marvin Herndon. Aluminum poisoning of humanity and earth's biota by clandestine geoengineering activity: implications for india. *Current Science*, 108(12):2173–2177, 2015. URL: https://www.jstor.org/stable/24905652.

[58] S.M. Hunt, M. Oppenheim, S. Close, P.G. Brown, F. McKeen, and M. Minardi. Determination of the meteoroid velocity distribution at the earth using high-gain radar. *Icarus*, 168(1):34–42, Mar 2004. URL: https://linkinghub.elsevier.com/retrieve/pii/S0019103503002586, doi:10.1016/j.icarus.2003.08.006.

[59] Michael J. Iacono, Jennifer S. Delamere, Eli J. Mlawer, Mark W. Shephard, Shepard A. Clough, and William D. Collins. Radiative forcing by long-lived greenhouse gases: Calculations with the aer radiative transfer models. *Journal of Geophysical Research*, 113(D13):D13103, Jul 2008. URL: http://doi.wiley.com/10.1029/2008JD009944, doi:10.1029/2008JD009944.

[60] Michael J. Iacono, Eli J. Mlawer, Shepard A. Clough, and Jean-Jacques Morcrette. Impact of an improved longwave radiation model, rrtm, on the energy budget and thermodynamic properties of the ncar community climate model, ccm3. *Journal of Geophysical Research: Atmospheres*, 105(D11):14873–14890, Jun 2000. URL: http://doi.wiley.com/10.1029/2000JD900091, doi:10.1029/2000JD900091.

[61] Asha Jain and Daniel Hastings. A model of space debris aluminum injection in the atmosphere. Paris, France, Sep 2022. International Astronautical Federation (IAF).

[62] Asha Jain and Daniel E. Hastings. Comparing meteor and rocket atmospheric emissions and their effects to space debris reentries: Towards understanding the atmospheric impact of space debris disposal. In *ASCEND 2022*, Las Vegas, Nevada & Online, Oct 2022. American Institute of Aeronautics and Astronautics. URL: https://arc.aiaa.org/doi/10.2514/6.2022-4224, doi:10.2514/6.2022-4224.

[63] Alexander D. James, James S. A. Brooke, Thomas P. Mangan, Thomas F. Whale, John M. C. Plane, and Benjamin J. Murray. Nucleation of nitric acid hydrates in polar stratospheric clouds by meteoric material. *Atmospheric Chemistry and Physics*, 18(7):4519–4531, Apr 2018. URL: https://acp.copernicus.org/articles/18/4519/2018/, doi:10.5194/acp-18-4519-2018.

[64] Duseong S. Jo, Rokjin J. Park, Jaein I. Jeong, Gabriele Curci, Hyung-Min Lee, and Sang-Woo Kim. *Key factors affecting single scattering albedo calculation: Implications for aerosol climate forcing*. Dec 2017. URL: https://acp.copernicus.org/preprints/acp-2017-1104/, doi:10.5194/acp-2017-1104.

[65] Karen L. Jones, Asha K. Jain, and Grant Cates. Green and circular space systems through environmental life cycle assessments. Austin, TX, Mar 2023. STM 2023 Conference. URL: https://web.tresorit.com/l/b2cgc#8T1h86yuZ2SdwScwfc_vtA&viewer=DcJLxyQkDlsgVsMPnHBrutChHI08AAZX.

[66] Ronny Kanzler, Bent Fritsche, Tobias Lips, Breslau Andreas, Adam Pagan, Georg Herdrich, Martin Spel, Silvia Sanvido, and Stijn Lemmens. Scarab4 – extension of the high-fidelity re-entry break-up simulation software based on new measurement types. Darmstadt, Germany, Apr 2021. ESA Space Debris Office. URL: https://conference.sdo.esoc.esa.int/proceedings/sdc8/paper/13/SDC8-paper13.pdf.

[67] Ziming Ke, Xiaohong Liu, Mingxuan Wu, Yunpeng Shan, and Yang Shi. Improved dust representation and impacts on dust transport and radiative effect in cam5. *Journal of Advances in Modeling Earth Systems*, 14(7), Jul 2022. URL: https://onlinelibrary.wiley.com/doi/10.1029/2021MS002845, doi:10.1029/2021MS002845.

[68] J. T. Kiehl and Kevin E. Trenberth. Earth's annual global mean energy budget. *Bulletin of the American Meteorological Society*, 78(2):197–208, Feb 1997. URL: http://journals.ametsoc.org/doi/10.1175/1520-0477(1997)078<0197:EAGMEB>2.0.CO;2, doi:10.1175/1520-0477(1997)078<0197:EAGMEB>2.0.CO;2.

[69] M Klöwer, M R Allen, D S Lee, S R Proud, L Gallagher, and A Skowron. Quantifying aviation's contribution to global warming. *Environmental Research Letters*, 16(10):104027, Oct 2021. URL: https://iopscience.iop.org/article/10.1088/1748-9326/ac286e, doi:10.1088/1748-9326/ac286e.

[70] NOAA Chemical Sciences Laboratory (CSL). Noaa csl: Scientific assessment of ozone depletion: 2014. URL: https://csl.noaa.gov/assessments/ozone/2014/.

[71] Jean Lachaud, Tom van Eekelen, James B Scoggins, Thierry E Magin, and Nagi N Mansour. Detailed chemical equilibrium model for porous ablative materials. *International Journal of Heat and Mass Transfer*, 90:1034–1045, 2015.

[72] John J Lamb and Sidney W Benson. Some kinetic and thermochemical aspects of sodium in the stratosphere. *Journal of Geophysical Research: Atmospheres*, 91(D8):8683–8689, 1986.

[73] Erik J. L. Larson, Robert W. Portmann, Karen H. Rosenlof, David W. Fahey, John S. Daniel, and Martin N. Ross. Global atmospheric response to emissions from a proposed reusable space launch system: Atmospheric response to rocket emissions. *Earth's Future*, 5(1):37–48, Jan 2017. URL: http://doi.wiley.com/10.1002/2016EF000399, doi:10.1002/2016ef000399.

[74] Andy Lawrence, Meredith L. Rawls, Moriba Jah, Aaron Boley, Federico Di Vruno, Simon Garrington, Michael Kramer, Samantha Lawler, James Lowenthal, Jonathan McDowell, and Mark McCaughrean. The case for space environmentalism. *Nature Astronomy*, 6(4):428–435, Apr 2022. URL: https://www.nature.com/articles/s41550-022-01655-6, doi:10.1038/s41550-022-01655-6.

[75] Jan Laštovička, Stanley C. Solomon, and Liying Qian. Trends in the neutral and ionized upper atmosphere. *Space Science Reviews*, 168(1–4):113–145, Jun 2012. URL: http://link.springer.com/10.1007/s11214-011-9799-3, doi:10.1007/s11214-011-9799-3.

[76] D.S. Lee, D.W. Fahey, A. Skowron, M.R. Allen, U. Burkhardt, Q. Chen, S.J. Doherty, S. Freeman, P.M. Forster, J. Fuglestvedt, A. Gettelman, R.R. De León, L.L. Lim, M.T. Lund, R.J. Millar, B. Owen, J.E. Penner, G. Pitari, M.J. Prather, R. Sausen, and L.J. Wilcox. The contribution of global aviation to anthropogenic climate forcing for 2000 to 2018. *Atmospheric Environment*, 244:117834, Jan 2021. URL: https://linkinghub.elsevier.com/retrieve/pii/S1352231020305689, doi:10.1016/j.atmosenv.2020.117834.

[77] J.C. Liou, M Matney, A Vavrin, A Manis, and D Gates. Nasa odpo's large constellation study, Sep 2018. URL: https://www.orbitaldebris.jsc.nasa.gov/quarterly-news/pdfs/odqnv22i3.pdf.

[78] T. Lips, B. Fritsche, R. Kanzler, T. Schleutker, A. Gülhan, B. Bonvoisin, T. Soares, and G. Sinnema. About the demisability of propellant tanks during atmospheric re-entry from leo. *Journal of Space Safety Engineering*, 4(2):99–104, Jun 2017. URL: https://linkinghub.elsevier.com/retrieve/pii/S2468896717300484, doi:10.1016/j.jsse.2017.07.004.

[79] Han-Li Liu. Whole atmosphere community climate model - extended (waccm-x): Development, validation, and capabilities, Jun 2018. URL: https://www2.hao.ucar.edu/sites/default/files/2021-12/LiuCedarWaccmX2018.pdf.

[80] X. Liu, R. C. Easter, S. J. Ghan, R. Zaveri, P. Rasch, X. Shi, J.-F. Lamarque, A. Gettelman, H. Morrison, F. Vitt, A. Conley, S. Park, R. Neale, C. Hannay, A. M. L. Ekman, P. Hess, N. Mahowald, W. Collins, M. J. Iacono, C. S. Bretherton, M. G. Flanner, and D. Mitchell. Toward a minimal representation of aerosols in climate models: description and evaluation in the community atmosphere model cam5, supplement document. *Geoscientific Model Development*, 5(3):709–739, May 2012. URL: https://gmd.copernicus.org/articles/5/709/2012/, doi:10.5194/gmd-5-709-2012.

[81] X. Liu, P.-L. Ma, H. Wang, S. Tilmes, B. Singh, R. C. Easter, S. J. Ghan, and P. J. Rasch. Description and evaluation of a new four-mode version of the modal aerosol module (mam4) within version 5.3 of the community atmosphere model. *Geoscientific Model Development*, 9(2):505–522, Feb 2016. URL: https://gmd.copernicus.org/articles/9/505/2016/gmd-9-505-2016.html, doi:10.5194/gmd-9-505-2016.

[82] Xiaohong Liu. Email communication with dr.xiaohong liu at the university of texas at a&m, Mar 2023.

[83] U. Lohmann. *AEROSOLS | Aerosol–Cloud Interactions and Their Radiative Forcing*, page 17–22. Elsevier, 2015. URL: https://linkinghub.elsevier.com/retrieve/pii/B9780123822253000529, doi:10.1016/B978-0-12-382225-3.00052-9.

[84] Christopher M Maloney, Robert W Portmann, Martin N Ross, and Karen H Rosenlof. The climate and ozone impacts of black carbon emissions from global rocket launches. *Journal of Geophysical Research: Atmospheres*, 127(12), Jun 2022. URL: https://onlinelibrary.wiley.com/doi/10.1029/2021JD036373, doi:10.1029/2021JD036373.

[85] Daniel R. Marsh, Michael J. Mills, Douglas E. Kinnison, Jean-Francois Lamarque, Natalia Calvo, and Lorenzo M. Polvani. Climate change from 1850 to 2005 simulated in cesm1(waccm). *Journal of Climate*, 26(19):7372–7391, Oct 2013. URL: https://journals.ametsoc.org/view/journals/clim/26/19/jcli-d-12-00558.1.xml, doi:10.1175/JCLI-D-12-00558.1.

[86] James Vedda Martin Ross. The policy and science of rocket emissions, Mar 2018. URL: https://csps.aerospace.org/papers/policy-and-science-rocket-emissions.

[87] N. McBride, S.F. Green, and J.A.M. McDonnell. Meteoroids and small sized debris in low earth orbit and at 1 au: Results of recent modelling. *Advances in Space Research*, 23(1):73–82, Jan 1999. URL: https://linkinghub.elsevier.com/retrieve/pii/S0273117798002324, doi:10.1016/S0273-1177(98)00232-4.

[88] Jonathan McDowell. Gcat: General catalog of artifical space objects, 5 2023. URL: https://planet4589.org/space/gcat/.

[89] William J. McNeil, Shu T. Lai, and Edmond Murad. Differential ablation of cosmic dust and implications for the relative abundances of atmospheric metals. *Journal of Geophysical Research: Atmospheres*, 103(D9):10899–10911, 1998. doi:10.1029/98jd00282.

[90] L. Megner, D. E. Siskind, M. Rapp, and J. Gumbel. Global and temporal distribution of meteoric smoke: A two-dimensional simulation study. *Journal of Geophysical Research*, 113(D3):D03202, Feb 2008. URL: http://doi.wiley.com/10.1029/2007JD009054, doi:10.1029/2007JD009054.

[91] R. L. Miller, I. Tegen, and Jan Perlwitz. Surface radiative forcing by soil dust aerosols and the hydrologic cycle: Dust forcing and the hydrologic cycle. *Journal of Geophysical Research: Atmospheres*, 109(D4):n/a–n/a, Feb 2004. URL: http://doi.wiley.com/10.1029/2003JD004085, doi:10.1029/2003JD004085.

[92] Shraeya Mithal and Dan Rutherford. Icao's 2050 net-zero co2 goal for international aviation, Jan 2023. URL: https://theicct.org/publication/global-aviation-icao-net-zero-goal-jan23/.

[93] Eli J. Mlawer, Steven J. Taubman, Patrick D. Brown, Michael J. Iacono, and Shepard A. Clough. Radiative transfer for inhomogeneous atmospheres: Rrtm, a validated correlated-k model for the longwave. *Journal of Geophysical Research: Atmospheres*, 102(D14):16663–16682, Jul 1997. URL: http://doi.wiley.com/10.1029/97JD00237, doi:10.1029/97JD00237.

[94] Mario J. Molina, Luisa T. Molina, Renyi Zhang, Roger F. Meads, and Darryl D. Spencer. The reaction of clono 2 with hcl on aluminum oxide. *Geophysical Research Letters*, 24(13):1619–1622, Jul 1997. URL: http://doi.wiley.com/10.1029/97GL01560, doi:10.1029/97gl01560.

[95] Stephen A. Montzka, Geoffrey S. Dutton, Robert W. Portmann, Martyn P. Chipperfield, Sean Davis, Wuhu Feng, Alistair J. Manning, Eric Ray, Matthew Rigby, Bradley D. Hall, Carolina Siso, J. David Nance, Paul B. Krummel, Jens Mühle, Dickon Young, Simon O'Doherty, Peter K. Salameh, Christina M. Harth, Ronald G. Prinn, Ray F. Weiss, James W. Elkins, Helen Walter-Terrinoni, and Christina Theodoridi. A decline in global cfc-11 emissions during 2018 - 2019. *Nature*, 590(7846):428–432,

Feb 2021. URL: https://www.nature.com/articles/s41586-021-03260-5, doi:10.1038/s41586-021-03260-5.

[96] Dave Mosher. Spacex may be a $120 billion company if its starlink global internet service takes off, morgan stanley research predicts. URL: https://www.businessinsider.com/spacex-future-multibillion-dollar-valuation-starlink-internet-morgan-stanley-2019-

[97] Edmond Murad, William Swider, and Sidney W Benson. Possible role for metals in stratospheric chlorine chemistry. *Nature*, 289(5795):273–274, 1981.

[98] D. M. Murphy, K. D. Froyd, J. P. Schwarz, and J. C. Wilson. Observations of the chemical composition of stratospheric aerosol particles. *Quarterly Journal of the Royal Meteorological Society*, 140(681):1269–1278, Apr 2014. URL: https://onlinelibrary.wiley.com/doi/10.1002/qj.2213, doi:10.1002/qj.2213.

[99] D. M. Murphy, D. S. Thomson, and M. J. Mahoney. In situ measurements of organics, meteoritic material, mercury, and other elements in aerosols at 5 to 19 kilometers. *Science*, 282(5394):1664–1669, Nov 1998. URL: https://www.science.org/doi/10.1126/science.282.5394.1664, doi:10.1126/science.282.5394.1664.

[100] et al. Myhre, G. Anthropogenic and natural radiative forcing. *Climate Change 2013: The Physical Science Basis. Contribution of Working Group I to the Fifth Assessment Report of the Intergovernmental Panel on Climate Change*.

[101] United Nations. Convention on registration of objects launched into outer space, 1974. URL: https://www.unoosa.org/oosa/en/ourwork/spacelaw/treaties/introregistration-convention.html.

[102] United Nations. Compendium: Space debris mitigation standards adopted by states and international organizations, Feb 2019. URL: https://www.unoosa.org/documents/pdf/spacelaw/sd/Space_Debris_Compendium_COPUOS_25_Feb_2019p.pdf.

[103] Brian Neuenfeldt and William Henderson. *A Survey of Uncontrolled Satellite Reentry and Impact Prediction*. PhD thesis, Naval Postgraduate School, Monterey, California, Sep 1993. URL: https://apps.dtic.mil/sti/pdfs/ADA274903.pdf.

[104] Brian D. Neuenfeldt and William K. Henderson. *A Survey of Uncontrolled Satellite Reentry and Impact Prediction*. PhD thesis, Naval Postgraduate School, Monterey, California, Jan 1994. URL: https://apps.dtic.mil/sti/pdfs/ADA274903.pdf.

[105] M. Nicolet and A. C. Aikin. The formation of the d region of the ionosphere. *Journal of Geophysical Research*, 65(5):1469–1483, May 1960. URL: http://doi.wiley.com/10.1029/JZ065i005p01469, doi:10.1029/JZ065i005p01469.

[106] Edward D. Palik. *Handbook of optical constants of solids*. Academic press, Orlando San Diego New York, 1985.

[107] Seong-Hyeon Park, Javier Navarro Laboulais, Pénélope Leyland, and Stefano Mischler. Re-entry survival analysis and ground risk assessment of space debris considering by-products generation. *Acta Astronautica*, 179:604–618, Feb 2021. URL: https://linkinghub.elsevier.com/retrieve/pii/S0094576520305737, doi:10.1016/j.actaastro.2020.09.034.

[108] Seong-Hyeon Park and Gisu Park. Reentry trajectory and survivability estimation of small space debris with catalytic recombination. *Advances in Space Research*, 60(5):893–906, Sep 2017. URL: https://linkinghub.elsevier.com/retrieve/pii/S0273117717303332, doi:10.1016/j.asr.2017.05.004.

[109] J.M.C. Plane. *MESOSPHERE | Metal Layers*, page 430–435. Elsevier, 2015. URL: https://linkinghub.elsevier.com/retrieve/pii/B9780123822253002188, doi:10.1016/B978-0-12-382225-3.00218-8.

[110] John M. C. Plane. Atmospheric chemistry of meteoric metals. *Chemical Reviews*, 103(12):4963–4984, Dec 2003. URL: https://pubs.acs.org/doi/10.1021/cr0205309, doi:10.1021/cr0205309.

[111] John M. C. Plane, Shane M. Daly, Wuhu Feng, Michael Gerding, and Juan Carlos Gómez Martín. Meteor-ablated aluminum in the mesosphere-lower thermosphere. *Journal of Geophysical Research: Space Physics*, 126(2), Feb 2021. URL: https://onlinelibrary.wiley.com/doi/10.1029/2020JA028792, doi:10.1029/2020ja028792.

[112] John M. C. Plane, Shane M. Daly, Wuhu Feng, Michael Gerding, and Juan Carlos Gómez Martín. Meteor-ablated aluminum in the mesosphere-lower thermosphere. *Journal of Geophysical Research: Space Physics*, 126(2), Feb 2021. URL: https://onlinelibrary.wiley.com/doi/10.1029/2020JA028792, doi:10.1029/2020JA028792.

[113] John M. C. Plane, Wuhu Feng, and Erin C. M. Dawkins. The mesosphere and metals: Chemistry and changes. *Chemical Reviews*, 115(10):4497–4541, May 2015. doi:10.1021/cr500501m.

[114] John M. C. Plane, Juan Carlos Gómez-Martín, Wuhu Feng, and Diego Janches. Silicon chemistry in the mesosphere and lower thermosphere. *Journal of Geophysical Research: Atmospheres*, 121(7):3718–3728, Apr 2016. URL: https://onlinelibrary.wiley.com/doi/10.1002/2015JD024691, doi:10.1002/2015JD024691.

[115] Y Prevereaud, Jean-luc Vérant, JM Moschetta, F Sourgen, and M Blanchard. Debris aerodynamic interactions during uncontrolled atmospheric reentry. In *AIAA atmospheric flight mechanics conference*, page 4582, 2012.

[116] Kristen J. Price, Francesco Panerai, Colby G. Borchetta, J. Matthew Hardy, Alexandre Martin, and Sean C.C. Bailey. Arc-jet measurements of low-density ablator spallation. *Experimental Thermal and Fluid Science*, 133:110544, May 2022. URL: https:

//linkinghub.elsevier.com/retrieve/pii/S0894177721001874, doi:10.1016/j.expthermflusci.2021.110544.

[117] Tereza Pultarova, Elizabeth HowellContributions from Daisy Dobrijevic, and Adam Mann last updated. Starlink satellites: Everything you need to know about the controversial internet megaconstellation, Apr 2022. URL: https://www.space.com/spacex-starlink-satellites.html.

[118] Jason Rainbow. Wyler raises $50 million for "sustainable" megaconstellation, Feb 2022. URL: https://spacenews.com/wyler-raises-50-million-for-sustainable-megaconstellation/.

[119] T. E. Ramabhadran, T. W. Peterson, and J. H. Seinfeld. Dynamics of aerosol coagulation and condensation. *AIChE Journal*, 22(5):840–851, Sep 1976. URL: https://onlinelibrary.wiley.com/doi/10.1002/aic.690220505, doi:10.1002/aic.690220505.

[120] Thomas Reichler, Martin Dameris, and Robert Sausen. Determining the tropopause height from gridded data. *Geophysical Research Letters*, 30(20):2003GL018240, Oct 2003. URL: https://onlinelibrary.wiley.com/doi/abs/10.1029/2003GL018240, doi:10.1029/2003GL018240.

[121] Brandon Rhodes. Skyfield: High precision research-grade positions for planets and Earth satellites generator. Astrophysics Source Code Library, record ascl:1907.024, July 2019. arXiv:1907.024.

[122] David L. Roberts. Climate sensitivity to black carbon aerosol from fossil fuel combustion. *Journal of Geophysical Research*, 109(D16):D16202, 2004. URL: http://doi.wiley.com/10.1029/2004JD004676, doi:10.1029/2004JD004676.

[123] M. N. Ross, D. W. Toohey, W. T. Rawlins, E. C. Richard, K. K. Kelly, A. F. Tuck, M. H. Proffitt, D. E. Hagen, A. R. Hopkins, P. D. Whitefield, J. R. Benbrook, and W. R. Sheldon. Observation of stratospheric ozone depletion associated with delta ii rocket emissions. *Geophysical Research Letters*, 27(15):2209–2212, Aug 2000. URL: http://doi.wiley.com/10.1029/1999GL011159, doi:10.1029/1999GL011159.

[124] Martin Ross and A. Vedda, James. *The Policy and Science of Rocket Emissions*. The Aerospace Corporation, Apr 2018. URL: https://aerospace.org/sites/default/files/2018-05/RocketEmissions_0.pdf.

[125] Martin N. Ross and Patti M. Sheaffer. Radiative forcing caused by rocket engine emissions. *Earth's Future*, 2(4):177–196, Apr 2014. doi:10.1002/2013ef000160.

[126] James M Russell III, Pingping Rong, Mark E Hervig, David E Siskind, Michael H Stevens, Scott M Bailey, and Jörg Gumbel. Analysis of northern midlatitude noctilucent cloud occurrences using satellite data and modeling. *Journal of Geophysical Research: Atmospheres*, 119(6):3238–3250, 2014.

[127] Robert G. Ryan, Eloise A. Marais, Chloe J. Balhatchet, and Sebastian D. Eastham. Impact of rocket launch and space debris air pollutant emissions on stratospheric ozone and global climate. *Earth's Future*, 10(6), Jun 2022. URL: https://onlinelibrary.wiley.com/doi/10.1029/2021EF002612, doi:10.1029/2021ef002612.

[128] Robert G. Ryan, Eloise Ann Marais, Chloe J. Balhatchet, and Sebastian David Eastham. *Impact of Rocket Launch and Space Debris Air Pollutant Emissions on Stratospheric Ozone and Global Climate*. Feb 2022. URL: http://www.essoar.org/doi/10.1002/essoar.10510460.1, doi:10.1002/essoar.10510460.1.

[129] Tate Ryan-Mosley, Erin Winick, and Konstantin Kakaes. The number of satellites orbiting earth could quintuple in the next decade. *MIT Technology Review*, Jun 2019. URL: https://www.technologyreview.com/2019/06/26/755/satellite-constellations-orbiting-earth-quintuple/.

[130] Ross J. Salawitch, Steven C. Wofsy, and Michael B. McElroy. Influence of polar stratospheric clouds on the depletion of antarctic ozone. *Geophysical Research Letters*, 15(8):871–874, Aug 1988. URL: http://doi.wiley.com/10.1029/GL015i008p00871, doi:10.1029/GL015i008p00871.

[131] N. Saleema, M. Farzaneh, R.W. Paynter, and D.K. Sarkar. Prevention of ice accretion on aluminum surfaces by enhancing their hydrophobic properties. *Journal of Adhesion Science and Technology*, 25(1–3):27–40, Jan 2011. URL: http://www.tandfonline.com/doi/abs/10.1163/016942410X508064, doi:10.1163/016942410x508064.

[132] R. W. Saunders, S. Dhomse, W. S. Tian, M. P. Chipperfield, and J. M. C. Plane. Interactions of meteoric smoke particles with sulphuric acid in the earth's stratosphere. *Atmospheric Chemistry and Physics*, 12(10):4387–4398, May 2012. URL: https://acp.copernicus.org/articles/12/4387/2012/, doi:10.5194/acp-12-4387-2012.

[133] Johannes Schneider, Ralf Weigel, Thomas Klimach, Antonis Dragoneas, Oliver Appel, Andreas Hünig, Sergej Molleker, Franziska Köllner, Hans-Christian Clemen, Oliver Eppers, Peter Hoppe, Peter Hoor, Christoph Mahnke, Martina Krämer, Christian Rolf, Jens-Uwe Groob, Andreas Zahn, Florian Obersteiner, Fabrizio Ravegnani, Alexey Ulanovsky, Hans Schlager, Monika Scheibe, Glenn S. Diskin, Joshua P. DiGangi, John B. Nowak, Martin Zoger, and Stephan Borrmann. Aircraft-based observation of meteoric material in lower-stratospheric aerosol particles between 15 and 68° n. *Atmospheric Chemistry and Physics*, 21(2):989–1013, Jan 2021. URL: https://acp.copernicus.org/articles/21/989/2021/, doi:10.5194/acp-21-989-2021.

[134] Tapio Schneider, Tobias Bischoff, and Gerald H. Haug. Migrations and dynamics of the intertropical convergence zone. *Nature*, 513(7516):45–53, Sep 2014. URL: http://www.nature.com/articles/nature13636, doi:10.1038/nature13636.

[135] Leonard Schulz and Karl-Heinz Glassmeier. On the anthropogenic and natural injection of matter into earth's atmosphere. *Advances in Space Research*, 67(3):1002–1025, Feb 2021. URL: https://linkinghub.elsevier.com/retrieve/pii/S0273117720307663, doi:10.1016/j.asr.2020.10.036.

[136] Rebecca H. Schwantes, Louisa K. Emmons, John J. Orlando, Mary C. Barth, Geoffrey S. Tyndall, Samuel R. Hall, Kirk Ullmann, Jason M. St. Clair, Donald R. Blake, Armin Wisthaler, and Thao Paul V. Bui. Comprehensive isoprene and terpene gas-phase chemistry improves simulated surface ozone in the southeastern us. *Atmospheric Chemistry and Physics*, 20(6):3739–3776, Mar 2020. URL: https://acp.copernicus.org/articles/20/3739/2020/, doi:10.5194/acp-20-3739-2020.

[137] Yi-ang Shi, Bai-lin Zha, Zhen-sheng Sun, Qing Shen, Wen-bo Miao, and Yong Gao. Air plasma ablation/erosion test for 4d c/c composites used in the throat of solid rocket motor. *Ceramics International*, 48(11):15582–15593, Jun 2022. URL: https://linkinghub.elsevier.com/retrieve/pii/S0272884222004898, doi:10.1016/j.ceramint.2022.02.092.

[138] Jamie D. Shutler, Xiaoyu Yan, Ingrid Cnossen, Leonard Schulz, Andrew J. Watson, Karl-Heinz Glaßmeier, Naomi Hawkins, and Hitoshi Nasu. Atmospheric impacts of the space industry require oversight. *Nature Geoscience*, 15(8):598–600, Aug 2022. URL: https://www.nature.com/articles/s41561-022-01001-5, doi:10.1038/s41561-022-01001-5.

[139] M Smirnova, E Belova, S Kirkwood, and Nicholas Mitchell. Polar mesosphere summer echoes with esrad, kiruna, sweden: Variations and trends over 1997–2008. *Journal of atmospheric and solar-terrestrial physics*, 72(5-6):435–447, 2010.

[140] K. L. Smith, R. R. Neely, D. R. Marsh, and L. M. Polvani. The specified chemistry whole atmosphere community climate model (sc-waccm). *Journal of Advances in Modeling Earth Systems*, 6(3):883–901, Sep 2014. URL: http://doi.wiley.com/10.1002/2014MS000346, doi:10.1002/2014MS000346.

[141] Tyrrel W Smith, John R Edwards, and Daniel Pilson. Summary of the impact of launch vehicle exhaust and deorbiting space and meteorite debris on stratospheric ozone. Technical report, Trw Inc Redondo Beach Ca Electronics And Technology Operations, 1999.

[142] Tyrrel W Smith, John R. Edwards, and Daniel Pilson. *Summary of the Impact of Launch Vehicle Exhaust and Deorbiting Space and Meteorite Debris on Stratospheric Ozone*. TRW INC REDONDO BEACH CA ELECTRONICS AND TECHNOLOGY OPERATIONS, 1999. URL: https://apps.dtic.mil/sti/citations/ADA414306.

[143] G. P. Stiller. An enhanced hno 3 second maximum in the antarctic midwinter upper stratosphere 2003. *Journal of Geophysical Research*, 110(D20):D20303, 2005. URL: http://doi.wiley.com/10.1029/2005JD006011, doi:10.1029/2005JD006011.

[144] Susann Tegtmeier, James Anstey, Sean Davis, Rossana Dragani, Yayoi Harada, Ioana Ivanciu, Robin Pilch Kedzierski, Kirstin Krüger, Bernard Legras, Craig Long, James S. Wang, Krzysztof Wargan, and Jonathon S. Wright. Temperature and tropopause characteristics from reanalyses data in the tropical tropopause layer. *Atmospheric Chemistry and Physics*, 20(2):753–770, Jan 2020. URL: https://acp.copernicus.org/articles/20/753/2020/, doi:10.5194/acp-20-753-2020.

[145] Etienne Terrenoire, Didier Hauglustaine, Yann Cohen, Anne Cozic, Richard Valorso, Franck Lefèvre, and Sigrun Matthes. *Impact of present and future aircraft NO_x and aerosol emissions on atmospheric composition and associated direct radiative forcing of climate*. Atmospheric Chemistry and Physics Discussions, Apr 2022. URL: https://acp.copernicus.org/preprints/acp-2022-222/, doi:10.5194/acp-2022-222.

[146] Simone Tilmes, Michael J. Mills, Yunqian Zhu, Charles G. Bardeen, Francis Vitt, Pengfei Yu, David Fillmore, Xiaohong Liu, Brian Toon, and Terry Deshler. *Description and performance of the CARMA sectional aerosol microphysical model in CESM2*. Apr 2023. URL: https://gmd.copernicus.org/preprints/gmd-2023-79/, doi:10.5194/gmd-2023-79.

[147] Engineering Toolbox. Metals and alloys - melting temperatures, 2005. URL: https://www.engineeringtoolbox.com/melting-temperature-metals-d_860.html.

[148] Owen B. Toon and Richard P. Turco. Polar stratospheric clouds and ozone depletion. *Scientific American*, 264(6):68–75, 1991. URL: https://www.jstor.org/stable/24936942.

[149] R. P. Turco, O. B. Toon, C. Park, R. C. Whitten, J. B. Pollack, and P. Noerdlinger. Tunguska meteor fall of 1908: Effects on stratospheric ozone. *Science*, 214(4516):19–23, Oct 1981. URL: https://www.science.org/doi/10.1126/science.214.4516.19, doi:10.1126/science.214.4516.19.

[150] UCAR. Aerosols. URL: https://wiki.ucar.edu/display/camchem/Aerosols.

[151] UCAR. Cam6.3 namelist definitions, Sep 2020. URL: https://www2.cesm.ucar.edu/models/cesm2/settings/current/cam_nml.html.

[152] Advanced Research Computing UCAR. Ucar allocations. URL: https://arc.ucar.edu/knowledge_base/74317835.

[153] David Vallado and Paul Crawford. Sgp4 orbit determination. In *AIAA/AAS Astrodynamics Specialist Conference and Exhibit*, Honolulu, Hawaii, Aug 2008. American Institute of Aeronautics and Astronautics. URL: https://arc.aiaa.org/doi/10.2514/6.2008-6770, doi:10.2514/6.2008-6770.

[154] Massimiliano L. Vasile, Edmondo Minisci, Romain Serra, James Beck, and Ian Holbrough. Analysis of the de-orbiting and re-entry of space objects with high area to mass ratio. In *AIAA/AAS Astrodynamics Specialist Conference*, Long Beach, California, Sep 2016. American Institute of Aeronautics and Astronautics. URL: https://arc.aiaa.org/doi/10.2514/6.2016-5678, doi:10.2514/6.2016-5678.

[155] Christiane Voigt, Jochen Schreiner, Andreas Kohlmann, Peter Zink, Konrad Mauersberger, Niels Larsen, Terry Deshler, Chris Kröger, Jim Rosen, Alberto Adriani, Francesco Cairo, Guido Di Donfrancesco, Maurizio Viterbini, Joelle Ovarlez, Henri Ovarlez, Christine David, and Andreas Dörnbrack. Nitric acid trihydrate (nat) in polar stratospheric clouds. *Science*, 290(5497):1756–1758, Dec 2000.

URL: https://www.science.org/doi/10.1126/science.290.5497.1756, doi:10.1126/science.290.5497.1756.

[156] Christiane Voigt, Ulrich Schumann, Kaspar Graf, and Klaus-Dirk Gottschaldt. Impact of rocket exhaust plumes on atmospheric composition and climate – an overview. In L DeLuca, C Bonnal, O Haidn, and S M Frolov, editors, *EUCASS 2011*, volume 4 of *Progress in Propulsion Physics*, pages 3–16, 2013. URL: https://elib.dlr.de/86521/.

[157] D. K. Weisenstein, D. W. Keith, and J. A. Dykema. Solar geoengineering using solid aerosol in the stratosphere. *Atmospheric Chemistry and Physics*, 15(20):11835–11859, Oct 2015. URL: https://acp.copernicus.org/articles/15/11835/2015/, doi:10.5194/acp-15-11835-2015.

[158] P. O. Wennberg, R. C. Cohen, R. M. Stimpfle, J. P. Koplow, J. G. Anderson, R. J. Salawitch, D. W. Fahey, E. L. Woodbridge, E. R. Keim, R. S. Gao, C. R. Webster, R. D. May, D. W. Toohey, L. M. Avallone, M. H. Proffitt, M. Loewenstein, J. R. Podolske, K. R. Chan, and S. C. Wofsy. Removal of stratospheric o 3 by radicals: In situ measurements of oh, ho 2 , no, no 2 , clo, and bro. *Science*, 266(5184):398–404, Oct 1994. URL: https://www.science.org/doi/10.1126/science.266.5184.398, doi:10.1126/science.266.5184.398.

[159] Mark Whiteside and J. Marvin Herndon. Previously unacknowledged potential factors in catastrophic bee and insect die-off arising from coal fly ash geoengineering. *Asian Journal of Biology*, 6(4):1–13, Aug 2018. URL: https://journalajob.com/index.php/AJOB/article/view/16, doi:10.9734/ajob/2018/43268.

[160] Ziniu Wu, Ruifeng Hu, Xi Qu, Xiang Wang, and Zhe Wu. Space debris reentry analysis methods and tools. *Chinese Journal of Aeronautics*, 24(4):387–395, Aug 2011. URL: https://linkinghub.elsevier.com/retrieve/pii/S1000936111600460, doi:10.1016/S1000-9361(11)60046-0.

[161] Junri Zhao, Weichun Ma, Kelsey R. Bilsback, Jeffrey R. Pierce, Shengqian Zhou, Ying Chen, Guipeng Yang, and Yan Zhang. *Simulating the radiative forcing of oceanic dimethylsulfide (DMS) in Asia based on Machine learning estimates*. Mar 2022. URL: https://acp.copernicus.org/preprints/acp-2022-3/acp-2022-3.pdf, doi:10.5194/acp-2022-3.

Appendix A

Modifications to CESM User Configuration Files

A.1 User Configuration File (*user_nl_cam*) Contents

The user configuration file, known as *user_nl_cam*, allows users of CAM to modify parameters and set emission files. In this file, double run calls are also specified with *rad_diag* variables. Output data is controlled by *fincl*. Surface emissions are controlled by *srf_emis_specifier* and 3D emissions are controlled by *ext_frc_specifier*. For further reference of namelist variables that can be modified in this file, see [151].

The contents of the *user_nl_cam* for the Base Case and Case 2 are shown below in their own subsections. These serve to show that perturbed cases are identical to the base case, except for the reentry dust emissions and the corresponding double radiation calls.

A.1.1 Base Case

```
1 ! Users should add all user specific namelist changes below in the form of
2 ! namelist_var = new_namelist_values
3 &cam_history_nl
4  avgflag_pertape                 = 'A', 'I','A'
5   fincl1='dst_a1_XFRC','dst_a2_XFRC', 'dst_a3_XFRC', 'UBOT', 'VBOT', 'dst_a1',
      'dst_a2', 'dst_a3', 'dst_c1', 'dst_c2', 'dst_c3', 'dst_a1DDF', '
```

```
dst_a1SFWET', 'dst_a1SF', 'SFdst_a1', 'dst_a2DDF', 'dst_a2SFWET', '
dst_a2SF', 'SFdst_a2', 'dst_a3DDF', 'dst_a3SFWET', 'dst_a3SF', 'SFdst_a3',
 'dst_c1DDF', 'dst_c1SFWET', 'dst_c2DDF', 'dst_c2SFWET', 'dst_c3DDF', '
dst_c3SFWET', 'FLNT', 'FSNT', 'FSNTOA', 'FLUT', 'FLNTC', 'FSNTC', 'FSNTOAC
', 'FLUTC', 'FLNR', 'FSNR', 'FLNS', 'FSNS', 'FSUTOA', 'FLNT_d1', 'FSNT_d1'
, 'FSNTOA_d1', 'FLUT_d1', 'FLNTC_d1', 'FSNTC_d1', 'FSNTOAC_d1', 'FLUTC_d1'
, 'FLNR_d1', 'FSNR_d1', 'FLNS_d1', 'FSNS_d1', 'FSUTOA_d1', 'FLNT_d2', '
FSNT_d2', 'FSNTOA_d2', 'FLUT_d2', 'FLNTC_d2', 'FSNTC_d2', 'FSNTOAC_d2', '
FLUTC_d2', 'FLNR_d2', 'FSNR_d2', 'FLNS_d2', 'FSNS_d2', 'FSUTOA_d2','
FLNT_d3', 'FSNT_d3', 'FSNTOA_d3', 'FLUT_d3', 'FLNTC_d3', 'FSNTC_d3', '
FSNTOAC_d3', 'FLUTC_d3', 'FLNR_d3', 'FSNR_d3', 'FLNS_d3', 'FSNS_d3', '
FSUTOA_d3','FLNT_d4', 'FSNT_d4', 'FSNTOA_d4', 'FLUT_d4', 'FLNTC_d4', '
FSNTC_d4', 'FSNTOAC_d4', 'FLUTC_d4', 'FLNR_d4', 'FSNR_d4', 'FLNS_d4', '
FSNS_d4', 'FSUTOA_d4','FLNT_d5', 'FSNT_d5', 'FSNTOA_d5', 'FLUT_d5', '
FLNTC_d5', 'FSNTC_d5', 'FSNTOAC_d5', 'FLUTC_d5', 'FLNR_d5', 'FSNR_d5', '
FLNS_d5', 'FSNS_d5', 'FSUTOA_d5', 'FSNT_d6', 'FSNTOA_d6', 'FLUT_d6', '
FLNTC_d6', 'FSNTC_d6', 'FSNTOAC_d6', 'FLUTC_d6', 'FLNR_d6', 'FSNR_d6', '
FLNS_d6', 'FSNS_d6', 'FSUTOA_d6', 'MASS', 'AREA', 'PS','RHO_CLUBB', 'T', '
FLNT_d6','FLNT_d7', 'FSNT_d7', 'FSNTOA_d7', 'FLUT_d7', 'FLNTC_d7', '
FSNTC_d7', 'FSNTOAC_d7', 'FLUTC_d7', 'FLNR_d7', 'FSNR_d7', 'FLNS_d7', '
FSNS_d7', 'FSUTOA_d7','CLOUD'
fincl2='dst_a1_XFRC','dst_a2_XFRC', 'dst_a3_XFRC', 'UBOT', 'VBOT','dst_a1','
num_a1', 'dst_a2', 'dst_a3', 'dst_c1', 'dst_c2', 'dst_c3', 'dst_a1DDF', '
dst_a1SFWET', 'dst_a1SF', 'SFdst_a1', 'dst_a2DDF', 'dst_a2SFWET', '
dst_a2SF', 'SFdst_a2', 'dst_a3DDF', 'dst_a3SFWET', 'dst_a3SF', 'SFdst_a3',
 'dst_c1DDF', 'dst_c1SFWET', 'dst_c2DDF', 'dst_c2SFWET', 'dst_c3DDF', '
dst_c3SFWET', 'FLNT', 'FSNT', 'FSNTOA', 'FLUT', 'FLNTC', 'FSNTC', 'FSNTOAC
', 'FLUTC', 'FLNR', 'FSNR', 'FLNS', 'FSNS', 'FSUTOA', 'FLNT_d1', 'FSNT_d1'
, 'FSNTOA_d1', 'FLUT_d1', 'FLNTC_d1', 'FSNTC_d1', 'FSNTOAC_d1', 'FLUTC_d1'
, 'FLNR_d1', 'FSNR_d1', 'FLNS_d1', 'FSNS_d1', 'FSUTOA_d1', 'FLNT_d2', '
FSNT_d2', 'FSNTOA_d2', 'FLUT_d2', 'FLNTC_d2', 'FSNTC_d2', 'FSNTOAC_d2', '
FLUTC_d2', 'FLNR_d2', 'FSNR_d2', 'FLNS_d2', 'FSNS_d2', 'FSUTOA_d2','
FLNT_d3', 'FSNT_d3', 'FSNTOA_d3', 'FLUT_d3', 'FLNTC_d3', 'FSNTC_d3', '
FSNTOAC_d3', 'FLUTC_d3', 'FLNR_d3', 'FSNR_d3', 'FLNS_d3', 'FSNS_d3', '
FSUTOA_d3','FLNT_d4', 'FSNT_d4', 'FSNTOA_d4', 'FLUT_d4', 'FLNTC_d4', '
FSNTC_d4', 'FSNTOAC_d4', 'FLUTC_d4', 'FLNR_d4', 'FSNR_d4', 'FLNS_d4', '
```

```
    FSNS_d4', 'FSUTOA_d4','FLNT_d5', 'FSNT_d5', 'FSNTOA_d5', 'FLUT_d5', '
    FLNTC_d5', 'FSNTC_d5', 'FSNTOAC_d5', 'FLUTC_d5', 'FLNR_d5', 'FSNR_d5', '
    FLNS_d5', 'FSNS_d5', 'FSUTOA_d5', 'FSNT_d6', 'FSNTOA_d6', 'FLUT_d6', '
    FLNTC_d6', 'FSNTC_d6', 'FSNTOAC_d6', 'FLUTC_d6', 'FLNR_d6', 'FSNR_d6', '
    FLNS_d6', 'FSNS_d6', 'FSUTOA_d6','MASS', 'AREA', 'PS','RHO_CLUBB', 'T', '
    FLNT_d6','FLNT_d7', 'FSNT_d7', 'FSNTOA_d7', 'FLUT_d7', 'FLNTC_d7', '
    FSNTC_d7', 'FSNTOAC_d7', 'FLUTC_d7', 'FLNR_d7', 'FSNR_d7', 'FLNS_d7', '
    FSNS_d7', 'FSUTOA_d7''CLOUD'
 fincl3='dst_a1_XFRC','dst_a2_XFRC', 'dst_a3_XFRC','UBOT', 'VBOT','dst_a1','
    num_a1', 'dst_a2', 'dst_a3', 'dst_c1', 'dst_c2', 'dst_c3', 'dst_a1DDF', '
    dst_a1SFWET', 'dst_a1SF', 'SFdst_a1', 'dst_a2DDF', 'dst_a2SFWET', '
    dst_a2SF', 'SFdst_a2', 'dst_a3DDF', 'dst_a3SFWET', 'dst_a3SF', 'SFdst_a3',
     'dst_c1DDF', 'dst_c1SFWET', 'dst_c2DDF', 'dst_c2SFWET', 'dst_c3DDF', '
    dst_c3SFWET', 'FLNT', 'FSNT', 'FSNTOA', 'FLUT', 'FLNTC', 'FSNTC', 'FSNTOAC
    ', 'FLUTC', 'FLNR', 'FSNR', 'FLNS', 'FSNS', 'FSUTOA', 'FLNT_d1', 'FSNT_d1'
    , 'FSNTOA_d1', 'FLUT_d1', 'FLNTC_d1', 'FSNTC_d1', 'FSNTOAC_d1', 'FLUTC_d1'
    , 'FLNR_d1', 'FSNR_d1', 'FLNS_d1', 'FSNS_d1', 'FSUTOA_d1', 'FLNT_d2', '
    FSNT_d2', 'FSNTOA_d2', 'FLUT_d2', 'FLNTC_d2', 'FSNTC_d2', 'FSNTOAC_d2', '
    FLUTC_d2', 'FLNR_d2', 'FSNR_d2', 'FLNS_d2', 'FSNS_d2', 'FSUTOA_d2','
    FLNT_d3', 'FSNT_d3', 'FSNTOA_d3', 'FLUT_d3', 'FLNTC_d3', 'FSNTC_d3', '
    FSNTOAC_d3', 'FLUTC_d3', 'FLNR_d3', 'FSNR_d3', 'FLNS_d3', 'FSNS_d3', '
    FSUTOA_d3','FLNT_d4', 'FSNT_d4', 'FSNTOA_d4', 'FLUT_d4', 'FLNTC_d4', '
    FSNTC_d4', 'FSNTOAC_d4', 'FLUTC_d4', 'FLNR_d4', 'FSNR_d4', 'FLNS_d4', '
    FSNS_d4', 'FSUTOA_d4','FLNT_d5', 'FSNT_d5', 'FSNTOA_d5', 'FLUT_d5', '
    FLNTC_d5', 'FSNTC_d5', 'FSNTOAC_d5', 'FLUTC_d5', 'FLNR_d5', 'FSNR_d5', '
    FLNS_d5', 'FSNS_d5', 'FSUTOA_d5','FSNT_d6', 'FSNTOA_d6', 'FLUT_d6', '
    FLNTC_d6', 'FSNTC_d6', 'FSNTOAC_d6', 'FLUTC_d6', 'FLNR_d6', 'FSNR_d6', '
    FLNS_d6', 'FSNS_d6', 'FSUTOA_d6', 'MASS', 'AREA', 'PS','RHO_CLUBB', 'T', '
    FLNT_d6','FLNT_d7', 'FSNT_d7', 'FSNTOA_d7', 'FLUT_d7', 'FLNTC_d7', '
    FSNTC_d7', 'FSNTOAC_d7', 'FLUTC_d7', 'FLNR_d7', 'FSNR_d7', 'FLNS_d7', '
    FSNS_d7', 'FSUTOA_d7','CLOUD'
 mfilt           =                1, 6, 6
 nhtfrq          =               0,-120, -120
 ndens       = 1, 1, 1
 empty_htapes = .true.
/
```

```
&cam_initfiles_nl
 ncdata          = '/glade/p/cesmdata/cseg/inputdata/cesm2_init/f.e21.
   FWsc2000climo.f09_f09_mg17.cesm2.1-exp011.001_v2/0003-01-01/f.e21.
   FWsc2000climo.f09_f09_mg17.cesm2.1-exp011.001_v2.cam.i.0003-01-01-00000.nc
   ',
/
&dust_nl
 dust_emis_fact=1D300
/
&chem_inparm
 ext_frc_cycle_yr                = 2000
 ext_frc_specifier               =
        'num_a1 -> /glade/p/cesmdata/cseg/inputdata/atm/cam/chem/emis/
   CMIP6_emissions_2000climo/emissions-cmip6_num_so4_a1_anthro-
   ene_vertical_2000climo_0.9x1.25_c20170616.nc',
        'num_a1 -> /glade/p/cesmdata/cseg/inputdata/atm/cam/chem/emis/
   CMIP6_emissions_2000climo/emissions-
   cmip6_num_a1_so4_contvolcano_vertical_2000climo_0.9x1.25_c20170724.nc',
        'num_a2 -> /glade/p/cesmdata/cseg/inputdata/atm/cam/chem/emis/
   CMIP6_emissions_2000climo/emissions-
   cmip6_num_a2_so4_contvolcano_vertical_2000climo_0.9x1.25_c20170724.nc',
        'SO2 ->    /glade/p/cesmdata/cseg/inputdata/atm/cam/chem/emis/
   CMIP6_emissions_2000climo/emissions-
   cmip6_SO2_contvolcano_vertical_2000climo_0.9x1.25_c20170322.nc',
        'so4_a1 -> /glade/p/cesmdata/cseg/inputdata/atm/cam/chem/emis/
   CMIP6_emissions_2000climo/emissions-cmip6_so4_a1_anthro-
   ene_vertical_2000climo_0.9x1.25_c20170616.nc',
        'so4_a1 -> /glade/p/cesmdata/cseg/inputdata/atm/cam/chem/emis/
   CMIP6_emissions_2000climo/emissions-
   cmip6_so4_a1_contvolcano_vertical_2000climo_0.9x1.25_c20170724.nc',
        'so4_a2 -> /glade/p/cesmdata/cseg/inputdata/atm/cam/chem/emis/
   CMIP6_emissions_2000climo/emissions-
   cmip6_so4_a2_contvolcano_vertical_2000climo_0.9x1.25_c20170724.nc',
     'bc_a4 -> /glade/p/cesmdata/cseg/inputdata/atm/cam/chem/emis/
   CMIP6_emissions_2000climo/emissions-
   cmip6_bc_a4_aircraft_vertical_2000climo_0.9x1.25_c20170322.nc',
```

```
30      'num_a4 -> /glade/p/cesmdata/cseg/inputdata/atm/cam/chem/emis/
    CMIP6_emissions_2000climo/emissions-
    cmip6_num_bc_a4_aircraft_vertical_2000climo_0.9x1.25_c20170322.nc',
31      'SO2 -> /glade/p/cesmdata/cseg/inputdata/atm/cam/chem/emis/
    CMIP6_emissions_2000climo/emissions-
    cmip6_SO2_aircraft_vertical_2000climo_0.9x1.25_c20170608.nc'
32  ext_frc_type            = 'CYCLICAL'
33  srf_emis_cycle_yr               = 2000
34  srf_emis_specifier              =
35          'dst_a1 -> /glade/work/ashajain/Terrestial_Dust_Emissions/
    dst_a1SF_terrestial_dust_emissions_0001_c.nc',
36          'dst_a2 -> /glade/work/ashajain/Terrestial_Dust_Emissions/
    dst_a2SF_terrestial_dust_emissions_0001_c.nc',
37          'dst_a3 -> /glade/work/ashajain/Terrestial_Dust_Emissions/
    dst_a3SF_terrestial_dust_emissions_0001_c.nc',
38          'num_a1 -> /glade/work/ashajain/Terrestial_Dust_Emissions/
    num_a1_terrestial_dust_emissions_0001_c.nc',
39          'num_a2 -> /glade/work/ashajain/Terrestial_Dust_Emissions/
    num_a2_terrestial_dust_emissions_0001_c.nc',
40          'num_a3 -> /glade/work/ashajain/Terrestial_Dust_Emissions/
    num_a3_terrestial_dust_emissions_0001_c.nc',
41          'bc_a4 -> /glade/p/cesmdata/cseg/inputdata/atm/cam/chem/emis/
    CMIP6_emissions_2000climo/emissions-cmip6_bc_a4_anthro_surface_2000climo_0
    .9x1.25_c20170322.nc',
42          'bc_a4 -> /glade/p/cesmdata/cseg/inputdata/atm/cam/chem/emis/
    CMIP6_emissions_2000climo/emissions-cmip6_bc_a4_bb_surface_2000climo_0.9x1
    .25_c20170322.nc',
43          'DMS -> /glade/p/cesmdata/cseg/inputdata/atm/cam/chem/emis/
    CMIP6_emissions_2000climo/emissions-cmip6_DMS_bb_surface_2000climo_0.9x1
    .25_c20170322.nc',
44          'DMS -> /glade/p/cesmdata/cseg/inputdata/atm/cam/chem/emis/
    CMIP6_emissions_2000climo/emissions-cmip6_DMS_other_surface_2000climo_0.9
    x1.25_c20170322.nc',
45          'num_a1 -> /glade/p/cesmdata/cseg/inputdata/atm/cam/chem/emis/
    CMIP6_emissions_2000climo/emissions-
    cmip6_num_so4_a1_bb_surface_2000climo_0.9x1.25_c20170322.nc',
```

```
46          'num_a1 -> /glade/p/cesmdata/cseg/inputdata/atm/cam/chem/emis/
    CMIP6_emissions_2000climo/emissions-cmip6_num_so4_a1_anthro-ag-
    ship_surface_2000climo_0.9x1.25_c20170616.nc',
47          'num_a2 -> /glade/p/cesmdata/cseg/inputdata/atm/cam/chem/emis/
    CMIP6_emissions_2000climo/emissions-cmip6_num_so4_a2_anthro-
    res_surface_2000climo_0.9x1.25_c20170616.nc',
48          'num_a4 -> /glade/p/cesmdata/cseg/inputdata/atm/cam/chem/emis/
    CMIP6_emissions_2000climo/emissions-cmip6_num_bc_a4_bb_surface_2000climo_0
    .9x1.25_c20170322.nc',
49          'num_a4 -> /glade/p/cesmdata/cseg/inputdata/atm/cam/chem/emis/
    CMIP6_emissions_2000climo/emissions-
    cmip6_num_bc_a4_anthro_surface_2000climo_0.9x1.25_c20170608.nc',
50          'num_a4 -> /glade/p/cesmdata/cseg/inputdata/atm/cam/chem/emis/
    CMIP6_emissions_2000climo/emissions-
    cmip6_num_pom_a4_anthro_surface_2000climo_0.9x1.25_c20170608.nc',
51          'num_a4 -> /glade/p/cesmdata/cseg/inputdata/atm/cam/chem/emis/
    CMIP6_emissions_2000climo/emissions-
    cmip6_num_pom_a4_bb_surface_2000climo_0.9x1.25_c20170509.nc',
52          'pom_a4 -> /glade/p/cesmdata/cseg/inputdata/atm/cam/chem/emis/
    CMIP6_emissions_2000climo/emissions-
    cmip6_pom_a4_anthro_surface_2000climo_0.9x1.25_c20170608.nc',
53          'pom_a4 -> /glade/p/cesmdata/cseg/inputdata/atm/cam/chem/emis/
    CMIP6_emissions_2000climo/emissions-cmip6_pom_a4_bb_surface_2000climo_0.9
    x1.25_c20170322.nc',
54          'SO2 ->     /glade/p/cesmdata/cseg/inputdata/atm/cam/chem/emis/
    CMIP6_emissions_2000climo/emissions-cmip6_SO2_anthro-ag-ship-
    res_surface_2000climo_0.9x1.25_c20170616.nc',
55          'SO2 ->     /glade/p/cesmdata/cseg/inputdata/atm/cam/chem/emis/
    CMIP6_emissions_2000climo/emissions-cmip6_SO2_anthro-
    ene_surface_2000climo_0.9x1.25_c20170616.nc',
56          'SO2 ->     /glade/p/cesmdata/cseg/inputdata/atm/cam/chem/emis/
    CMIP6_emissions_2000climo/emissions-cmip6_SO2_bb_surface_2000climo_0.9x1
    .25_c20170322.nc',
57          'so4_a1 -> /glade/p/cesmdata/cseg/inputdata/atm/cam/chem/emis/
    CMIP6_emissions_2000climo/emissions-cmip6_so4_a1_anthro-ag-
    ship_surface_2000climo_0.9x1.25_c20170616.nc',
```

```
58          'so4_a1 -> /glade/p/cesmdata/cseg/inputdata/atm/cam/chem/emis/
    CMIP6_emissions_2000climo/emissions-cmip6_so4_a1_bb_surface_2000climo_0.9
    x1.25_c20170322.nc',
59          'so4_a2 -> /glade/p/cesmdata/cseg/inputdata/atm/cam/chem/emis/
    CMIP6_emissions_2000climo/emissions-cmip6_so4_a2_anthro-
    res_surface_2000climo_0.9x1.25_c20170616.nc',
60          'SOAG ->    /glade/p/cesmdata/cseg/inputdata/atm/cam/chem/emis/
    CMIP6_emissions_2000climo/emissions-cmip6_SOAGx1.5
    _anthro_surface_2000climo_0.9x1.25_c20170608.nc',
61          'SOAG ->    /glade/p/cesmdata/cseg/inputdata/atm/cam/chem/emis/
    CMIP6_emissions_2000climo/emissions-cmip6_SOAGx1.5_bb_surface_2000climo_0
    .9x1.25_c20170322.nc',
62          'SOAG ->    /glade/p/cesmdata/cseg/inputdata/atm/cam/chem/emis/
    CMIP6_emissions_2000climo/emissions-cmip6_SOAGx1.5
    _biogenic_surface_2000climo_0.9x1.25_c20170322.nc'
63  srf_emis_type           = 'CYCLICAL'
64
65 /
66 &rad_cnst_nli
67  mode_defs               =
68          'mam4_mode1:accum:=',
69                  'A:num_a1:N:num_c1:num_mr:+',
70                  'A:so4_a1:N:so4_c1:sulfate:/glade/p/cesmdata/cseg/inputdata/
    atm/cam/physprops/sulfate_rrtmg_c080918.nc:+',
71                  'A:pom_a1:N:pom_c1:p-organic:/glade/p/cesmdata/cseg/inputdata/
    atm/cam/physprops/ocpho_rrtmg_c130709.nc:+',
72                  'A:soa_a1:N:soa_c1:s-organic:/glade/p/cesmdata/cseg/inputdata/
    atm/cam/physprops/ocphi_rrtmg_c100508.nc:+',
73                  'A:bc_a1:N:bc_c1:black-c:/glade/p/cesmdata/cseg/inputdata/atm/
    cam/physprops/bcpho_rrtmg_c100508.nc:+',
74                  'A:dst_a1:N:dst_c1:dust:/glade/p/cesmdata/cseg/inputdata/atm/
    cam/physprops/dust_aeronet_rrtmg_c141106.nc:+',
75                  'A:ncl_a1:N:ncl_c1:seasalt:/glade/p/cesmdata/cseg/inputdata/
    atm/cam/physprops/ssam_rrtmg_c100508.nc',
76          'mam4_mode2:aitken:=',
77                  'A:num_a2:N:num_c2:num_mr:+',
```

```
78                 'A:so4_a2:N:so4_c2:sulfate:/glade/p/cesmdata/cseg/inputdata/
    atm/cam/physprops/sulfate_rrtmg_c080918.nc:+',
79                 'A:soa_a2:N:soa_c2:s-organic:/glade/p/cesmdata/cseg/inputdata/
    atm/cam/physprops/ocphi_rrtmg_c100508.nc:+',
80                 'A:ncl_a2:N:ncl_c2:seasalt:/glade/p/cesmdata/cseg/inputdata/
    atm/cam/physprops/ssam_rrtmg_c100508.nc:+',
81                 'A:dst_a2:N:dst_c2:dust:/glade/p/cesmdata/cseg/inputdata/atm/
    cam/physprops/dust_aeronet_rrtmg_c141106.nc',
82           'mam4_mode3:coarse:=',
83                 'A:num_a3:N:num_c3:num_mr:+',
84                 'A:dst_a3:N:dst_c3:dust:/glade/p/cesmdata/cseg/inputdata/atm/
    cam/physprops/dust_aeronet_rrtmg_c141106.nc:+',
85                 'A:ncl_a3:N:ncl_c3:seasalt:/glade/p/cesmdata/cseg/inputdata/
    atm/cam/physprops/ssam_rrtmg_c100508.nc:+',
86                 'A:so4_a3:N:so4_c3:sulfate:/glade/p/cesmdata/cseg/inputdata/
    atm/cam/physprops/sulfate_rrtmg_c080918.nc',
87           'mam4_mode4:primary_carbon:=',
88                 'A:num_a4:N:num_c4:num_mr:+',
89                 'A:pom_a4:N:pom_c4:p-organic:/glade/p/cesmdata/cseg/inputdata/
    atm/cam/physprops/ocpho_rrtmg_c130709.nc:+',
90                 'A:bc_a4:N:bc_c4:black-c:/glade/p/cesmdata/cseg/inputdata/atm/
    cam/physprops/bcpho_rrtmg_c100508.nc',
91          'mam4_mode1_nodust:accum:=',
92                 'A:num_a1:N:num_c1:num_mr:+',
93                 'A:so4_a1:N:so4_c1:sulfate:/glade/p/cesmdata/cseg/inputdata/
    atm/cam/physprops/sulfate_rrtmg_c080918.nc:+',
94                 'A:pom_a1:N:pom_c1:p-organic:/glade/p/cesmdata/cseg/inputdata/
    atm/cam/physprops/ocpho_rrtmg_c130709.nc:+',
95                 'A:soa_a1:N:soa_c1:s-organic:/glade/p/cesmdata/cseg/inputdata/
    atm/cam/physprops/ocphi_rrtmg_c100508.nc:+',
96                 'A:bc_a1:N:bc_c1:black-c:/glade/p/cesmdata/cseg/inputdata/atm/
    cam/physprops/bcpho_rrtmg_c100508.nc:+',
97                 'A:ncl_a1:N:ncl_c1:seasalt:/glade/p/cesmdata/cseg/inputdata/
    atm/cam/physprops/ssam_rrtmg_c100508.nc',
98           'mam4_mode2_nodust:aitken:=',
99                 'A:num_a2:N:num_c2:num_mr:+',
```

```
100                 'A:so4_a2:N:so4_c2:sulfate:/glade/p/cesmdata/cseg/inputdata/
    atm/cam/physprops/sulfate_rrtmg_c080918.nc:+',
101                 'A:soa_a2:N:soa_c2:s-organic:/glade/p/cesmdata/cseg/inputdata/
    atm/cam/physprops/ocphi_rrtmg_c100508.nc:+',
102                 'A:ncl_a2:N:ncl_c2:seasalt:/glade/p/cesmdata/cseg/inputdata/
    atm/cam/physprops/ssam_rrtmg_c100508.nc',
103         'mam4_mode3_nodust:coarse:=',
104                 'A:num_a3:N:num_c3:num_mr:+',
105                 'A:ncl_a3:N:ncl_c3:seasalt:/glade/p/cesmdata/cseg/inputdata/
    atm/cam/physprops/ssam_rrtmg_c100508.nc:+',
106                 'A:so4_a3:N:so4_c3:sulfate:/glade/p/cesmdata/cseg/inputdata/
    atm/cam/physprops/sulfate_rrtmg_c080918.nc'
107 rad_diag_1 = 'A:Q:H2O', 'N:O2:O2',
108         'N:CO2:CO2', 'N:ozone:O3',
109         'A:N2O:N2O', 'A:CH4:CH4',
110         'N:CFC11STAR:CFC11', 'A:CFC12:CFC12',
111         'N:VOLC_MMR1:/glade/p/cesmdata/cseg/inputdata/atm/cam/physprops/
    volc_camRRTMG_byradius_sigma1.6_mode1_c170214.nc', 'N:VOLC_MMR2:/glade/p/
    cesmdata/cseg/inputdata/atm/cam/physprops/volc_camRRTMG_byradius_sigma1.6
    _mode2_c170214.nc',
112         'N:VOLC_MMR3:/glade/p/cesmdata/cseg/inputdata/atm/cam/physprops/
    volc_camRRTMG_byradius_sigma1.2_mode3_c170214.nc'
113 rad_diag_2 = 'A:Q:H2O', 'N:O2:O2',
114         'N:CO2:CO2', 'N:ozone:O3',
115         'A:N2O:N2O', 'A:CH4:CH4',
116         'N:CFC11STAR:CFC11', 'A:CFC12:CFC12',
117         'M:mam4_mode1_nodust:/glade/p/cesmdata/cseg/inputdata/atm/cam/
    physprops/mam4_mode1_rrtmg_aeronetdust_sig1.6_dgnh.48_c140304.nc', 'M:
    mam4_mode2:/glade/p/cesmdata/cseg/inputdata/atm/cam/physprops/
    mam4_mode2_rrtmg_aitkendust_c141106.nc',
118         'M:mam4_mode3:/glade/p/cesmdata/cseg/inputdata/atm/cam/physprops/
    mam4_mode3_rrtmg_aeronetdust_sig1.2_dgnl.40_c150219.nc', 'M:mam4_mode4:/
    glade/p/cesmdata/cseg/inputdata/atm/cam/physprops/mam4_mode4_rrtmg_c130628
    .nc',
119         'N:VOLC_MMR1:/glade/p/cesmdata/cseg/inputdata/atm/cam/physprops/
    volc_camRRTMG_byradius_sigma1.6_mode1_c170214.nc', 'N:VOLC_MMR2:/glade/p/
```

```
cesmdata/cseg/inputdata/atm/cam/physprops/volc_camRRTMG_byradius_sigma1.6
_mode2_c170214.nc',
120         'N:VOLC_MMR3:/glade/p/cesmdata/cseg/inputdata/atm/cam/physprops/
volc_camRRTMG_byradius_sigma1.2_mode3_c170214.nc'
121 rad_diag_3 = 'A:Q:H2O', 'N:O2:O2',
122         'N:CO2:CO2', 'N:ozone:O3',
123         'A:N2O:N2O', 'A:CH4:CH4',
124         'N:CFC11STAR:CFC11', 'A:CFC12:CFC12',
125         'M:mam4_mode1_nodust:/glade/p/cesmdata/cseg/inputdata/atm/cam/
physprops/mam4_mode1_rrtmg_aeronetdust_sig1.6_dgnh.48_c140304.nc', 'M:
mam4_mode2_nodust:/glade/p/cesmdata/cseg/inputdata/atm/cam/physprops/
mam4_mode2_rrtmg_aitkendust_c141106.nc',
126         'M:mam4_mode3:/glade/p/cesmdata/cseg/inputdata/atm/cam/physprops/
mam4_mode3_rrtmg_aeronetdust_sig1.2_dgnl.40_c150219.nc', 'M:mam4_mode4:/
glade/p/cesmdata/cseg/inputdata/atm/cam/physprops/mam4_mode4_rrtmg_c130628
.nc',
127         'N:VOLC_MMR1:/glade/p/cesmdata/cseg/inputdata/atm/cam/physprops/
volc_camRRTMG_byradius_sigma1.6_mode1_c170214.nc', 'N:VOLC_MMR2:/glade/p/
cesmdata/cseg/inputdata/atm/cam/physprops/volc_camRRTMG_byradius_sigma1.6
_mode2_c170214.nc',
128         'N:VOLC_MMR3:/glade/p/cesmdata/cseg/inputdata/atm/cam/physprops/
volc_camRRTMG_byradius_sigma1.2_mode3_c170214.nc'
129 rad_diag_4 = 'A:Q:H2O', 'N:O2:O2',
130         'N:CO2:CO2', 'N:ozone:O3',
131         'A:N2O:N2O', 'A:CH4:CH4',
132         'N:CFC11STAR:CFC11', 'A:CFC12:CFC12',
133         'M:mam4_mode1:/glade/p/cesmdata/cseg/inputdata/atm/cam/physprops/
mam4_mode1_rrtmg_aeronetdust_sig1.6_dgnh.48_c140304.nc', 'M:mam4_mode2:/
glade/p/cesmdata/cseg/inputdata/atm/cam/physprops/
mam4_mode2_rrtmg_aitkendust_c141106.nc',
134         'M:mam4_mode3_nodust:/glade/p/cesmdata/cseg/inputdata/atm/cam/
physprops/mam4_mode3_rrtmg_aeronetdust_sig1.2_dgnl.40_c150219.nc', 'M:
mam4_mode4:/glade/p/cesmdata/cseg/inputdata/atm/cam/physprops/
mam4_mode4_rrtmg_c130628.nc',
135         'N:VOLC_MMR1:/glade/p/cesmdata/cseg/inputdata/atm/cam/physprops/
volc_camRRTMG_byradius_sigma1.6_mode1_c170214.nc', 'N:VOLC_MMR2:/glade/p/
```

```
cesmdata/cseg/inputdata/atm/cam/physprops/volc_camRRTMG_byradius_sigma1.6
_mode2_c170214.nc',
136         'N:VOLC_MMR3:/glade/p/cesmdata/cseg/inputdata/atm/cam/physprops/
volc_camRRTMG_byradius_sigma1.2_mode3_c170214.nc'
137 rad_diag_5 = 'A:Q:H2O', 'N:O2:O2',
138         'N:CO2:CO2', 'N:ozone:O3',
139         'A:N2O:N2O', 'A:CH4:CH4',
140         'N:CFC11STAR:CFC11', 'A:CFC12:CFC12',
141         'M:mam4_mode1:/glade/p/cesmdata/cseg/inputdata/atm/cam/physprops/
mam4_mode1_rrtmg_aeronetdust_sig1.6_dgnh.48_c140304.nc', 'M:
mam4_mode2_nodust:/glade/p/cesmdata/cseg/inputdata/atm/cam/physprops/
mam4_mode2_rrtmg_aitkendust_c141106.nc',
142         'M:mam4_mode3:/glade/p/cesmdata/cseg/inputdata/atm/cam/physprops/
mam4_mode3_rrtmg_aeronetdust_sig1.2_dgnl.40_c150219.nc', 'M:mam4_mode4:/
glade/p/cesmdata/cseg/inputdata/atm/cam/physprops/mam4_mode4_rrtmg_c130628
.nc',
143         'N:VOLC_MMR1:/glade/p/cesmdata/cseg/inputdata/atm/cam/physprops/
volc_camRRTMG_byradius_sigma1.6_mode1_c170214.nc', 'N:VOLC_MMR2:/glade/p/
cesmdata/cseg/inputdata/atm/cam/physprops/volc_camRRTMG_byradius_sigma1.6
_mode2_c170214.nc',
144         'N:VOLC_MMR3:/glade/p/cesmdata/cseg/inputdata/atm/cam/physprops/
volc_camRRTMG_byradius_sigma1.2_mode3_c170214.nc'
145 rad_diag_6 = 'A:Q:H2O', 'N:O2:O2',
146         'N:CO2:CO2', 'N:ozone:O3',
147         'A:N2O:N2O', 'A:CH4:CH4',
148         'N:CFC11STAR:CFC11', 'A:CFC12:CFC12',
149         'M:mam4_mode1_nodust:/glade/p/cesmdata/cseg/inputdata/atm/cam/
physprops/mam4_mode1_rrtmg_aeronetdust_sig1.6_dgnh.48_c140304.nc', 'M:
mam4_mode2:/glade/p/cesmdata/cseg/inputdata/atm/cam/physprops/
mam4_mode2_rrtmg_aitkendust_c141106.nc',
150         'M:mam4_mode3_nodust:/glade/p/cesmdata/cseg/inputdata/atm/cam/
physprops/mam4_mode3_rrtmg_aeronetdust_sig1.2_dgnl.40_c150219.nc', 'M:
mam4_mode4:/glade/p/cesmdata/cseg/inputdata/atm/cam/physprops/
mam4_mode4_rrtmg_c130628.nc',
151         'N:VOLC_MMR1:/glade/p/cesmdata/cseg/inputdata/atm/cam/physprops/
volc_camRRTMG_byradius_sigma1.6_mode1_c170214.nc', 'N:VOLC_MMR2:/glade/p/
```

```
cesmdata/cseg/inputdata/atm/cam/physprops/volc_camRRTMG_byradius_sigma1.6
_mode2_c170214.nc',
152          'N:VOLC_MMR3:/glade/p/cesmdata/cseg/inputdata/atm/cam/physprops/
volc_camRRTMG_byradius_sigma1.2_mode3_c170214.nc'
153  rad_diag_7 = 'A:Q:H2O', 'N:O2:O2',
154          'N:CO2:CO2', 'N:ozone:O3',
155          'A:N2O:N2O', 'A:CH4:CH4',
156          'N:CFC11STAR:CFC11', 'A:CFC12:CFC12',
157          'M:mam4_mode1_nodust:/glade/p/cesmdata/cseg/inputdata/atm/cam/
physprops/mam4_mode1_rrtmg_aeronetdust_sig1.6_dgnh.48_c140304.nc', 'M:
mam4_mode2_nodust:/glade/p/cesmdata/cseg/inputdata/atm/cam/physprops/
mam4_mode2_rrtmg_aitkendust_c141106.nc',
158          'M:mam4_mode3_nodust:/glade/p/cesmdata/cseg/inputdata/atm/cam/
physprops/mam4_mode3_rrtmg_aeronetdust_sig1.2_dgnl.40_c150219.nc', 'M:
mam4_mode4:/glade/p/cesmdata/cseg/inputdata/atm/cam/physprops/
mam4_mode4_rrtmg_c130628.nc',
159          'N:VOLC_MMR1:/glade/p/cesmdata/cseg/inputdata/atm/cam/physprops/
volc_camRRTMG_byradius_sigma1.6_mode1_c170214.nc', 'N:VOLC_MMR2:/glade/p/
cesmdata/cseg/inputdata/atm/cam/physprops/volc_camRRTMG_byradius_sigma1.6
_mode2_c170214.nc','N:VOLC_MMR3:/glade/p/cesmdata/cseg/inputdata/atm/cam/
physprops/volc_camRRTMG_byradius_sigma1.2_mode3_c170214.nc'
```

A.1.2 Case 2

```
1 ! Users should add all user specific namelist changes below in the form of
2 ! namelist_var = new_namelist_values
3 &cam_history_nl
4  avgflag_pertape                    = 'A', 'I','A'
5   fincl1= 'UBOT', 'VBOT', 'dst_a1_XFRC', 'dst_a2_XFRC', 'dst_a3_XFRC','dst_a1'
     , 'dst_a2', 'dst_a3', 'dst_c1', 'dst_c2', 'dst_c3', 'dst_a1DDF', '
    dst_a1SFWET', 'dst_a1SF', 'SFdst_a1', 'dst_a2DDF', 'dst_a2SFWET', '
    dst_a2SF', 'SFdst_a2', 'dst_a3DDF', 'dst_a3SFWET', 'dst_a3SF', 'SFdst_a3',
     'dst_c1DDF', 'dst_c1SFWET', 'dst_c2DDF', 'dst_c2SFWET', 'dst_c3DDF', '
    dst_c3SFWET', 'FLNT', 'FSNT', 'FSNTOA', 'FLUT', 'FLNTC', 'FSNTC', 'FSNTOAC
```

```
', 'FLUTC', 'FLNR', 'FSNR', 'FLNS', 'FSNS', 'FSUTOA', 'FLNT_d1', 'FSNT_d1'
, 'FSNTOA_d1', 'FLUT_d1', 'FLNTC_d1', 'FSNTC_d1', 'FSNTOAC_d1', 'FLUTC_d1'
, 'FLNR_d1', 'FSNR_d1', 'FLNS_d1', 'FSNS_d1', 'FSUTOA_d1', 'MASS', 'AREA',
 'PS','RHO_CLUBB', 'T','FLNT_d2', 'FSNT_d2', 'FSNTOA_d2', 'FLUT_d2', '
FLNTC_d2', 'FSNTC_d2', 'FSNTOAC_d2', 'FLUTC_d2', 'FLNR_d2', 'FSNR_d2', '
FLNS_d2', 'FSNS_d2', 'FSUTOA_d2', 'CLOUD', 'TROP_P', 'TS', 'T500'
 fincl2= 'UBOT', 'VBOT','dst_a1_XFRC', 'dst_a2_XFRC', 'dst_a3_XFRC','dst_a1',
 'num_a1', 'dst_a2', 'dst_a3', 'dst_c1', 'dst_c2', 'dst_c3', 'dst_a1DDF', '
dst_a1SFWET', 'dst_a1SF', 'SFdst_a1', 'dst_a2DDF', 'dst_a2SFWET', '
dst_a2SF', 'SFdst_a2', 'dst_a3DDF', 'dst_a3SFWET', 'dst_a3SF', 'SFdst_a3',
 'dst_c1DDF', 'dst_c1SFWET', 'dst_c2DDF', 'dst_c2SFWET', 'dst_c3DDF', '
dst_c3SFWET', 'FLNT', 'FSNT', 'FSNTOA', 'FLUT', 'FLNTC', 'FSNTC', 'FSNTOAC
', 'FLUTC', 'FLNR', 'FSNR', 'FLNS', 'FSNS', 'FSUTOA', 'FLNT_d1', 'FSNT_d1'
, 'FSNTOA_d1', 'FLUT_d1', 'FLNTC_d1', 'FSNTC_d1', 'FSNTOAC_d1', 'FLUTC_d1'
, 'FLNR_d1', 'FSNR_d1', 'FLNS_d1', 'FSNS_d1', 'FSUTOA_d1', 'MASS', 'AREA',
 'PS','RHO_CLUBB', 'T','FLNT_d2', 'FSNT_d2', 'FSNTOA_d2', 'FLUT_d2', '
FLNTC_d2', 'FSNTC_d2', 'FSNTOAC_d2', 'FLUTC_d2', 'FLNR_d2', 'FSNR_d2', '
FLNS_d2', 'FSNS_d2', 'FSUTOA_d2', 'CLOUD', 'TROP_P', 'TS', 'T500'
 fincl3= 'UBOT', 'VBOT','dst_a1_XFRC', 'dst_a2_XFRC', 'dst_a3_XFRC','dst_a1',
 'num_a1', 'dst_a2', 'dst_a3', 'dst_c1', 'dst_c2', 'dst_c3', 'dst_a1DDF', '
dst_a1SFWET', 'dst_a1SF', 'SFdst_a1', 'dst_a2DDF', 'dst_a2SFWET', '
dst_a2SF', 'SFdst_a2', 'dst_a3DDF', 'dst_a3SFWET', 'dst_a3SF', 'SFdst_a3',
 'dst_c1DDF', 'dst_c1SFWET', 'dst_c2DDF', 'dst_c2SFWET', 'dst_c3DDF', '
dst_c3SFWET', 'FLNT', 'FSNT', 'FSNTOA', 'FLUT', 'FLNTC', 'FSNTC', 'FSNTOAC
', 'FLUTC', 'FLNR', 'FSNR', 'FLNS', 'FSNS', 'FSUTOA', 'FLNT_d1', 'FSNT_d1'
, 'FSNTOA_d1', 'FLUT_d1', 'FLNTC_d1', 'FSNTC_d1', 'FSNTOAC_d1', 'FLUTC_d1'
, 'FLNR_d1', 'FSNR_d1', 'FLNS_d1', 'FSNS_d1', 'FSUTOA_d1',  'MASS', 'AREA'
, 'PS','RHO_CLUBB', 'T', 'FLNT_d2', 'FSNT_d2', 'FSNTOA_d2', 'FLUT_d2', '
FLNTC_d2', 'FSNTC_d2', 'FSNTOAC_d2', 'FLUTC_d2', 'FLNR_d2', 'FSNR_d2', '
FLNS_d2', 'FSNS_d2', 'FSUTOA_d2', 'CLOUD', 'TROP_P', 'TS', 'T500'
 mfilt            =                1, 6, 6
 nhtfrq           =               0,-120, -120
 ndens       = 1, 1, 1
 empty_htapes = .true.
/
&cam_initfiles_nl
```

```
 ncdata          = '/glade/p/cesmdata/cseg/inputdata/cesm2_init/f.e21.
   FWsc2000climo.f09_f09_mg17.cesm2.1-exp011.001_v2/0003-01-01/f.e21.
   FWsc2000climo.f09_f09_mg17.cesm2.1-exp011.001_v2.cam.i.0003-01-01-00000.nc
   '
/
&dust_nl
 dust_emis_fact=1D300
/
&chem_inparm
 ext_frc_cycle_yr                = 2000
 ext_frc_specifier               =
     'dst_a2 -> /glade/scratch/ashajain/ImpulseEmission/OptimisticCase/
   ScaledEmissions/Alumina_mass_sampled_forecast.nc',
          'num_a2 -> /glade/scratch/ashajain/ImpulseEmission/OptimisticCase/
   ScaledEmissions/Alumina_num_sampled_forecast_dsta2_c.nc',
          'num_a1 -> /glade/p/cesmdata/cseg/inputdata/atm/cam/chem/emis/
   CMIP6_emissions_2000climo/emissions-cmip6_num_so4_a1_anthro-
   ene_vertical_2000climo_0.9x1.25_c20170616.nc',
          'num_a1 -> /glade/p/cesmdata/cseg/inputdata/atm/cam/chem/emis/
   CMIP6_emissions_2000climo/emissions-
   cmip6_num_a1_so4_contvolcano_vertical_2000climo_0.9x1.25_c20170724.nc',
          'num_a2 -> /glade/p/cesmdata/cseg/inputdata/atm/cam/chem/emis/
   CMIP6_emissions_2000climo/emissions-
   cmip6_num_a2_so4_contvolcano_vertical_2000climo_0.9x1.25_c20170724.nc',
          'SO2 ->     /glade/p/cesmdata/cseg/inputdata/atm/cam/chem/emis/
   CMIP6_emissions_2000climo/emissions-
   cmip6_SO2_contvolcano_vertical_2000climo_0.9x1.25_c20170322.nc',
          'so4_a1 -> /glade/p/cesmdata/cseg/inputdata/atm/cam/chem/emis/
   CMIP6_emissions_2000climo/emissions-cmip6_so4_a1_anthro-
   ene_vertical_2000climo_0.9x1.25_c20170616.nc',
          'so4_a1 -> /glade/p/cesmdata/cseg/inputdata/atm/cam/chem/emis/
   CMIP6_emissions_2000climo/emissions-
   cmip6_so4_a1_contvolcano_vertical_2000climo_0.9x1.25_c20170724.nc',
          'so4_a2 -> /glade/p/cesmdata/cseg/inputdata/atm/cam/chem/emis/
   CMIP6_emissions_2000climo/emissions-
   cmip6_so4_a2_contvolcano_vertical_2000climo_0.9x1.25_c20170724.nc',
```

```
31      'bc_a4 -> /glade/p/cesmdata/cseg/inputdata/atm/cam/chem/emis/
    CMIP6_emissions_2000climo/emissions-
    cmip6_bc_a4_aircraft_vertical_2000climo_0.9x1.25_c20170322.nc',
32      'num_a4 -> /glade/p/cesmdata/cseg/inputdata/atm/cam/chem/emis/
    CMIP6_emissions_2000climo/emissions-
    cmip6_num_bc_a4_aircraft_vertical_2000climo_0.9x1.25_c20170322.nc',
33      'SO2 -> /glade/p/cesmdata/cseg/inputdata/atm/cam/chem/emis/
    CMIP6_emissions_2000climo/emissions-
    cmip6_SO2_aircraft_vertical_2000climo_0.9x1.25_c20170608.nc'
34  ext_frc_type            = 'CYCLICAL'
35  srf_emis_cycle_yr               = 2000
36  srf_emis_specifier              =
37          'dst_a1 -> /glade/work/ashajain/Terrestial_Dust_Emissions/
    dst_a1SF_terrestial_dust_emissions_0001_c.nc',
38          'dst_a2 -> /glade/work/ashajain/Terrestial_Dust_Emissions/
    dst_a2SF_terrestial_dust_emissions_0001_c.nc',
39          'dst_a3 -> /glade/work/ashajain/Terrestial_Dust_Emissions/
    dst_a3SF_terrestial_dust_emissions_0001_c.nc',
40          'num_a1 -> /glade/work/ashajain/Terrestial_Dust_Emissions/
    num_a1_terrestial_dust_emissions_0001_c.nc',
41          'num_a2 -> /glade/work/ashajain/Terrestial_Dust_Emissions/
    num_a2_terrestial_dust_emissions_0001_c.nc',
42          'num_a3 -> /glade/work/ashajain/Terrestial_Dust_Emissions/
    num_a3_terrestial_dust_emissions_0001_c.nc',
43          'bc_a4 ->  /glade/p/cesmdata/cseg/inputdata/atm/cam/chem/emis/
    CMIP6_emissions_2000climo/emissions-cmip6_bc_a4_anthro_surface_2000climo_0
    .9x1.25_c20170322.nc',
44          'bc_a4 ->  /glade/p/cesmdata/cseg/inputdata/atm/cam/chem/emis/
    CMIP6_emissions_2000climo/emissions-cmip6_bc_a4_bb_surface_2000climo_0.9x1
    .25_c20170322.nc',
45          'DMS ->    /glade/p/cesmdata/cseg/inputdata/atm/cam/chem/emis/
    CMIP6_emissions_2000climo/emissions-cmip6_DMS_bb_surface_2000climo_0.9x1
    .25_c20170322.nc',
46          'DMS ->    /glade/p/cesmdata/cseg/inputdata/atm/cam/chem/emis/
    CMIP6_emissions_2000climo/emissions-cmip6_DMS_other_surface_2000climo_0.9
    x1.25_c20170322.nc',
```

```
47          'num_a1 -> /glade/p/cesmdata/cseg/inputdata/atm/cam/chem/emis/
    CMIP6_emissions_2000climo/emissions-
    cmip6_num_so4_a1_bb_surface_2000climo_0.9x1.25_c20170322.nc',
48          'num_a1 -> /glade/p/cesmdata/cseg/inputdata/atm/cam/chem/emis/
    CMIP6_emissions_2000climo/emissions-cmip6_num_so4_a1_anthro-ag-
    ship_surface_2000climo_0.9x1.25_c20170616.nc',
49          'num_a2 -> /glade/p/cesmdata/cseg/inputdata/atm/cam/chem/emis/
    CMIP6_emissions_2000climo/emissions-cmip6_num_so4_a2_anthro-
    res_surface_2000climo_0.9x1.25_c20170616.nc',
50          'num_a4 -> /glade/p/cesmdata/cseg/inputdata/atm/cam/chem/emis/
    CMIP6_emissions_2000climo/emissions-cmip6_num_bc_a4_bb_surface_2000climo_0
    .9x1.25_c20170322.nc',
51          'num_a4 -> /glade/p/cesmdata/cseg/inputdata/atm/cam/chem/emis/
    CMIP6_emissions_2000climo/emissions-
    cmip6_num_bc_a4_anthro_surface_2000climo_0.9x1.25_c20170608.nc',
52          'num_a4 -> /glade/p/cesmdata/cseg/inputdata/atm/cam/chem/emis/
    CMIP6_emissions_2000climo/emissions-
    cmip6_num_pom_a4_anthro_surface_2000climo_0.9x1.25_c20170608.nc',
53          'num_a4 -> /glade/p/cesmdata/cseg/inputdata/atm/cam/chem/emis/
    CMIP6_emissions_2000climo/emissions-
    cmip6_num_pom_a4_bb_surface_2000climo_0.9x1.25_c20170509.nc',
54          'pom_a4 -> /glade/p/cesmdata/cseg/inputdata/atm/cam/chem/emis/
    CMIP6_emissions_2000climo/emissions-
    cmip6_pom_a4_anthro_surface_2000climo_0.9x1.25_c20170608.nc',
55          'pom_a4 -> /glade/p/cesmdata/cseg/inputdata/atm/cam/chem/emis/
    CMIP6_emissions_2000climo/emissions-cmip6_pom_a4_bb_surface_2000climo_0.9
    x1.25_c20170322.nc',
56          'SO2 ->     /glade/p/cesmdata/cseg/inputdata/atm/cam/chem/emis/
    CMIP6_emissions_2000climo/emissions-cmip6_SO2_anthro-ag-ship-
    res_surface_2000climo_0.9x1.25_c20170616.nc',
57          'SO2 ->     /glade/p/cesmdata/cseg/inputdata/atm/cam/chem/emis/
    CMIP6_emissions_2000climo/emissions-cmip6_SO2_anthro-
    ene_surface_2000climo_0.9x1.25_c20170616.nc',
58          'SO2 ->     /glade/p/cesmdata/cseg/inputdata/atm/cam/chem/emis/
    CMIP6_emissions_2000climo/emissions-cmip6_SO2_bb_surface_2000climo_0.9x1
    .25_c20170322.nc',
```

```
59          'so4_a1 -> /glade/p/cesmdata/cseg/inputdata/atm/cam/chem/emis/
    CMIP6_emissions_2000climo/emissions-cmip6_so4_a1_anthro-ag-
    ship_surface_2000climo_0.9x1.25_c20170616.nc',
60          'so4_a1 -> /glade/p/cesmdata/cseg/inputdata/atm/cam/chem/emis/
    CMIP6_emissions_2000climo/emissions-cmip6_so4_a1_bb_surface_2000climo_0.9
    x1.25_c20170322.nc',
61          'so4_a2 -> /glade/p/cesmdata/cseg/inputdata/atm/cam/chem/emis/
    CMIP6_emissions_2000climo/emissions-cmip6_so4_a2_anthro-
    res_surface_2000climo_0.9x1.25_c20170616.nc',
62          'SOAG ->    /glade/p/cesmdata/cseg/inputdata/atm/cam/chem/emis/
    CMIP6_emissions_2000climo/emissions-cmip6_SOAGx1.5
    _anthro_surface_2000climo_0.9x1.25_c20170608.nc',
63          'SOAG ->    /glade/p/cesmdata/cseg/inputdata/atm/cam/chem/emis/
    CMIP6_emissions_2000climo/emissions-cmip6_SOAGx1.5_bb_surface_2000climo_0
    .9x1.25_c20170322.nc',
64          'SOAG ->    /glade/p/cesmdata/cseg/inputdata/atm/cam/chem/emis/
    CMIP6_emissions_2000climo/emissions-cmip6_SOAGx1.5
    _biogenic_surface_2000climo_0.9x1.25_c20170322.nc'
65  srf_emis_type           = 'CYCLICAL'
66
67 /
68 &rad_cnst_nli
69  mode_defs               =
70          'mam4_mode1:accum:=',
71                  'A:num_a1:N:num_c1:num_mr:+',
72                  'A:so4_a1:N:so4_c1:sulfate:/glade/p/cesmdata/cseg/inputdata/
    atm/cam/physprops/sulfate_rrtmg_c080918.nc:+',
73                  'A:pom_a1:N:pom_c1:p-organic:/glade/p/cesmdata/cseg/inputdata/
    atm/cam/physprops/ocpho_rrtmg_c130709.nc:+',
74                  'A:soa_a1:N:soa_c1:s-organic:/glade/p/cesmdata/cseg/inputdata/
    atm/cam/physprops/ocphi_rrtmg_c100508.nc:+',
75                  'A:bc_a1:N:bc_c1:black-c:/glade/p/cesmdata/cseg/inputdata/atm/
    cam/physprops/bcpho_rrtmg_c100508.nc:+',
76                  'A:dst_a1:N:dst_c1:dust:/glade/p/cesmdata/cseg/inputdata/atm/
    cam/physprops/dust_aeronet_rrtmg_c141106.nc:+',
77                  'A:ncl_a1:N:ncl_c1:seasalt:/glade/p/cesmdata/cseg/inputdata/
```

```
atm/cam/physprops/ssam_rrtmg_c100508.nc',
78          'mam4_mode2:aitken:=',
79                  'A:num_a2:N:num_c2:num_mr:+',
80                  'A:so4_a2:N:so4_c2:sulfate:/glade/p/cesmdata/cseg/inputdata/
atm/cam/physprops/sulfate_rrtmg_c080918.nc:+',
81                  'A:soa_a2:N:soa_c2:s-organic:/glade/p/cesmdata/cseg/inputdata/
atm/cam/physprops/ocphi_rrtmg_c100508.nc:+',
82                  'A:ncl_a2:N:ncl_c2:seasalt:/glade/p/cesmdata/cseg/inputdata/
atm/cam/physprops/ssam_rrtmg_c100508.nc:+',
83                  'A:dst_a2:N:dst_c2:dust:/glade/p/cesmdata/cseg/inputdata/atm/
cam/physprops/dust_aeronet_rrtmg_c141106.nc',
84          'mam4_mode3:coarse:=',
85                  'A:num_a3:N:num_c3:num_mr:+',
86                  'A:dst_a3:N:dst_c3:dust:/glade/p/cesmdata/cseg/inputdata/atm/
cam/physprops/dust_aeronet_rrtmg_c141106.nc:+',
87                  'A:ncl_a3:N:ncl_c3:seasalt:/glade/p/cesmdata/cseg/inputdata/
atm/cam/physprops/ssam_rrtmg_c100508.nc:+',
88                  'A:so4_a3:N:so4_c3:sulfate:/glade/p/cesmdata/cseg/inputdata/
atm/cam/physprops/sulfate_rrtmg_c080918.nc',
89          'mam4_mode4:primary_carbon:=',
90                  'A:num_a4:N:num_c4:num_mr:+',
91                  'A:pom_a4:N:pom_c4:p-organic:/glade/p/cesmdata/cseg/inputdata/
atm/cam/physprops/ocpho_rrtmg_c130709.nc:+',
92                  'A:bc_a4:N:bc_c4:black-c:/glade/p/cesmdata/cseg/inputdata/atm/
cam/physprops/bcpho_rrtmg_c100508.nc',
93        'mam4_mode1_nodust:accum:=',
94                  'A:num_a1:N:num_c1:num_mr:+',
95                  'A:so4_a1:N:so4_c1:sulfate:/glade/p/cesmdata/cseg/inputdata/
atm/cam/physprops/sulfate_rrtmg_c080918.nc:+',
96                  'A:pom_a1:N:pom_c1:p-organic:/glade/p/cesmdata/cseg/inputdata/
atm/cam/physprops/ocpho_rrtmg_c130709.nc:+',
97                  'A:soa_a1:N:soa_c1:s-organic:/glade/p/cesmdata/cseg/inputdata/
atm/cam/physprops/ocphi_rrtmg_c100508.nc:+',
98                  'A:bc_a1:N:bc_c1:black-c:/glade/p/cesmdata/cseg/inputdata/atm/
cam/physprops/bcpho_rrtmg_c100508.nc:+',
99                  'A:ncl_a1:N:ncl_c1:seasalt:/glade/p/cesmdata/cseg/inputdata/
```

```
    atm/cam/physprops/ssam_rrtmg_c100508.nc',
100         'mam4_mode2_nodust:aitken:=',
101             'A:num_a2:N:num_c2:num_mr:+',
102             'A:so4_a2:N:so4_c2:sulfate:/glade/p/cesmdata/cseg/inputdata/
    atm/cam/physprops/sulfate_rrtmg_c080918.nc:+',
103             'A:soa_a2:N:soa_c2:s-organic:/glade/p/cesmdata/cseg/inputdata/
    atm/cam/physprops/ocphi_rrtmg_c100508.nc:+',
104             'A:ncl_a2:N:ncl_c2:seasalt:/glade/p/cesmdata/cseg/inputdata/
    atm/cam/physprops/ssam_rrtmg_c100508.nc',
105         'mam4_mode3_nodust:coarse:=',
106             'A:num_a3:N:num_c3:num_mr:+',
107             'A:ncl_a3:N:ncl_c3:seasalt:/glade/p/cesmdata/cseg/inputdata/
    atm/cam/physprops/ssam_rrtmg_c100508.nc:+',
108             'A:so4_a3:N:so4_c3:sulfate:/glade/p/cesmdata/cseg/inputdata/
    atm/cam/physprops/sulfate_rrtmg_c080918.nc'
109 rad_diag_1 = 'A:Q:H2O', 'N:O2:O2',
110         'N:CO2:CO2', 'N:ozone:O3',
111         'A:N2O:N2O', 'A:CH4:CH4',
112         'N:CFC11STAR:CFC11', 'A:CFC12:CFC12',
113         'N:VOLC_MMR1:/glade/p/cesmdata/cseg/inputdata/atm/cam/physprops/
    volc_camRRTMG_byradius_sigma1.6_mode1_c170214.nc', 'N:VOLC_MMR2:/glade/p/
    cesmdata/cseg/inputdata/atm/cam/physprops/volc_camRRTMG_byradius_sigma1.6
    _mode2_c170214.nc',
114         'N:VOLC_MMR3:/glade/p/cesmdata/cseg/inputdata/atm/cam/physprops/
    volc_camRRTMG_byradius_sigma1.2_mode3_c170214.nc'
115 rad_diag_2 = 'A:Q:H2O', 'N:O2:O2',
116         'N:CO2:CO2', 'N:ozone:O3',
117         'A:N2O:N2O', 'A:CH4:CH4',
118         'N:CFC11STAR:CFC11', 'A:CFC12:CFC12',
119         'M:mam4_mode1_nodust:/glade/p/cesmdata/cseg/inputdata/atm/cam/
    physprops/mam4_mode1_rrtmg_aeronetdust_sig1.6_dgnh.48_c140304.nc', 'M:
    mam4_mode2_nodust:/glade/p/cesmdata/cseg/inputdata/atm/cam/physprops/
    mam4_mode2_rrtmg_aitkendust_c141106.nc',
120         'M:mam4_mode3_nodust:/glade/p/cesmdata/cseg/inputdata/atm/cam/
    physprops/mam4_mode3_rrtmg_aeronetdust_sig1.2_dgnl.40_c150219.nc', 'M:
    mam4_mode4:/glade/p/cesmdata/cseg/inputdata/atm/cam/physprops/
```

```
mam4_mode4_rrtmg_c130628.nc',
121         'N:VOLC_MMR1:/glade/p/cesmdata/cseg/inputdata/atm/cam/physprops/
volc_camRRTMG_byradius_sigma1.6_mode1_c170214.nc', 'N:VOLC_MMR2:/glade/p/
cesmdata/cseg/inputdata/atm/cam/physprops/volc_camRRTMG_byradius_sigma1.6
_mode2_c170214.nc',
122         'N:VOLC_MMR3:/glade/p/cesmdata/cseg/inputdata/atm/cam/physprops/
volc_camRRTMG_byradius_sigma1.2_mode3_c170214.nc'
```

A.2 Chemical Mechanism File

The chemical mechanism file describes what chemistry was specified in the CESM. This file was modified from the default settings to include dust (listed as dst_a1, dst_a2, and dst_a3) as species which can be specified with a dataset. Corresponding changes were made in the *mo_sim_dat.F90* file, shown in the next section.

Importantly, the *CAM_CONFIG_OPTS* in *env_build.xml* must be updated to point to the user-specified chemical mechanism file. In this case, *CAM_CONFIG_OPTS* was set to `'-phys cam6 -age_of_air_trcs -chem waccm_sc_mam4 -usr_mech_infile /glade/work/ashajain/cesm2.2_cases/dsta2_optimistic_scaled/SourceMods/src.cam/pp_waccm_sc_mam4_alldst.in'`.

```
SPECIES

 Solution
CH4, N2O, CFC11 -> CFCl3, CFC12 -> CF2Cl2
H2O2, H2SO4, SO2, DMS -> CH3SCH3, SOAG -> C
so4_a1 -> NH4HSO4
pom_a1 -> C, soa_a1 -> C, bc_a1 -> C
dst_a1 -> AlSiO5, ncl_a1 -> NaCl
num_a1 -> H
so4_a2 -> NH4HSO4
soa_a2 -> C, ncl_a2 -> NaCl
num_a2 -> H
dst_a2 -> AlSiO5
dst_a3 -> AlSiO5, ncl_a3 -> NaCl
so4_a3 -> NH4HSO4
num_a3 -> H
pom_a4 -> C, bc_a4 -> C
num_a4 -> H
H2O
 End Solution

 Fixed
M, N2, O2, O3, OH, NO3, HO2, HALONS->CFCl3
```

```
24        End Fixed
25
26        Col-int
27  O3 = 0.
28  O2 = 0.
29        End Col-int
30
31    End SPECIES
32
33    Solution Classes
34        Explicit
35        End Explicit
36        Implicit
37          CH4, N2O, CFC11, CFC12, H2O
38          H2O2, H2SO4, SO2, DMS, SOAG
39          so4_a1, pom_a1
40          soa_a1, bc_a1, dst_a1, ncl_a1
41          num_a1
42          so4_a2, soa_a2, ncl_a2, num_a2
43          dst_a2
44          dst_a3, ncl_a3, so4_a3, num_a3
45          pom_a4, bc_a4, num_a4
46        End Implicit
47    End Solution Classes
48
49  CHEMISTRY
50        Photolysis
51  [jh2o2]     H2O2 + hv ->
52        End Photolysis
53
54        Reactions
55      [ch4_loss]     CH4    -> 2.* H2O
56      [n2o_loss]     N2O    ->
57      [cfc11_loss]   CFC11  ->
58      [cfc12_loss]   CFC12  ->
59      [lyman_alpha]  H2O    ->
```

```
60      [usr_HO2_HO2]  HO2 + HO2 -> H2O2
61                     H2O2 + OH -> H2O + HO2
            ; 2.9e-12, -160
62      [usr_SO2_OH]   SO2 + OH -> H2SO4
63                     DMS + OH -> SO2
            ; 9.6e-12, -234.
64      [usr_DMS_OH]   DMS + OH -> .5 * SO2 + .5 * HO2
65                     DMS + NO3 -> SO2 + HNO3
            ; 1.9e-13,  520.
66        End Reactions
67
68        Ext Forcing
69          dst_a1 <- dataset
70          dst_a2 <- dataset
71          dst_a3 <- dataset
72          SO2 <- dataset
73          so4_a1 <- dataset
74          so4_a2 <- dataset
75          pom_a1 <- dataset
76          pom_a4 <- dataset
77          bc_a1 <- dataset
78          bc_a4  <- dataset
79          num_a1 <- dataset
80          num_a2 <- dataset
81          num_a4 <- dataset
82          H2O <- dataset
83        End Ext Forcing
84
85    END CHEMISTRY
86
87    SIMULATION PARAMETERS
88
89      Version Options
90          model    = cam
91          machine = intel
92          architecture = hybrid
```

```
93          vec_ftns  = on
94          multitask = on
95          namemod = on
96          modules = on
97       End Version Options
98
99    END SIMULATION PARAMETERS
```

A.3 Modified File to Allow User-specified Dust Emissions

In the CESM source code, modifications were made to allow user-specified dust emissions in the *mo_sim_dat.F90* file. Specifically, the *extfrc_list* and *frc_from_dataset* variables were modified to include dust (listed as dst_a1, dst_a2 and dst_a3). Importantly, the order of the species in *extfrc_list* must match the order of the species in *Ext Forcing* in the chemical mechanism file.

One can find the *mo_sim_dat.F90* file at the following path: $CESM_root$/components/cam/src/chemistry/$YOUR CHEMICAL MECHANISM$. Be sure to select the correct chemical mechanism. In this work, the chemical mechanism is *pp_waccm_sc_mam4*.

```
1       module mo_sim_dat
2
3       private
4       public :: set_sim_dat
5
6       contains
7
8       subroutine set_sim_dat
9
10      use chem_mods,      only : clscnt, cls_rxt_cnt, clsmap, permute, adv_mass
    , fix_mass, crb_mass
11      use chem_mods,      only : diag_map
12      use chem_mods,      only : phtcnt, rxt_tag_cnt, rxt_tag_lst, rxt_tag_map
13      use chem_mods,      only : pht_alias_lst, pht_alias_mult
14      use chem_mods,      only : extfrc_lst, inv_lst, slvd_lst
15      use chem_mods,      only : enthalpy_cnt, cph_enthalpy, cph_rid, num_rnts,
    rxntot
16      use cam_abortutils,only : endrun
17      use mo_tracname,    only : solsym
18      use chem_mods,      only : frc_from_dataset
19      use chem_mods,      only : is_scalar, is_vector
```

```
20        use shr_kind_mod,   only : r8 => shr_kind_r8
21        use cam_logfile,    only : iulog
22
23        implicit none
24
25  !-----------------------------------------------------------------------
26  !       ... local variables
27  !-----------------------------------------------------------------------
28        integer :: ios
29
30        is_scalar = .true.
31        is_vector = .false.
32
33        clscnt(:) = (/       0,      0,      0,     29,      0 /)
34
35        cls_rxt_cnt(:,4) = (/       1,     11,      0,     29 /)
36
37        solsym(: 29) = (/ 'CH4               ','N2O               ','CFC11
      ','CFC12             ','H2O2              ', &
38                          'H2SO4             ','SO2               ','DMS
      ','SOAG              ','so4_a1            ', &
39                          'pom_a1            ','soa_a1            ','bc_a1
      ','dst_a1            ','ncl_a1            ', &
40                          'num_a1            ','so4_a2            ','soa_a2
      ','ncl_a2            ','num_a2            ', &
41                          'dst_a2            ','dst_a3            ','ncl_a3
      ','so4_a3            ','num_a3            ', &
42                          'pom_a4            ','bc_a4             ','num_a4
      ','H2O               ' /)
43
44        adv_mass(: 29) = (/     16.040600_r8,     44.012880_r8,    137.367503_r8,
      120.913206_r8,     34.013600_r8, &
45                            98.078400_r8,     64.064800_r8,     62.132400_r8,
       12.011000_r8,    115.107340_r8, &
46                            12.011000_r8,     12.011000_r8,     12.011000_r8,
      135.064039_r8,     58.442468_r8, &
```

```
47                                 1.007400_r8,    115.107340_r8,     12.011000_r8,
      58.442468_r8,      1.007400_r8, &
48                               135.064039_r8,    135.064039_r8,     58.442468_r8,
     115.107340_r8,      1.007400_r8, &
49                                12.011000_r8,     12.011000_r8,      1.007400_r8,
      18.014200_r8 /)
50
51       crb_mass(: 29) = (/      12.011000_r8,      0.000000_r8,     12.011000_r8,
      12.011000_r8,      0.000000_r8, &
52                                 0.000000_r8,      0.000000_r8,     24.022000_r8,
      12.011000_r8,      0.000000_r8, &
53                                12.011000_r8,     12.011000_r8,     12.011000_r8,
       0.000000_r8,      0.000000_r8, &
54                                 0.000000_r8,      0.000000_r8,     12.011000_r8,
       0.000000_r8,      0.000000_r8, &
55                                 0.000000_r8,      0.000000_r8,      0.000000_r8,
       0.000000_r8,      0.000000_r8, &
56                                12.011000_r8,     12.011000_r8,      0.000000_r8,
       0.000000_r8 /)
57
58       fix_mass(:  8) = (/ 0.00000000_r8, 28.0134800_r8, 31.9988000_r8,
     47.9982000_r8, 17.0068000_r8, &
59                           62.0049400_r8, 33.0062000_r8, 137.367503_r8 /)
60
61       clsmap(: 29,4) = (/     1,   2,   3,   4,  29,   5,   6,   7,   8,   9, &
62                              10,  11,  12,  13,  14,  15,  16,  17,  18,  19, &
63                              20,  21,  22,  23,  24,  25,  26,  27,  28 /)
64
65       permute(: 29,4) = (/     1,   2,   3,   4,   5,   6,   7,   8,   9,  10,
     &
66                               11,  12,  13,  14,  15,  16,  17,  18,  19,  20,
     &
67                               21,  22,  23,  24,  25,  26,  27,  28,  29 /)
68
69       diag_map(: 29) = (/     1,   3,   4,   5,   6,   8,   9,  11,  13,  14, &
70                              15,  16,  17,  18,  19,  20,  21,  22,  23,  24, &
```

```
71                                25,  26,  27,  28,  29,  30,  31,  32,  33 /)
72        extfrc_lst(: 14) = (/ 'dst_a1            ','dst_a2            ','dst_a3
              ','SO2              ','so4_a1         ',&
73                              'so4_a2            ','pom_a1            ','pom_a4
              ','bc_a1            ','bc_a4          ',&
74                              'num_a1            ','num_a2            ','num_a4
              ','H2O              ' /)
75
76        frc_from_dataset(: 14) = (/ .true., .true., .true., .true., .true., &
77                                    .true., .true., .true., .true., .true., &
78                                    .true., .true., .true., .true. /)
79
80
81        inv_lst(:  8) = (/ 'M                ', 'N2               ', 'O2
            ', 'O3               ', 'OH               ', &
82                           'NO3              ', 'HO2              ', 'HALONS
            ' /)
83
84        if( allocated( rxt_tag_lst ) ) then
85           deallocate( rxt_tag_lst )
86        end if
87        allocate( rxt_tag_lst(rxt_tag_cnt),stat=ios )
88        if( ios /= 0 ) then
89           write(iulog,*) 'set_sim_dat: failed to allocate rxt_tag_lst; error =
      ',ios
90           call endrun
91        end if
92        if( allocated( rxt_tag_map ) ) then
93           deallocate( rxt_tag_map )
94        end if
95        allocate( rxt_tag_map(rxt_tag_cnt),stat=ios )
96        if( ios /= 0 ) then
97           write(iulog,*) 'set_sim_dat: failed to allocate rxt_tag_map; error =
      ',ios
98           call endrun
99        end if
```

```
100       rxt_tag_lst(      1:      9) = (/ 'jh2o2                         ', '
      ch4_loss                       ', &
101                                       'n2o_loss                        ', '
      cfc11_loss                     ', &
102                                       'cfc12_loss                      ', '
      lyman_alpha                    ', &
103                                       'usr_HO2_HO2                     ', '
      usr_SO2_OH                     ', &
104                                       'usr_DMS_OH                      ' /)
105       rxt_tag_map(:rxt_tag_cnt) = (/     1,    2,    3,    4,    5,    6,    7,    9,
       11 /)
106       if( allocated( pht_alias_lst ) ) then
107          deallocate( pht_alias_lst )
108       end if
109       allocate( pht_alias_lst(phtcnt,2),stat=ios )
110       if( ios /= 0 ) then
111          write(iulog,*) 'set_sim_dat: failed to allocate pht_alias_lst; error
      = ',ios
112          call endrun
113       end if
114       if( allocated( pht_alias_mult ) ) then
115          deallocate( pht_alias_mult )
116       end if
117       allocate( pht_alias_mult(phtcnt,2),stat=ios )
118       if( ios /= 0 ) then
119          write(iulog,*) 'set_sim_dat: failed to allocate pht_alias_mult; error
       = ',ios
120          call endrun
121       end if
122       pht_alias_lst(:,1) = (/ '                    ' /)
123       pht_alias_lst(:,2) = (/ '                    ' /)
124       pht_alias_mult(:,1) = (/ 1._r8 /)
125       pht_alias_mult(:,2) = (/ 1._r8 /)
126       allocate( num_rnts(rxntot-phtcnt),stat=ios )
127       if( ios /= 0 ) then
128          write(iulog,*) 'set_sim_dat: failed to allocate num_rnts; error = ',
```

```
ios
129           call endrun
130        end if
131        num_rnts(:) = (/       1,      1,      1,      1,      1,      2,      2,
2,      2,      2, &
132                                2 /)
133
134        end subroutine set_sim_dat
135
136        end module mo_sim_dat
```

Appendix B

Mass to Number Emissions Conversion Proof

Unlike gaseous species, aerosol emissions require both number and mass emissions. This appendix shows how to derive number emissions from mass emissions and explains the unusual unit of *(particles/cm3/s)(molecules/moles)(g/kg)* used in WACCM for number emissions.

Aerosols are assumed to have spherical shapes. With this assumption, we can express the mass of a single particle as the multiplicative of aerosol density and volume of sphere (shown in Equation B.1). We take the units of the aerosol density, ρ, as kg/m^3 and the units of the aerosol diameter, d, in meters, resulting in M_p in kilograms.

$$M_p = \frac{\pi}{6}\rho d^3 \tag{B.1}$$

If the total mass of the aerosol is known, then the total number of particles emitted is simply the total emitted mass divided by the mass of a single particle:

$$N = \frac{M_{tot}}{M_p} \tag{B.2}$$

To get the number of particles emitted per second and per grid cell area, we exchange M_{tot} to E_m with units of $molecules/cm^3/s$. Equation B.3 shows how M_{tot} and E_m are related where MW is the molecular weight of the aerosol and A is Avogadro's number.

$$M_{tot} = E_m \frac{MW}{1000A} \tag{B.3}$$

Substituting this relationship into Equation B.2, we find can express the number emission flux, E_n, in units of $(particles/cm^3/s)$ as:

$$E_n = E_m \frac{MW}{1000AM_p} \tag{B.4}$$

However, WACCM applies a default scaling to all user emission files to convert emissions to mass mixing ratios [150]. This default scaling, σ is based on mass emission files, where converting from $molecules/cm^3/s$ to $kg/cm^3/s$ requires dividing mass emissions by Avagrado's number and a factor of 1000.

$$\sigma = \frac{1}{1000A} \tag{B.5}$$

This scaling factor is not appropriate for number emission files. We must, therefore, prescale our number emissions by $\frac{1}{s}$ to cancel out the default scaling, $sigma$. As a result, the correct equation to compute number emissions from mass emissions for WACCM in CESM is:

$$E_n = E_m \frac{MW}{M_p} \tag{B.6}$$

This final expression for E_n leads to number emission units of $(particles/cm^3/s)(molecules/mole)(g/kg)$.

Appendix C

List of Assumptions in Methodology

A number of assumptions are used in this methodology in order to approximate the atmospheric effects of reentry-ablated alumina. This appendix serves to summarize these assumptions in a consolidated list for clarity and quick reference.

In this work, we assume:

1. 21% of a satellite's dry mass is aluminum while 70% of which 58% ablations
2. 70% of a rocket body's dry mass is aluminum of which 31% ablates
3. an ablation profile for satellites and rocket bodies, as shown in Figure 4-3
4. all of the ablated aluminum becomes alumina, following the results of Park et al [107]
5. a future reentry population of 13,900 reentering satellites with an average mass of 600 kg and 500 rocket bodies with an average mass of 2,800 kg
6. the reentry population is constant, leading to identical aluminum emissions year-over-year
7. a reentry location distribution (shown in Figure 6-5
8. each second of the year has an equal probability of experiencing a reentry
9. reentry emissions occur along a vertical line to Earth's surface and neglect to consider that the reentry emissions should be displaced along a reentry trajectory

10. dust is an acceptable proxy for alumina to generate first order estimations of the distribution, lifetime and radiative forcing of reentry-ablated alumina, including implicit assumptions that the reentry alumina particle distribution is similar to the distributions available in MAM4 for dust and that alumina has similar coagulation and optical properties as dust

11. prescribing the surface dust emissions results does not significantly alter the distribution and lifetime of the reentry "dust" particles

12. the differences in the radiative contribution of the surface dust in the base and perturbed case are negligible item scaling the reentry "dust" emissions introduces no additional atmospheric effects that would not occur in a non-scaled case and assume that the radiative effect is linearly dependent on the emitted mass

Appendix D

Vertical Profiles of Dust in All Test Cases

D.1 Case 1

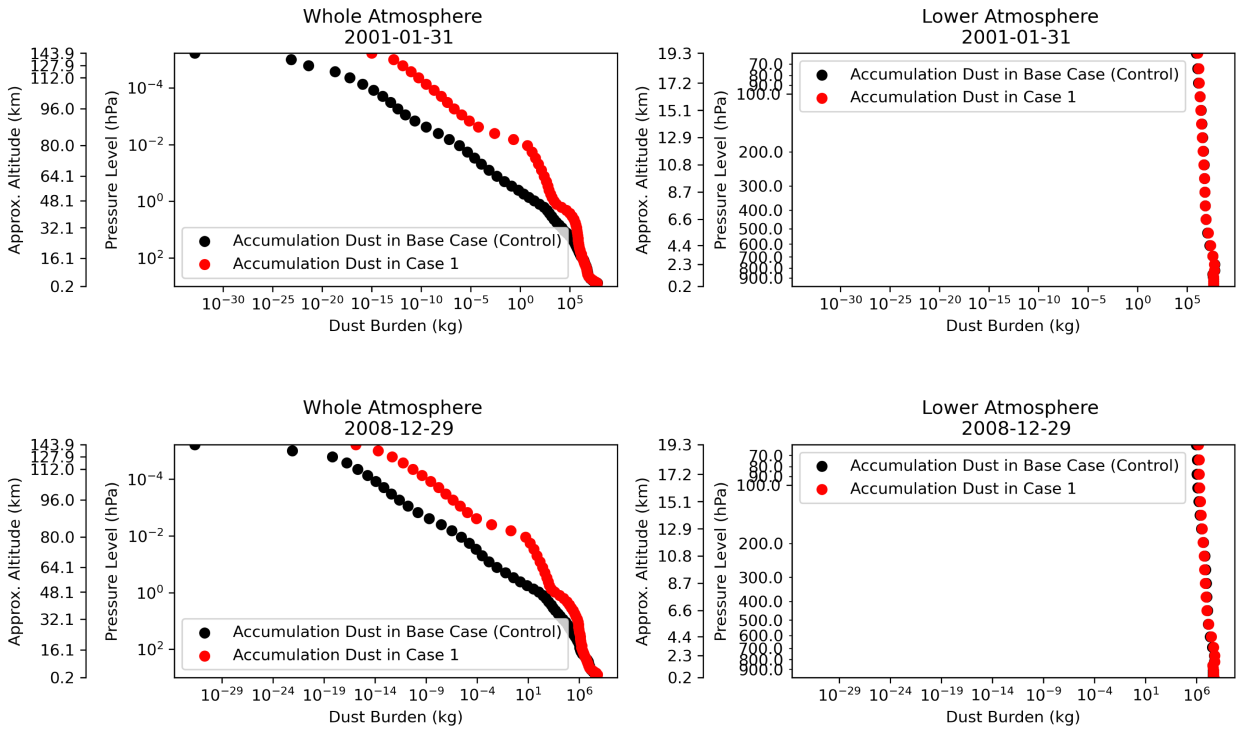

Figure D-1: Vertical Profiles of Accumulation Dust in Case 1 at Different Times

,

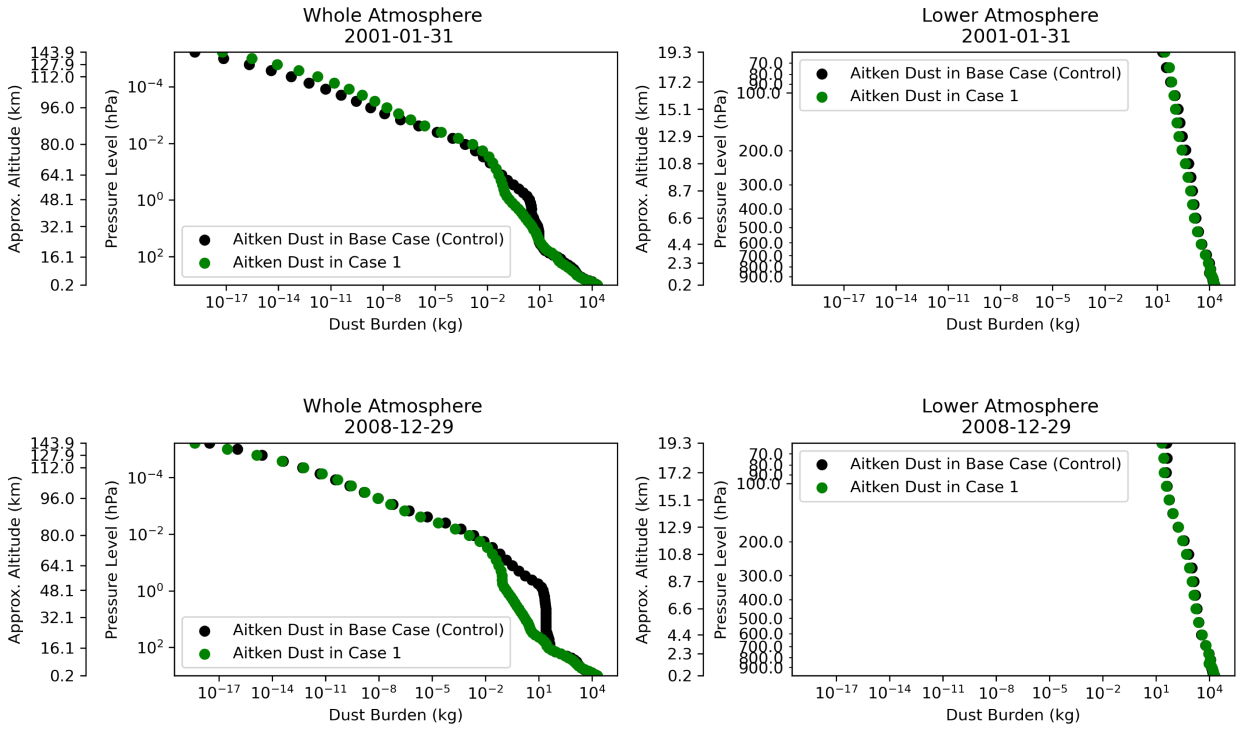

Figure D-2: Vertical Profiles of Aitken Dust in Case 1 at Different Times

,

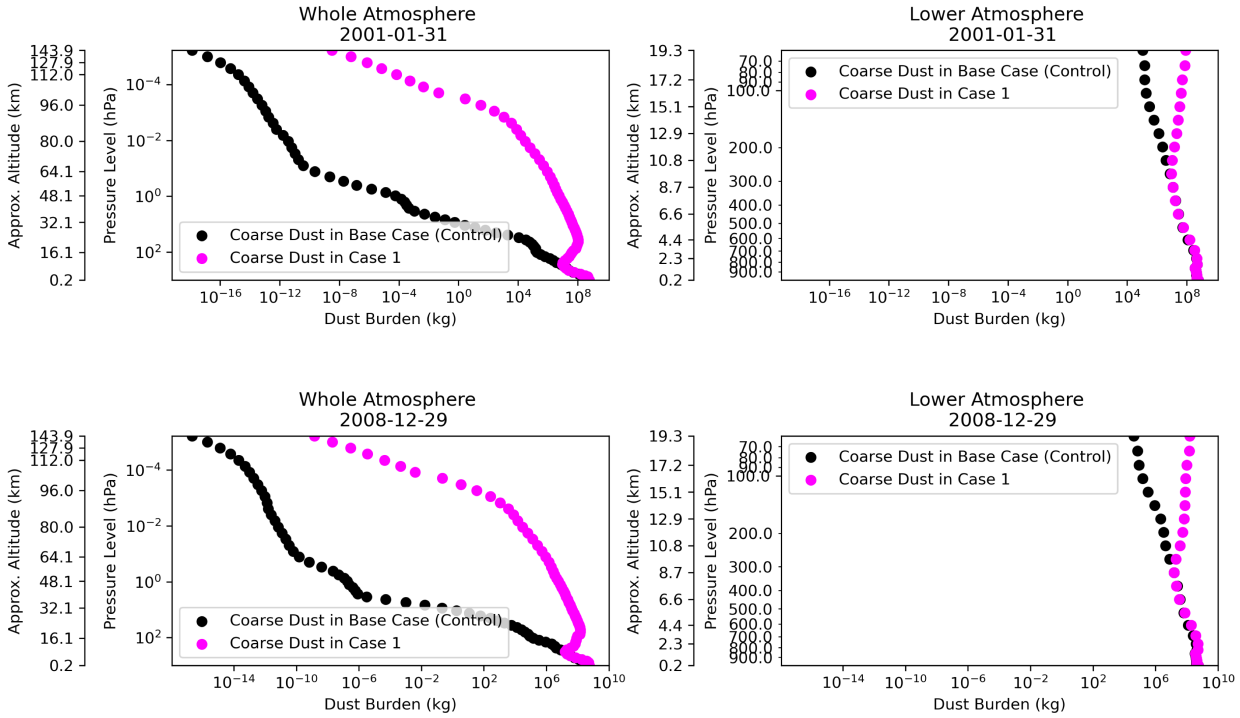

Figure D-3: Vertical Profiles of Coarse Dust in Case 1 at Different Times

,

D.2 Case 2

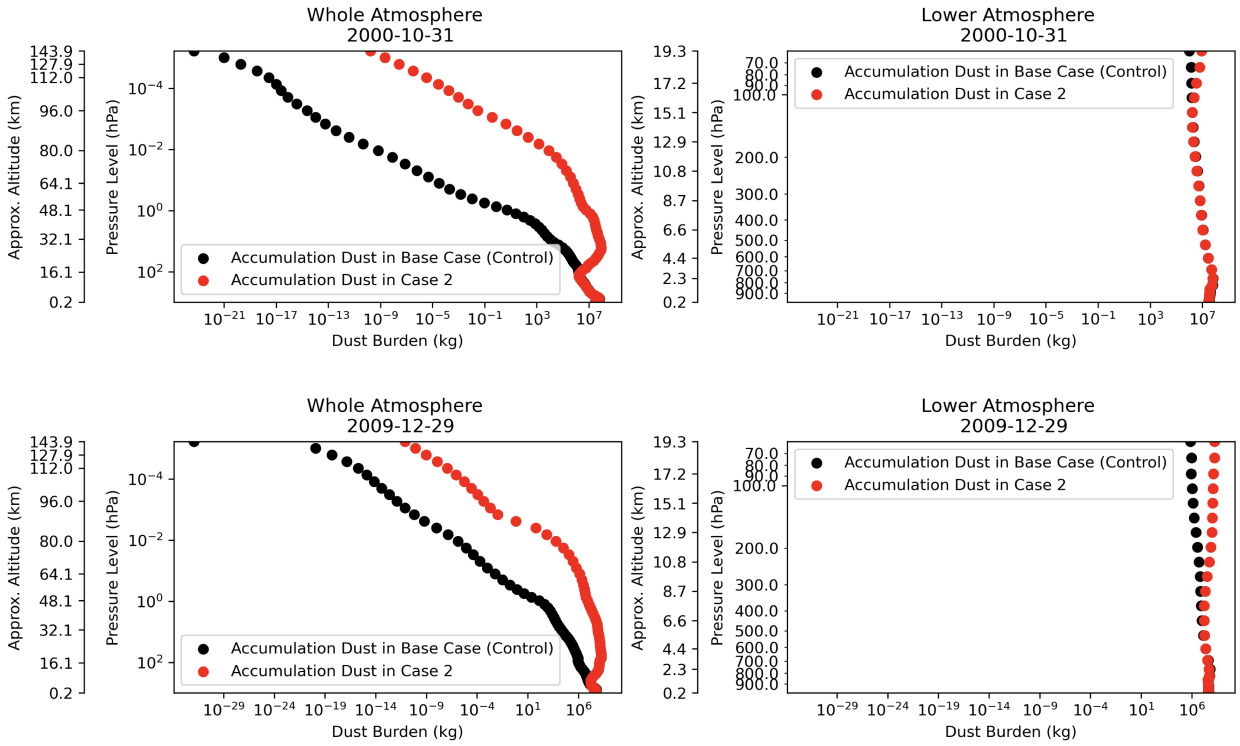

Figure D-4: Vertical Profiles of Accumulation Dust in Case 2 at Different Times

,

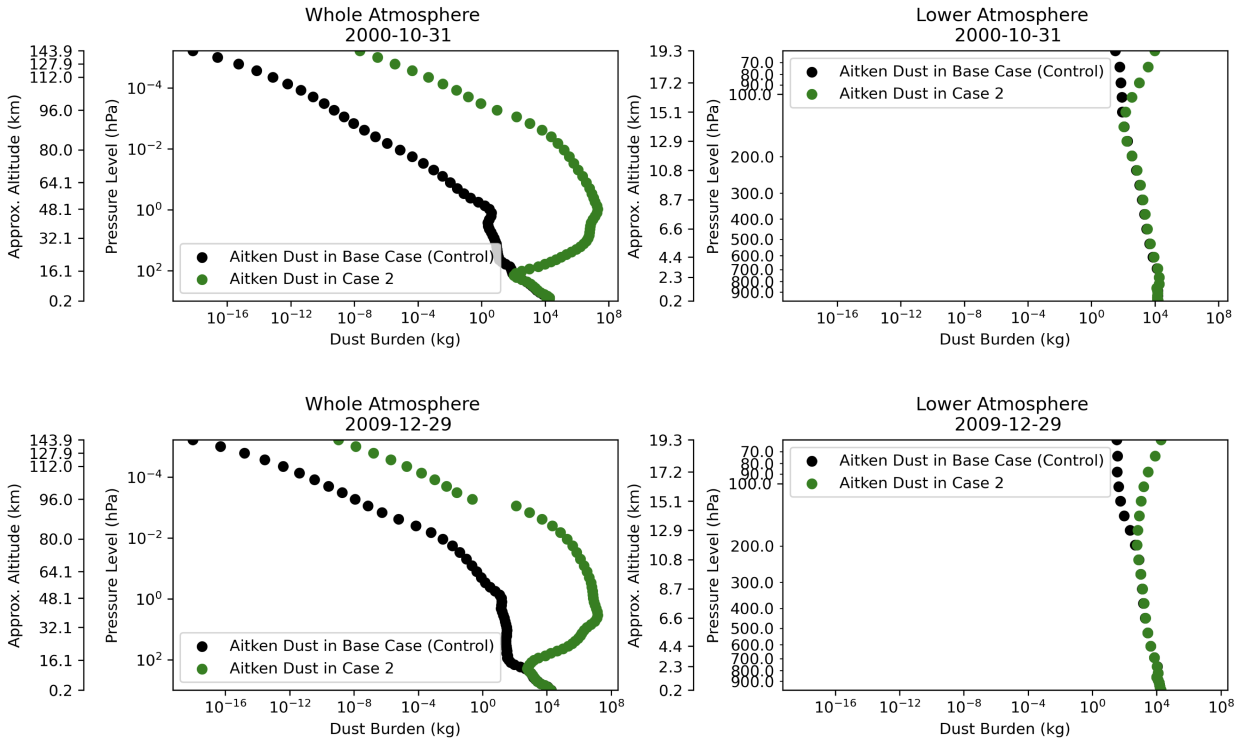

Figure D-5: Vertical Profiles of Aitken Dust in Case 2 at Different Times

,

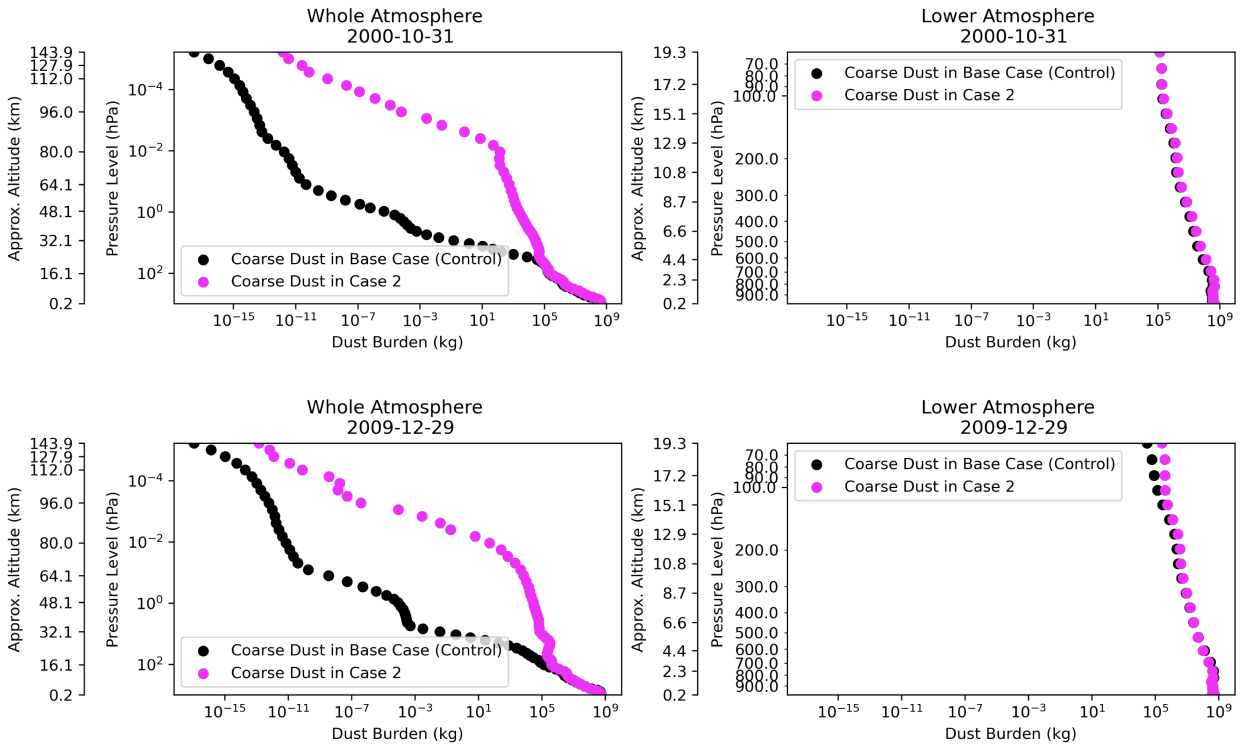

Figure D-6: Vertical Profiles of Coarse Dust in Case 2 at Different Times

,

D.3 Case 3

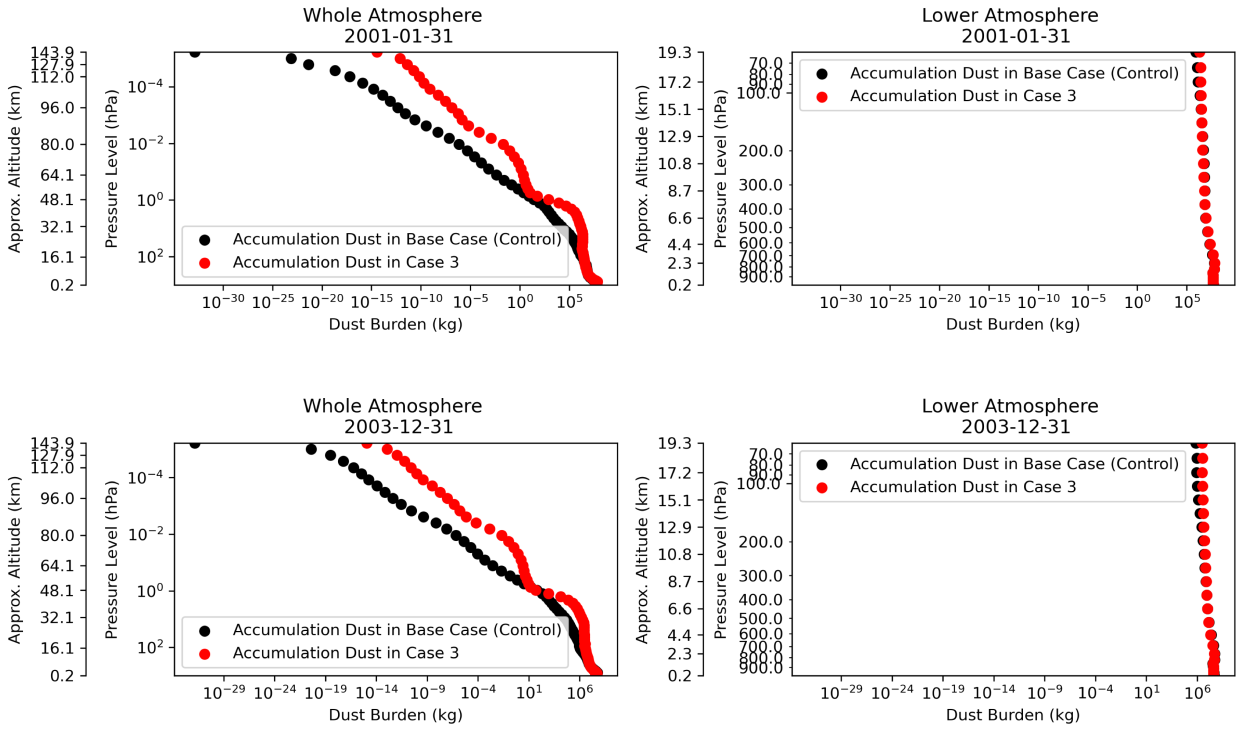

Figure D-7: Vertical Profiles of Accumulation Dust in Case 3 at Different Times

,

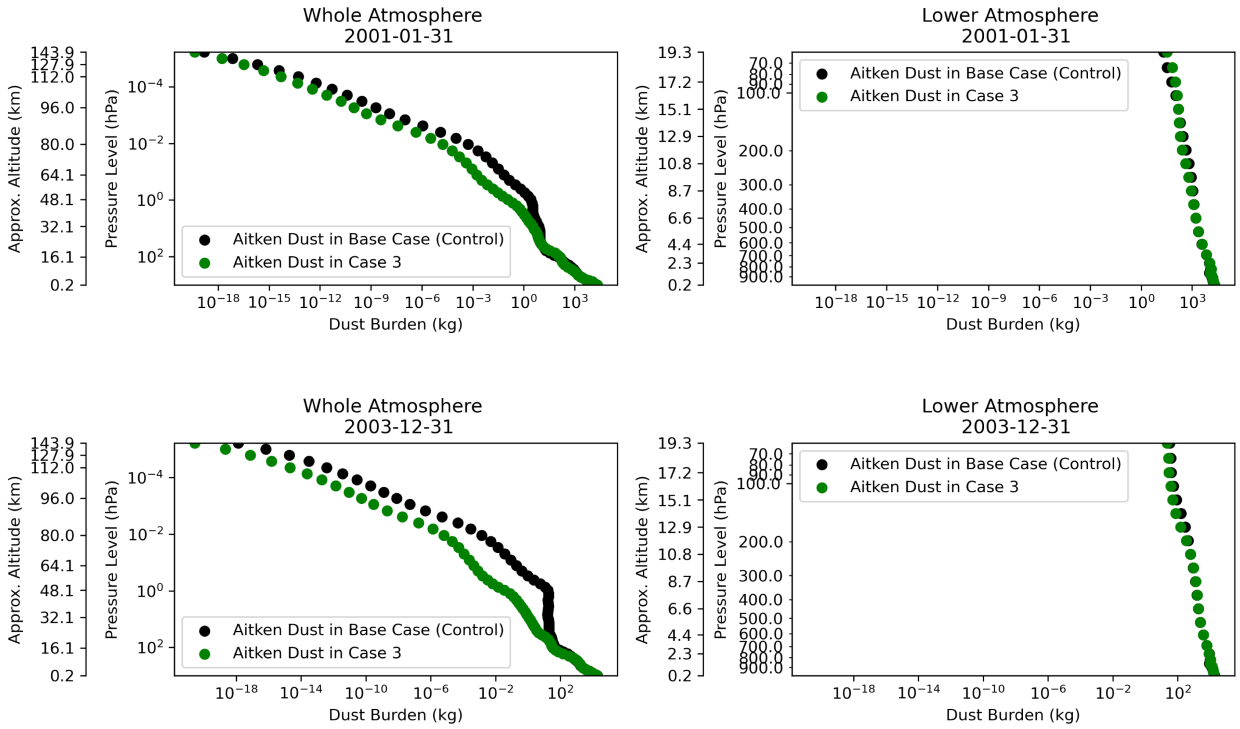

Figure D-8: Vertical Profiles of Aitken Dust in Case 3 at Different Times

,

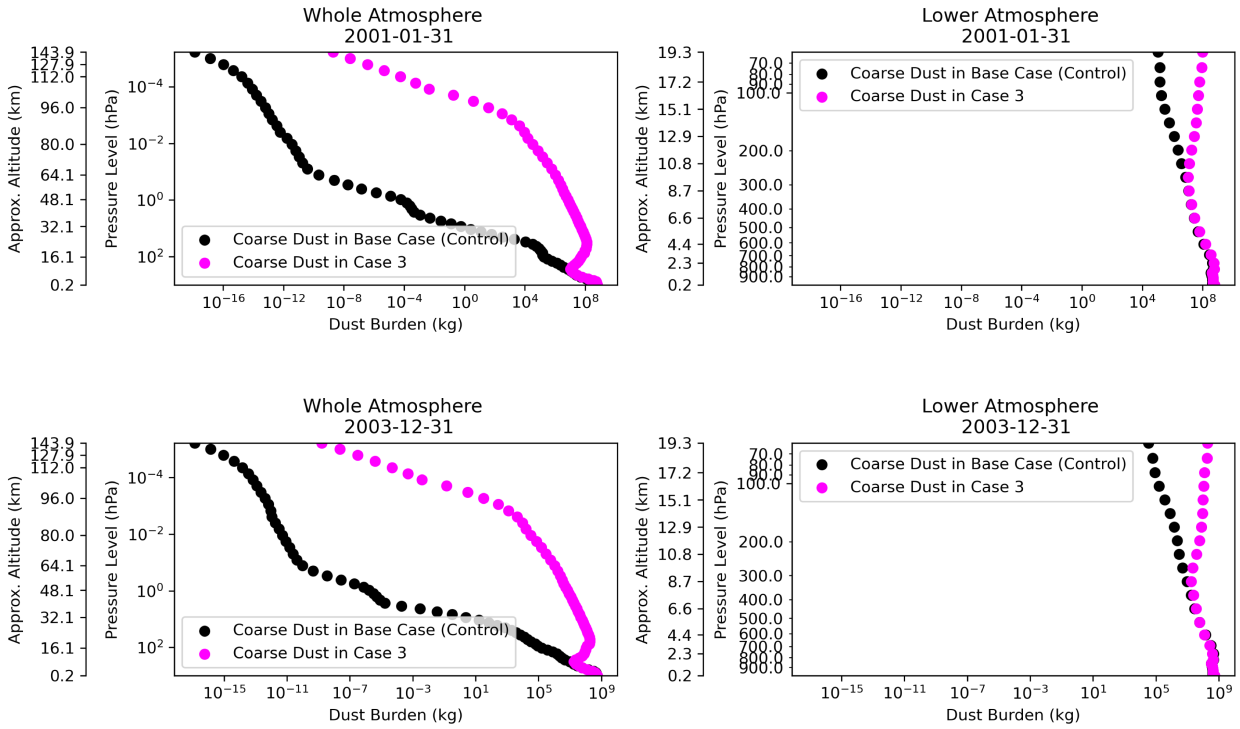

Figure D-9: Vertical Profiles of Coarse Dust in Case 3 at Different Times

,

D.4 Case 4

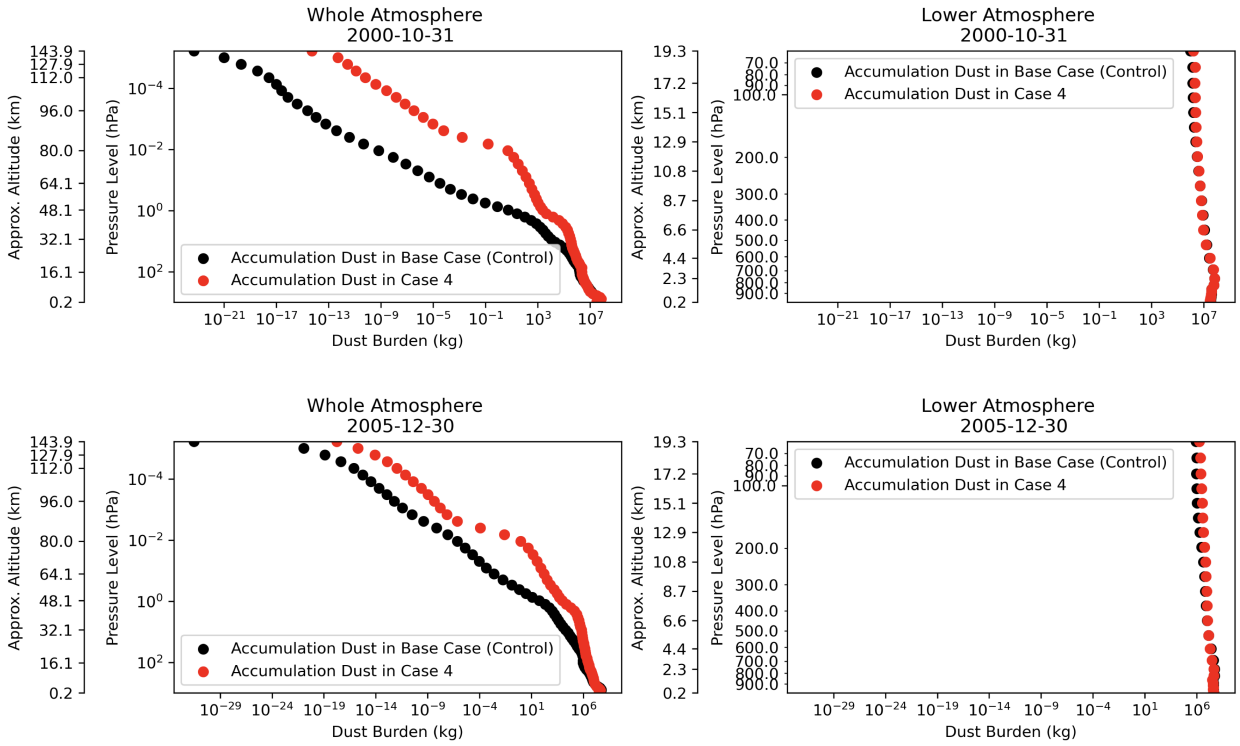

Figure D-10: Vertical Profiles of Accumulation Dust in Case 4 at Different Times

,

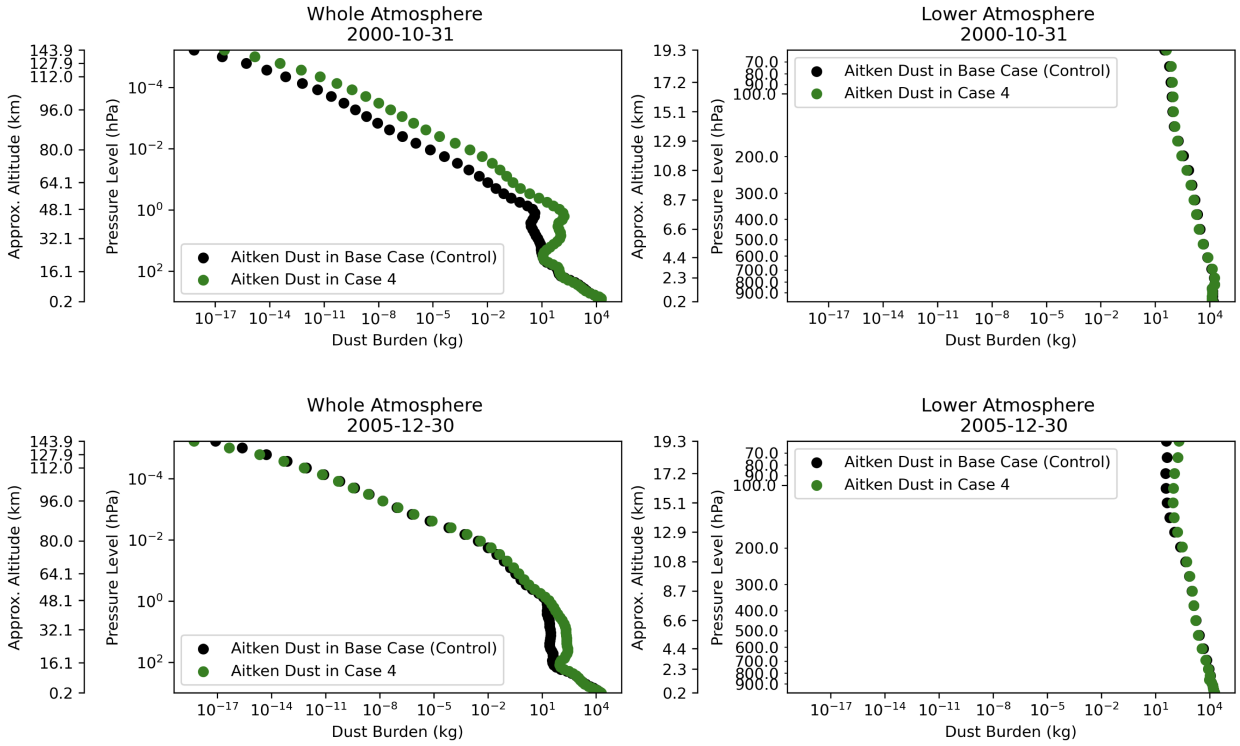

Figure D-11: Vertical Profiles of Aitken Dust in Case 4 at Different Times

,

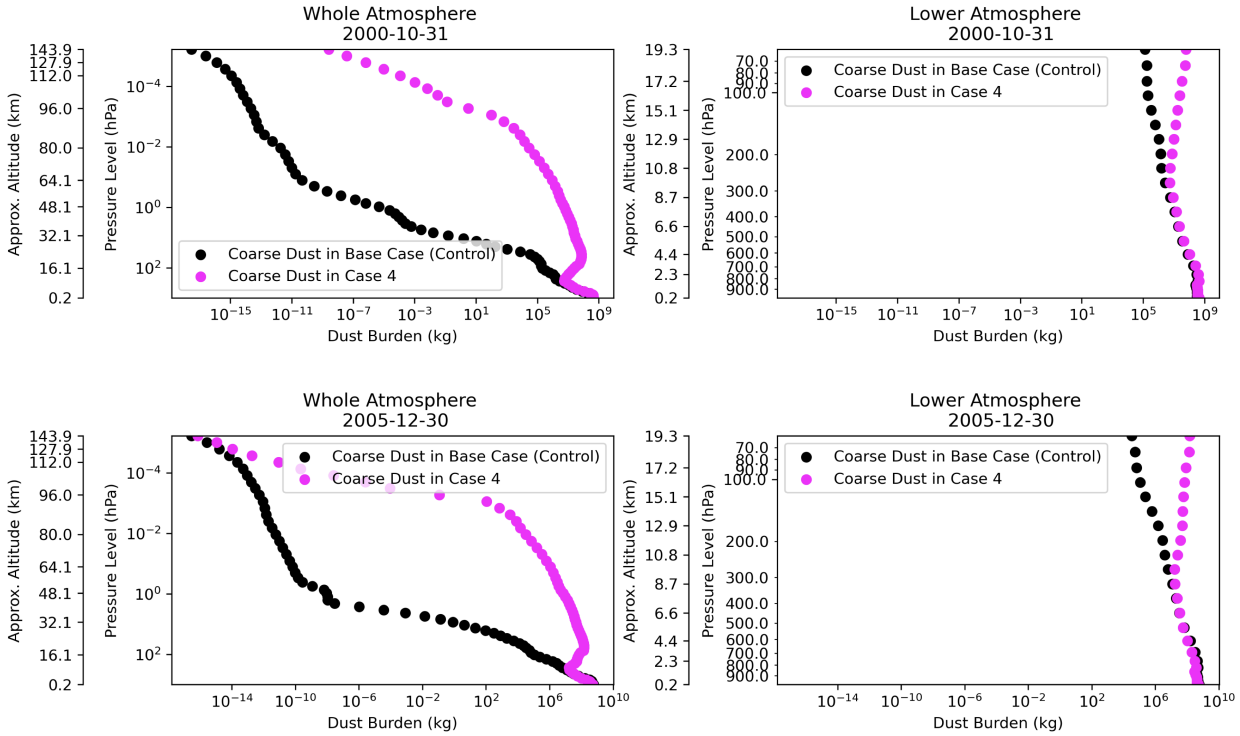

Figure D-12: Vertical Profiles of Coarse Dust in Case 4 at Different Times

Appendix E

Average Zonal Concentration of Reentry Dust Across Test Cases

E.1 Case 1

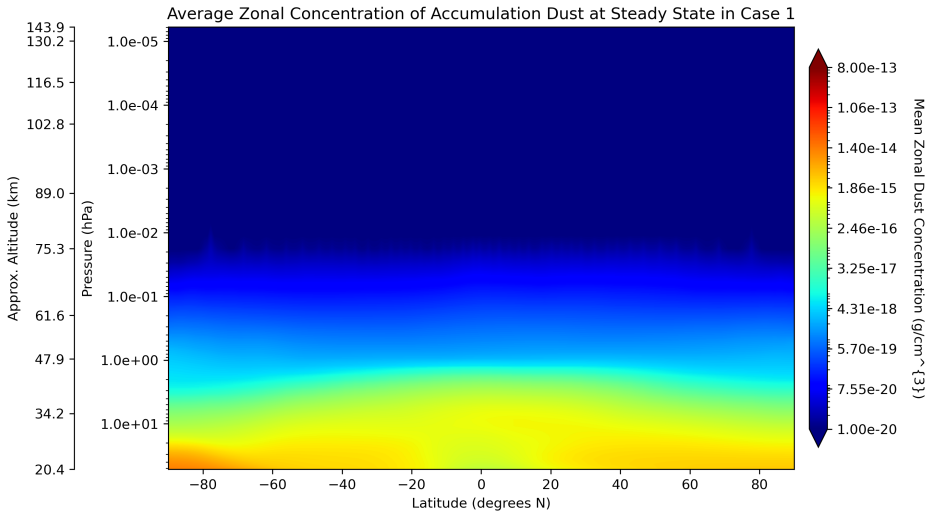

Figure E-1: Case 1: Average Zonal Concentration of Accumulation Dust at Steady State

,

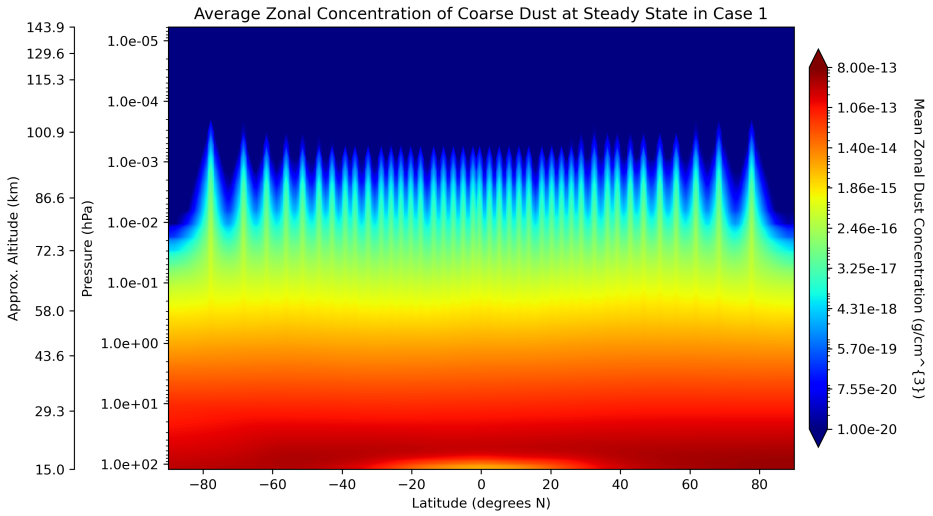

Figure E-2: Case 1: Average Zonal Concentration of Coarse Dust at Steady State

,

E.2 Case 2

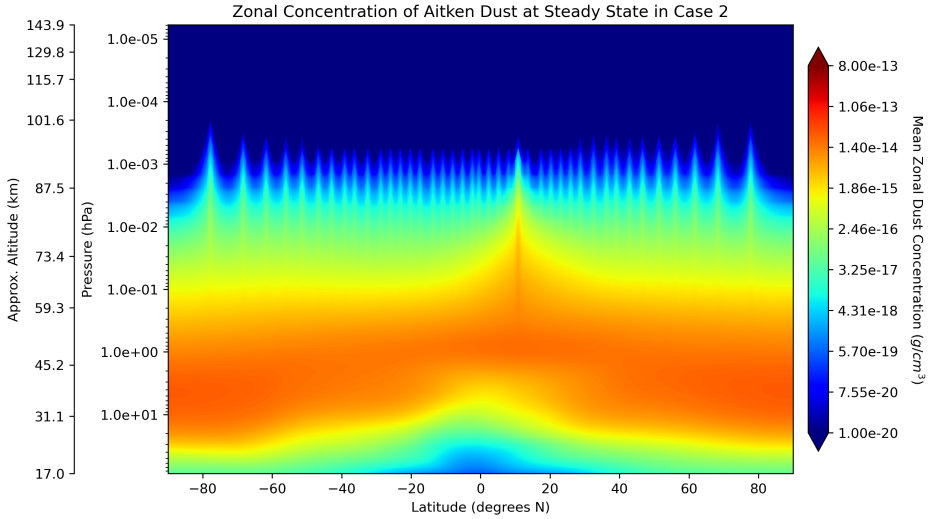

Figure E-3: Case 2: Average Zonal Concentration of Aitken Dust at Steady State

,

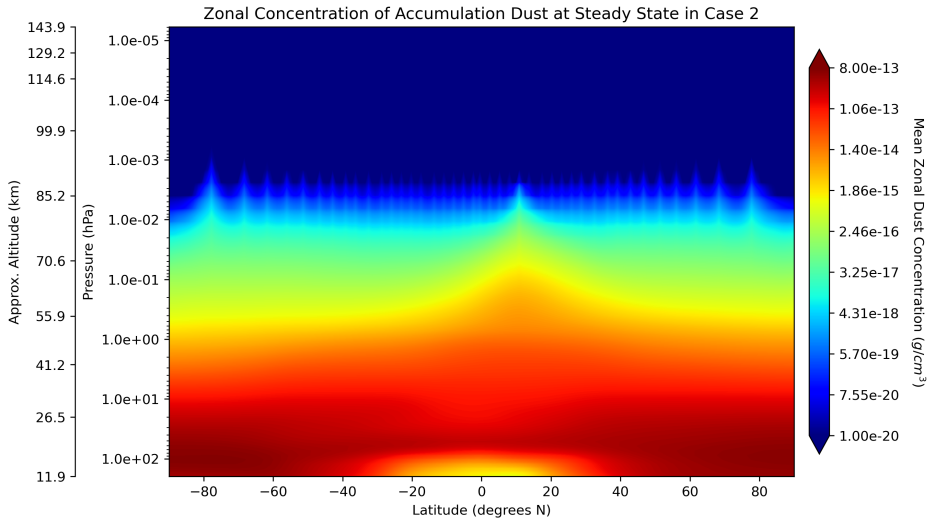

Figure E-4: Case 2: Average Zonal Concentration of Accumulation Dust at Steady State

,

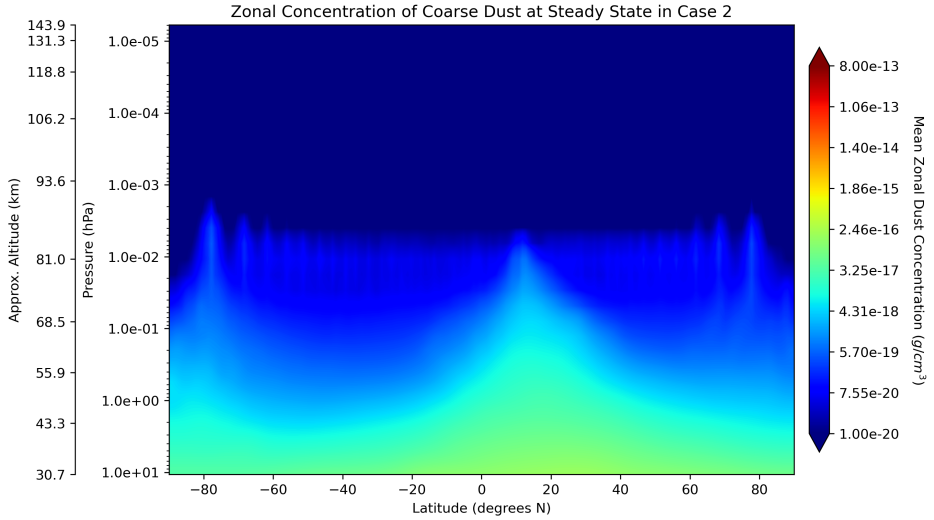

Figure E-5: Case 2: Average Zonal Concentration of Coarse Dust at Steady State

,

E.3 Case 3

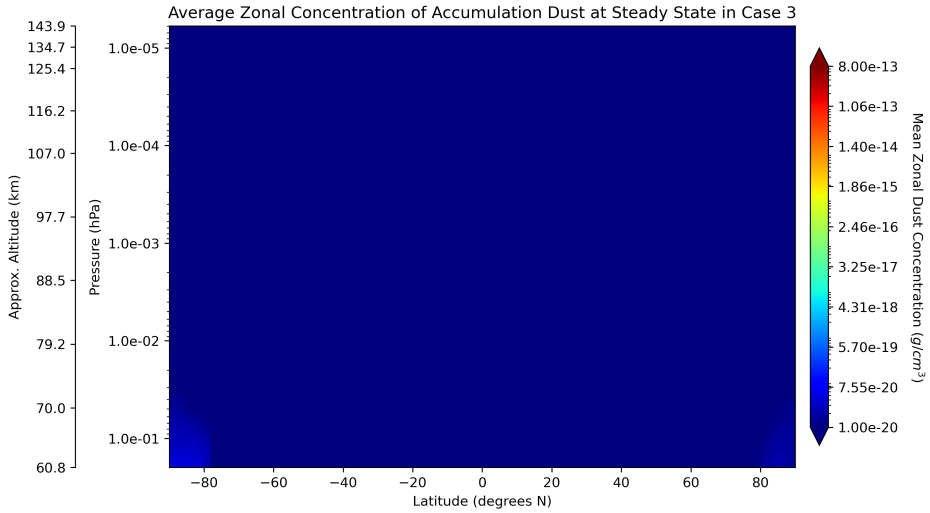

Figure E-6: Case 3:Average Zonal Concentration of Accumulation Dust at Steady State

,

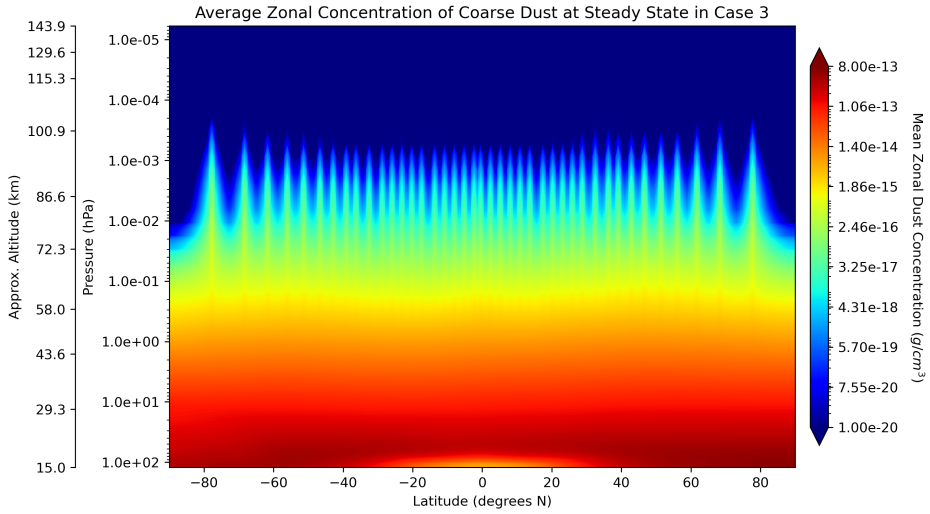

Figure E-7: Case 3:Average Zonal Concentration of Coarse Dust at Steady State

,

E.4 Case 4

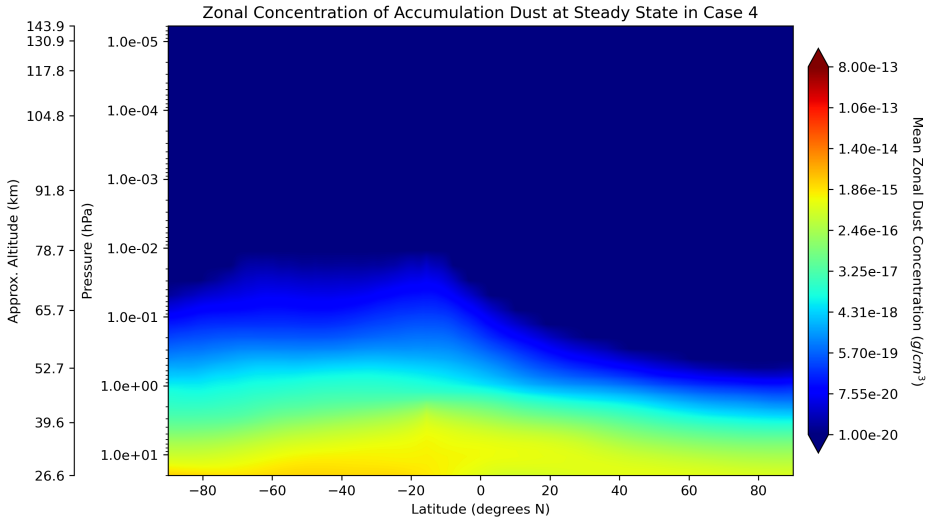

Figure E-8: Case 4: Average Zonal Concentration of Accumulation Dust at Steady State

,

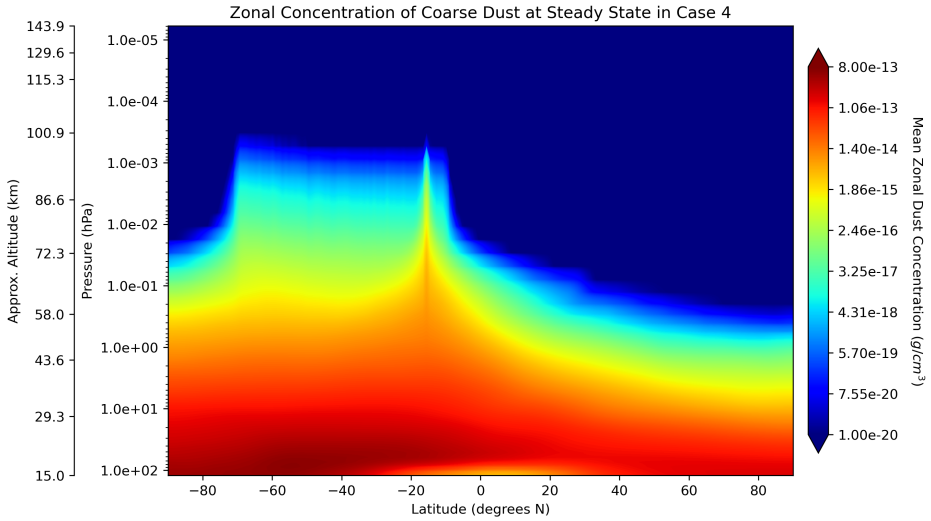

Figure E-9: Case 4: Average Zonal Concentration of Coarse Dust at Steady State

,

Appendix F

Column Sum Distribution of Reentry "Dust"

F.1 Case 1

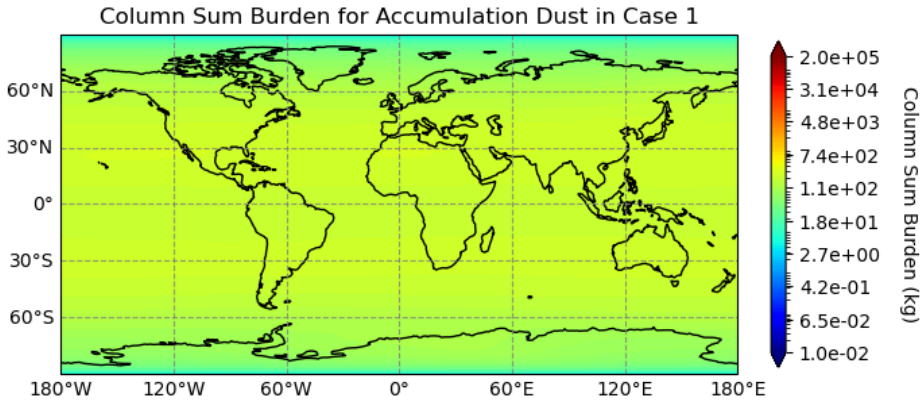

Figure F-1: Case 1: Column Sum Distribution of Accumulation Dust at Steady State

,

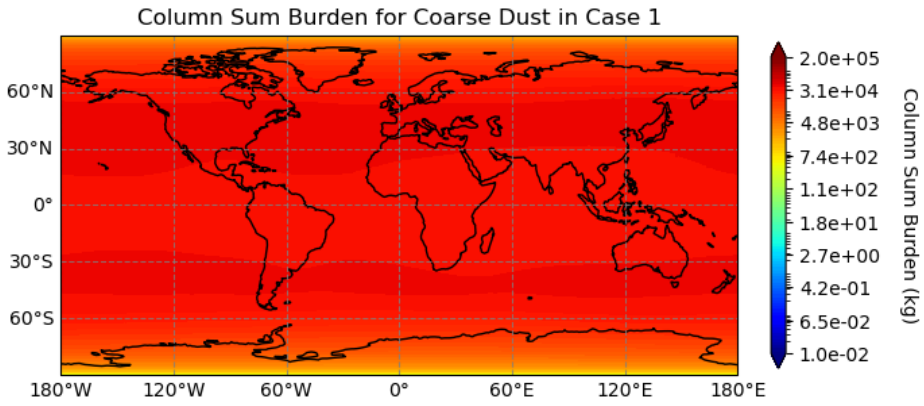

Figure F-2: Case 1: Column Sum Distribution of Coarse Dust at Steady State

,

F.2 Case 2

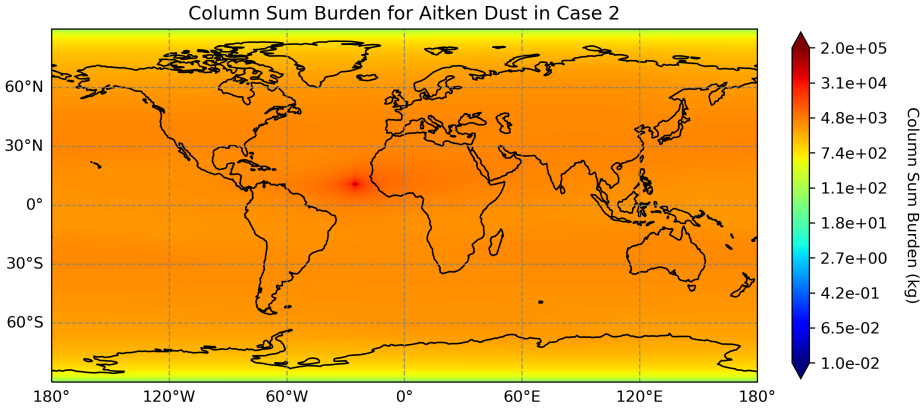

Figure F-3: Case 2: Column Sum Distribution of Aitken Dust at Steady State

,

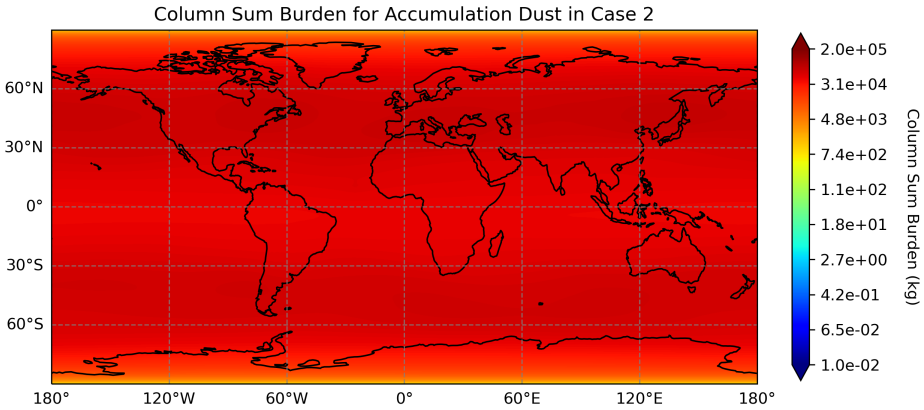

Figure F-4: Case 2: Column Sum Distribution of Accumulation Dust at Steady State

,

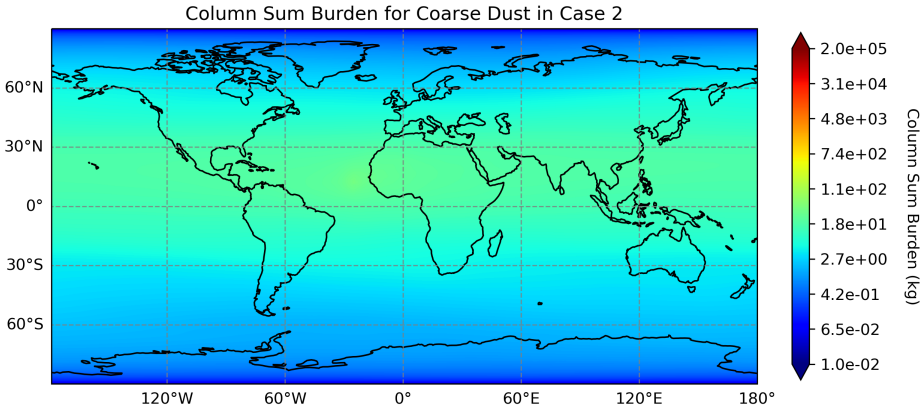

Figure F-5: Case 2: Column Sum Distribution of Coarse Dust at Steady State

,

F.3 Case 3

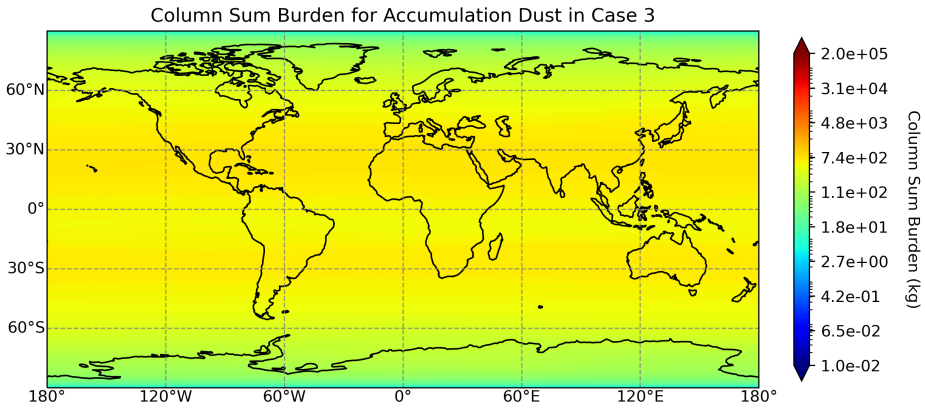

Figure F-6: Case 3: Column Sum Distribution of Accumulation Dust at Steady State

,

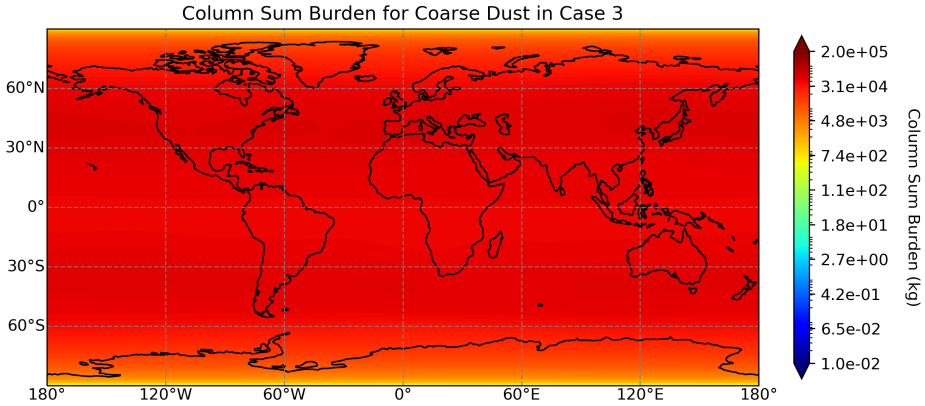

Figure F-7: Case 3: Column Sum Distribution of Coarse Dust at Steady State

,

F.4 Case 4

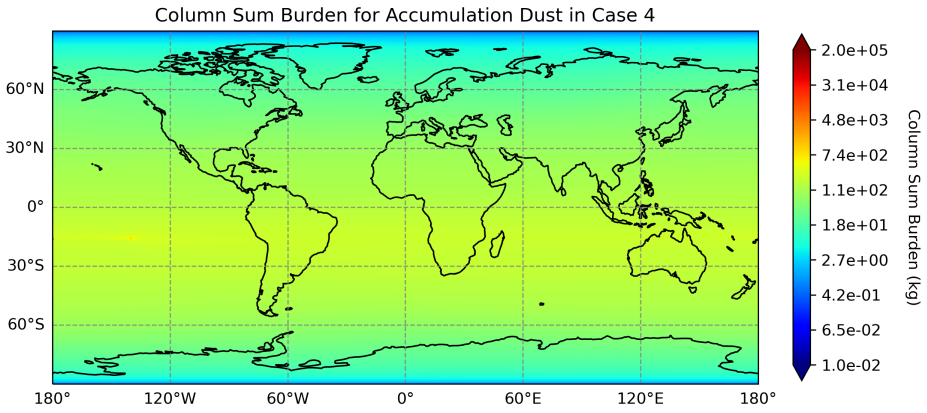

Figure F-8: Case 4: Column Sum Distribution of Accumulation Dust at Steady State

,

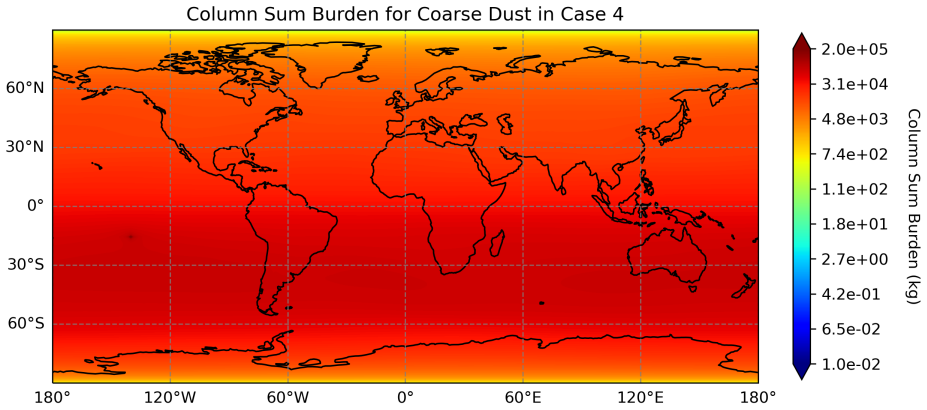

Figure F-9: Case 4: Column Sum Distribution of Coarse Dust at Steady State

,

Appendix G

Aviation Industry Breakdown

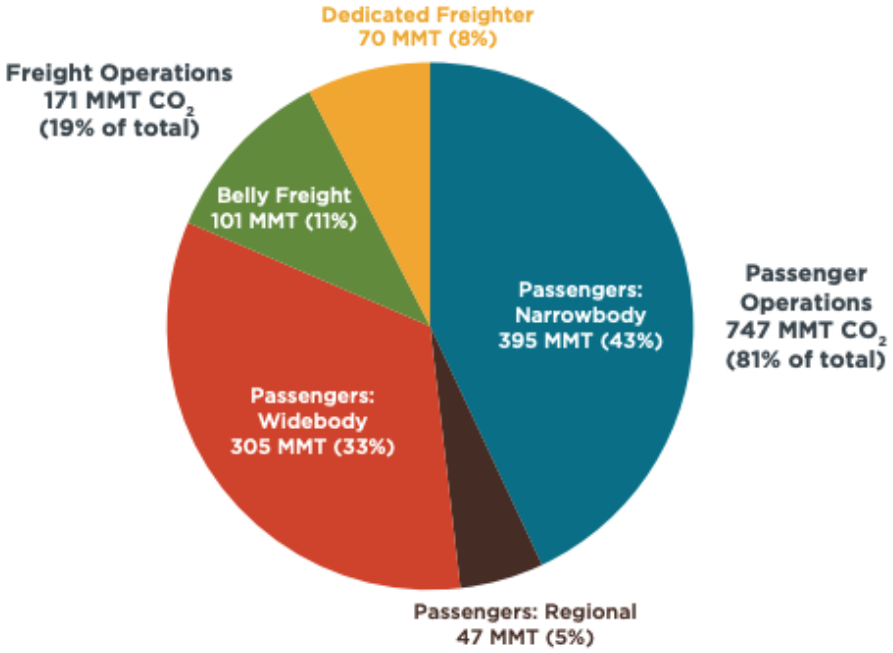

Figure G-1: Commercial Aviation Breakdown in 2018 [16]

,

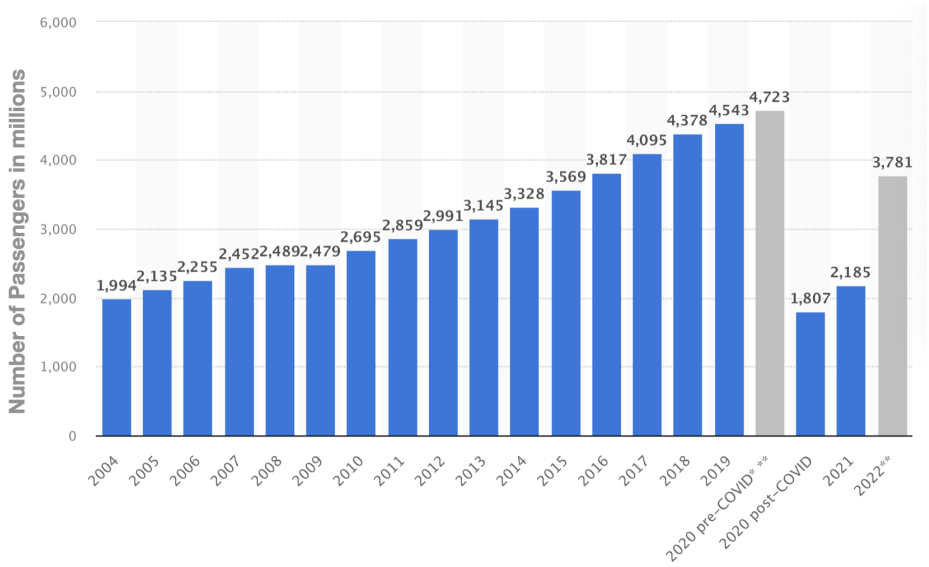

Figure G-2: Aviation Passenger Volumes from 2004 to 2022 [1]

,

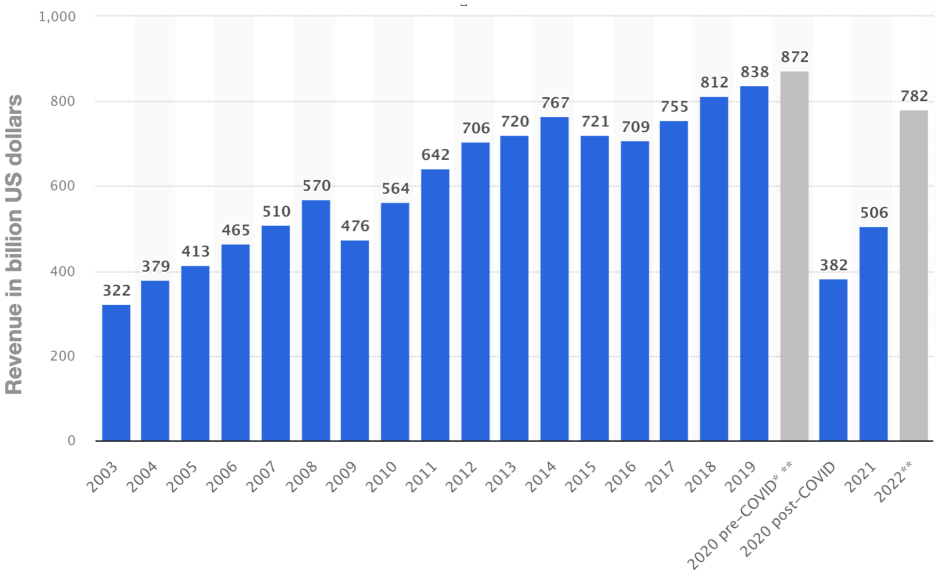

Figure G-3: Aviation Revenues in Billions USD [7]

,